THE ROLE OF HEAT CONDUCTION AT THE LEADING EDGE OF A HYPERSONIC WING.

Sadnu Ram Aggarwal, B. Sc.

Thesis submetted for the degree of Ph. D.

To the Faculty of Engineering,

The University of Glasgow.

Department of Aeronautics and
Fluid Mecnanics.

January, 1971.

ACKNOWLEDGEMENTS

The work embodied in this thesis has been carried out with the financial assistance of a Ministry of Technology contract, No. PD/48/09/ADM.

The author wishes to acknowledge his indebtedness to Professor T.R.F. Nonweiler and Dr. H.Y. Wong for their most valuable advice and guidance in pursuing this work and would like to sincerely thank them. He also acknowledges with gratitude the assistance provided by all those with whom he has come in contact during the course of his research.

LIST OF CONTENTS

List of Figures

LIST OF TABLES

NOMENCLATURE

Principal symbols used throughout this Thesis

SYMBOL		UNITS
h	thickness of plate - Chapter VII only	m
k	Thermal conductivity of the material	$W/m\ ^{o}K$
l	conduction length	m
t	thickness of the conducting material	m
u,v	set of an orthogonal curvilinear co-ordinates	
w	component of displacement normal to x-y plane	m
x,y,z	Rectangular co'ordinate system	
x_o	constant	m
A	area of cross-section	m^2
C	non-dimensional chord length	
E	Young's Modulus of Elasticity	N/m^2
H_o	het input parameter	$W/m^{3/2}$
L	length of conducting surface	m
Q	Local rate of heat flux	W/m^2
S	Semi-span, non-dimensional	
T	Temperature	^{o}K
X	Non-dimensional measure of length in stream direction	
X_o	constant, non-dimensional	
Y	Non-dimensional measure of length in spanwise direction	
α	coefficient of thermal expansion	$/^{o}K$
γ	ratio of specific heats	
ϵ	coefficient of emissivity	
ϵ_x, ϵ_y	components of normal strain	
γ_{xy}	compnent of shear strain	

θ	Temperature, non-dimensional	
λ	Critical buckling factor	
ν	Poisson's ratio	
σ	Stefan-Boltzman constant - 5.67×10^{-8} $W/m^2.{}^\circ K^4$	
σ_x, σ_y	components of normal stress	N/m^2
τ	non-dimensional parameter	
τ_{xy}	shear stress	N/m^2
ϕ	angle of sweepback	
ω	over-relaxation parameter	

Subscripts

$( )_o$	Values of parameters at X = 0
$( )_L$	Values of parameters at X = L

SUMMARY

One of the requirements of the leading edge of a hypersonic wing is that it should be able to withstand the extremely severe rates of aerodynamic heating. By taking the thermal conduction of the material into consideration, the temperature at the nose of the wing may be substantially modified as compared with the case where the boundary layer heating is balanced by radiation alone. The present investigation covering both the two-dimensional and three-dimensional wings shows that not only can the nose temperature be reduced by the inclusion of the effects of heat conduction within the material close to the leading edge but also that the temperature distribution in the leading edge region can be predicted quite accurately.

Making certain simplifying assumptions, we formulate the steady state heat transfer equations within a "conducting plate". The laminar boundary layer heat transfer characteristics at high speeds are adopted here to describe the heating phenomenon over a region close to the leading edge with finite rates of heat flux at the leading edge. The effects of heat conduction are significant over lengths of the order of the "conduction length" only; further downstream the temperatures being quite close to the radiation equilibrium value. This conduction length is a function of parameters such as, the thermal conductivity and the thickness of the material, the rates of heat flux and the temperatures associated with it.

For the two-dimensional plates, we have obtained solutions of the non-linear heat conduction equation by means of three independent numerical methods with the help of a high speed digital computer. A

family of bodies whose streamwise cross-section of the conducting material varies trapezoidally is studied in detail. For such a distribution of the material, the nose thickness is shown to be the most important factor in the determination of the temperature distribution. The theory has been extended to three-dimensional wings to include the effects of finite span and the angle of sweep of the leading edge. The three-dimensional wings may be considered simplified versions of a caret wing which belongs to the wave-rider type of hypersonic wings. The merits of a uniformly rounded apex of a swept wing (subject to a couple of restraints) are compared with the results obtained for the sharp apex.

The two-dimensional theory of conducting plates has been satisfactorily verified by experiments which cover a sufficiently wide range of possibilities represented by some non-dimensional parameter. The experimental technique has also been applied for studies of leading edge heating problems on models the solutions of which are difficult to obtain by numerical methods. In carrying out experimental studies, development of certain instruments such as radiometers and heaters became necessary. Also, property data of the material used for the models had to be acquired by separate investigations.

A preliminary study has also been undertaken to investigate the two-dimensional thermal stresses that may be induced by the actual temperature distributions close to the leading edge. Thermal stability of the leading edge region of plates tapered in thickness (streamwise) is analysed with a view to relate the onset of thermal buckling with the aerodynamic heating. Since the temperature distribution near the

leading edge is closely connected with the heat conducting ability of the material, the criterion used in thermal buckling must be dependent also on this ability of the material in removing heat from the nose downstream.

CHAPTER 1

1. Introduction

In high speed flight the aerodynamic heat transfer from the boundary layer to an aircraft is an important factor and has a profound influence on the design. In particular, the leading edge of a hypersonic wing is subjected to extremely high rates of heat transfer. Regardless of the shape of the leading edge it must be able not only to withstand the high temperatures associated with the aerodynamic heat input but also the thermal stresses induced by the variation of temperature.

Hypersonic heat transfer was first encountered in vehicles re-entering the earth's atmosphere. Such bodies undergo high rates of deceleration for relatively short periods when the "windward" surfaces are subjected to very severe heating. Unless some means of dissipating the heat is provided, the body would simply "burn-up".

There are at least two distinct ways in which orbital vehicles may be brought back to earth; either by using a glider trajectory (in which case the vehicle must provide aerodynamic lift) or on a ballistic trajectory (where the vehicle has considerable aerodynamic drag but hardly any lift). The ballistic re-entering body is subjected to extremely high rates of heat transfer for short periods as compared with the glider type of bodies which undergo lower rates of heat transfer over much longer flight times. For a spacecraft returning from orbit the total amount of heat generated per unit body mass is roughly equal to $\frac{C_f}{C_D} \cdot \frac{V^2}{2}$ where C_f is the average skin-friction

coefficient, C_D is the coefficient of total drag, and V is the initial velocity of the vehicle (reference 1). Straightaway it is evident that in order to minimise the total heat input the ratio $\frac{C_f}{C_D}$ should be minimised; that is, the fraction of the total resistance to motion represented by friction drag should be minimised. For a sphere this ratio might be about 0.01 but for a flat plate at low angles of incidence it would be close to unity. A simple calculation (using the relation just quoted) shows that the total heat transferred to a decelerating body re-entering the atmosphere at orbital speed can exceed the heat capacity (including the heats of fusion and evaporation) of most known materials if the body is streamlined.

Upto now hypersonic heat transfer has been encountered in ballistic missiles and space vehicles returning to earth. In both cases a ballistic re-entry is employed. Ablative heat shields are provided to absorb the heat energy converted from the initial kinetic energy of the body. For these types of bodies, radiation cooling of the surface is negligible compared with the heating rates being input.

One can distinguish two extreme types of ballistic re-entry heads; the low-drag (e.g. a blunted cone) and the high-drag head (e.g. a hemispherical forebody). The high drag decelerates at a higher altitude than the low-drag head (reference 2). Because the high drag head has a higher value of $\frac{C_f}{C_D}$, it undergoes a higher total input of heat per unit mass than the low drag head. A high drag head also has a lower velocity in the final part of the trajectory and has been chosen for the manned re-entry capsules. On the other hand, the low drag-head because of its high terminal velocity, gives greater accuracy

(less influenced by winds) and has been adopted for long range missile warheads. The average heat flux to the re-entry bodies is proportional to $\frac{1}{2} \cdot \frac{m}{S} \frac{C_f}{C_D} \cdot \frac{V^2}{2}$ where m is the mass of the vehicle and S is the total wetted area. For bodies of a given mass to wetted surface area the heat flux (quantity of heat per unit area) increases as the ratio $\frac{C_f}{C_D}$ increases i.e. a low drag head is subjected to a higher value of average heat flux as compared with the high drag head. Whereas if we consider a particular type of head (e.g. the high drag head), then the average heat flux value can be decreased by reducing the ratio of the mass to the wetted surface area of the re-entering vehicle.

The present outlook envisages the design of spacecraft which are capable of flying back to earth and landing like "conventional" aircraft. One of the requirements dictated by economic factors is that the space vehicle should be re-usable. One answer is to use lifting-body or winged-body configurations. However, as we have seen above, as the body is streamlined the total heat input to it is likely to be large. On the other hand the effect of increasing the lift to drag ratio $(\frac{L}{D})$ is to increase the time taken during the re-entry phase of the flight, so that the average rate of heat transfer may not be unduly large and cooling by radiation presents a reasonable possibility.

For the streamlined bodies, protection of the internal structure by heat sink and ablative cooling becomes impractical because of the large mass needed. Both these forms of cooling are attractive only where the structure is subjected to limited total heat transfer. In the case of ballistic trajectories, once re-entry has been effected, there is little control on the actual point of touchdown.

As the ratio $(\frac{L}{D})$ is increased the spacecraft can glide down to any point within a much larger area (the so-called "foot-print").

In general, with an increasing nose radius of a wing the ratio of lift to drag $(\frac{L}{D})$ shows a decrease. If the wing is made sharper at the leading edge, the problem of aerodynamic heating becomes one of the spatial distribution of heat input (as against the average rate of heat transfer being excessive). In this context, one design philosophy has been to utilise wing leading edges with large nose radii (of the order of 1m., say). By maintaining a small curvature of the surface a near uniform intensity of heat input is obtained for the leading edge, which will in equilibrium be balanced by the amount of heat being radiated away from the surface. It has been proposed to use such a wing for booster vehicles which will assist in the take-off phase of spacecraft. After separating from the main structure employed in the launching, which by then has reached hypersonic mach numbers, the booster vehicles will fly back to land like conventional aircraft. Using suitably rounded leading edges, it is possible to maintain the equilibrium temperatures to within an acceptable level. However, when this concept of designing a large nose radius so as to provide minimum energy transfer at hypersonic speeds [3] is used for vehicles re-entering the atmosphere with orbital speeds, the equilibrium temperatures that can be expected are still beyond the operating limit of present day high-temperature superalloys.

Where long range hypersonic flight within the earth's atmosphere is to be undertaken or a very large foot-print area is desired, the range of the aircraft becomes of primary importance. Since the range

is proportional to $\frac{L}{D}$ it is obvious that the $(\frac{L}{D})$ ratio must be maximised. For hypersonic mach numbers, one solution lies in the use of slender wings and especially "sharp-edged" leading edges. In this context, Nonweiler[4,5] was the first to suggest the use of caret wings (also called the waverider or inverted "V"). In general the heating problem with sharp leading edges is one of overcoming the spatial distribution of heat intensities, particularly the area close to the nose of the wing. Theoretical as well as experimental evidence gathered by various researchers indicates that the nose of a slender wing is subjected to extremely high rates of heat flux which decrease very rapidly with the distance from the leading edge. Radiation still provides the bulk of cooling of the leading edge but is found to be inadequate at the nose where the radiation equilibrium temperature can tend to the local thermometer value (which is the adiabatic wall temperature). The magnitude of the thermometer value at the nose can be of the order of several thousand degrees which is clearly beyond the operating limit of most refractory materials.

One method of cooling that has been suggested is by internal convection, and / or transpiration whereby the coolant is injected into the boundary layer. Both these processes require complex and expensive manufacturing and fabrication techniques, heavy pumping gear necessary to circulate the coolant and the equipment required to ensure that the operation of the system is fail-safe. Transpiration cooling necessitates the carrying of a bulk of the coolant. On the other hand if the fuel is used as the medium for convective cooling, it is limited to the specific heat of the fuel. Vapourisation of the coolant is to be

avoided since it would require a much higher volume to be pumped. Also the fuel may become chemically unstable above a certain limiting value of temperature.

There is an alternative solution for the aerodynamic heating of "sharp-edged" leading edges where the material properties of the leading edge are employed to reduce the maximum equilibrium temperatures. In this investigation we demonstrate how the mechanism of thermal conduction (for reasonable values of conductivity) helps to redistribute the heat transfer within the structure of the leading edge and thereby maintain the nose temperature to within an acceptable level for presently available heat-sustaining materials. Heat is conducted away from the nose at the expense of heating regions further downstream. The surface temperature everywhere is in equilibrium; the average rate of heat input being equal to the quantity of heat being radiated away.

Steady state conditions at the surface can be expected to exist when the hypersonic flight times exceed the time required to heat up the structure to the equilibrium value. This value of time would depend on the heat capacity of the wing and the net heat input to the wing, which in turn depends upon the time history of the flight. In the case of spacecraft re-entering the atmosphere, the duration of flight may well be less than the time required for steady state conditions to be established. Since the nose region of a "sharp-edged" leading edge is subjected to extremely high rates of heat transfer (the boundary layer theory predicting an infinite rate), equilibrium conditions close to the nose of such wings are likely to exist throughout the flight at hypersonic speeds.

In principle, there should be no difficulty in applying numerical processes to obtain solutions (with the help of a digital computer) of the steady state temperature distributions within a conducting and radiating body subjected to aerodynamic heat transfer. However, where the body is as complicated as an aircraft structure, and the heating is aerodynamic in orgin, the problem can well be beyond the reasonable capabilities of present day computers, unless some simplifying assumptions are introduced in setting up the problem.

A simplified approach to the problem was first introduced by Nonweiler[6,7] in estimating the leading edge temperatures by what may be called "slide-rule" methods. The simplifying assumptions consisted of idealising the leading edge section of the wing as a "conducting plate" whose thickness is small compared with the chordwise dimension of length. With the possibility of sustained hypersonic flight, in the foreseable future, other researchers[8,9,10] have taken interest in this problem. In particular, reference 10, describes, in detail, the development of experimental apparatus to test the theory put forward by Nonweiler and also presents preliminary results.

In the present investigation, a systematic study is undertaken into the role of heat conduction at the leading edges subjected to aerodynamic heat transfer at hypersonic mach numbers. It is shown that heat conduction within the body can play a predominant role in the determination of the temperature distribution close to the leading edge. Further downstream the temperature everywhere tends to the well-known radiation equilibrium temperature (which has been computed in reference 11, for a range of mach numbers and altitudes for laminar as well as

turbulent boundary layers). We have developed numerical methods to obtain solutions of the governing heat transfer equations. The theory of conducting plates[10,12] has been extended to include the effects of finite span and sweepback. Wherever necessary the assumptions made in the numerical solutions have been experimentally verified. The calculated temperature distributions are also used in the investigation of the thermal stability of the leading edge.

Basically, we have in mind geometrically thin and "sharp" edged wings. More precisely we envisage a leading edge radius of 1cm. or so, rather than 1m., which would be sufficient to alleviate the intense heat transfer rates to the nose of the wing. The excessive heat input at the leading edge is conducted within the body to regions further downstream where the heat transfer is not quite so severe.

If the conducting material is excluded from the leading edge, the problem becomes trivial and the radiation equilibrium or the "thermometer" value at the leading edge is obtained which can be considerably higher than that predicted in this study.

In chapter II we discuss the factors that influence the aerodynamic rates of heat transfer to the leading edge from a hypersonic viscous boundary layer. Since as we shall see later, we need only solve the equations over a short length from the nose of the wing, it is reasonable to assume that the boundary layer will stay laminar over this region. At hypersonic mach numbers, the heat transfer to slender wings can be predicted with reasonable accuracy by considering the case of a flat plate. We outline how factors such as real gas effects, leading edge bluntness, surface irregularities, wing incidence, pressure gradients

and so on can be expected to affect the heat transfer distribution close to the leading edge of a hypersonic wing.

In chapter III we outline the basic assumptions of the conducting plate theory (which is discussed in greater detail in reference 12). Theoretical solutions are presented in a parametric form for two-dimensional leading edges. Temperature distributions are calculated numerically for the aerodynamic heat transfer which is taken to vary as $x^{-\frac{1}{2}}$ (x being measured from the leading edge). For such a variation of heat transfer, the governing laws of similarity can be derived[12]. Certain similarity relations suggest how laboratory experiments in a relatively low temperature environment may be scaled up to provide information of practical value, and vice versa. The use of the $x^{-\frac{1}{2}}$ law predicts an infinite rate of heat transfer at the nose of the wing. Realistic forms of aerodynamic heating can be obtained by a simple modification whereby the rates of heat transfer are taken to vary as $(x + x_o)^{-\frac{1}{2}}$ (where x_o is a small constant). The influence of the constant x_o on the temperature distribution is investigated. In Chapter IV, by using the specially designed reflector (reference 10), the radiation from an electric filament is used to obtain heat distributions resembling aerodynamic heating near the leading edge. By improving some of the apparatus as well as experimental procedures, good agreement has been obtained with the theoretical solutions (using the relation $(x + x_o)^{-\frac{1}{2}}$ for the variation of heat transfer) over a range of leading edge geometries. It is also intended to use the reflector to investigate certain conditions which would still be troublesome to study theoretically.

The two-dimensional leading edges are extended to three-dimensional

wing shapes in Chapter V. Some of the results of Chapters III, IV and V are also presented in reference 13. The effects of finite span and sweepback are found to be slight, even at extreme angles of sweepback. Two methods are used to demonstrate how to counteract the local rise of temperature at the apex of a pointed swept wing. Wherever necessary, assumptions are made regarding the boundary layer heat transfer consistent with the flow over a caret wing (or the waverider), first suggested by Nonweiler[4,5] for hypersonic flight regimes. In Chapter VI details are given of a heater capable of producing reasonable variations of heat transfer over delta plan forms. Away from the leading edge region, the heater is capable of providing higher gradients of heat transfer than those predicted by the $x^{-\frac{1}{2}}$ distribution. The theory of conducting plates has been successfully applied to calculate the temperature distribution under experimental simulation of aerodynamic heat transfer.

The temperature distributions calculated in Chapter III are used in the investigation of thermal stability of the leading edge in Chapter VII. In particular we show the significance of the leading edge thickness in the determination of the temperature distribution as well as of the onset of thermal buckling.

Finally, in Chapter VIII an overall discussion and conclusions regarding the role of heat conduction at the leading edge of a hypersonic wing are presented.

CHAPTER II

2.1. Aerodynamic heat transfer to hypersonic leading edges of slender wings.

In order to determine the role of heat conduction in the leading edge region of a hypersonic wing, we need to express the variation of aerodynamic heat input along the surfaces in a general form. In the present investigation we use a solution [1,7,14-16] of the equations of the classical laminar boundary layer theory as the basis for defining the variation of heat transfer. The heat transfer distribution is expressed by the simple relation,

$$Q \propto x^{-1/2} \qquad (2.1)$$

where x is the distance from the leading edge, measured along the surface.

The formulation of the relevant simplified boundary layer equations from the more general Navier-Stokes equations requires the following assumptions to be made regarding the hypersonic ($M_\infty >> 1$) fluid flow:

1. The gas in the boundary layer acts as a homogeneous medium.
2. Effects of finite relaxation time are ignored.
3. The Reynolds number is large compared with unity - implying that the boundary layer thickness is very much smaller than the length of the surface.
4. The flow in the boundary layer is laminar.
5. The pressure gradient along the surface is zero.
6. Low-density effects are negligible - which excludes the consideration of slip velocity and temperature jump at the surface.

7. The wall temperature is constant, or negligible compared with the recovery temperature.

8. The flow is two-dimensional in character.

As a consequence of assumption 5, equation (2.1) is valid for unseparated boundary layers only.

2.2. Factors influencing the variation of heat transfer.

We shall now examine more critically each of the assumptions, in turn, which lead to the solution expressed in equation (2.1).

2.2.1. Real gas effects.

Perhaps the most important factors to be taken into account when considering flight at extreme mach numbers are the real gas effects. For increasing mach number, the recovery temperature (T_r) of the boundary layer goes up very roughly as M_∞^2. Even at relatively low temperatures (around $1000^\circ K$) the vibrational modes of freedom of oxygen and nitrogen molecules are sufficiently excited to affect the specific heats of air. At around $M_\infty = 7$ when T_r is about $2000^\circ K$, oxygen molecules in the air start to dissociate. Beyond $M_\infty = 10$, corresponding to $T_r > 4000^\circ K$, nitrogen molecules undergo dissociation. At higher temperatures still ($> 9000^\circ K$) the oxygen atoms begin to ionise, followed by the ionisation of nitrogen molecules at even higher temperatures. These chemical reactions within the boundary layer reduce the stagnation as well as the recovery temperature considerably because a part of the frictional energy goes into the breaking of molecular and electron bonds. Under these conditions air no longer behaves as a gas made up of diatomic molecules and the transport properties of air

(viscosity, specific heats, conductivity etc.) deviate substantially from those assumed for a perfect gas.

The relation expressed in equation (2.1) is still valid for a laminar dissociated boundary layer, provided that the gas can be considered either,

a) as in thermodynamic equilibrium, which will be so if molecules dissociate or the atoms recombine virtually instantaneously, or, in general, reaction rates are infinitely fast;

or b) as in frozen equilibrium, which will be so if the gas phase chemical reactions are extremely slow and the relaxation times are consequently large compared with the time spent by the particles inside the boundary layer. Similar considerations apply also to the equilibrium of vibrational excitation.

However, where the boundary layer fits neither of these two descriptions but may be in a transient state of "non-equilibrium", the relation (equation 2.1) describing the heat transfer distribution may be affected. The transient case may exist by either affecting the external inviscid layer (via the pressure gradient term) or by altering the velocity distribution within the boundary layer.

In general, where a dissociated boundary layer exists, a surface non-catalytic to the process of recombination (which is exothermic) could reduce the heat transfer to the surface [1,15].

2.2.2. A laminar boundary layer.

In this investigation we are, in general, interested only in lengths of the surface which are so short (as we shall show later) compared with the lengths over which the flow is likely to be laminar

that it is reasonable to assume that transition is absent. A turbulent boundary layer is normally associated with much higher rates of heat transfer than the laminar boundary layer. It is, therefore, desirable, where possible, to keep the flow laminar. The region of transition from laminar to turbulent flow is expected to produce another maximum in the heat transfer distribution. Heat conduction within the material may play a beneficial role in the determination of the temperature distribution in this region. However, it is often difficult to predict with any certainty the location of the transition region and hence there is a problem as to where to put the conducting material.

In almost all the research that has been done, the surface of the flat plate is taken to be smooth or even highly polished. On the other hand, when the heat balance equations are solved to provide a measure of the leading edge temperature, an emissivity value as high as 0.8 might well be quoted. Such a high value can only be achieved after considerable oxidation or (say) sand-blasting of the metal surface. It would therefore be desirable to find out the effect of surface roughness on the heat transfer. As for slow speed flow, surface irregularities, and especially surface roughness, tend to induce early transition from a laminar to a turbulent boundary layer, which from considerations of limiting the overall heat transfer should be avoided. For rough surfaces, there is a great deal of scatter in the data obtained (reference 17) and comparison with available theories becomes very difficult. Particularly of interest would be to find out whether the surface treatments necessary to produce high values of

emissivity are sufficient to induce transition close to the leading edge for hypersonic flight at high altitudes.

2.2.3 The effects of leading edge bluntness and pressure gradients along the surface.

The relation expressed in equation 2.1. (i.e. $Q \propto x^{-\frac{1}{2}}$) is strictly true only if the pressure gradient is negligible and this can only be expected for a sharp-edged plane surface in hypersonic flow, and this application has received considerable attention of many researchers[18-21]. However some blunting of the leading edge is not only inevitable but in fact essential (as we shall show later) in order to conduct heat away from the nose of the wing. Hence, what can be said of the effects of leading edge bluntness?

In addition to the self induced pressure field generated by the boundary layer growth, a blunt leading edge gives rise to even greater inviscid surface pressures. This inviscid pressure field is usually dominant over the forward portion of the blunt body and determines the initial growth of the boundary layer which in turn influences the heat transfer vàriation close to the nose of the wing.

For a blunted plate or wedge, the shock structure at the leading edge is detached and stands off at some distance forward of the leading edge. The influence of leading edge blunting on the local heat transfer at present cannot be predicted with ease because of some of the complicating factors such as shock shape and detatchment distance.

References (22-24) present experimental data on the effects of leading edge bluntness on the pressure as well as the heat transfer rates. Even a very slight blunting of the flat plate (compared with

a truly sharp leading edge) gives rise to a stagnation region and produces finite rates of heat transfer at the nose of the wing. Further blunting, although it may reduce the local heat transfer rate to the leading edge, will also produce a substantial increase in the average value of the heat flux to the region adjacent to the nose of the wing. Experimental evidence[24] also suggests that small and moderate leading edge blunting delays transition from a laminar to a turbulent boundary layer because of the introduction of favourable pressure gradients. One of the present difficulties resides in the inability of the experimental techniques to record meaningful data very close to the leading edge.

The shape of the surface apart from giving rise to an inviscid pressure field can also lead to viscous interaction between the boundary layer and the shock structure which may produce fundamental changes in the flow over the wing surface close to the leading edge. More than one flow regime can exist close to the leading edge. The different regimes are mathematically defined by introducing the interaction parameter, χ_∞ as

$$\chi_\infty = M_\infty^3 \left(\frac{C_\infty}{R_{x,\infty}}\right)^{\frac{1}{2}} \qquad (2.2)$$

where the subscript ∞ refers to the free stream conditions and x the distance along the body. C is the Chapman-Rubesin viscosity constant given by $\mu = CT$. Summarising very briefly, we have

regime	χ_∞
weak interaction	0
strong interaction	$\gg 1$
merged flow	$0\ (M^2)$
kinetic flow	$\gg 0\ (M^2)$

The heat transfer to a sharp flat plate has received considerable attention in the various regimes[18-21]. The relation $Q \propto x^{-\frac{1}{2}}$ is strictly only valid in the weak interaction region, where a distinct boundary layer (viscous) can be differentiated from the inviscid flow and the boundary layer displacement thickness is small compared with the normal distance of the shock wave from the surface. The analysis of heat transfer in the strong interaction region and the merged layer regime is complicated because of the interaction between the viscous and the inviscid flow and in addition slip velocity and a temperature jump at the wall surface have to be taken into account.

In addition to leading edge bluntness, surface irregularities can be expected to exist on full-scale vehicles because of manufacturing methods, load deformations and/or thermal conditions. Reference (25) provides experimental results of an investigation into the heat transfer and pressure distributions due to sinusoidal distortions on a flat plate at $M_\infty = 20$ in helium. In the region of surface distortions, the values of the local rates of heat transfer were found to oscillate from maximum to minimum as a result of the wavy surface which causes boundary layer separation and attachment. The maximum heating rate occurs just ahead of the peak of the protruberances and can be over twice the local flat plate value for zero incidence and considerably higher at even moderate angles of incidence. The heat transfer level returns to the undisturbed flat plate value within a short distance downstream of the distorted section.

2.2.4 Low-density effects.

Whereas a decrease in atmospheric density produces a reduction in

the average value of heat transfer to the surface, at very high altitudes low-density effects start to play an increasingly important role. Low atmospheric density enhances the effects of some of the other factors discussed in this chapter, as for example.

a) viscous interactions effects predominate in hypersonic flight at extreme altitudes because of the small Reynolds Number (vide equation 2.2);

b) not only does the dissociation of oxygen and nitrogen molecules start at lower temperatures (although this in itself is not expected to influence the variation of heat transfer), but what may be significant is that for decreasing density of air, the relaxation times of these chemical reactions decreases;

c) delays transition from a laminar to a turbulent boundary layer;

d) the boundary layer thickens considerably and the local displacement thickness may no longer be negligible compared with the measure of distance from the leading edge;

e) when the magnitude of the mean free path of the molecules within the boundary layer becomes comparable to, say, the leading edge radius, the gas can no longer be considered to be a homogeneous medium. When the mean free path is greater than the boundary layer thickness, slip velocity and a temperature jump at the wall surface has to be taken into consideration. At extremely high altitudes and Mach numbers, the kinetic theory of gases predicts the heat transfer to the leading edge of a wing in the free-molecular regime as having a finite value (as against the predictions of equation 2.1).

It is believed that in the context of re-entry vehicles, the surface pressures are such as not to introduce slip effects. In the derivation of equation (2.1), a temperature jump at the wall is irrelevant because a constant wall temperature is assumed in the analysis.

2.2.5 Constant wall temperature.

In calculating the heat transfer from the boundary layer to the wall, the effect of the variation of the wall temperature on the rate of the local heat transfer is usually neglected. This assumption can be justified only if the wall temperature is much lower than the recovery temperature, T_r. Since the quantity of heat transferred to the wall depends upon the temperature difference between the actual wall temperature and the recovery temperature, a cooling of the wall should give a higher rate of heat input. However, the primary effect of cooling[16] is to thin the boundary layer and hence to reduce the induced pressure. The skin friction and heat transfer rates are thereby reduced because of the effect of the decreased wall temperature on the coefficient of viscosity.

2.2.6 Three-dimensional effects.

Most of the research effort, as yet, has been put into the study of two-dimensional flow and the more difficult three-dimensional problem has not had its fair share of attention. More experimental as well as theoretical investigations would be very welcome indeed. In reference (26) an attempt is made to solve the boundary layer equations for a finite plate with a sharp leading edge.

Where the wing has high incidence, sweep and leading edge bluntness,

three-dimensional effects become important. Especially if the swept leading edge is blunt, the fluid exhibits the tendency to drift along the leading edge, so complicating the study of the boundary layer heating at the leading edge. Pressure and heat transfer measurements on a 70^{o} sweep delta wing are given in reference (27). The models had cylindrical leading edges. For zero incidence and low angles of attack, the maximum heat transfer occurs along the leading edge and the magnitude is independent of the distance from the apex of the delta. For higher values of incidence the rate of heat transfer along the leading edge decreases appreciably with the distance from the apex. At low incidence both a spherical as well as a pointed nose yield similar results.

2.3 Reasons for modifying the relation $Q \propto x^{-\frac{1}{2}}$

We have briefly mentioned how the heat transfer to the area close to the leading edge of slender hypersonic wings is governed by many factors. From the present knowledge of hypersonic flow it is virtually impossible to include the effects of the variations in heat transfer introduced by all these parameters when estimating the heat transfer distribution to a realistic wing. Furthermore, such an expression would be applicable to a particular wing only.

In this respect, the solutions obtained for the problem of aerodynamic heating are only as general as the expression used to describe the variation of heat transfer. The relation quoted in equation (2.1) which is that $Q \propto x^{-\frac{1}{2}}$ is the most widely quoted variation of heat transfer over a wide range of laminar hypersonic boundary layers.

The relation $Q \propto x^{-\frac{1}{2}}$ presents an undesirable numerical difficulty arising from its singularity as $x \rightarrow 0$. In practice, as we have seen, an infinite rate of heat transfer cannot occur. It would, indeed appear from the published literature that, at the nose of the wing, the heat transfer rate might typically be (say) ten times higher than the value further downstream. A still more powerful and equally general method is therefore to assume that Q varies as $(x + x_o)^{-\frac{1}{2}}$ where x_o is a constant. This relation enables us to set up realistic rates of heat transfer at the nose while elsewhere the variation of heat transfer is essentially proportional to $x^{-\frac{1}{2}}$.

CHAPTER III

Two-dimensional heat conduction in leading edge heating.

3.1 Introduction

Two-dimensional theory and results are presented as a separate entity because they can be applied to a wide range of wing configurations. For example, we shall later show that for three-dimensional wings (apart perhaps for the regions close to centre-section and the wing tips) a very large proportion of the leading edge can be considered as if it were two-dimensional.

In this chapter we undertake a systematic study into the problem of two-dimensional leading edge heating. Solutions of the heat conduction equation have already been published in reports by Nonweiler, Wong and Aggarwal [12,13] for $Q \propto x^{-\frac{1}{2}}$. In the following sections an outline is provided of the contents of these reports. We shall also generalise the results for the heat transfer distributions like $(x + x_o)^{-\frac{1}{2}}$, where x_o is a small constant, the nose of the wing being subjected to finite rates of heat transfer. Details are given of the numerical methods developed which are capable of handling variable material properties.

3.2. Theory of conducting plates.

In general, the aircraft wing structure is fairly complex. Before formulating the heat transfer equations to such a structure, there is a need to idealize the leading edge section by some simple configurations which can be studied analytically. In particular, our aim is to investigate the role played by thermal conduction in the

problem of leading edge heating. For this reason it is convenient to regard the leading edge region as what we shall term "a conducting plate". Such an idealization of the leading edge allows us to derive quite general results which can provide reasonable estimates of the temperature distributions that can be expected to exist close to the nose of hypersonic wings. For thin wings it is reasonable to assume that the portion adjacent to the leading edge has small surface slope.

The basic mathematical assumption is that the thickness of the conducting plate is vanishingly small. If k is the thermal conductivity of the material and t the thickness, then the product kt remains finite while the ratio $\frac{t}{k} \to 0$. A detailed discussion of the assumption is provided in references (12) and (13). One of the important implications of this assumption is that within the body heat transfer normal to the surface can be ignored. Hence the dimensionality of the equation is reduced by one.

3.2.1. Derivation of heat conduction equation.

For a hypersonic leading edge (two dimensional) subjected to aerodynamic heating, the various modes of heat transfer can be classified as follows:

1. Convective heat transfer from the boundary layer $Q = f(x)$.
2. Heat flux radiated away from the body - $\epsilon \sigma T^4$. where ϵ is the coefficient of emissivity and σ the Stefan-Boltzmann constant.
3. Heat transferred inside the body by thermal conductivity of the material, (k, say).

We adopt an axes system whose origin is taken at the nose of the wing with x measured in the chordwise direction, y in the spanwise direction

and z normal to the plane of the wing. Consider the heat transfer to and from an element situated at some plane x = constant, and of length dx and unit span. Let t be the thickness of the material at this plane.

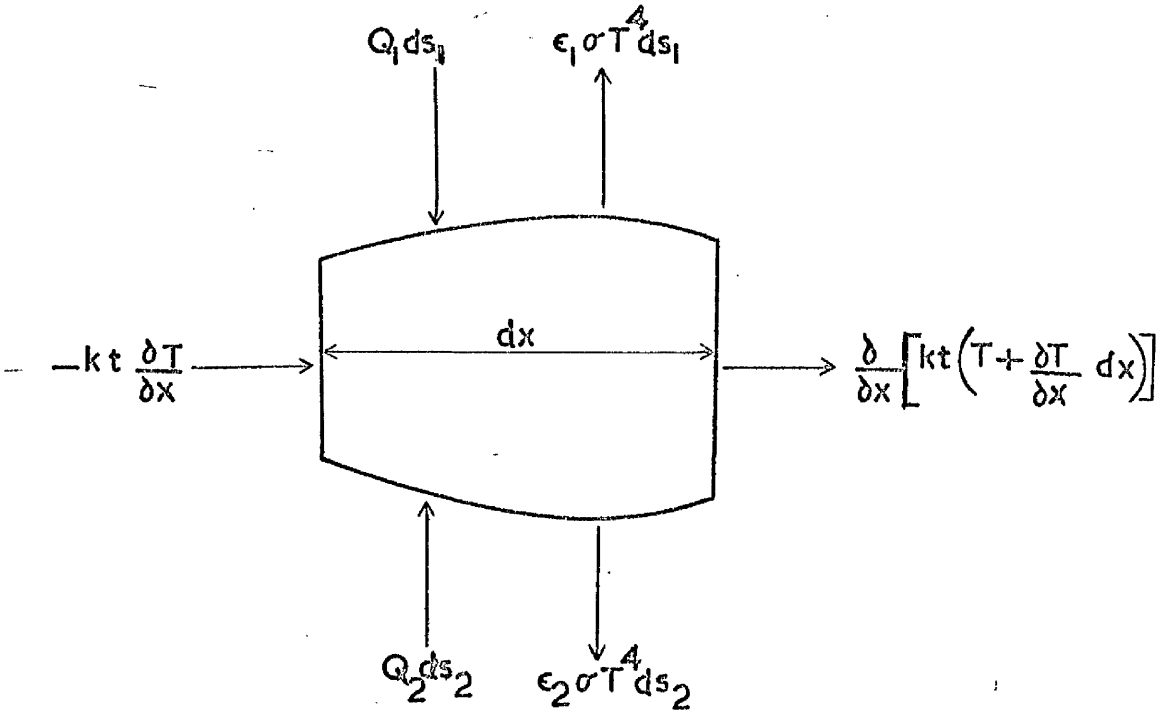

For a geometrically thin leading edge it is reasonable to assume that the elements of surface area shown in the appended sketch are such that $ds_1 \simeq ds_2 \simeq dx.\ 1$ where we consider unit span. This assumption is valid where $dx^2 \gg dz^2 = dt^2$, in other words the two surfaces are inclined at small angles to the x - axis. The subscripts 1 and 2 refer to the top and bottom surfaces respectively.

For equilibrium, we get

$$-kt\frac{\partial T}{\partial x} + \frac{\partial}{\partial x}\left[kt\left(T + \frac{\partial T}{\partial x}.dx\right)\right] + Q_1 dx + Q_2 dx - \epsilon_1 \sigma T^4 dx - \epsilon_2 \sigma T^4 dx = 0$$

$$\text{i.e.}\quad \frac{\partial}{\partial x}\left(kt.\frac{\partial T}{\partial x}\right) = (\epsilon_1 + \epsilon_2)\ T^4 - (Q_1 + Q_2)$$

Denoting by ϵ the sum of the emissivities of the two surfaces and by Q the total convective heat into the two surfaces, we get

$$\frac{\partial}{\partial x}\left(kt\,\frac{\partial T}{\partial x}\right) = \epsilon\sigma T^4 - Q \qquad (3.1)$$

In deriving equation (3.1) we have assumed equilibrium conditions i.e. the temperature distribution is independent of the time history of flight. Strictly speaking, equilibrium temperatures at the surface are likely to exist when the hypersonic flight time exceeds the time required to heat up the wing structure to the steady state value. However, for "sharp-edged" leading edges of slender wings the aerodynamic rates of heat transfer are extremely severe close to the nose of the wing. In this region the wing also has a very limited thermal capacity. Therefore the regions close to the nose of the wing can be expected to be under the influence of steady state temperature distributions for practically the entire duration of hypersonic flight.

Before a numerical solution of equation (3.1) is attempted, some of the factors that affect both the method of solution and the solution itself need mentioning. In general, the thermal conductivity of the material plays a dominant role in the determination of the temperature distribution where the rate of heat transfer to the body is varying substantially. In hypersonic flow, the maximum heat transfer occurs at the nose ($x = 0$) of the body and thereafter decreases very rapidly in the streamwise direction. If the conduction of heat within the body is ignored (i.e. a non-conducting plate) the radiation equilibrium temperature would become equal to the local thermometer value. At the nose the thermometer value can exceed the operating limits of most materials and be several times higher than the temperatures further

downstream. In this context, it has been shown in references (12,13) that over some length (l, say) thermal conduction can be expected to play a predominant role in moderating the temperature distributions. This length l will be referred to as the "conduction" length.

3.2.2. Non-dimensionalising of the heat conduction equation.

Here again we use the notation which has been introduced in reference (12). In the physical problem, the length l may be substantially less than that length of surface subjected to heating. Since it is only over lengths of the order of l that longitudinal conduction is important, it is convenient to regard the conducting plate as of bounded extent. If we denote such a "closed" length by L, then we seek a solution of equation (3.1) in terms of the independent variable $(\frac{x}{L})$.

In particular we write

$$X = \frac{x}{L}\ , \quad \theta = \frac{T}{T_L}\ , \quad e = \frac{\epsilon}{\epsilon_L}\ , \quad q = \frac{Q}{Q_L} \qquad (3.2)$$

where the subscript L refers to the values at x = L. T_L is the value of the radiation equilibrium temperature at x = L, which is

$$T_L = \left(\frac{Q_L}{\epsilon_L \sigma}\right)^{\frac{1}{4}} \qquad (3.3)$$

We also place $K = \frac{k\,t}{k_m t_m}$ (3.4)

where the subscript m refers to the mean values.

We can now define l mathematically as

$$l = \left(\frac{k_m t_m T_L}{Q_L}\right)^{\frac{1}{2}} \qquad (3.5)$$

In addition we define

$$\tau = \frac{kt}{(\epsilon_L \sigma Q_L^3)^{1/4} . L^2} \qquad (\text{i.e. } \tau = (\tfrac{l}{L})^2 . K) \quad (3.6)$$

With the notation just described in equations (3.2) - (3.6) the heat conduction equation (3.1) can now be expressed in a non-dimensional form as

$$\frac{d}{dX}\left(\tau \frac{d\theta}{dX}\right) = e\theta^4 - q \qquad (3.7)$$

Equation (3.7) yields the two well known but trivial solutions in the two extremes. For example, as $\tau(X) \to 0$.

$$\theta = \left(\frac{q}{e}\right)^{\frac{1}{4}} \qquad (3.8)$$

i.e. the temperature everywhere tends to the radiation equilibrium value. The other extreme $\tau(X) \to \infty$ gives rise to the solution

$$\theta = \left(\frac{\int_0^1 q\,dX}{\int_0^1 e\,dX}\right)^{\frac{1}{4}} \qquad (3.9)$$

which is a constant temperature throughout corresponding to a plate of "infinite conductivity".

But in general we shall be interested in values of τ of unit order.

We seek solutions of equation (3.7) subject to the boundary conditions that there is no longitudinal heat conduction at the nose ($X = 0$) and at the rear edge ($X = 1$). They take the form

$$\tau \frac{d\theta}{dX} = 0 \quad \text{at} \quad X = 0, 1 \qquad (3.10)$$

It can be shown that the solution is unaffected if the heat transfer from the ends ($X = 0,1$) i.e. $\tau \frac{d\theta}{dX} \neq 0$, but is small in magnitude compared with the heat transfer from the two surfaces. For a detailed discussion, the reader is referred to reference (12).

3.3. Solution for Q varying as $x^{-\frac{1}{2}}$

For the purpose of this investigation, we have supposed that the

aerodynamic heat transfer is proportional to $x^{-\frac{1}{2}}$. Therefore we may write

$$Q = \frac{H_o}{x^{\frac{1}{2}}} \qquad (3.11)$$

where the constant H_o can be related to the flight regime. Substituting equation (3.11) into (3.7) gives

$$\frac{d}{dX}\left(\gamma \frac{d\theta}{dX}\right) = e\theta^4 - \frac{1}{X^{\frac{1}{2}}} \qquad (3.12)$$

Solutions of equation (3.12) with k and ϵ assumed constants are presented in a parametric form in figures 1 - 10 of reference (12) for families of five plate geometries together with the similarity relations that exist. In particular one relation defines the choice of material properties in scaled laboratory experiments which can only be carried out in low temperature environments.

There are many ways of interpreting these results. The importance of conducting material near the nose of the leading edge is best illustrated perhaps by means of the specific example that was considered in reference (12). For a given heat input, the amount of optimum material for each of the five shapes was calculated to give a prescribed nose temperature. The results are reproduced in figure 3.3.1. At the top is the particular distribution of thickness that gives the minimum nose temperature for a specified heat input and of course requires the minimum amount of conducting material. The second shape has a linear temperature gradient and compares favourably with the optimal thickness distribution. The "efficiency" of the first two shapes arises from a rounded nose coupled with the tapering off of the material towards the rear. On the other hand, the parabolic and the

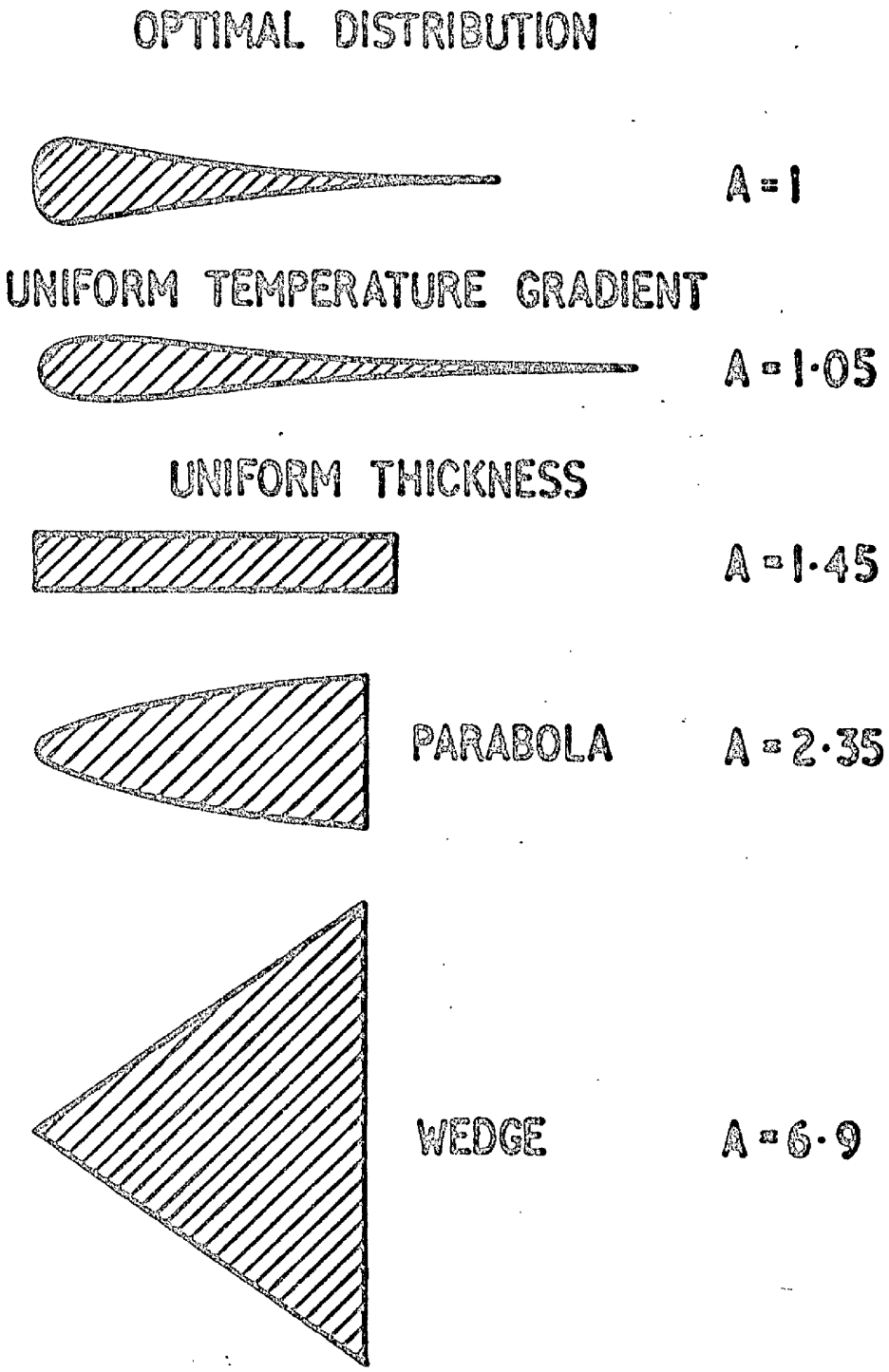

Figure 3.3.1 Optimised shapes providing the same nose temperature (thcikness and length scales common but undefined).

wedge thickness distributions may be desirable from aerodynamic considerations but require respectively as much as 2.35 and 6.9 times the conducting material as the first shape.

It is important to realise that the various thickness distributions of figure (3.3.1) are not necessarily intended to be the external wing leading edge shapes. Aerodynamic and the structural considerations will determine the amounts of conducting material necessary to transfer the heat away from the nose of the wing.

3.4 Solution for Q varying as $(x + x_o)^{-\frac{1}{2}}$.

Up to now we have discussed the solutions for the $Q = \frac{H_o}{x^{\frac{1}{2}}}$ distribution of heat transfer which require special techniques because of the singularity at $x = 0$. Such a hypothetical variation of heat transfer cannot exist in practice and the solutions obtained are therefore mainly of academic interest. For reproducing realistic heat transfer rates while maintaining generality of the solutions, we propose to solve the heat conduction equation with

$$Q = \frac{H_o}{(x + x_o)^{\frac{1}{2}}} \qquad (3.13)$$

where x_o is a constant.

Instead of being limited to infinite rate of heat transfer at $x = 0$, we can now reproduce any appropriate magnitude of heat transfer at the nose. Provided x_o is small compared with L, the heat transfer distribution away from the nose of the leading edge remains virtually unaltered. The ratio of heat transfer at $x = 0$ to that at the rear edge of the conducting plate ($x = L$) is simply

$$\frac{Q_o}{Q_L} = \left(\frac{L + x_o}{x_o}\right)^{\frac{1}{2}} = \left(1 + \frac{L}{x_o}\right)^{1/2} \qquad (3.14)$$

This control on the ratio (Q_o/Q_L) is particularly useful when comparing the theoretical solutions with experimental results. For a fair comparison to be made it is important that the expression for the heat input used in the heat conduction equation should represent as closely as possible the experimental heat distribution.

In this section we seek solutions of the following heat conduction equation in the non-dimensional notation of equations (3.2) - (3.6).

$$\frac{d}{dX}\left(\tau \frac{d\theta}{dX}\right) = e\theta^4 - \frac{1}{(X + X_o)^{\frac{1}{2}}} \qquad (3.15)$$

where the coefficients τ and e can be functions of temperature (θ) and position (X). The boundary conditions are the same as in equation (3.10) i.e.

$$\tau \frac{d\theta}{dX} = 0 \quad \text{at} \quad X = 0,1. \qquad (3.16)$$

3.5 Methods of solution of heat conduction equation.

Fortunately, equation (3.15) can be solved by more than one numerical method and we have in fact tried three. Full use was made of the opportunity to study the comparative merits of the various methods available to solve the ordinary differential equation (3.15). The three methods attempted are as follows:

1. Adaptation of iterative Runge-Kutta integration techniques.
2. Finite-difference boundary value problem, where the interval of X (0,1) is divided into N equal intervals and we solve iteratively the N + 1 finite difference algebraic equations by
   a) an explicit method (Gaussian elimination);
   b) an implicit method (over-relaxation).

A brief discussion of each of the three methods now follows.

3.5.1. Runge-Kutta integration.

This method is very often used to obtain accurate solutions of ordinary differential equations which have to be integrated subject to prescribed initial values[47]. However, ours is a boundary value problem and information is not available on the stability of the solution (because of the essentially non-linear character of the equation).

We express equation (3.15) as two simultaneous first-order differential equations; that is, we put

$$\frac{d\theta}{dX} = U \qquad (3.17)$$

and

$$\frac{dU}{dX} = e\theta^4 - \frac{1}{(X + X_o)^{\frac{1}{2}}} \qquad (3.18)$$

The solution is started with a guessed value of temperature (θ_1, say) and zero temperature gradient. A step by step integration of the two equations is carried out. Each step is of length h which is adjusted adaptively, depending on the magnitude of the derivative $\frac{d\theta}{dX}$. Corresponding to the arbitrary value θ_1, a value U_1 is obtained at the rear edge ($X = 1$). This process is repeated with a second value of nose temperature θ_2, which gives us a corresponding value U_2. From the boundary conditions expressed in equation (3.16), we should have $U = 0$, at $X = 1$. Using a root finding technique (based on regula falsi) a better estimate of the nose temperature (θ_3) is made from the two values U_1 and U_2. The calculation proceeds iteratively so as to converge to the particular value of nose temperature that satisfies equation (3.16) within some specified tolerance.

In the execution of the programme using the method of Runge-Kutta, the local value of h depends on how rapidly the derivatives are changing. For a typical solution (with $x_o/L = 0.001$) the value of h at the nose of the leading edge is very small and could be increased by a factor of over 1000 before reaching the rear edge.

If a "good" guess (i.e. close to the value θ_o) of the starting value of the nose temperature is not supplied, the solution starts to diverge very rapidly causing the length $h \rightarrow 0$. Provided this instability in the solution is not encountered, however, the method works satisfactorily and converges to the solution in a matter of about 10 - 20 seconds on the English-Electric KDF9 digital computer, using a programme compiled by the Kidsgrove ALGOL optimised translator.

3.5.2. The method of "Bandsolve".

For this method (as well as the next one), we have to linearise equation (3.15) and also express it in a finite differences form (for details refer to Appendix A). The final form of the heat conduction equation becomes,

$$\tau_{n+\frac{1}{2}}\,\theta_{n+1}^{i-1} + \tau_{n-\frac{1}{2}}\,\theta_{n-1}^{i} - \left[\tau_{n+\frac{1}{2}} + \tau_{n-\frac{1}{2}} + 4h^2 e_n \left(\theta_n^{i-1}\right)^3\right]\theta_n^{i}$$

$$= -h^2\left[\frac{1}{(n+X_o)^{\frac{1}{2}}} + 3e_n\left(\theta_n^{i-1}\right)^4\right] \qquad (n = 0,1,\ldots.N) \qquad (3.19)$$

where the interval X= 0,1 has been divided into equal divisions of length h $\left(=\frac{1}{N}\right)$ with end points $X_o, X_1, \ldots. X_n, \ldots X_N$ and the value of θ at X_n is denoted by θ_n. The superscript i refers to the value of the parameter after the ith iteration.

We can represent equation (3.19) more concisely by the matrix

equation,

$$\underline{C}^{i-1}.\underline{\theta}^{i} = \underline{B}^{i-1} \qquad (3.20)$$

where the value of θ_n^{i-1} is used in the elements of $\underline{C}$ and $\underline{B}$ whilst solving for θ_n^i. Comparing equations (3.20) and (3.19) it is evident that $\underline{\theta}$ is the vector $(\theta_o,\theta_1,.....\theta_N)$; $\underline{B}$ is the column vector whose general element is $-h^2(\frac{1}{(n+x_o)^{\frac{1}{2}}} + 3e_n\theta_o^4)$ and $\underline{C}$ is a band matrix containing the coefficients of $\underline{\theta}$, appearing on the left hand side of equation (3.19). The boundary conditions can be incorporated inside the matrix $\underline{C}$ which is indicated in Appendix A.

The method of "Bandsolve" consists of solving for the N+1 unknowns $(\theta_o,\theta_1,.....\theta_N)$ from N+1 simultaneous equations which are unfortunately not a set of linear equations. Since most of the terms of the matrix $\underline{C}$ are zero (a maximum of three non-zero terms), the matrix is stored as a band matrix (of size (N+1)x3) and then we employ Gaussian elimination to solve for the unknowns. By the use of a band matrix, the number of operations as well as the storage required is reduced from $(N+1)^2$ to 3x(N+1) for each iterative process.

At the start of the computer programme the interval X=0,1 is divided into 4 equal divisions. An arbitrary starting value of temperature (θ). is supplied to every point. Using equation (3.20), a solution of the vector $\underline{\theta}$ is obtained. At the end of each iteration, a check is made on the convergence error and the vectors $\underline{B}$ and $\underline{C}$ are updated using the values of $\underline{\theta}$ just obtained. The iterative process is stopped and $\underline{\theta}$ accepted as a converged solution when the following convergence criterion is satisfied,

$$\frac{1}{N+1}\sum_{n=o}^{N}\left|\theta_n^{i+1} - \theta_n^{i}\right| \leqslant \text{epso} \qquad (3.21)$$

where "epso" specifies the limiting tolerance.

The value of N is doubled ($N' = 2N$), the new points thus introduced being interpolated from the existing ones. The above mentioned iterative process governing the convergence criterion is carried out within an outer iterative loop that keeps a check on the discretisation error which exists because the interval (0,1) of X has been divided into a finite number of intervals. If θ' is the new converged solution but having twice the grid points, then at the corresponding points we form

$$\frac{1}{N+1} \sum_{n=o}^{N} \left| \theta'_{2n} - \theta_n \right| \leqslant \text{epso} \qquad (3.22)$$

If this discretisation error criterion is not satisfied, the last value of N' is doubled again and the whole procedure repeated. This routine of doubling N and reiterating is repeated until the solution having both the convergence and the discretisation error within the same tolerance (epso) has been obtained.

Unlike the Runge-Kutta method, the interval ($X = 0,1$) is divided into equal divisions. The final value h is dictated by the discretisation error near the nose of the leading edge(at least where x_o/L is small compared with unity). Hence some unnecessary operations are carried out away from the nose. This technique is preferrable to the Runge-Kutta method in that (within reason) any starting value of temperature leads to a converged solution.

As far as the computional time is concerned it is of the same order as the Runge-Kutta method, i.e. between 10 - 20 seconds.

3.5.3 The method of over-relaxation.

Alternatively, equation (3.19) may be solved by the method of "relaxation". Here each stage of the iteration for θ is also a stage

in an iterative process aimed at solving the set of N + 1 simultaneous equations so that values of θ change whilst we solve the equations, instead (as in the explicit method of Bandsolve) of afterwards. Briefly this method consists of finding $\theta^{(i)}$ (having already determined $\theta^{(i-1)}$) and solving for $\theta_o^{(i)}$, $\theta_1^{(i)}$....$\theta_N^{(i)}$ in order, from a modified form of equation (3.19), which is

$$\theta_n^i = \frac{\tau_{n+\frac{1}{2}}\,\theta_{n+1}^{i-1} + \tau_{n-\frac{1}{2}}\,\theta_{n-1}^{i} + h^2\left[\frac{1}{(n+X_o)^{\frac{1}{2}}} + 3e_n(\theta_n^{i-1})^4\right]}{\tau_{n+\frac{1}{2}} + \tau_{n-\frac{1}{2}} + 4h^2 e_n(\theta_n^{i-1})^3} \qquad (3.23)$$

A still more powerful scheme is that of over-relaxation where we -form

$$\theta_n^i = (1-\omega)\theta_n^{i-1} + \omega\left[\frac{\tau_{n+\frac{1}{2}}\,\theta_{n+1}^{i-1} + \tau_{n-\frac{1}{2}}\,\theta_{n-1}^{i} + h^2\left(\frac{1}{(n+X_o)^{1/2}} + 3e_n\left(\theta_n^{i-1}\right)^4\right)}{\tau_{n+\frac{1}{2}} + \tau_{n-\frac{1}{2}} + 4h^2 e_n\left(\theta_n^{i-1}\right)^3}\right] \qquad (3.24)$$

where ω is the over-relaxation parameter.

The boundary conditions at X = 0,1 require special provisions as indicated in the Appendix A for the last method. The sequential operation of the computer programme is essentially the same as for the method of Bandsolve. Convergence and discretisation criterions are the same as in equations (3.21) and (3.22) respectively. As for the last method, over-relaxation yields a converged solution for any starting value (within reason) of temperature.

For a linear differential equation the norm of the error can be used to provide an estimate of the optimum value of while solving the set of N + 1 equations. Such an attempt proved unsuccessful in the solution of the present equations (3.24). For a particular value of τ_o = 0.98 and with the grid size fixed at N = 16, the number of

iterations required to obtain a converged solution for various values of ω is shown in figure (3.5.1). For N = 16, the optimum value of ω is 1.8. To show how the solution converges, we have plotted in figure (3.5.2) the nose temperature vs iterations for ω = 1.7,1.8 and 1.9. After an initially divergent mode for $\omega > 1.8$, the solution exhibits a damped oscillatory behaviour, while for $\omega < 1.8$, an exponentially decayed path is followed to convergence.

Whereas the optimum value of ω is 1.8 for N = 16, this value unfortunately changes with the grid size. As we have already indicated, the value of N is repetitively doubled within the programme. In table (3.5.1) we have listed the number of iterations carried out at each grid size for the range of ω = 1.4(0.1) 1.9, with $X_o = 10^{-2}$ and $\tau_o = 0.98$. The computation time is virtually independent of the over-relaxation parameter ω. However, for $\omega < 1.5$ the rate of convergence is slow and the convergence criterion of equation (3.21) can sometimes terminate the solution prematurely. Finally in figure 3.5.3 we show how the nose temperature reaches the required value for ω = 1.5 and 1.7, when N is allowed to vary.

Table 3.5.1 Convergence behaviour of the solution for various values of ω.

ω	Computation time. secs.	Iterations at each grid size with N =					
		8	16	32	64	128	256
1.4	42	28	61	107	2	1	-
1.5	39	20	50	94	7	1	-
1.6	40	17	38	80	21	1	-
1.7	42	24	25	63	37	1	-
1.8	43	37	24	43	44	1	-
1.9	44	74	51	34	33	2	1

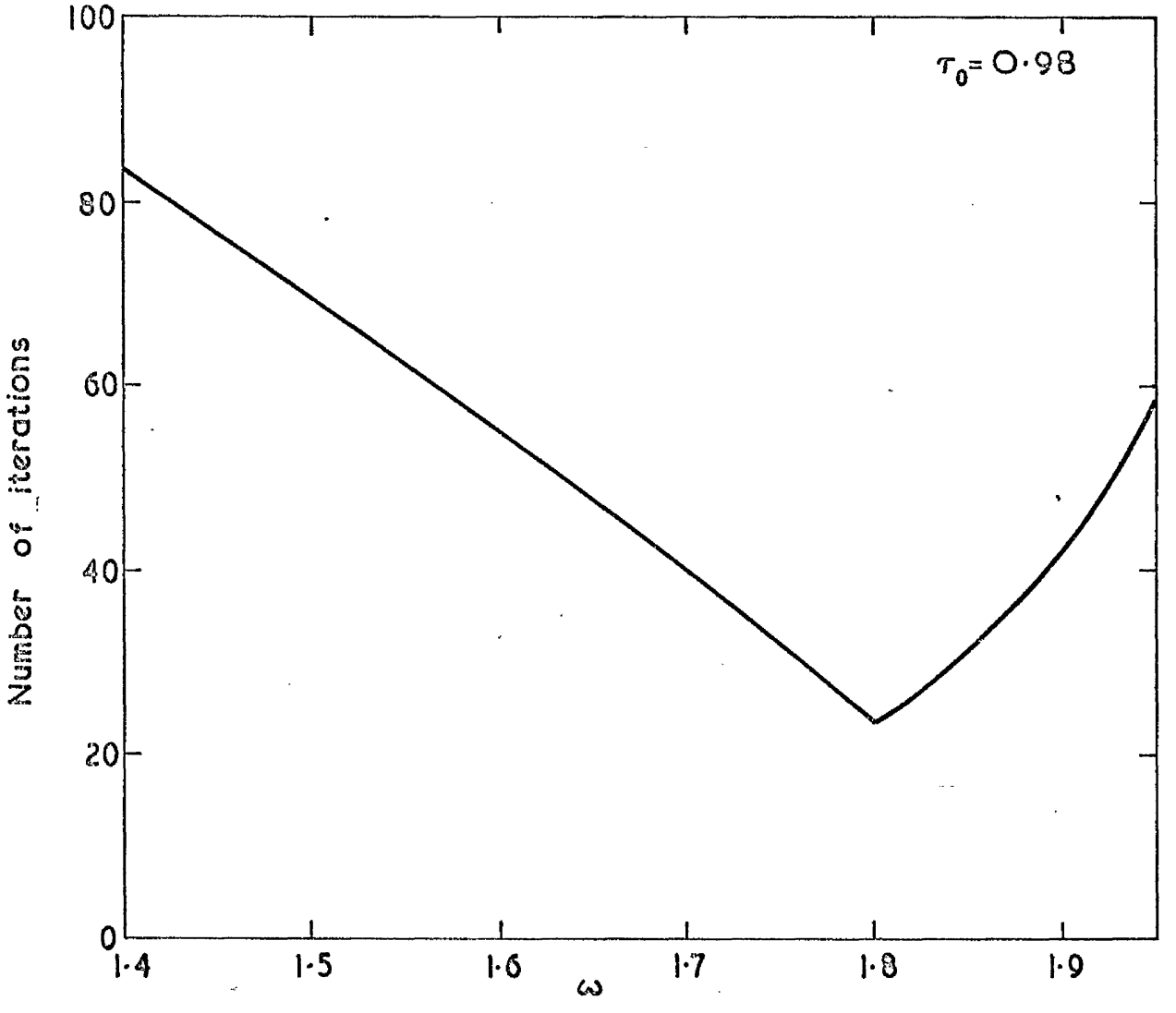

Figure 3·5·1. The effect of over-relaxation parameter on the convergence of the numerical solution for grid size (N = 16.)

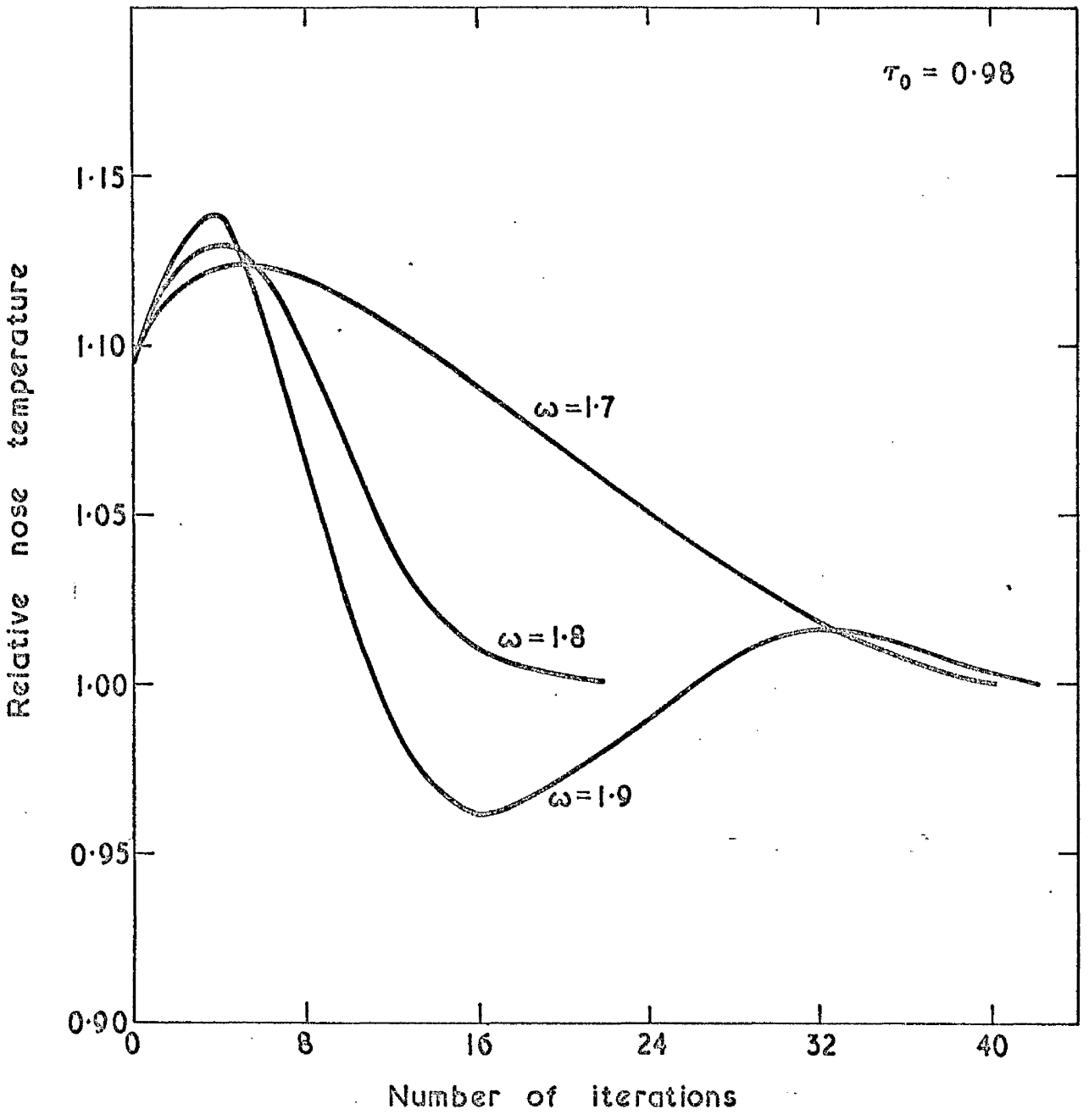

Figure 3.5.2. The convergence pattern of the numerical solution for grid size (N = 16)

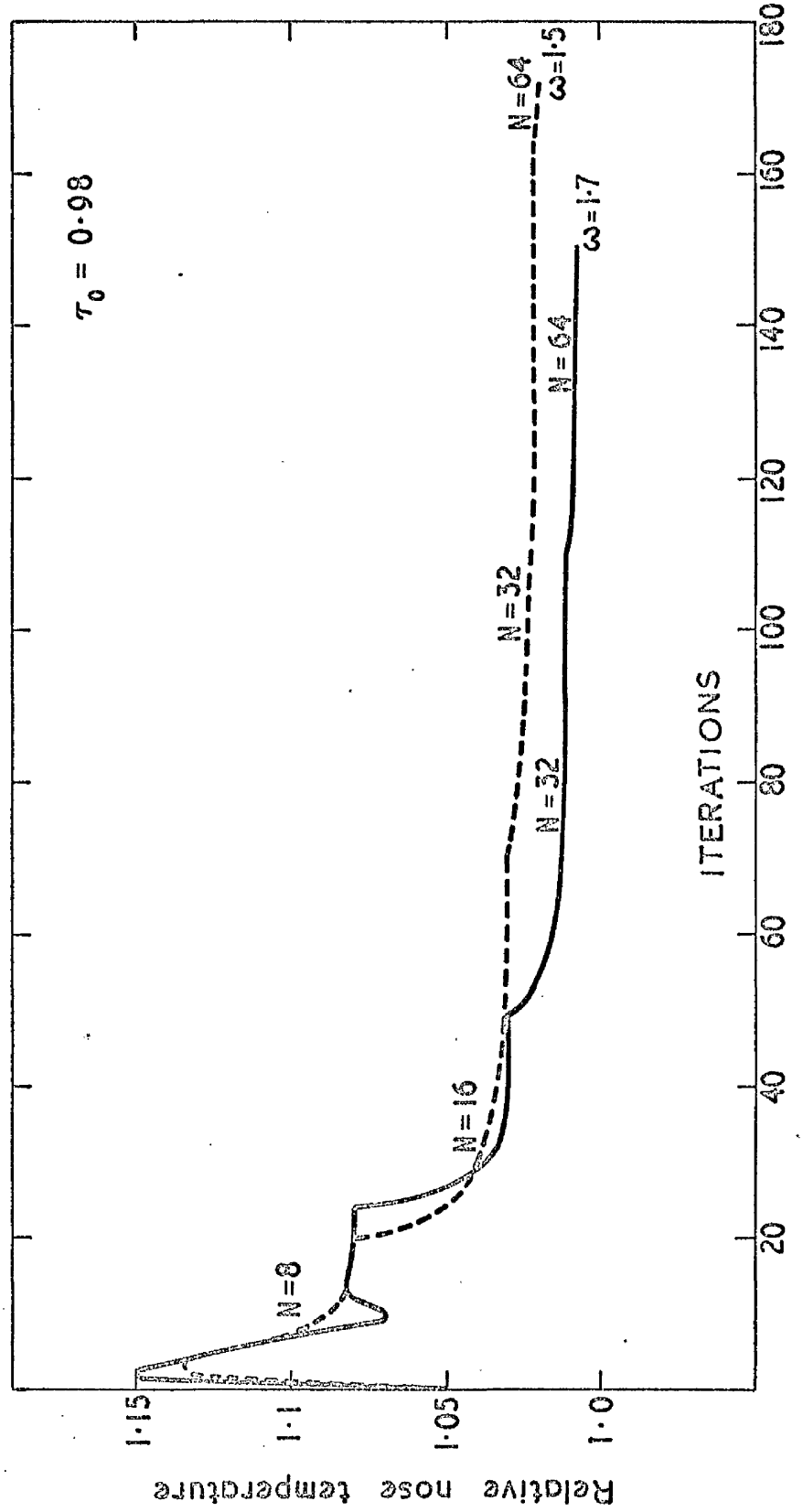

Figure 3.5.3. The convergence pattern for the numerical solutions with variable N.

Using the value of ω selected in this way, i.e. a value between 1.5 and 1.8, this method still takes at least 4 - 5 times longer in computation than the other two methods. Where the method of over-relaxation is superior to the other two is that it can be easily modified to include the additional dimension when we come to solve the three-dimensional heat conduction equation.

3.6 Discussion of numerical results for Q varying as $(x + x_o)^{-\frac{1}{2}}$

The introduction of the constant X_o raises one question straight-away - what is the effect of X_o on the temperature distribution? Solutions of equation (3.15) were sought where we vary $X_o = {}^{x_o}/_{L}$ from 1 to 10^{-8} while keeping the other parameters fixed. Figure 3.6.1 plots the variation of the nose and the rear edge temperatures against X_o. For $X_o < 10^{-4}$ the temperature distribution becomes independent of X_o. Hence the solution of equation (3.12) which is singular at $X = 0$, can be reproduced from equation (3.15) with $X_o < 10^{-4}$. Needless to say, equation (3.15) is the much simpler of the two equations to solve. The deductions from figure (3.6.1) are applicable over the whole range of τ of interest. For $\tau_0 = 0.98$, the chordwise temperature distribution is plotted in figure (3.6.2) for several values of X_o. As X_o increases, the temperature gradients everywhere are reduced with the greatest effect close to the leading edge ($X = 0$).

The results for families of parabolic and wedge sections have already been published[12]. We now present solutions of equation (3.15) for a linearly varying thickness distribution. The thickness of the conducting material at the rear can either be less or greater than that

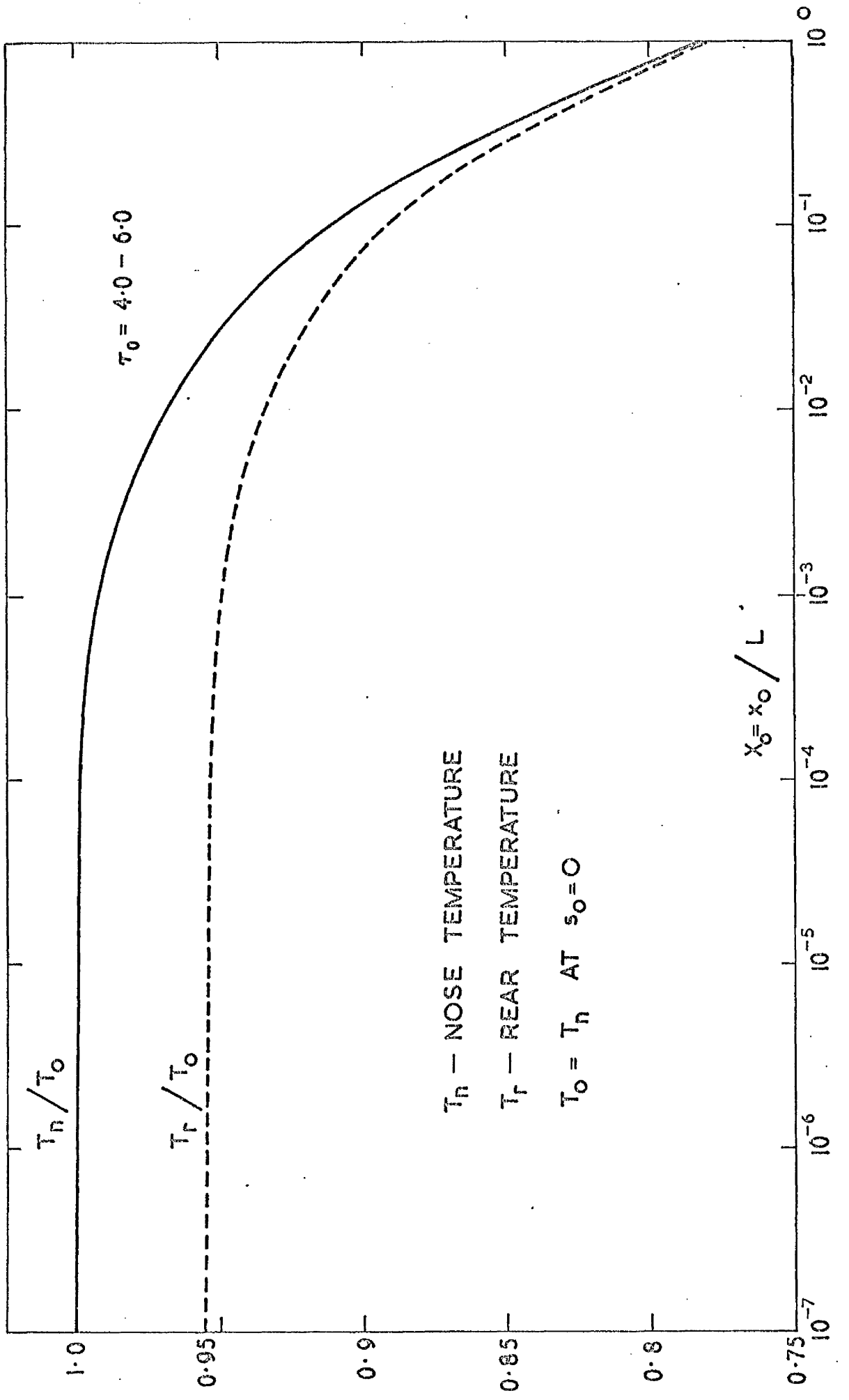

Fig 3.6.1. Effect of X_o on nose and rear temperature.

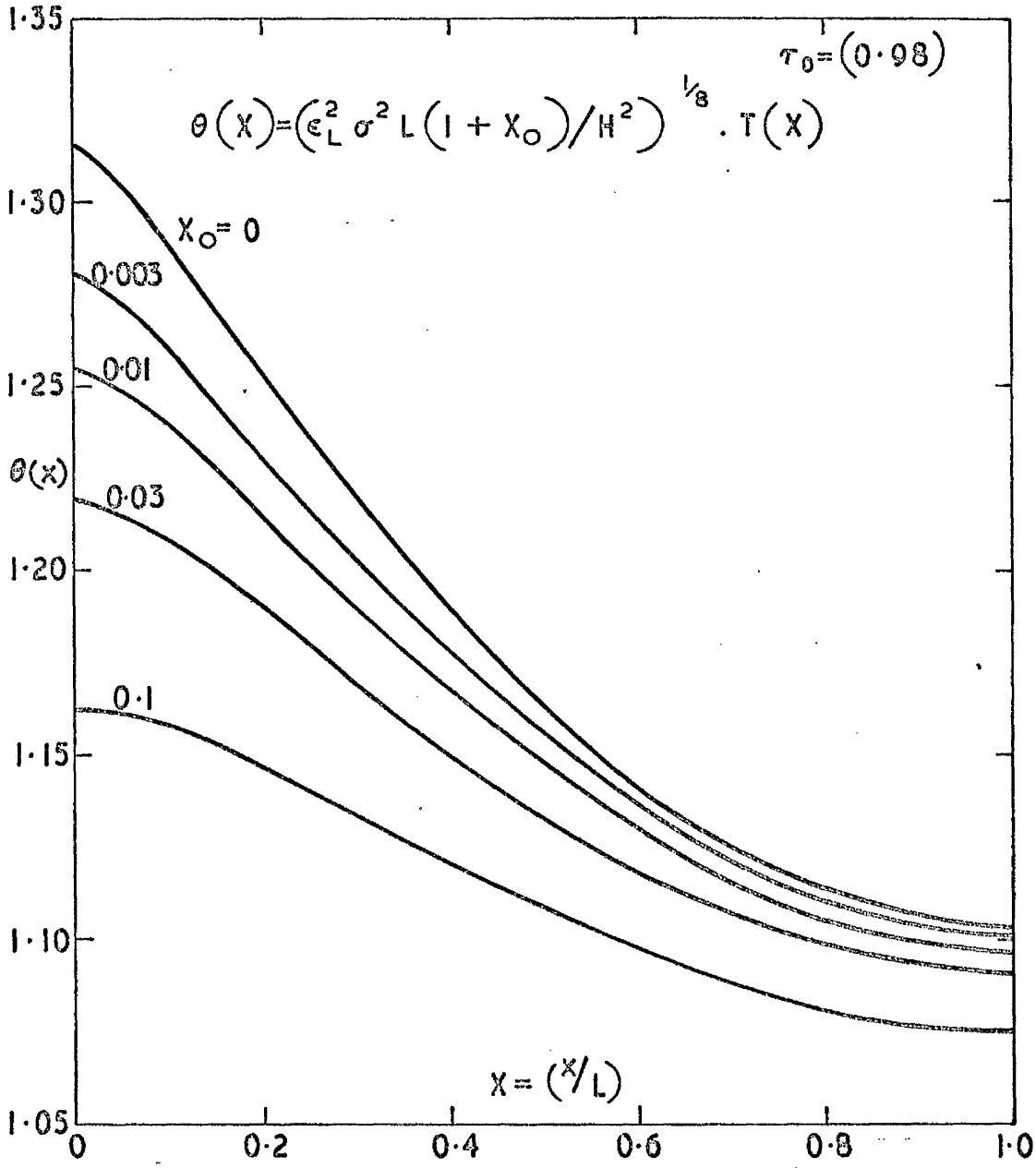

Figure 3.6.2 The effect of X_o on the temperature distribution.

at the leading edge. For a basis of comparison we use a slab section having the same thickness as the nose of the trapezoidal section.

For a given nose thickness t_o, if we vary the thickness at the rear, the changes produced in the temperature distribution are so small that we have to use a very exaggerated scale to show the differences. It is for this reason that we use the solution of the slab section as the reference temperature distribution and plot the fractional variations from this solution when the rear thickness (t_L) is altered. For a linearly varying thickness distribution, the results for $X_o = 10^{-2}$ and $\tau_o = 0.98$ (based on the slab thickness value) are presented in figure (3.6.3) where $t_o > t_L$ and in figure (3.6.4) for $t_o < t_L$. It is worth mentioning at this stage, that these solutions have a convergence and discretisation error (section 3.5.2) of about $\pm$ 0.01%.

For a given nose thickness, any change in the rear thickness (t_L) of a trapezium produces a proportionate change in the total amount of conducting material (i.e cross-sectional area A_t, say). The effects of varying A_t relative to the area of the reference slab (of area A_s, say) upon the leading edge and rear temperatures are shown in figure (3.6.5). One of the extremes is a wedge section when $t_L \rightarrow 0$ giving $A_{t/A_s} = 0.5$. These two temperatures vary almost linearly with the total cross-sectional area. Increasing the overall area by a factor of 5 produces a reduction in the nose temperature of only 0.7%.

In addition to the cross-sectional area, two other factors, namely τ_o (based on the reference slab thickness) and X_o influence the temperature distribution. The effects on nose and rear temperatures due to both these

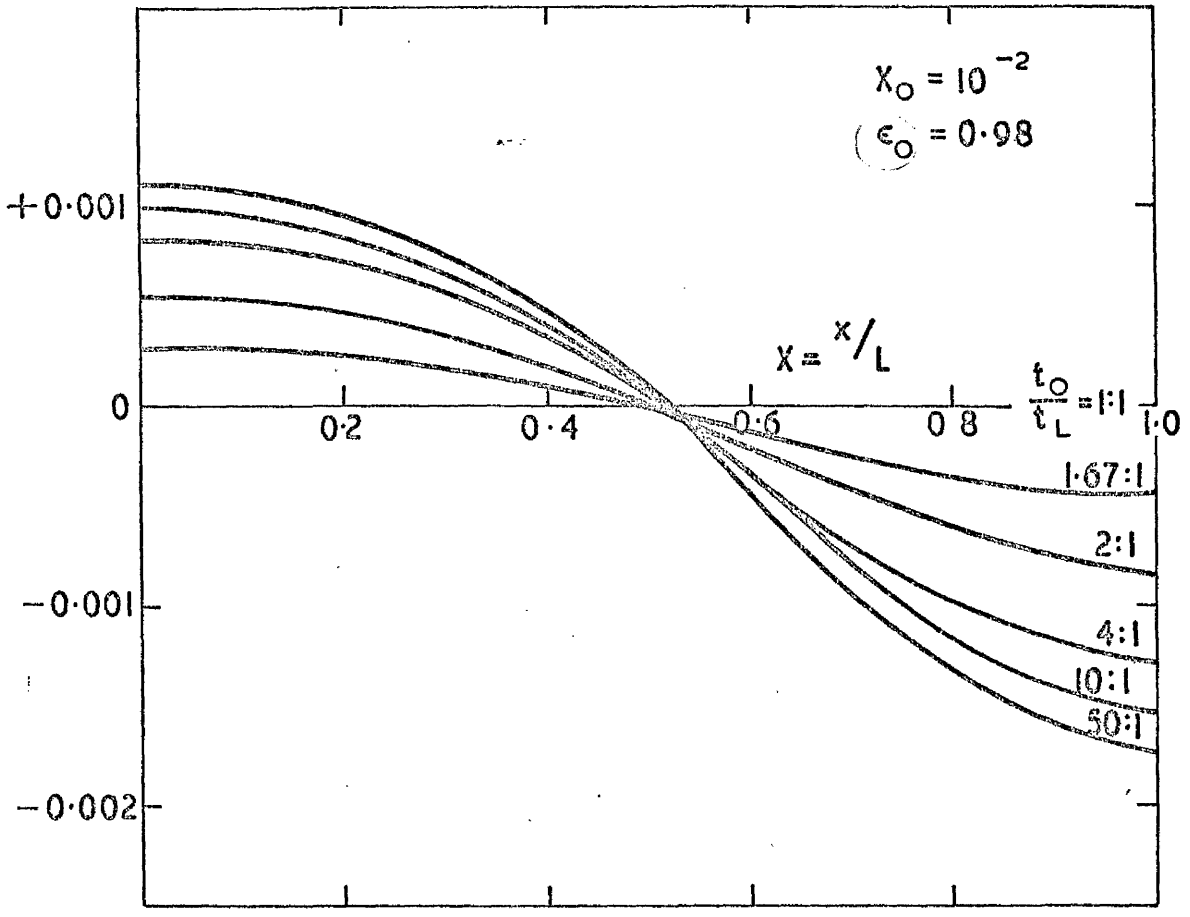

Figure 3.6.3 The effect on the temperature distribution due to a linear variation of thickness, $t_o > t_L$ (plotted as fraction of the temperature distribution for the slab of the same nose thickness)

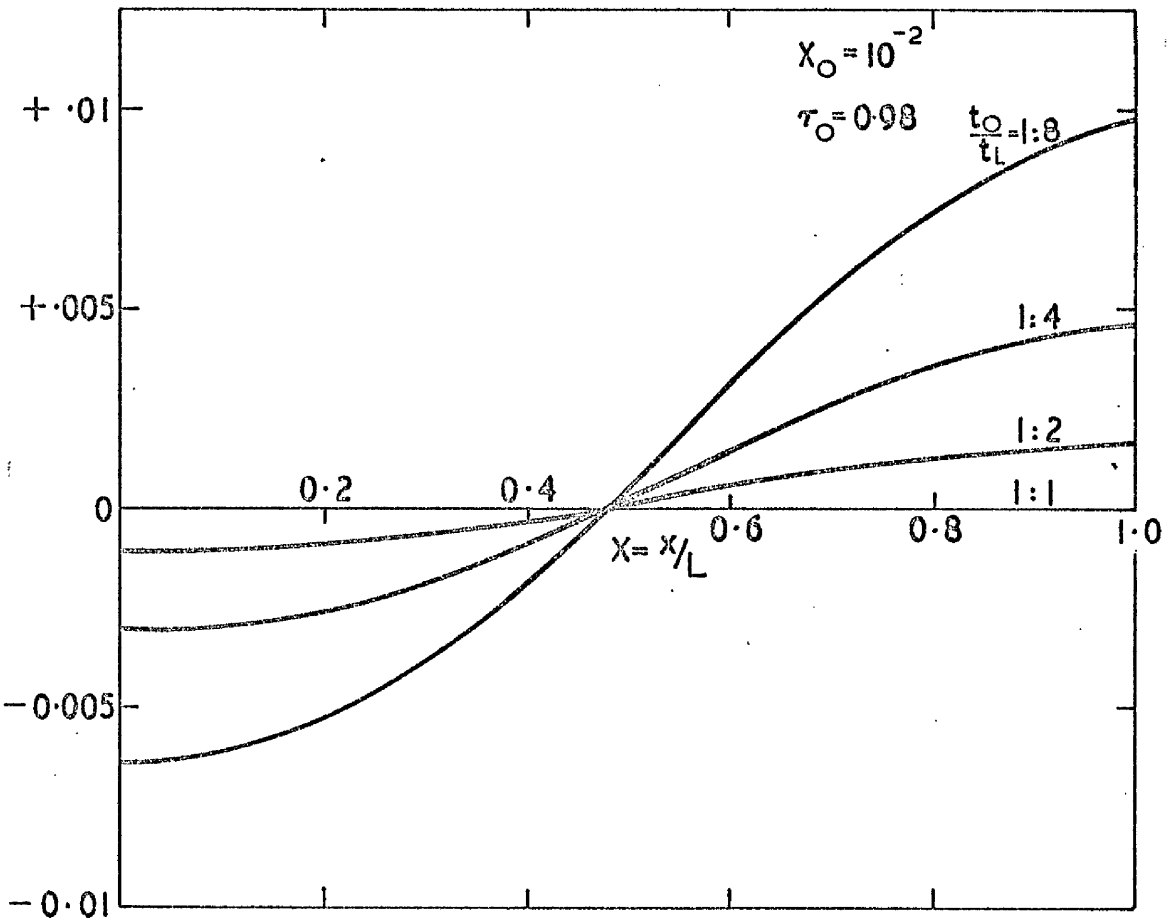

Figure 3.6.4 The effect on the temperature distribution due to a linear variation of thickness, $t_o < t_L$ (plotted as fraction of the temperature distribution for the slab of the same nose thickness).

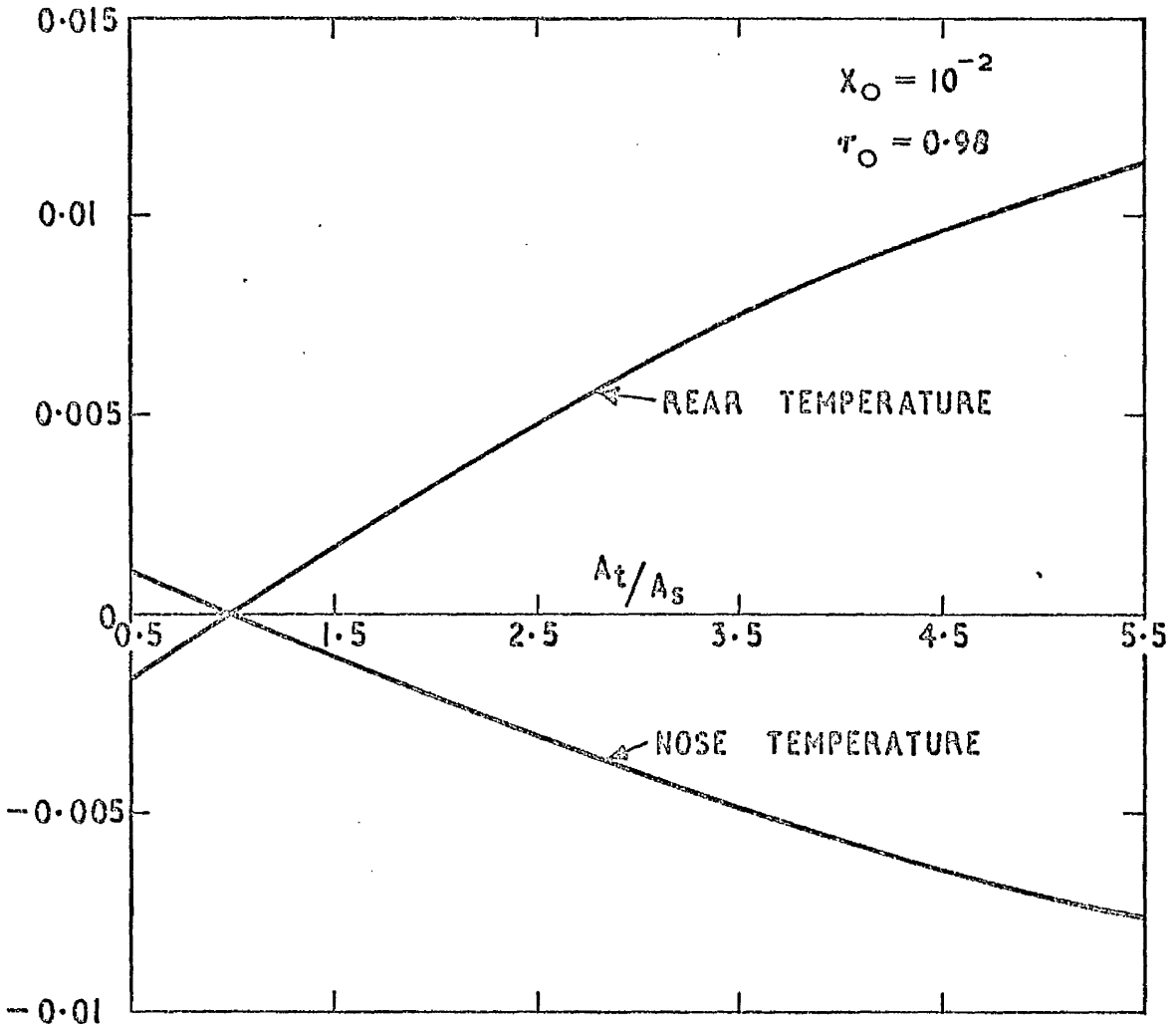

Figure 3.6.5 The effect of the total cross-sectional area (A_t) upon the nose and rear temperatures of a trapezoidal section (plotted relative to the slab values of the same nose thickness).

parameters are plotted in figures (3.6.6) and (3.6.7). As X_o decreases the changes produced in the temperature distributions become larger. For $\tau_o \rightarrow 0$ and ∞ , the temperature distributions within a trapezium must of course be 0. The maximum deviations are obtained at very roughly $\tau_o = 1.0$.

From the results presented in figures (3.6.3 - 3.6.7) we can conclude that for linearly tapered thickness distribution the slab predicts quite reasonably the temperature distribution. For $t_o > t_L$, the predictions are within $\pm$ 0.2% and in general for $t_o < t_L$ the estimates using the slab are well within $\pm$1% of the actual distribution. Provided we are prepared to sacrifice this order of accuracy, we can generalise the results of a slab section to cover any linear variation of thickness if we redefine τ_o (cf. reference 12) as

$$\tau_o = k_L t_o / (\epsilon_L^2 \sigma^2 H^6 L^{13})^{1/8} \qquad (3.25)$$

where t_o is the nose (X = 0) thickness of the conducting material.

Looking back at the results discussed in section (3.3) it is evident now why the optimal distribution of thickness is tapered towards the rear and the reason why the wedge makes the poorest use of the conducting material.

In figure (3.6.8) we present the variation of the nose temperature vs. τ_o for several values of X_o. The corresponding effect upon the rear temperature of a body with a linear variation of thickness is shown in figure (3.6.9).

How does the nose thickness (t_o) of the conducting plate affect the temperature distribution? To answer this question, we have plotted in figures (3.6.10 - 3.6.13) the temperature distributions for several values

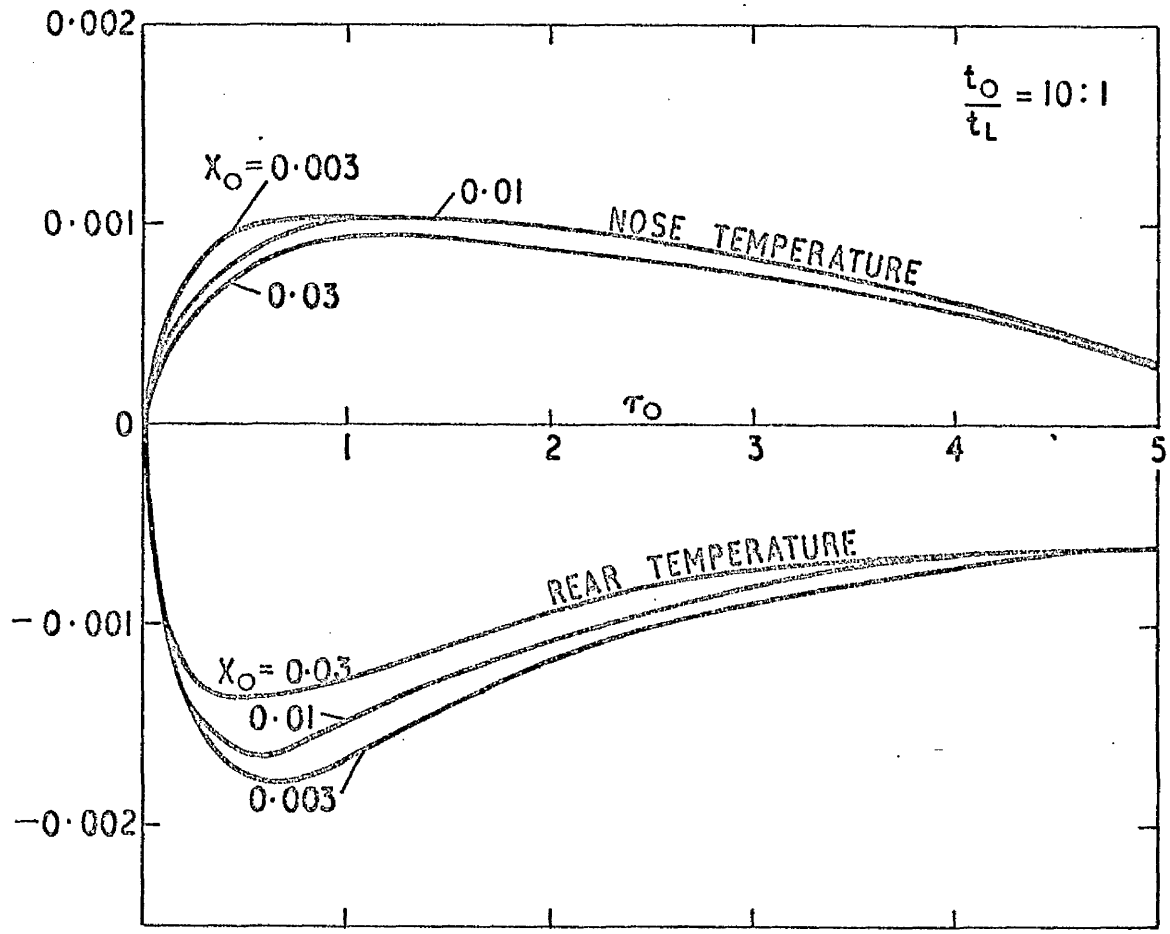

Figure 3.6.6 The effect of X_o and τ_o on the nose and rear temperatures of a trapezoidal section, t_o/t_L = 10:1 (plotted as fraction of the values for the slab of the same nose thickness).

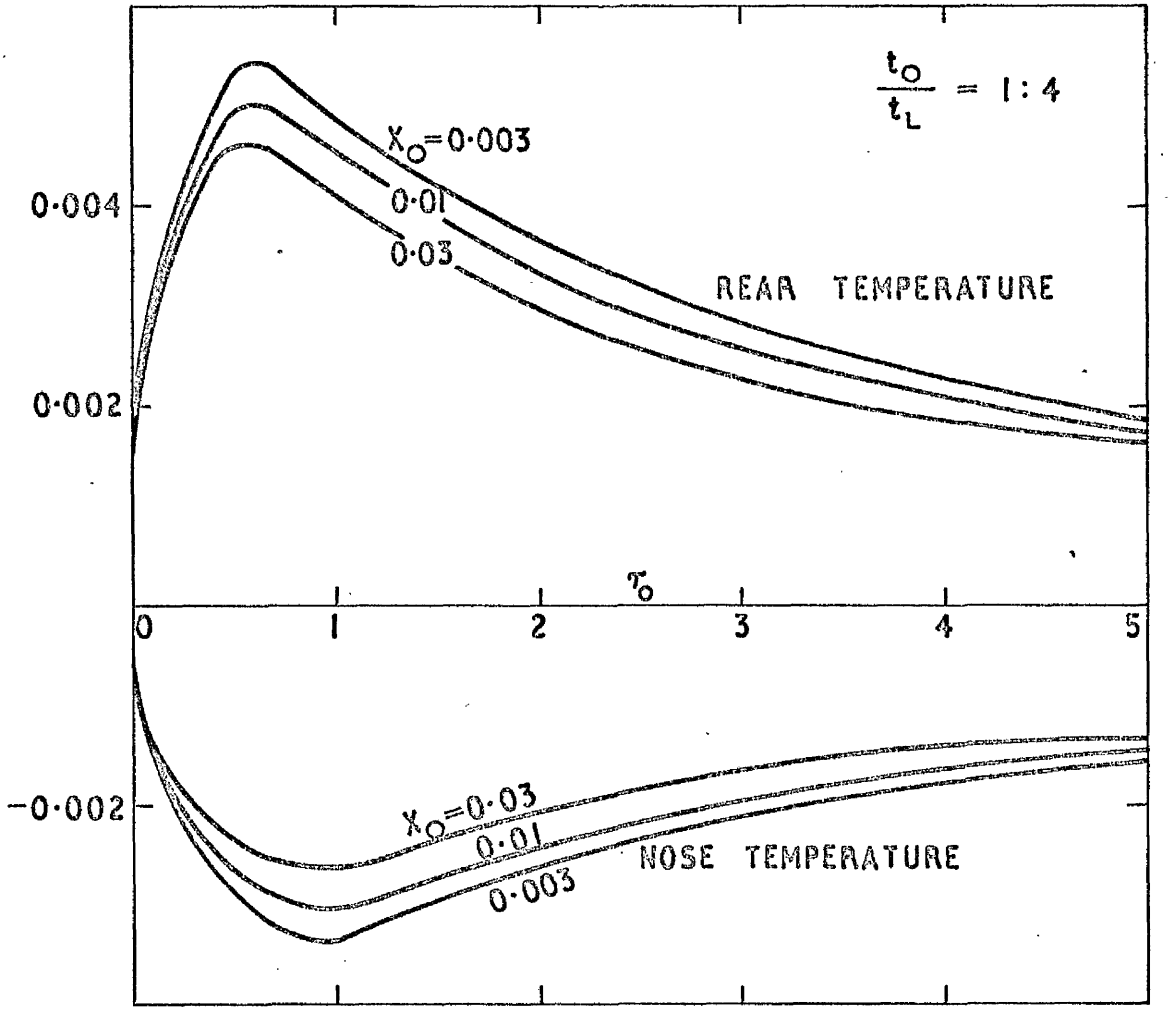

Figure 3.6.7 The effect of X_o and τ_o on the nose and rear temperatures of a trapezoidal section, t_o/t_L = 1:4 (plotted as fraction of the values for the slab of the same nose thickness).

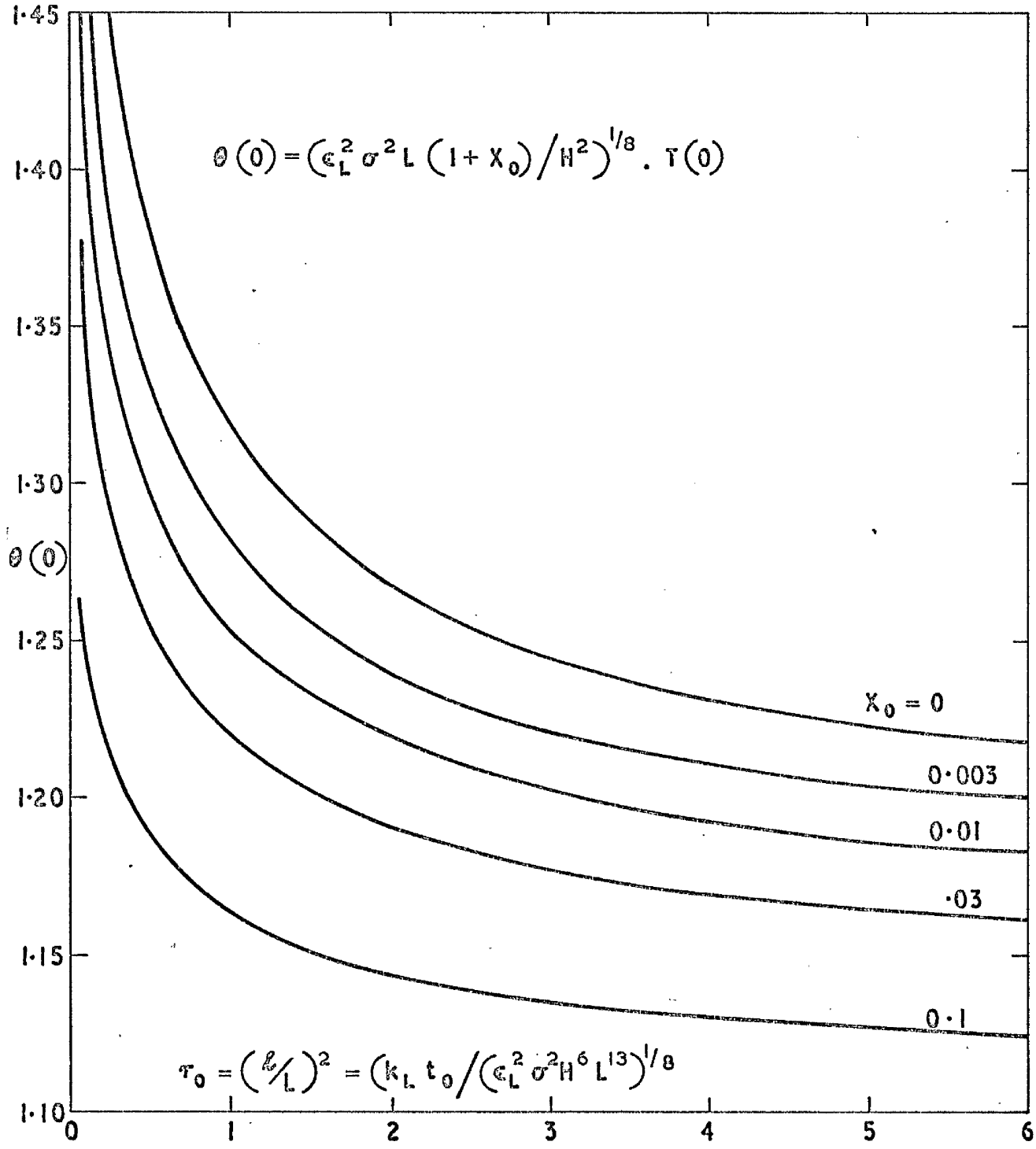

Fig. 3.6·8 Nose temperatures for a linear variation of thickness distribution.

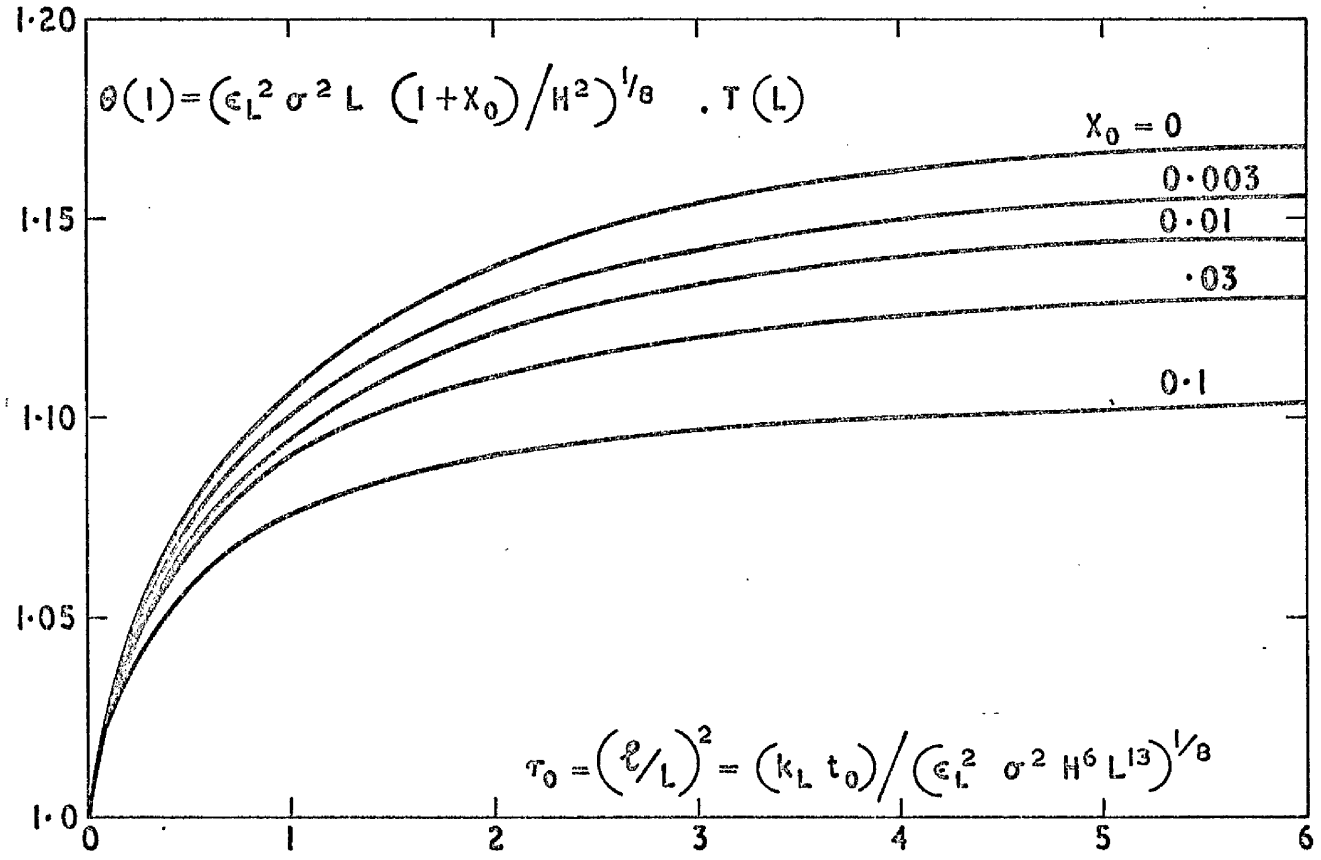

Fig. 3.6·9 Rear temperatures for a linear variation of thickness distribution.

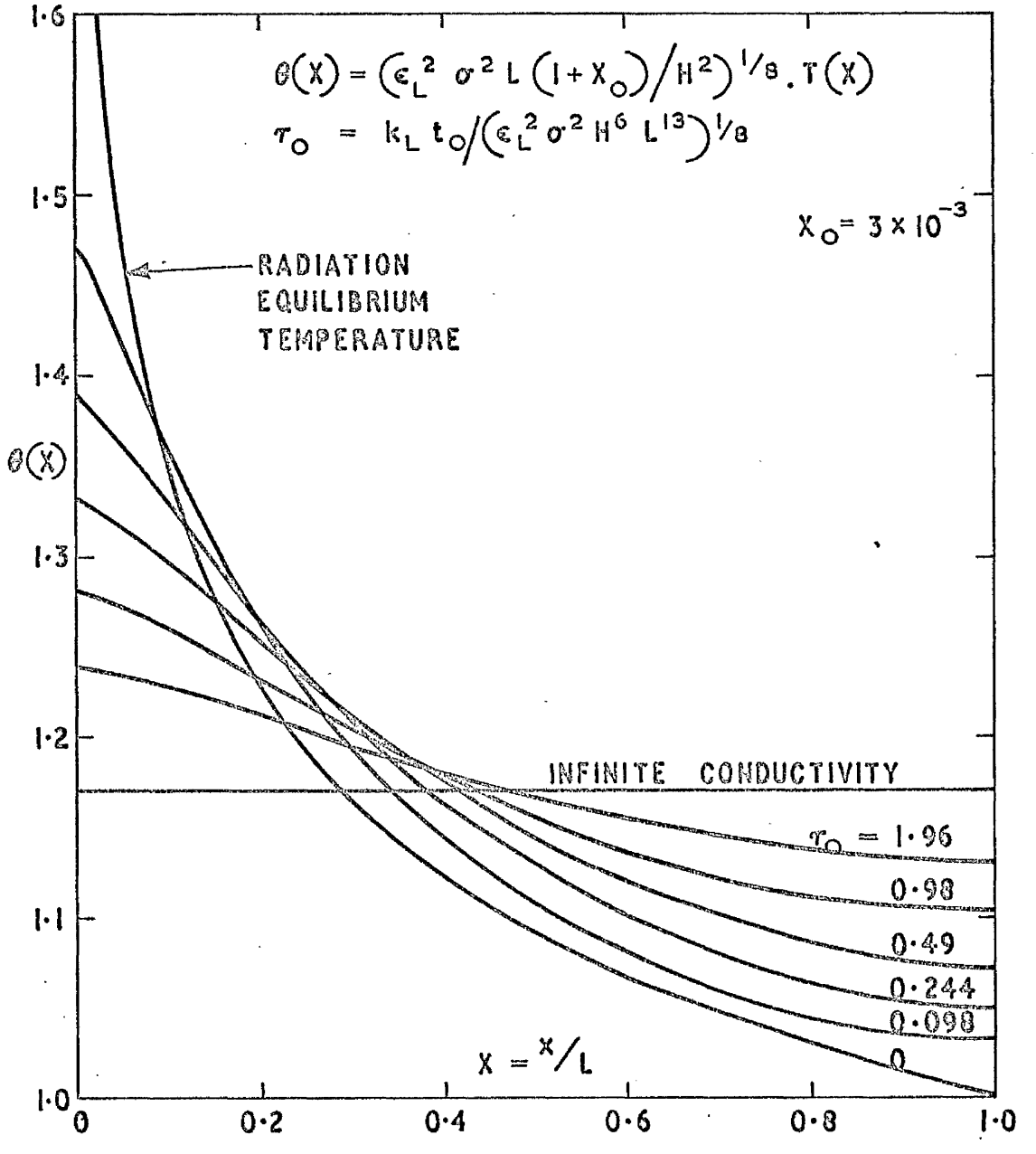

Figure 3.6.10 Some temperature distributions in trapezoidal sections. X_o = 0.003.

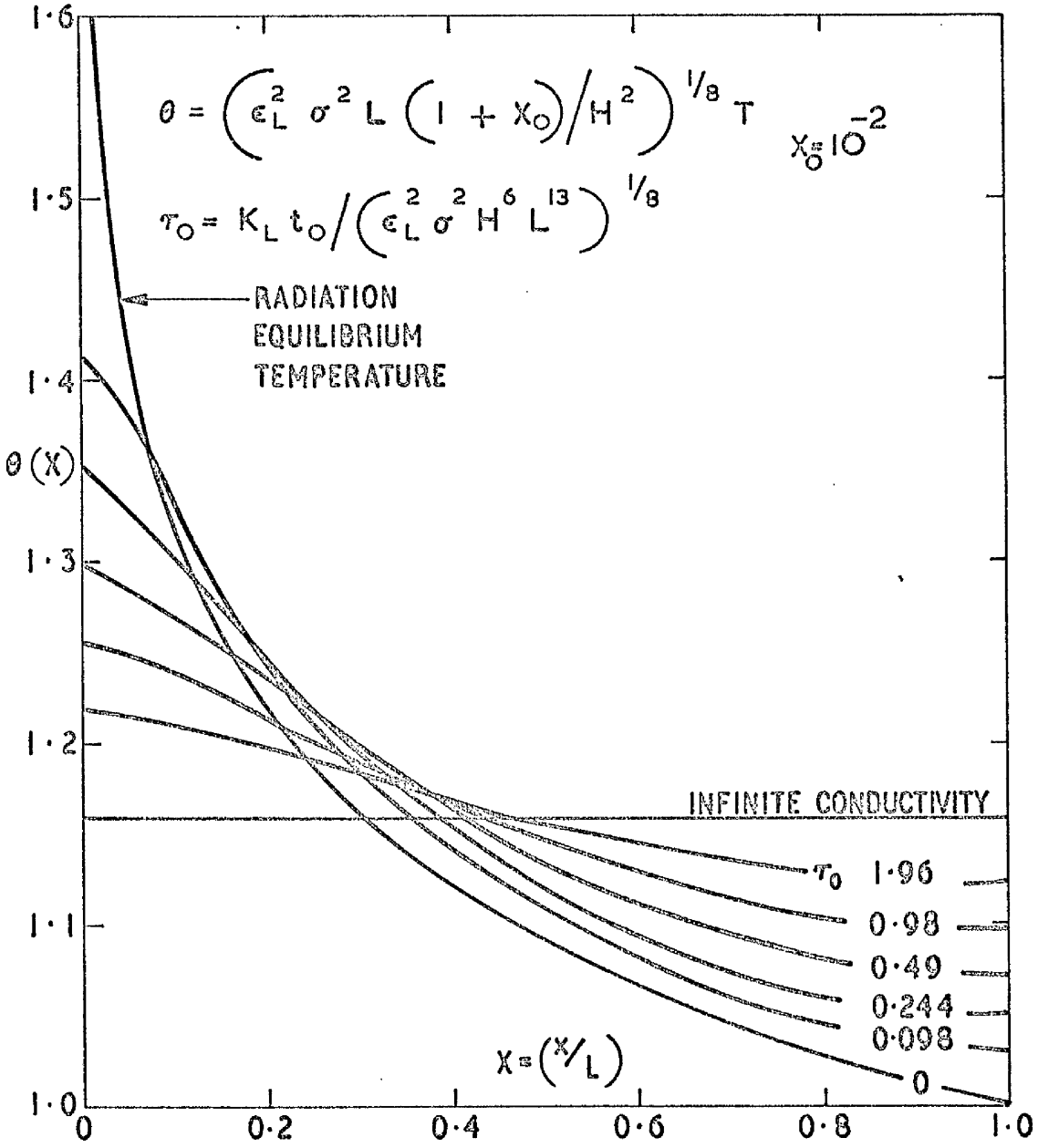

Figure 3.6.11 Some temperature distributions in trapezoidal sections. $X_o = 0.01$.

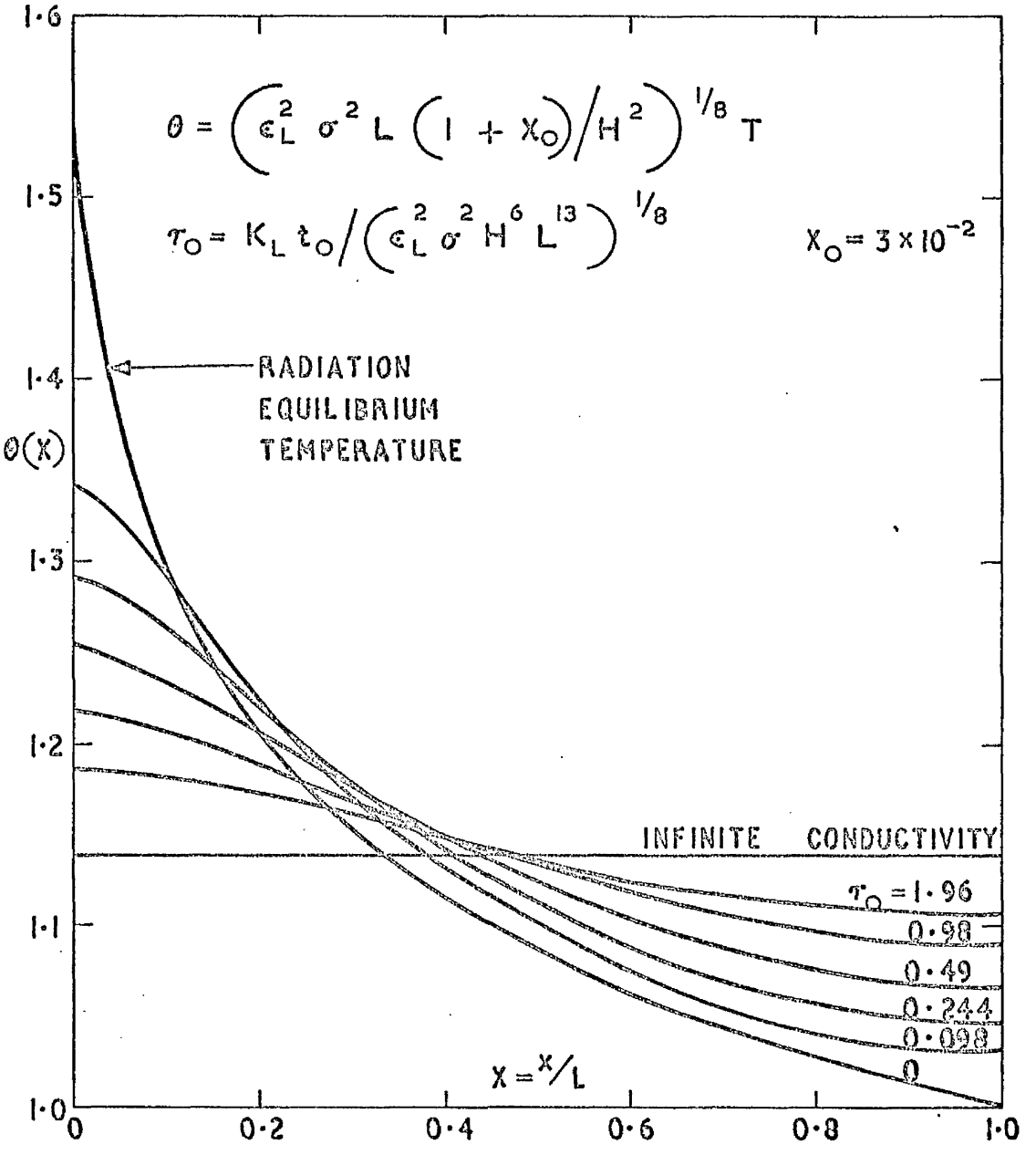

Figure 3.6.12 Some temperature distributions in trapezoidal sections. X_o = 0.03.

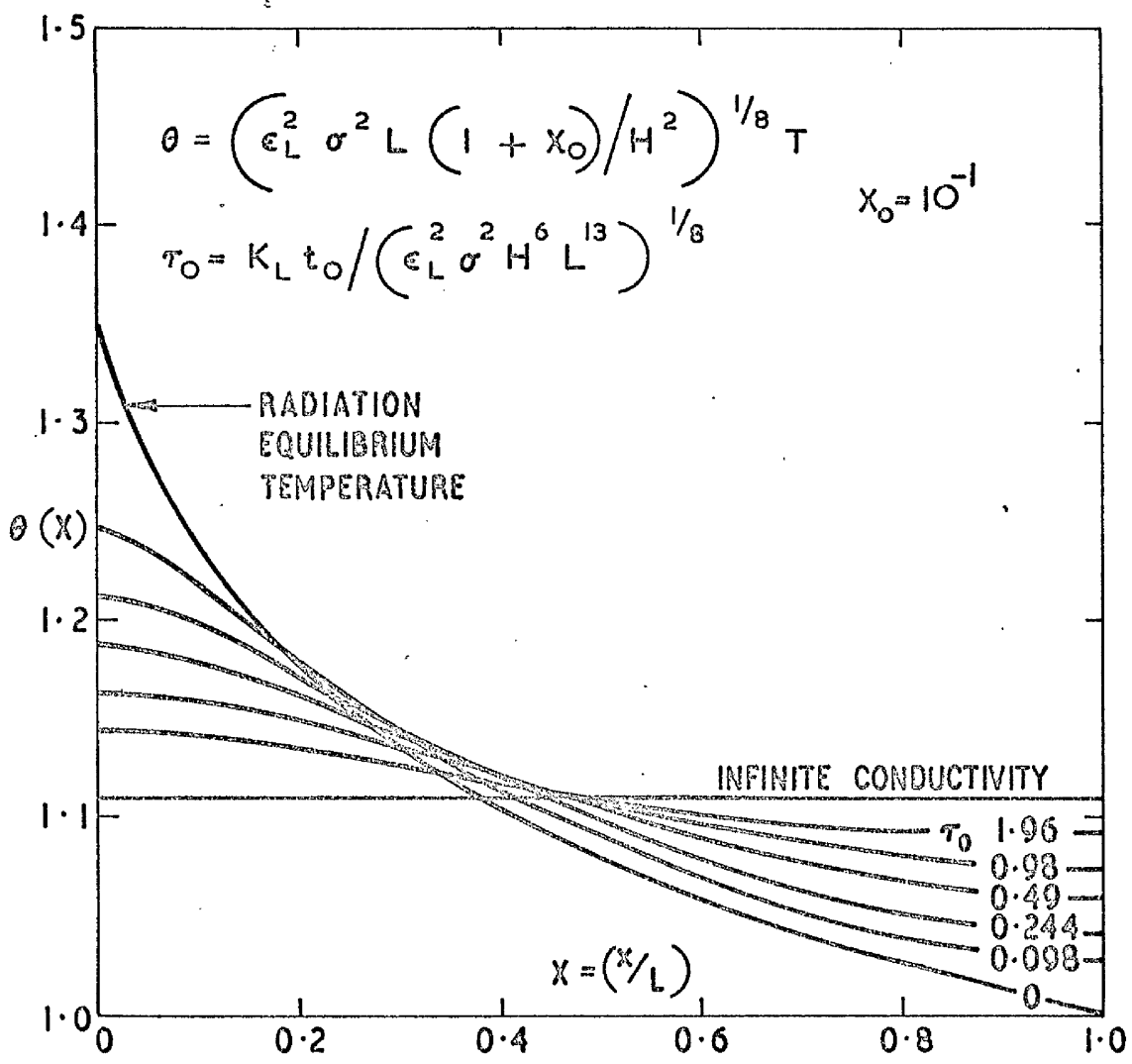

Figure 3.6.13 Some temperature distributions in trapezoidal sections. $X_o = 0.1$.

of τ_o and X_o. Also superimposed on top are the two extreme temperature distributions, namely, the radiation equilibrium temperature and the "infinite conductivity" solution. If we now interpret the variations of τ_o due to changes in the nose thickness of the conducting material, t_o (using equation 3.25), we see from these figures that as the ratio t_o/L increases, the temperature gradients everywhere are reduced and the temperature distribution tends towards that obtained for the "infinite conductivity" solution. On the other hand as the ratio t_o/L decreases, the temperature distribution tends towards the radiation equilibrium value everywhere (which is essentially a non-conducting plate solution).

In the rest of our discussions, unless otherwise stated, the solutions presented are for finite rates of heat transfer at the leading edge, given by the relation

$$Q = \frac{H_o}{(X + X_o)^{\frac{1}{2}}}$$

CHAPTER IV

Experimental verification of the theory of two-dimensional conducting plates

4.1 Introduction

The purpose of experimental investigation is two-fold. Firstly, it is to seek experimental verification of the theoretical prediction of the leading edge temperature distributions based on certain prescribed boundary conditions as described in chapter III. Models which are used to represent the leading edge are subjected to a simulated aerodynamic heat flux corresponding approximately to the $x^{-\frac{1}{2}}$ distribution along one surface of the model. The second purpose of the investigation is to enable studies to be made on models whose theoretical solutions are sometimes difficult to obtain.

Sinha[10] conducted some preliminininary tests of two-dimensional models of constant thickness. By the use of a specially designed reflector[28], aerodynamic heating was simulated roughly proportional to $x^{-\frac{1}{2}}$, except for the region very close to the leading edge where for practical reasons the reflector is capable only of producing limited rates of heat transfer. Assuming material properties to be independent of temperature, he compared his experimental results with the theoretical solutions obtained by using the relation $Q = H_o/x^{-\frac{1}{2}}$. In his work he reported a discrepancy of about 10% between the experiments and theory.

While Sinha has obtained useful information from his preliminary work, a number of factors which may well be influential on the final results have not been considered. These factors are now discussed in detail which constitute part of the reasons for the present

investigation. Moreover the types of model that have been tested covered only a particular case, i.e. uniform thickness and does not necessarily provide sufficient information for definite conclusions to be drawn.

Power available for heating the model. The capability of power output from the reflector is largely restricted by the type of heating element used. With a greater amount of power available a higher temperature and temperature gradients in the model of moderate thermal conductivity value can be expected. This has at least two advantages. A high absolute temperature minimizes the effect of background radiation whereas a higher temperature gradient facilitates the effect of heat conduction to be observed. In the earlier version the heating element was made from oxidized nickel wire. It has a fairly high emittance value among oxidized metals. Unfortunately the oxide layer tends to become unstable in vacuum when the surface temperature reaches about 1000°C. The maximum power output was 1.2kW . A higher value of maximum power that can be dissipated is desired.

Performance of the reflector. The temperature distribution in the model may be influenced by the distribution of thermal radiation impinging upon the model, which is its source of heat input. Although the reflector was designed to simulate a desired distribution of radiation, its performance was measured by an instrument which was not fully developed. As the author was involved in the development of this instrument[29] at the time when the reflector was being calibrated, it seems prudent to carry out a recalibration of the reflector now that the radiometer has been further developed[30]. By doing this we would

be in a position to find out if and where there is any substantial deviation of the reflector performance from its expected behaviour, and better still by using the measured values be able to assess their effect on the expected temperature distribution.

Location of model. During the calibration of the reflector it became apparent that the distribution of radiant energy was very sensitive to the exact location of the plane on which it was being measured. This aspect has not been considered in the previous tests. The detailed technique of setting up the model in the present tests is merely mechanical and has no great significance. It suffices to say that we ensure that all the models lie in the desired plane with their leading edge lying along a required straight line.

Surface properties of the models. Heat exchange between the heat source and the model and between the model and the environment has been arranged to take place through the surface of the model which is exposed to radiation. If this surface were a perfect reflector, the experiment would be nullified. On the other hand, if the surface were a black surface, the heating of the model would follow the exact heat distribution simulated by the design of the reflector. Since it is not possible to provide a black surface for our models, the absorptive power of the surface should be aimed at being as high as possible. Both the surface absorptivity (for a grey metallic surface this is usually identical with the emissivity value) and its dependency on temperature are of importance for these data will influence the exact behaviour of the mathematical model in our theoretical analysis. This part has not been included in the previous experiment.

Test models. We consider the theory presented in Chapter III to be general. Hence it is important that the experimental verification to be carried out should also be general. In practice we will be content to examine results from a small number of models of various types provided they cover a wide enough range. In previous experiments only slab models were tested. This can only be considered as a particular case

4.2 Simulation of aerodynamic heating.

We require some means of simulating steady state aerodynamic heating (which we have shown in Chapter II can be reasonably taken to vary as $x^{-\frac{1}{2}}$) of models used to represent the leading edge section of a hypersonic wing. The simplest method of providing heating is to use an electrically heated element as a source of infra-red radiation. Sinha[10,28] has designed and constructed a reflector 0.305m. long, which is capable of producing a heat distribution roughly proportional to $x^{-\frac{1}{2}}$ in a given irradiated plane. Altogether the reflector consists of seven curved surfaces blending smoothly to form a quasi-continuous profile.

The source of heat is a wire coiled round a ceramic (alumina) tube which is reinforced by the insertion of a tungsten rod through its centre to prevent sagging at high temperatures. Heating received by the model is due largely to the reflected radiation and to a very small percentage to the direct radiation from the element.

4.2.1 Power output from the filament.

The similarity laws derived in reference (12) permit us to carry out scaled experiments provided we select the other parameters accordingly. A low value of the heat input parameter H_o restricts the use

of materials to those with relatively poor thermal conductivity (as we shall show later in paragraph 4.3). In addition as we increase the value of H_o, the temperature values within the model everywhere are higher and the effect of the background temperature upon the temperature distribution is reduced. In the experimental investigations the value of H_o is directly proportional to the power dissipated in the heater filament. It is therefore desirable to increase the power output of the electric element as much as possible.

The emissive power from a uniformly heated filament is proportional to ϵT^4. With the use of oxidised nickel wire a maximum power output of about 1.2kW has been obtained. Whereas it may not be possible to increase the emissivity any higher than that of oxidised nickel, there is a considerable scope for some materials to operate at a much higher temperature. In this respect we may still be able to increase the heating power. Three materials holding good promise are tungsten, molybdenum and tantalum with their melting points[31] at 3410°C, 2620°C and 2996°C respectively.

The suitable material should have a high operating temperature in high vacuum and workability. Tungsten is notoriously brittle at room temperature while molybdenum is rather unpredictable and can transform rather suddenly from a ductile to a brittle state[32]. Tantalum is the most ductile material of the three at room temperatures. In as far as the vapour pressure [31,33] is concerned tantalum has a vapour pressure of 12.5 nN/m^2 at 2000°K as compared with 13.3 nN/m^2 (about 10^{-10}torr) for tungsten at the same temperature and only 3.3 $\mu N/m^2$ for molybdenum at a lower temperature of 1870°K. These figures suggest that in a high vacuum environment, tantalum is likely to have a higher

service temperature than either tungsten or molybdenum.

At a given temperature the radiative power of an element can be increased by increasing the surface emissivity which can usually be achieved by oxidation. Unfortunately, although all three materials are relatively inactive chemically at room temperature, when heated in air above 500°C they oxidize violently. Prolonged oxidation at higher temperatures can lead to a total disintegration of the materials. Only limited oxidation can be carried out at room temperatures below 500°C. All three materials possess just about the same values of surface emissivity at elevated temperatures[33].

Thus tantalum has been selected as the material for the heating filament. Oxidation was limited to 30 minutes at about 450°C, producing a modest increase in the value of emissivity of about 0.3. Oxidation changes the smooth and shiny surface texture of tantalum to one which is quite rough and greyish in appearance. An increase of 50% in the maximum power available is obtained if we replace the oxidized nickel wire by an oxidized tantalum wire and we can safely dissipate in the filament around 1.8kW of electrical power in a high vacuum environment. The diameter of the tantalum wire is 0.08cm. This increase in the operating temperature of the filament has not caused sagging at the middle of the element.

4.2.2 Calibration of the reflector

A brief description is given here of the radiometer which is specially designed to measure the thermal radiation intensity over the model. Its working principle is of a thermopile. The hot junctions of a thermopile are arranged to lie in a straight line,

which is placed in the irradiated plane at right angles to the axis along which the radiation intensity is varying. The cold junctions are kept at a constant temperature. With proper shielding the incident radiation will pass through a slit just wide enough for it to impinge on the hot junctions so that the radiation intensity thus measured will represent the mean value over the distance corresponding to the diameter of the hot junction beads. By making the beads as small as possible, the resolution (i.e. the ability to sense the true value of the local intensity) can be improved, at the expense unfortunately of the sensitivity of the instrument. By increasing the number of thermocouples, the sensitivity can be improved.

This instrument[30] is used to recalibrate the performance of the reflector. The measured performance of the reflector is shown in figures (4.2.1) and (4.2.2). The greater resolution of the present radiometer has confirmed the fact that there exists at some distance from the leading edge (about $X = 0.6$) large deviations of radiation intensity from the desired trend of distribution. During the calibration it also became apparent that the measured output was very sensitive to the plane in which the measurements were being made. Any small departure from the designed irradiated plane produces a deteriorating effect on the performance of the reflector.

The reflector was designed to simulate a $x^{-\frac{1}{2}}$ distribution of heat transfer. From the results presented in figure (4.2.1) it is evident that very close to the leading edge the reflector can only produce finite and very limited rates of heat flux. However over the range $0.0275 \leq X \leq 1$ the reflector reproduces the desired distribution

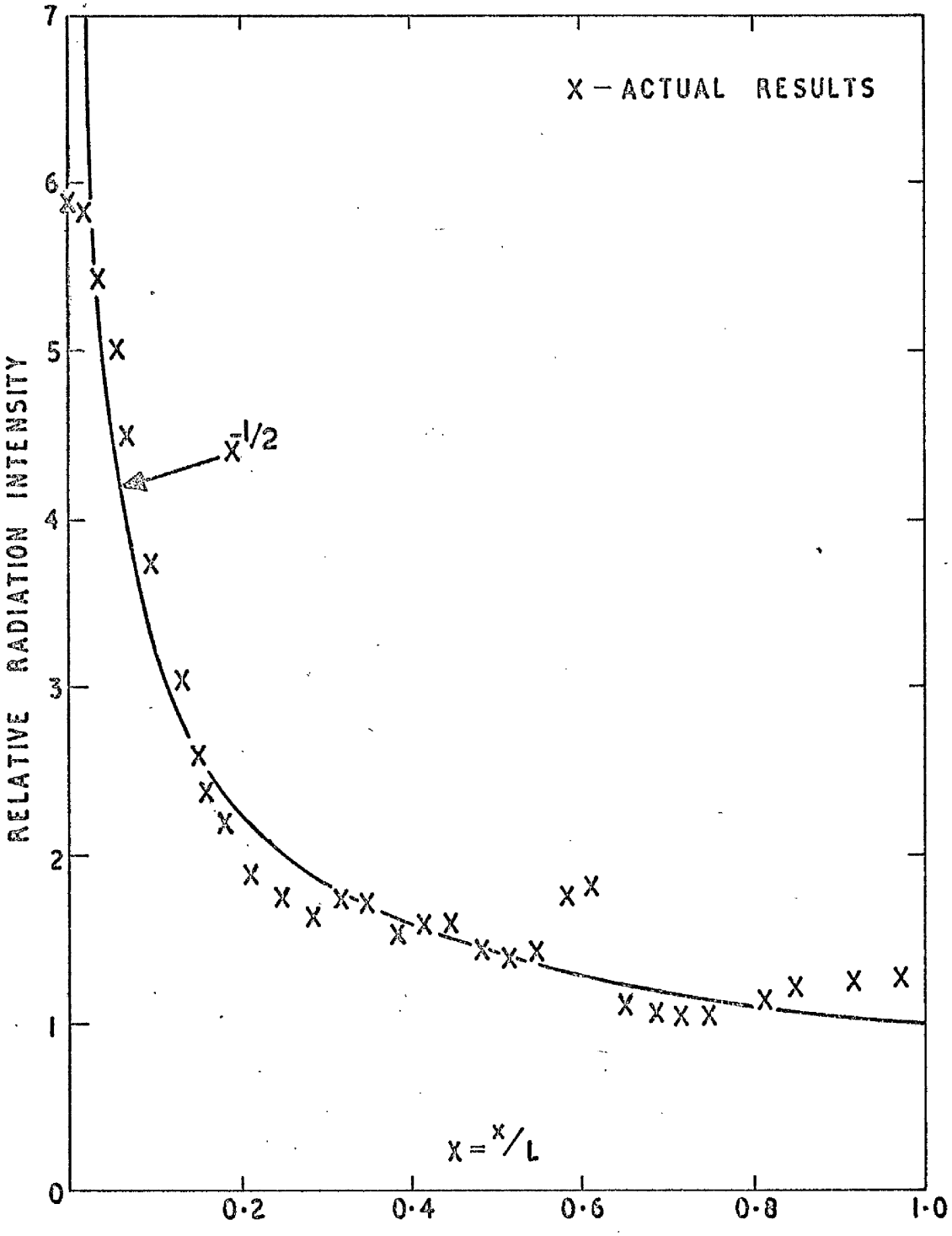

Figure 4.2.1 Comparison of the performance of reflector with $X^{-1/2}$ distribution.

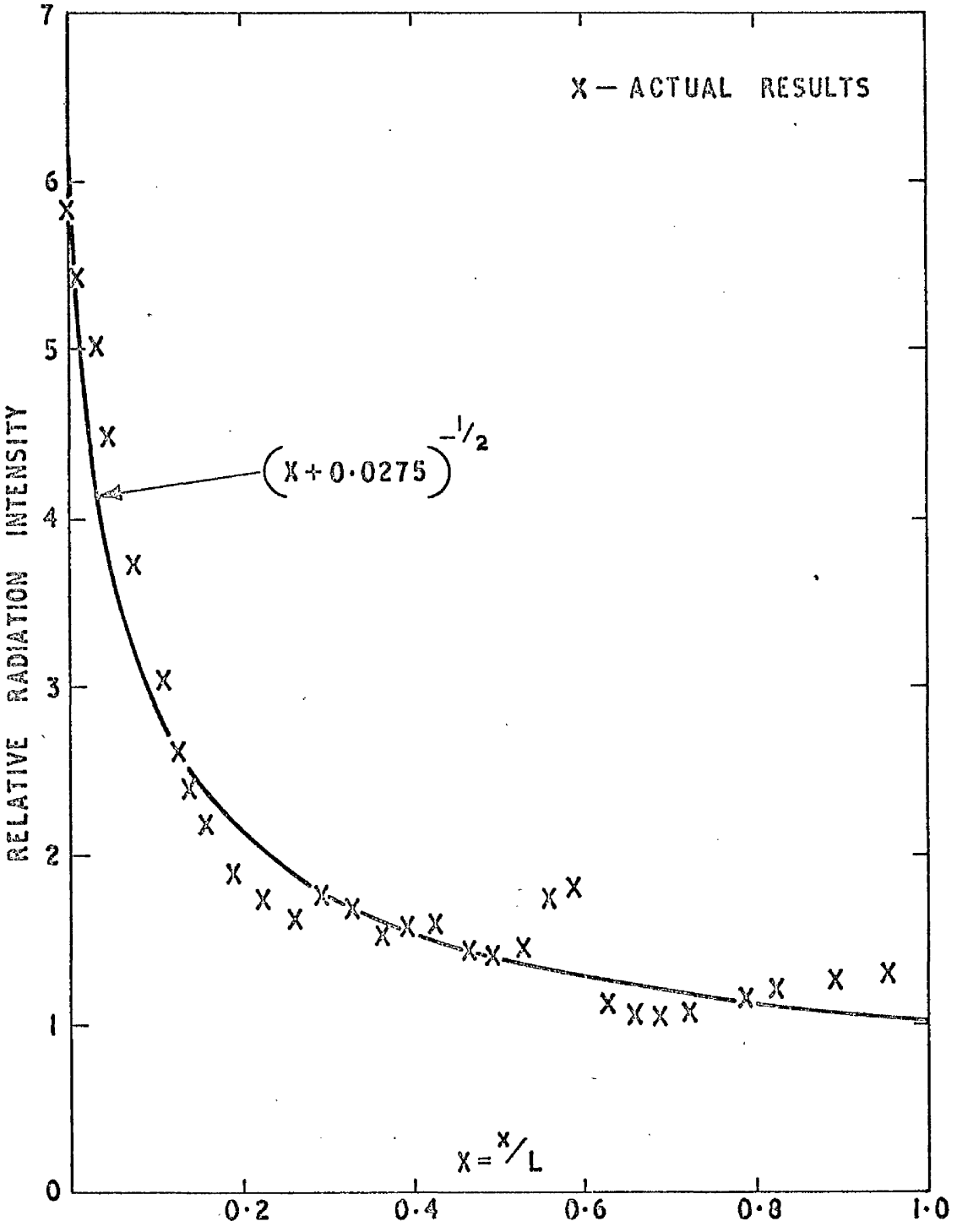

Figure 4.2.2 Comparison of the performance of reflector with $(X + X_o)^{-1/2}$ distribution.

fairly well. It seems sensible to place the nose of the model at $X = 0.0275$ instead of $X = 0$. By shifting the nose of the model to $X = 0.0275$ we also ensure the maximum heat flux gradients occur along the leading edge in accordance with the actual phenomenon of boundary layer heating.

Since the magnitude of the ratio $\frac{Q_o}{Q_L}$ is about 5.8 only, it would no longer be justifiable to compare the measured temperature distributions in the models with those predicted by the theory using the $x^{-1/2}$ variation. It would be interesting to see how the results from the actual performance of the reflector differ from those based on the $(x + x_o)^{-1/2}$ distribution. In figure (4.2.2) the actual results are compared with $X_o = 0.0275$. The choice of $X_o = 0.0275$ is simply derived from the fact that the nose of the model is placed at $X = 0.0275$ in figure (4.2.1). With X_o taken to be equal to 0.0275 the intensity ratio is given by

$$\frac{Q_o}{Q_L} = \left(\frac{1 + 0.0275}{0.0275}\right)^{\frac{1}{2}} = 6.1$$

which is about the same as the measured value. A direct comparison between the experimental results and the numerical solutions of equation (3.15) can now be made with $X_o = 0.0275$ and an appropriate value of H_o. This gives the nose temperature about 4% lower than that if we use $X_o = 0$ (refer to figure 3.5.1).

4.3 Test models

The size of the reflector and consequently the planform of the models is largely determined by the size of the vacuum chamber. With the equipment available we can test models of planform area of

$0.305 \times 0.152 m^2$.

We propose to conduct experiments over as wide a range as possible of the parameter τ_o defined in equations (3.6) and (3.25) as

$$\tau_o = \left(\frac{l}{L}\right)^2 = \frac{k_L t_o}{\left(\epsilon_L^2 \sigma^2 H_o^6 L^{13}\right)^{1/8}} \qquad (4.1)$$

From the performance of the reflector it transpires that ideally all the models should have the same length to ensure that they are subjected to the same heat transfer distribution. We therefore fix the value of length L = 0.152m for the models. For reasons already outlined in section (4.2.1) it is advisable to use the highest value of H_o. As we shall show a little later on it is also recommended to employ a high value of surface absorptivity which for a metallic body implies an equally high value of emissivity ϵ. That leaves us with two parameters k and t which can be selected to suit. Although these two parameters always appear together in equation (3.15) as the product kt, it is still necessary from practical considerations to choose the values of k and t individually.

To select a suitable material for the models, theoretical solutions of equation 3.15 (with $X_o \longrightarrow 0$) were obtained for a wide range of thermal conductivities and for three different fine-ness ratios $\left(\frac{L}{t}\right)$. The nose and the rear edge temperatures are plotted in figure (4.3.1) with $H_o = 1680\ W/m^{3/2}$ and $\epsilon = 0.8$. A low value of H is used to represent the limited amount of heating available under experimental conditions. It can be seen that highly conducting materials such as copper and aluminium would give near uniform temperatures. It is important that the material so chosen should produce a

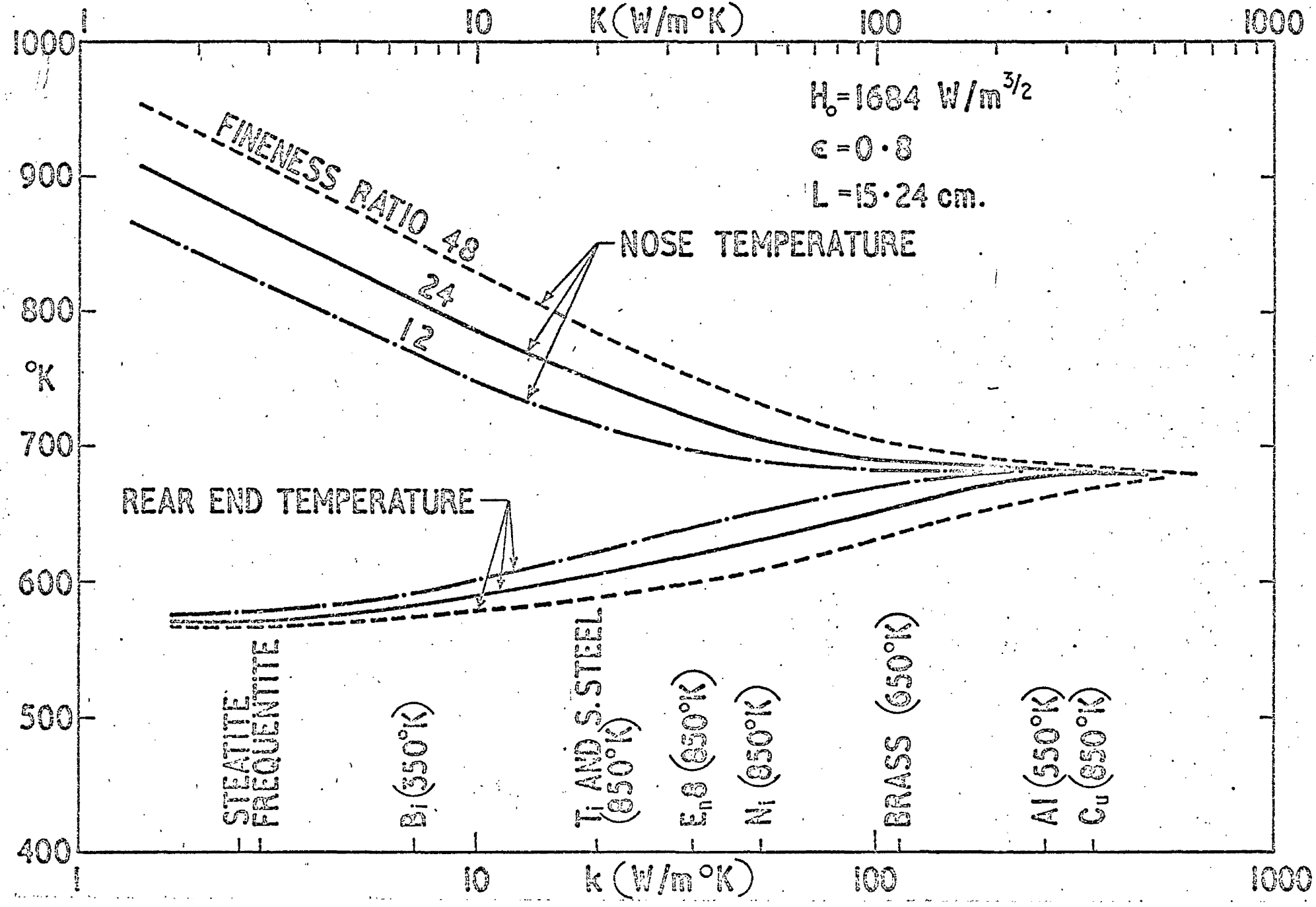

Figure 4.3.1 Effect of thermal conductivity on nose and rear temperatures.

substantial temperature difference between the nose and the rear edge of the model in order to reduce any error in the measurement of temperature. Insulating materials would be undesirable for they would contradict the basic assumption that the ratio $\frac{t}{k}$ is negligible compared with the product kt. Materials having very low thermal conductivity are also unsuitable because the conduction of heat along the thermocouple wires may occur more readily than through the model.

One common metal that meets the general requirements is stainless steel. The particular type of stainless steel chosen was F.C.B. Staybrite also designated as AISI - 347. Its coefficient of thermal conductivity is given by the manufacturers[34] (Firth-Vickers Stainless Steel Ltd.) as $k = 15.9\ (1+0.00039 \times T^{\circ}C)\ W/m^{\circ}K$.

Having decided on the value of the thermal conductivity (k), we now have at our disposal the parameter t (material thickness) to effect a change in the non-dimensional parameter τ_o. From the theoretical results presented in the last chapter we discovered that if we keep the other parameters fixed, not only is the nose temperature but the entire temperature distribution within the model sensitive to the nose thickness. We therefore embark upon testing a family of trapezoidal sections (with a linear variation of thickness) with a wedge section on the one extreme and a slab of constant thickness on the other. In addition we wish to find out the effect on the temperature distribution of the amount of conducting material and of the nose thickness. For this purpose we construct models having the same nose thickness but different thicknesses at the rear. The details regarding the dimensions of all the nine models is given in

table (4.3.1). These arrangements enable us to conduct experiments for the range of τ_o (based on the nose thickness) from 0.3 to 15.

A typical test model is shown in figure (4.3.2). Apart from the top surface of the model, all the other surfaces are highly polished using diamond powders. The temperature measurements are taken at the middle section of the model where two-dimensional conditions are expected to prevail.

4.3.1 Treatment of the model surface exposed to radiation.

The top surface of the model is exposed to thermal radiation. It should possess a high value of surface absorptivity in order to utilise as much of the limited heating available as possible. To minimise the effects of background radiation it is necessary in the experimental investigations to maximise the absolute measurements of temperature recorded on the model. This would require that while we use a high value of surface absorptivity, the top surface should have a low emissivity. For most grey metallic surfaces, however, the two coefficients are almost identical. In practice also, it would be desirable for the surface of the wing to have a high value of surface emissivity to take full advantage of radiation cooling under equilibrium conditions.

One of the studies undertaken was to investigate the effects of surface roughness and oxidation on the variation of surface emissivity with temperature for the type of stainless steel used in this experiment. We have in fact developed apparatus to measure the total hemispherical emissivity[35] of solid materials. This method uses an

Table 4.3.1 Test Models

Model No.	Material	Description
1	Stainless Steel (AISI-347)	Slab a = b = 1.27 cm
2	"	Slab a = b = 0.635 cm
3	"	Slab a = b = 0.317 cm
4	"	Trapezoidal a = 0.635 cm b = 1.27 cm
5	"	Trapezoidal a = 0.317 cm b = 1.27 cm
6	"	Wedge a = 0.0508 cm b = 1.27 cm
7	"	Trapezoidal a = 0.317 cm b = 0.635 cm
8	"	Wedge a = 0.0254 cm b = 0.635 cm
9	"	Wedge a = 0.0254 cm b = 0.317 cm

Note: For all models, d = 30.48 cm, L = 15.24cm. See Figure 4.5.2

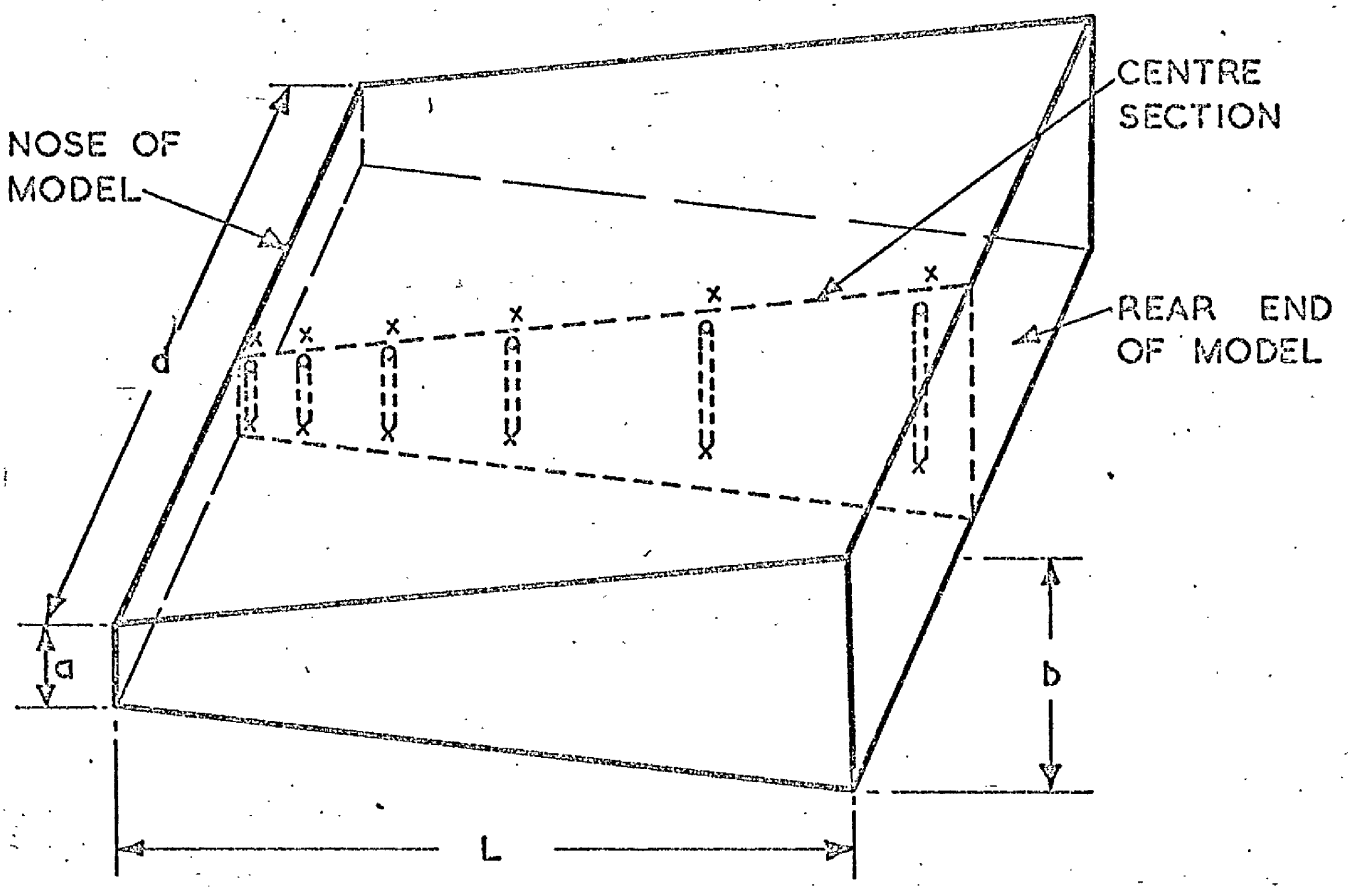

FIG. 4.3.2 TEST MODEL.

indirect heating approach and thus enables us to test both electrically conducting and non-conducting materials. For materials which obey the Lamberts' Cosine Law of diffuse emission, the total hemispherical emittance can be taken to be equal to the total normal emittance. Some of the observations made in reference (36) relevant to the present study are:-

1) Roughening the steel surface by shot-blasting increases the emittance values slightly as compared with the as received conditions.

2) The combined effects of shot-blasting and oxidation give more favourable results than those of individual surface treatment.

3) The effect of oxidation on emittance is pronounced when the temperature of oxidation is as high as 900°C with the emittance values quite close already to the blackbody value.

Based on this experience we shot-blasted and then oxidized the top surface of the stainless steel models at 900°C for 20 minutes. After this treatment to stainless steel AISI - 347, reference (37) suggests that the emissivity of the surface can be taken as $\epsilon = 0.735\ (1 + 0.000297 \times T^{\circ}C)$.

4.4 Apparatus and experimental procedure.

The models are subjected to simulated aerodynamic heating by using the specially designed reflector housed inside a vacuum chamber. The object of carrying out the testing of models in vacuum is to avoid convective heat transfer so that the entire heat input to the model and heat dissipation from the model will be by thermal radiation alone. Heat transfer by natural convection[38] becomes insignificant if the Grashof number (based on a mean representative temperature of the

equipment) is less than 100. This would be possible if the working pressure inside the vacuum chamber is maintained below 1 N/m^2. The experiments are in fact conducted at pressures of the order of $2mN/m^2$.

The inside walls of the vacuum chamber are painted black using an enamel paint which is claimed to have an absorptivity of 0.9. Any thermal radiation being reflected from the walls of the chamber is thus reduced to a minimum. Further, the vacuum chamber walls are water cooled so that the background radiation can be maintained at a known and definitely low level. The level of background radiation can be estimated to provide a small correction to the rates of heat input to the test model.

Apart from the top surface of the model which is sand-blasted and oxidized, the rest of the surfaces are highly polished. Additional shielding against radiation heat loss is provided by placing highly reflecting surfaces parallel and close to the polished faces of the model. The experimental set up is shown in figures (4.4.1) and (4.4.2).

Heat loss by conduction from the model is reduced by resting it on four pointed ceramic pins, placed near the four corners. Heat transfer to the ceramic supports through four pin-points can thus be ignored. These pins are mounted on jacks which are used to adjust the height of the model from a reference surface inside the vacuum chamber. With the help of this arrangement it is possible to set the top surface of the model precisely in the irradiated plane. In addition extra care is taken to ensure that the line of the leading edge corresponds exactly with the axis X = 0 of figure (4.3.2).

Measurements of temperature were made by means of thermocouples

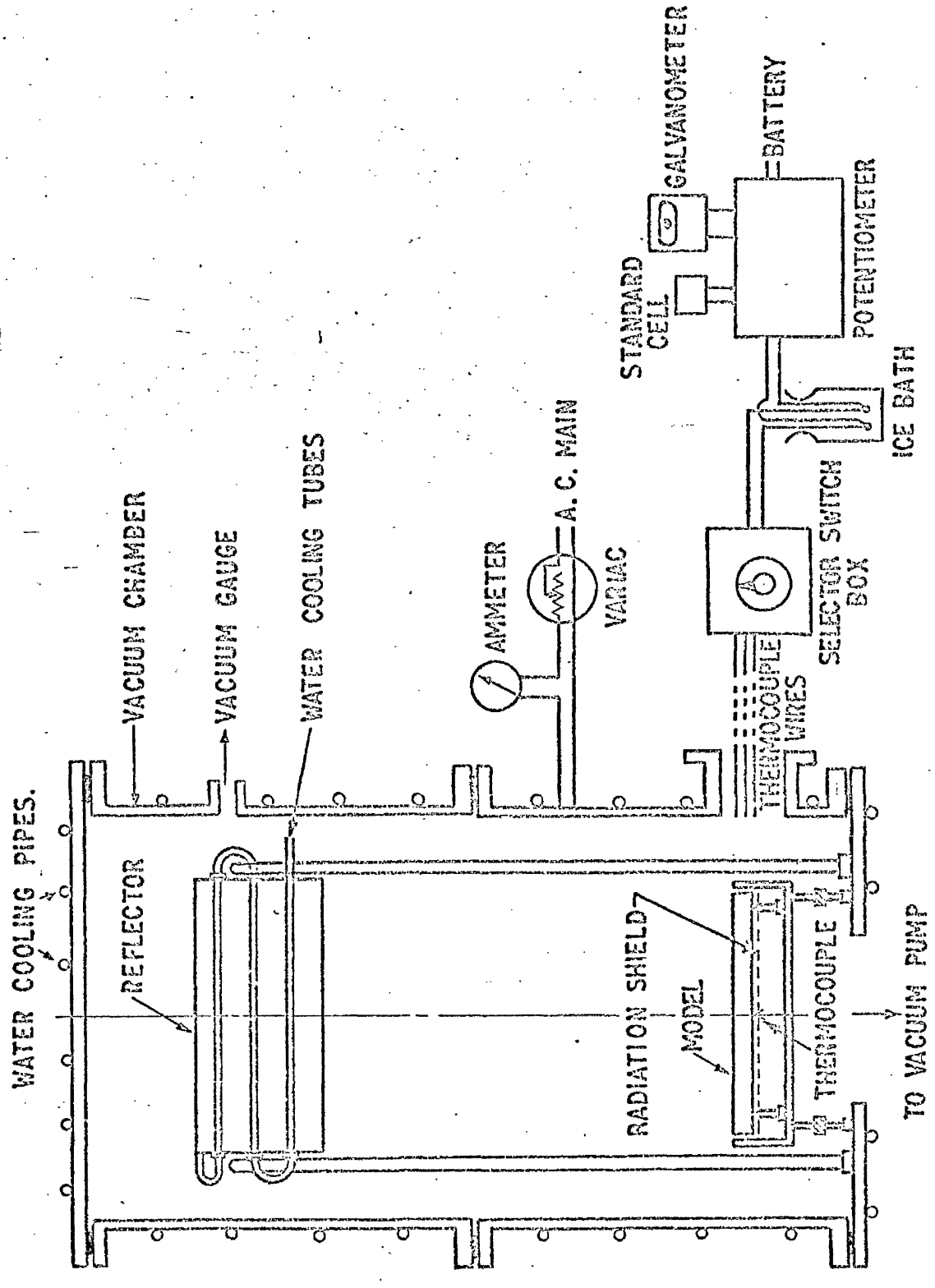

GENERAL LAYOUT OF APPARATUS

Fig.4.4

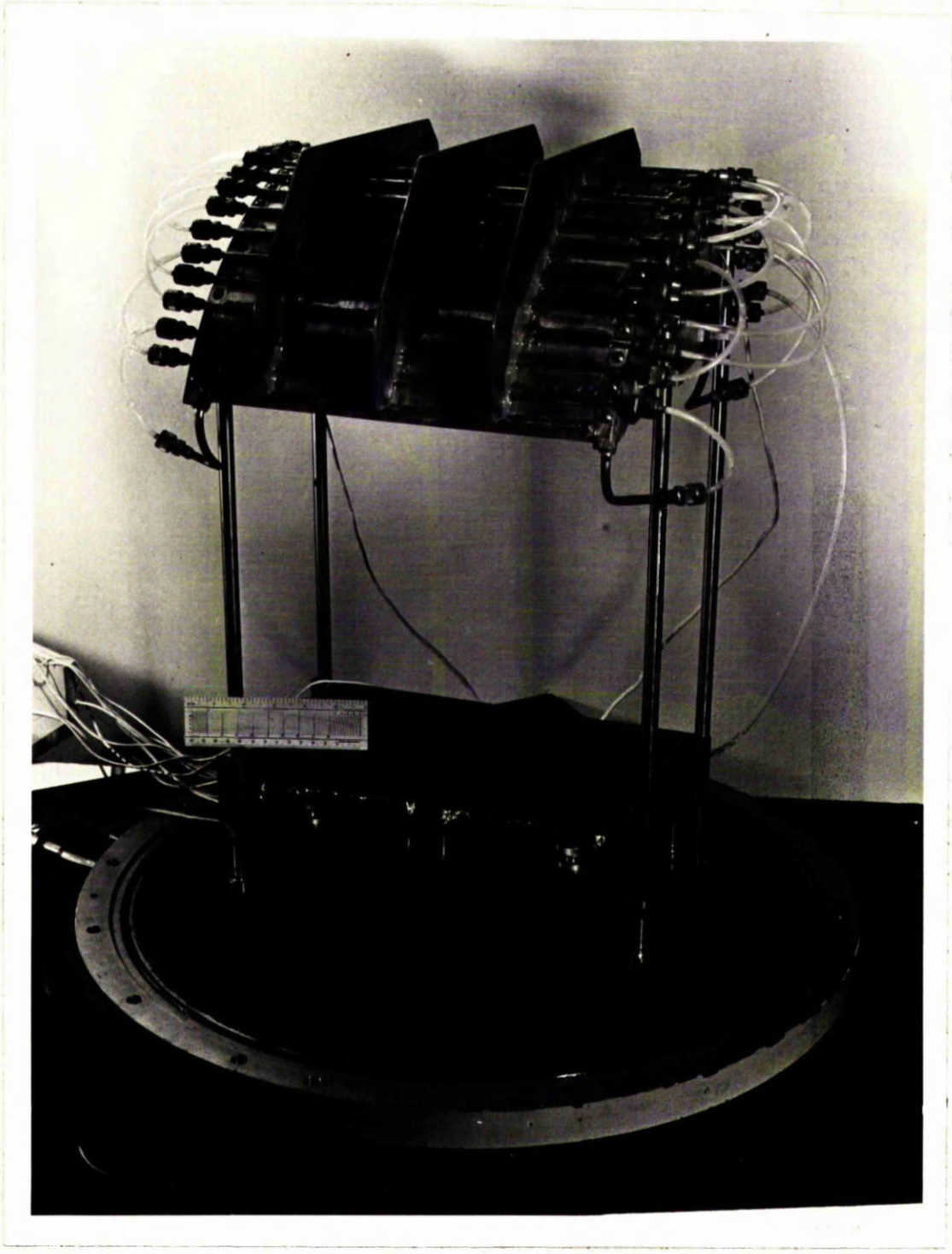

Figure 4.4.2 General arrangement of model and reflector.

embedded into the stainless steel or where the thickness is insufficient by spot-welding the thermocouples onto the surface. The two methods have been found to give the same results. The thermocouples are made from 40 SWG (0.012cm diameter) Eureka-constantan wire. Wires having such a small diameter have been selected in order to reduce the heat loss by conduction. Altogether twelve thermocouples are placed in two rows (0.635cm apart) in the middle section of the model at six prescribed locations. To detect any variation of temperature across the thickness of the model one row of thermocouples was placed near the top surface of the model and the other row near the bottom surface. The thermocouple emf (which is a measure of the temperature) was originally recorded by means of a potentiometric set up as shown in figure (4.4.1). This has been replaced by a digital d.c. voltmeter capable of measuring to an accuracy of $\pm 1\ \mu V$. Although this in itself might have no direct bearing on the results, it is considered to be a definite improvement in the laboratory methods in use.

The vacuum chamber is evacuated by means of a 6" diffusion pump backed by a single stage rotary pump. Once the working pressure of less than $2mN/m^2$ (about 10^{-5} torr) is reached, the electrical power to the reflector filament is switched on and thereafter increased by definite increments. After each increment of power and as soon as steady state conditions are reached the temperature distribution in the model is recorded. Only the comparison between the temperature distributions corresponding to the maximum power and the theoretical values is presented in the discussion later on. Table (4.4.1) gives the results of the nine models that have been tested. Note that less than 14% of heat dissipated in the filament in fact reaches the model.

Table 4.4.1 Experiment Results.

Model No.	Total Power from heater (W)	Power received by model (W)	H_o ($W/m^{3/2}$)	Temperature in ^oK at					
				X=.0208	.1043	.271	.397	.647	.96
1	1806	237.5	1179	609.0 607.4	605.0 604.1	595.8 595.2	583.4 582.6	569.2 568.2	559.1 557.9
2	1748	213.5	1165	619.8 616.8	611.8 613.1	598.9 598.3	580.6 580.6	554.2 560.2	545.7 548.2
3	1889	258.2	1281	654.4 658.2	629.8 648.5	613.9 621.6	589.9 593.8	560.5 565.0	543.5 548.7
4	1852	246.0	1220	625.5 623.9	618.8 617.6	603.5 602.1	- 585.8	- 568.2	- 558.4
5	1835	236.0	1167	628.7 629.5	- 619.5	598.1 598.9	- 578.5	- 558.3	545.4 547.6
6	1886	240.6	1192	646.7 660.4	638.5 636.2	599.6 602.6	574.5 574.7	553.2 553.4	544.8 544.3
7	1866	255.2	1266	651.0 653.0	643.2 643.5	617.1 616.4	589.4 588.6	563.2 563.3	550.7 542.8
8	1886	247.7	1228	683.2 678.1	650.0 647.3	610.0 608.7	574.2 573.9	548.9 554.7	541.2 541.6
9	1868	240.2	1190	667.6 669.4	645.4 642.6	605.3 604.1	571.8 572.1	547.1 551.2	535.1 540.2

Note: For each model the upper row temperatures were taken near the top surface while the lower row temperatures near the bottom surface.

4.4.1 Experimental errors.

Whereas every precaution is taken to eliminate any experimental errors, there are certain errors that are unavoidable. We present here the sources of error that may exist in the experimental results.

a) Although convective heat transfer can be ignored at pressures below $2mN/m^2$, heat transfer by free-molecular conduction does exist. It is shown in Appendix B, that under the prevalent conditions, heat transfer by free-molecular conduction is negligible.

b) Since the model is isolated from the surroundings by resting it on four pointed ceramic pins, heat loss by conduction through the supports can be ignored. A very small amount of heat is lost through the fine thermocouple wires, but this is unavoidable and negligible compared with the longitudinal conduction of heat.

c) Except the top surface, all the other surfaces are highly polished and shielded against radiation heat loss. However some heat loss from the sides is inevitable.

d) The Eureka-constantan thermocouples used in the measurement of temperature have been calibrated at the National Physical Laboratory to within $\pm$ 0.2°C.

e) A small amount of heat is reflected from the vacuum chamber walls onto the model.

f) Back-ground radiation from the vacuum chamber walls which are maintained at the cooling water temperature.

4.5. Discussion and comparison of theory with experiment.

Figure (4.5.1) shows the calculated temperature distributions of the nine stainless steel models under a heating value given by

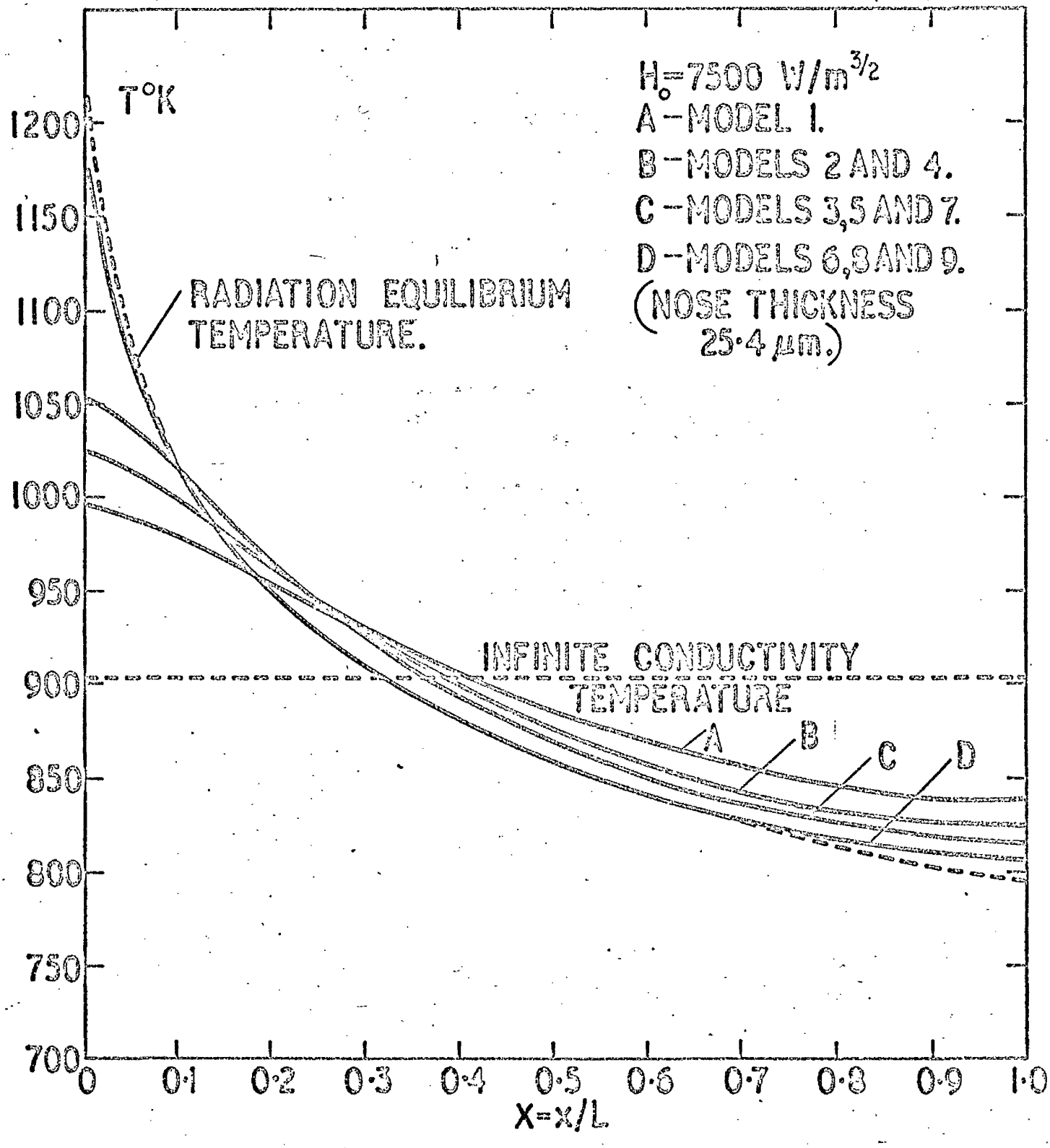

FIG. 4.5.1 COMPUTED TEMPERATURE DISTRIBUTION IN MODELS SUBJECT TO A GIVEN HEAT INPUT.

$H_o = 7500\ W/m^{3/2}$ (and $X_o = 0.0275$). The numbers associated with the models are the same as in tables (4.3.1) and (4.4.1). Also plotted are the calculated results for the two extreme conditions namely, the radiation equilibrium temperature and the infinite conductivity temperature which is constant along the model. Since the total input of heat to the models must equal the total amount of heat radiated away from the models, the family of curves satisfies the relation

$$\sigma \int_o^L \epsilon\, T^4\, dx = \int_o^L \frac{H_o}{\sqrt{(x + x_o)}}\, dx \qquad (4.2)$$

As compared with the non-conducting plate, the role of the thermal conductivity of the material is to reduce the nose temperature of the model at the expense of the rear edge value. In the last chapter we found that in a conducting plate which has a linear variation of thickness but constant thermal conductivity and emissivity, the temperature distribution is a function essentially only of the nose thickness. A slab can be used to predict within 1% the temperature distribution of any trapezoidal section that has the same nose thickness. The results pesented in figure (4.5.1) are for stainless steel models where the coefficients of thermal conductivity and surface emissivity are taken as functions of temperature; the product kt becoming a function of X and θ. Any differences in the temperature distribution due to the variations in the thickness distribution are too small to be plotted in figure (4.5.1). The nose temperature as well as the temperature gradients everywhere can be significantly reduced by increasing the nose thickness, which of course represents the quantity of conducting material employed at the most crucial point. Alternatively,

the same benefit could be obtained by increasing the thermal conductivity of the material in the same ratio.

The other factor that is varied in the experiment is the quantity of heat input to the models. Figure (4.5.2) shows the variation of nose and rear temperatures plotted against the heat flux parameter H_o for models 1 and 6 (i.e. a slab and wedge section of the same rear thickness respectively). An increase by a factor of about 10 is required in the value of H_o to double the absolute nose temperature.

There are two possible ways of comparing the experimental results with those calculated from the numerical solutions. Looking again at the performance of the reflector (figure 4.2.1) we see that the actual measurements depart locally in many places from the ideal distribution based on $(X + 0.0275)^{-\frac{1}{2}}$. For model 1, we compare in figure (4.5.3) the temperature distribution calculated for the $(X + 0.0275)^{-\frac{1}{2}}$ distribution of heat transfer with the numerical solution obtained for the actual measured output of the reflector. Since the two temperature distributions are so close to one another, we can conclude that the local variations in the rates of heat input have little or no effect on the temperature distribution. The very slight difference between the two calculations that exists can be virtually eliminated by a slight decrease in the value of the constant X_o. This, perhaps, could have been used as a basis for selecting the value of the constant X_o.

Test results from the nine models are plotted in figures (4.5.4) to (4.5.12). The agreement between the experimental results and theory (using $X_o = 0.0275$) for models 1,2,3,4,5 and 7 is remarkably good. We have used the relation expressed in equation (4.2) to

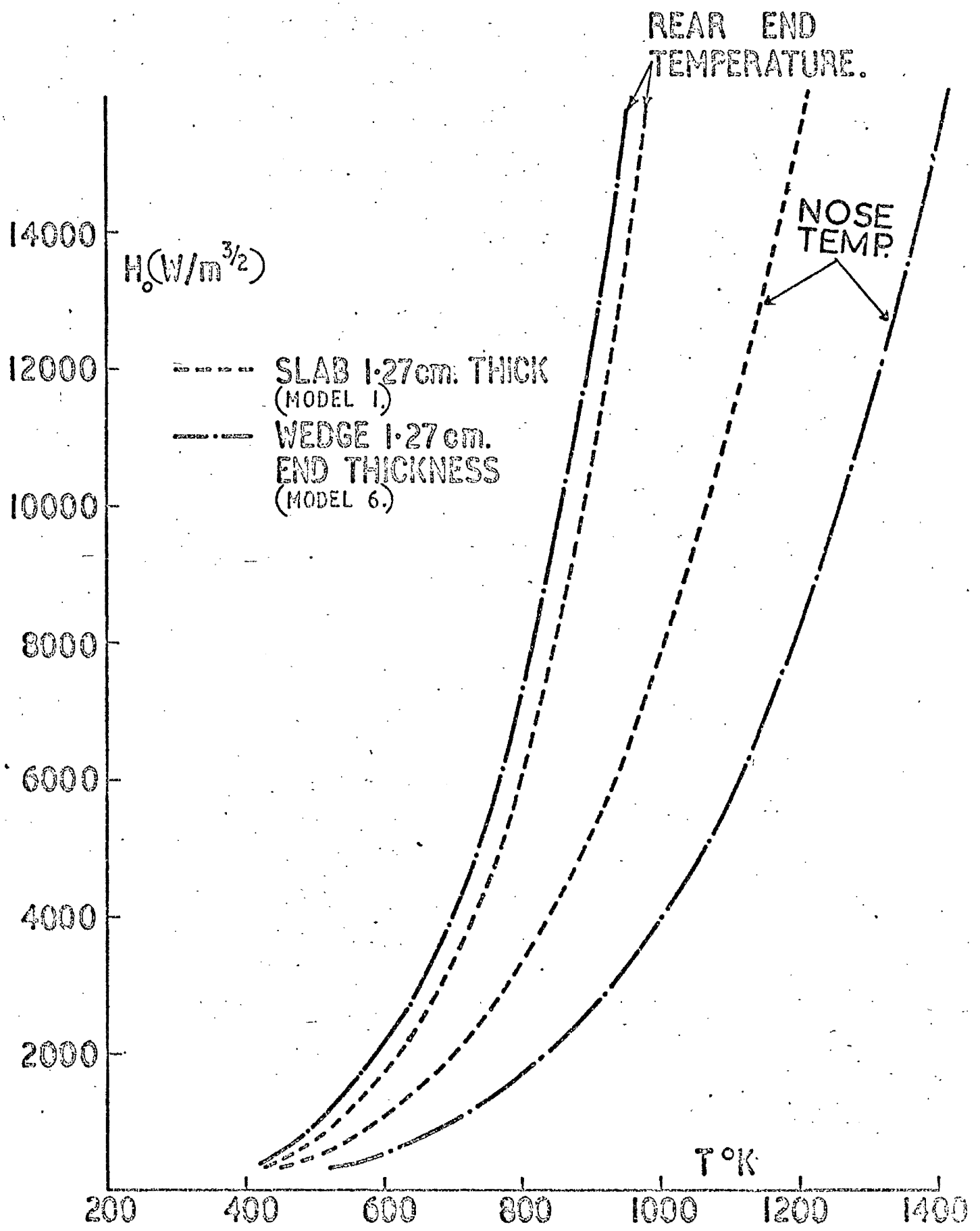

Figure 4.5.2 Effect of heat input on nose and rear end temperatures of slab and wedge models.

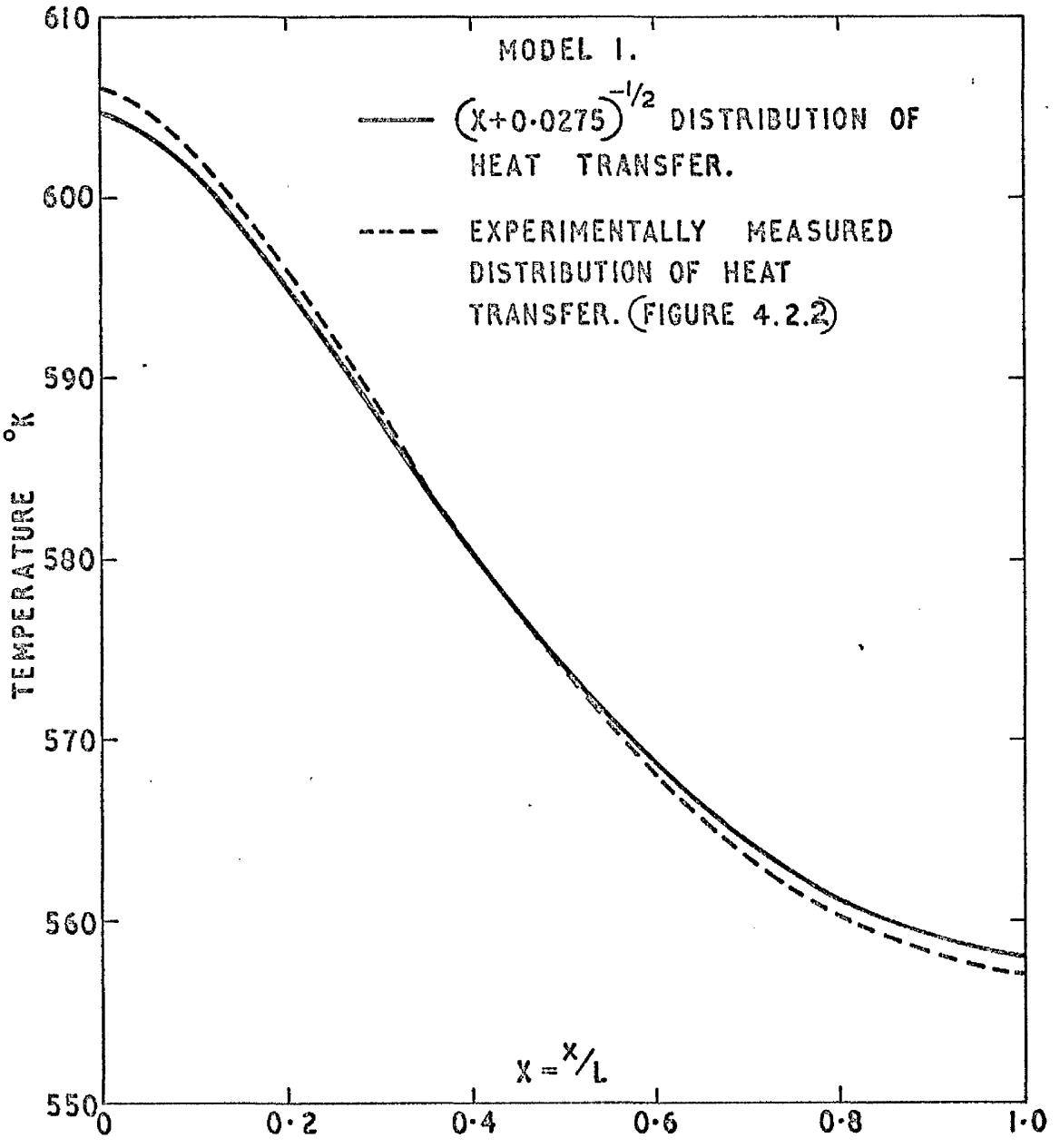

Figure 4.5.3 Calculated temperature distributions based on theortical and experimental rates of heat transfer.

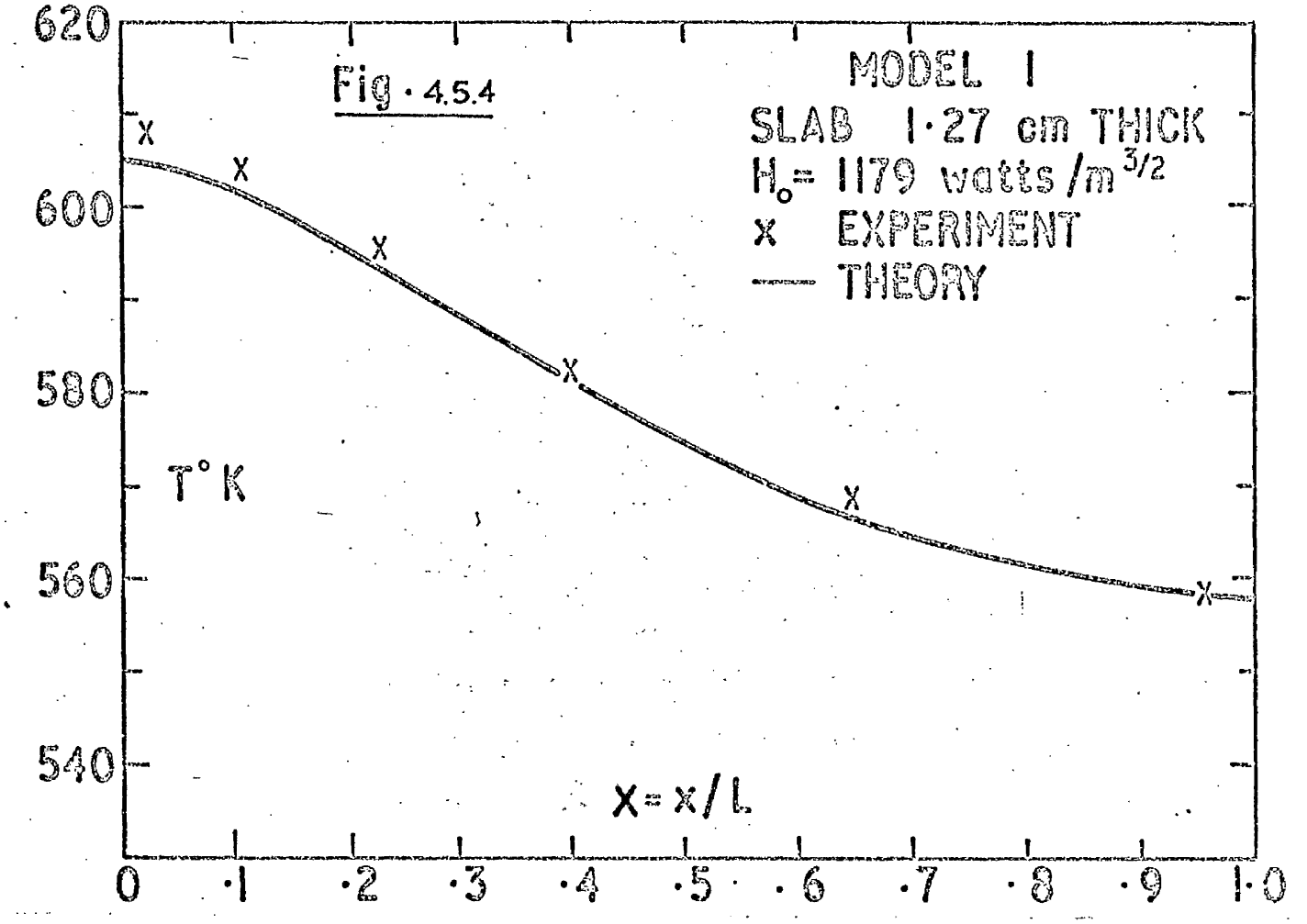
620
600
580
560
540
T°K
X = x/L
0
·1
·2
·3
·4
·5
·6
·7
·8
·9
1·0
MODEL 1
SLAB 1·27 cm THICK
H_o = 1179 watts /$m^{3/2}$
X EXPERIMENT
— THEORY

Fig · 4.5.4

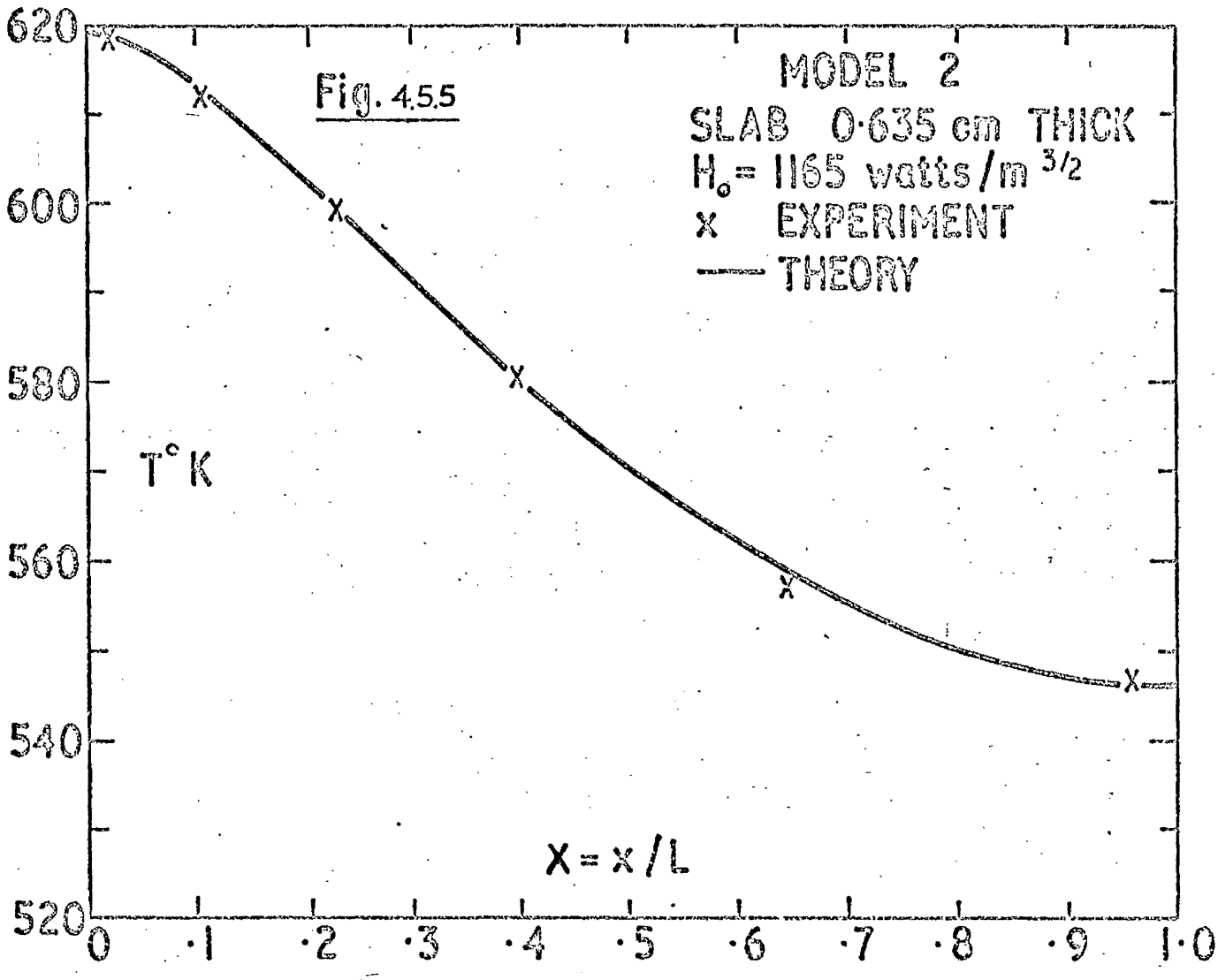
Fig. 4.5.5
MODEL 2
SLAB 0·635 cm THICK
H_o = 1165 watts/m $^{3/2}$
X EXPERIMENT
— THEORY
T° K
X = x/L
620
600
580
560
540
520
0
·1
·2
·3
·4
·5
·6
·7
·8
·9
1·0

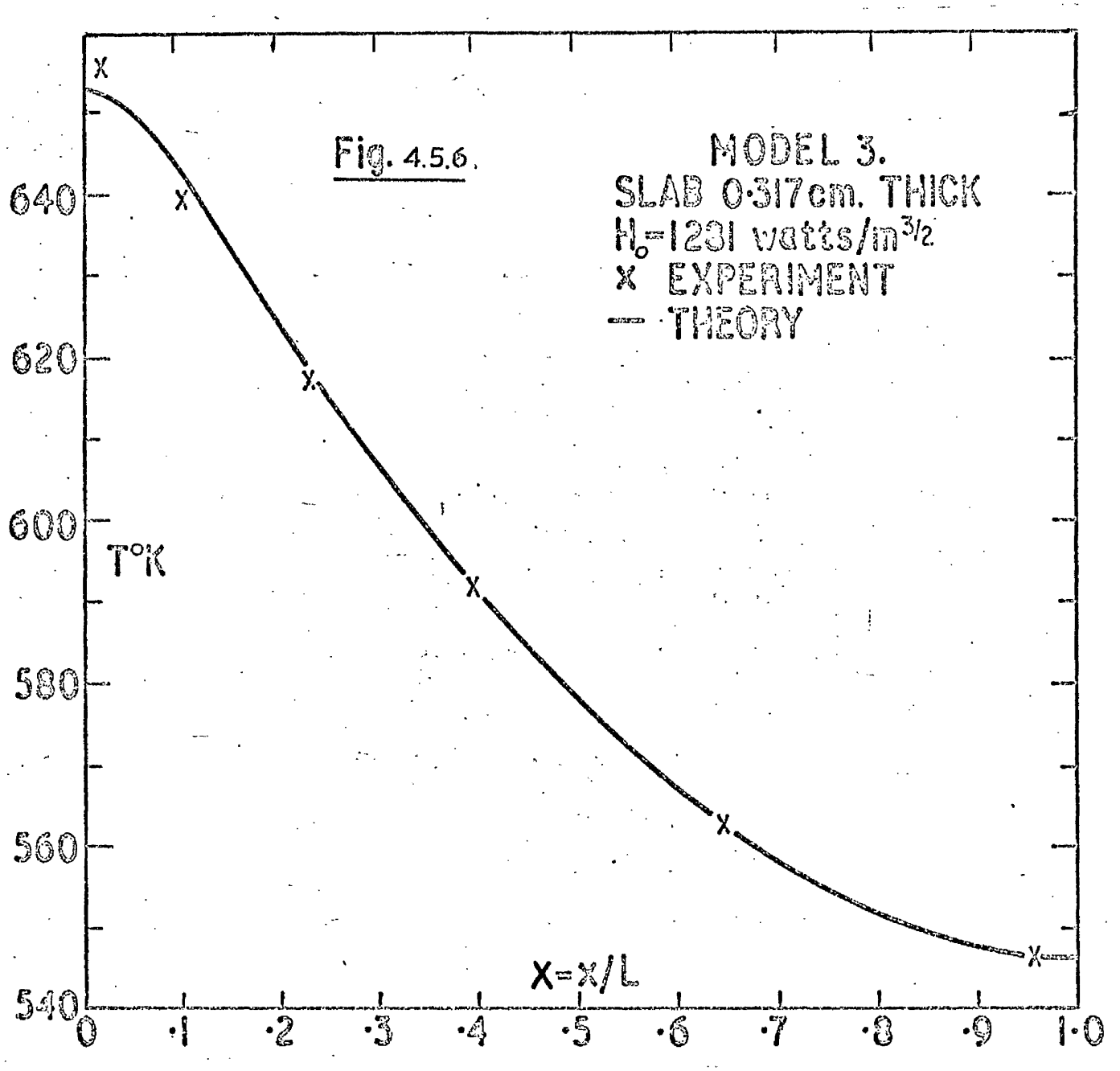
Fig. 4.5.6.
MODEL 3.
SLAB 0·317cm. THICK
H_o=1231 watts/$m^{3/2}$
X EXPERIMENT
— THEORY
640
620
600
580
560
540
T°K
X=x/L
0
·1
·2
·3
·4
·5
·6
·7
·8
·9
1·0

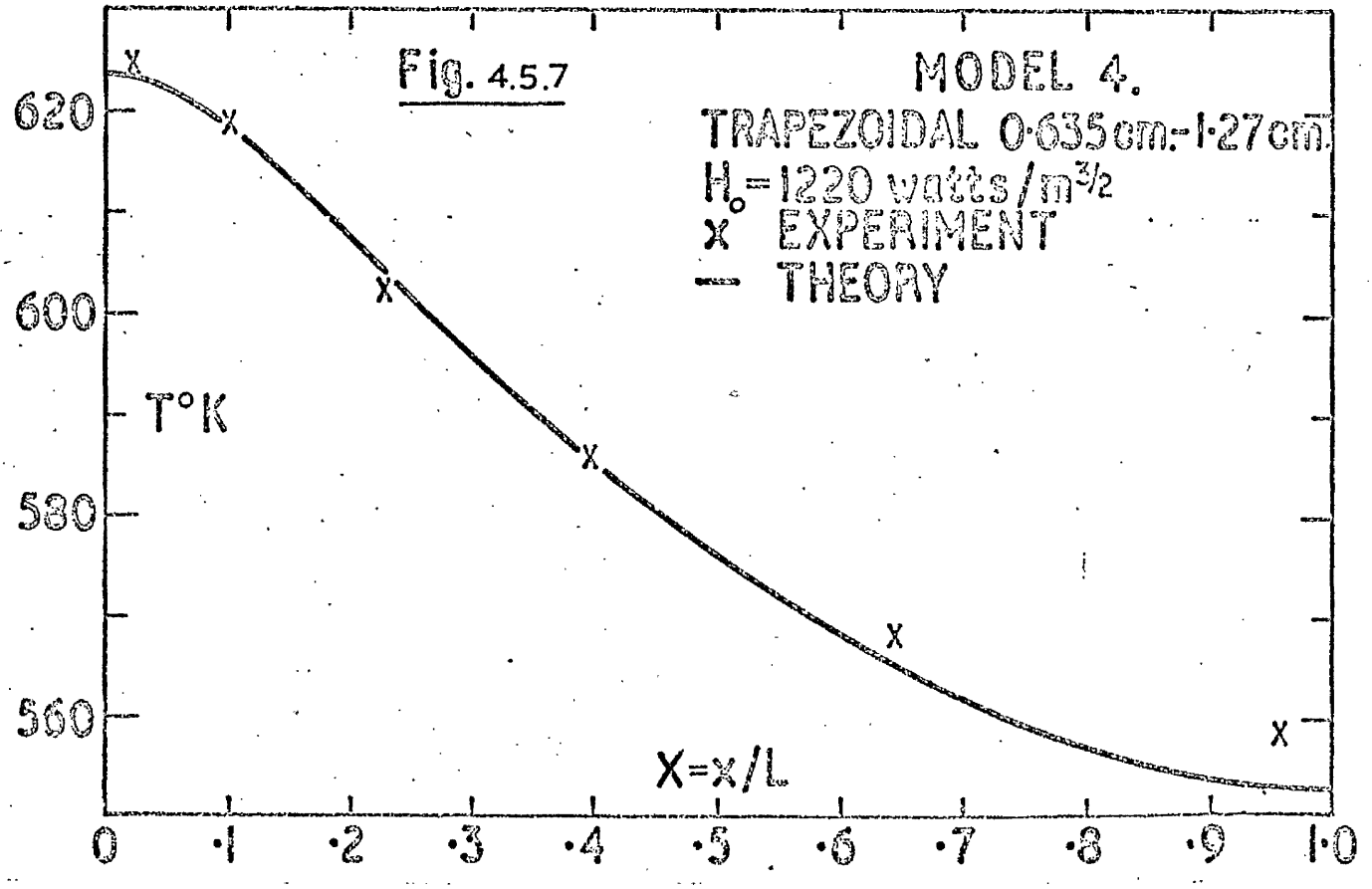
Fig. 4.5.7
MODEL 4.
TRAPEZOIDAL 0·635cm.-1·27cm.
H_o=1220 watts/$m^{3/2}$
X EXPERIMENT
— THEORY
620
600
580
560
T°K
X=x/L
0
·1
·2
·3
·4
·5
·6
·7
·8
·9
1·0

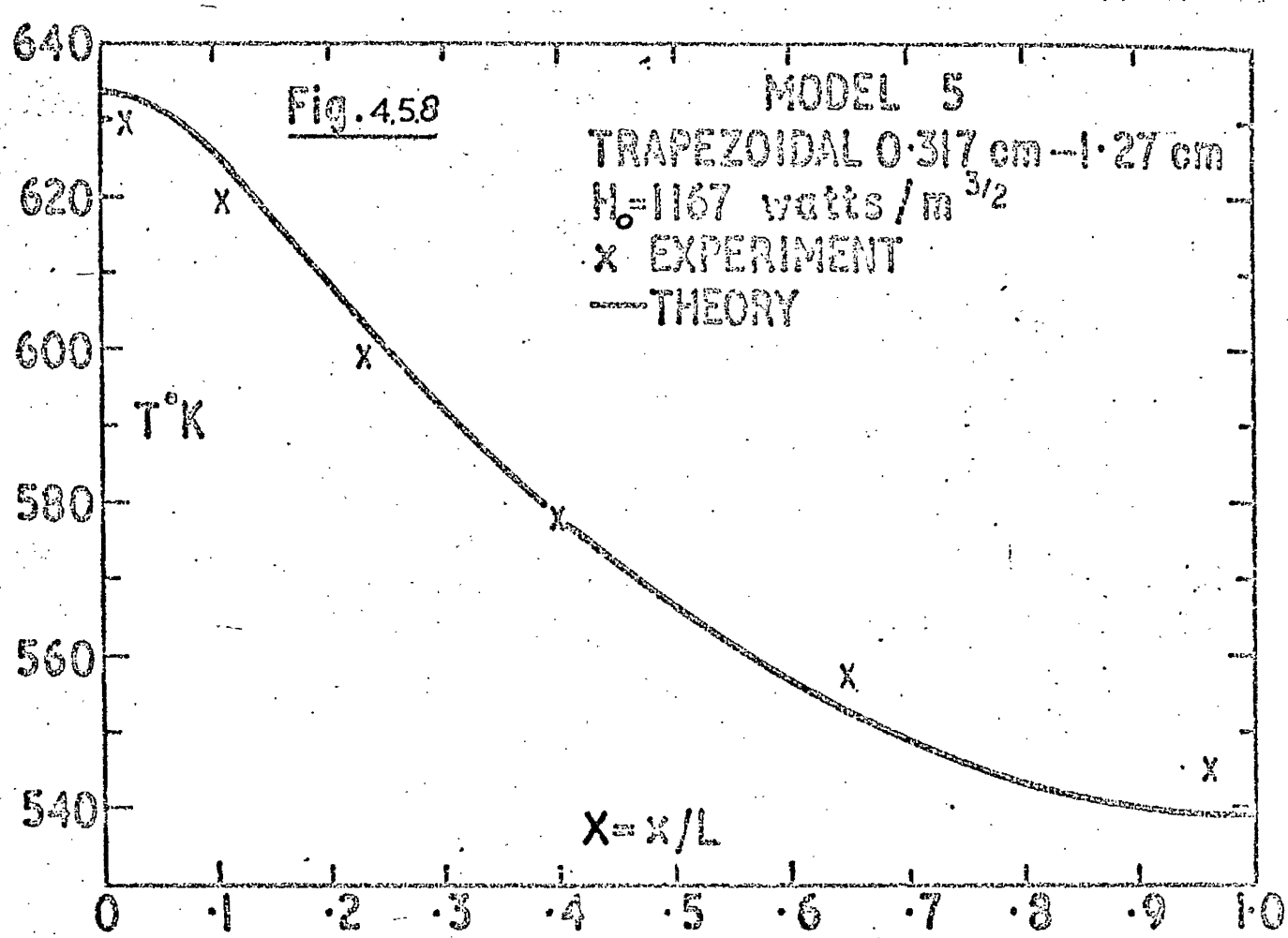
Fig. 4.5.8
MODEL 5
TRAPEZOIDAL 0·317 cm – 1·27 cm
H_o=1167 watts / m $^{3/2}$
X EXPERIMENT
—THEORY
T°K
X= x/L
640
620
600
580
560
540
0
·1
·2
·3
·4
·5
·6
·7
·8
·9
1·0

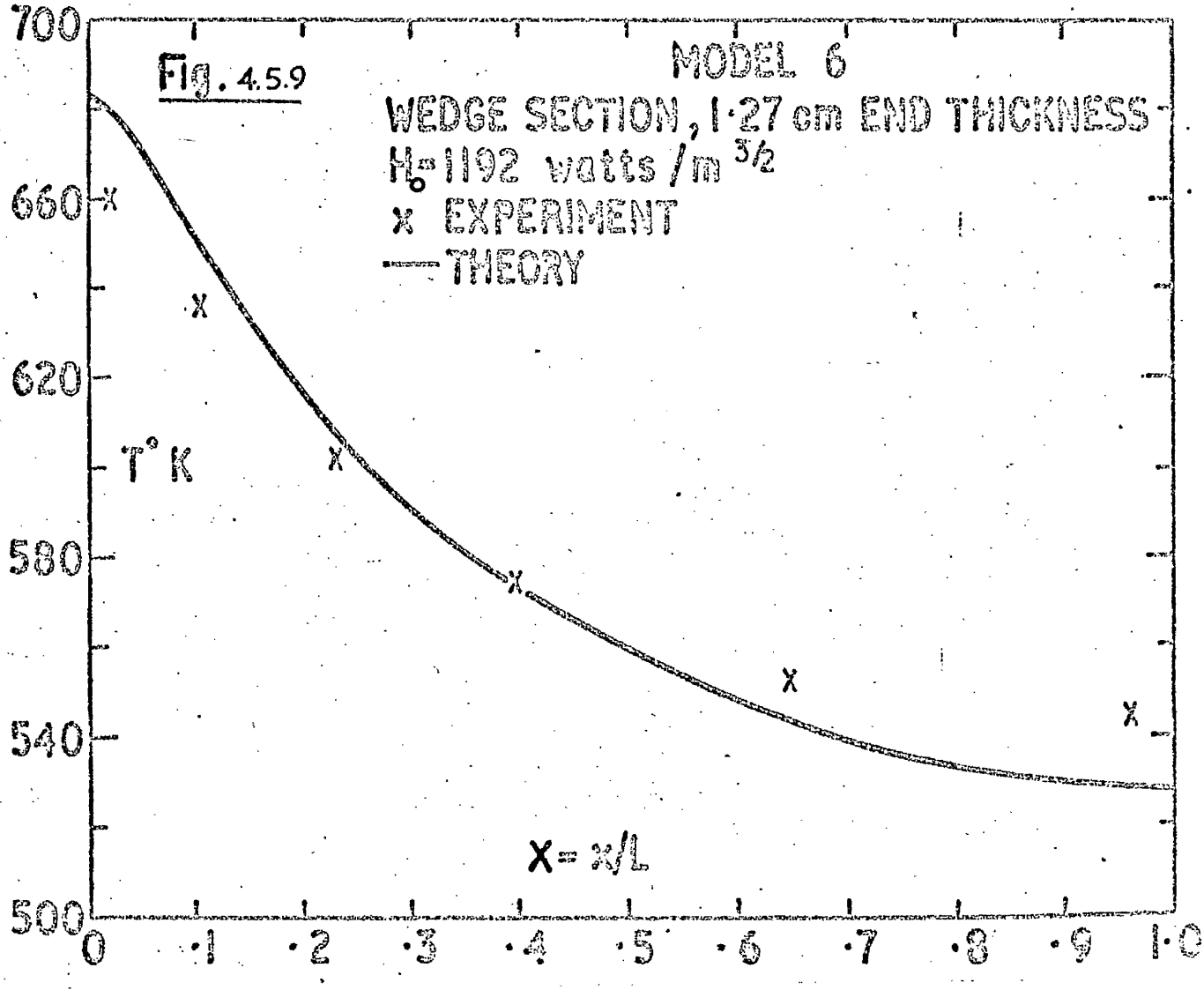
MODEL 6
WEDGE SECTION, 1·27 cm END THICKNESS
H_o = 1192 watts / m $^{3/2}$
x EXPERIMENT
— THEORY
T° K
X = x/L
700
660
620
580
540
500
0
·1
·2
·3
·4
·5
·6
·7
·8
·9
1·0

Fig. 4.5.9

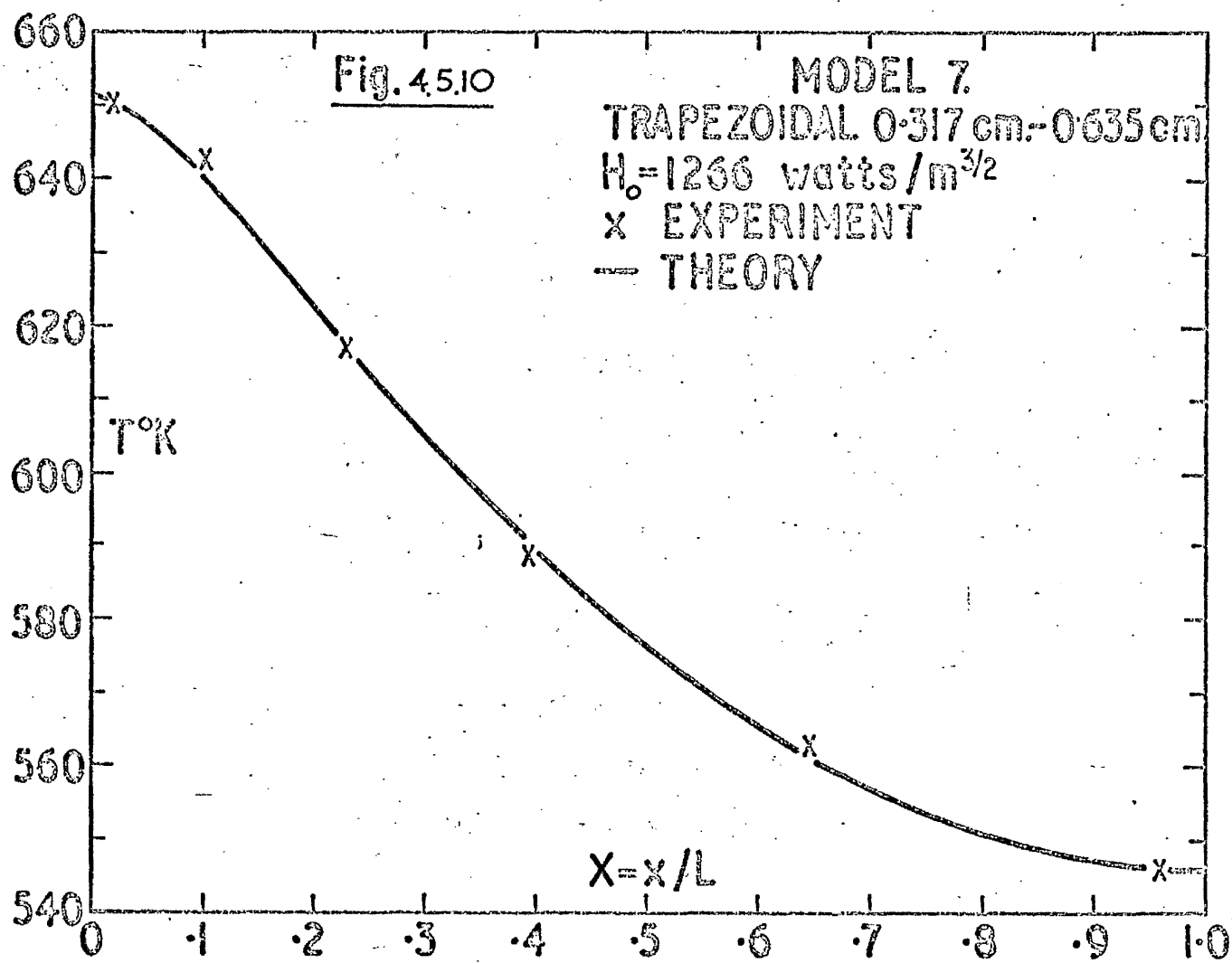
Fig. 4.5.10
MODEL 7.
TRAPEZOIDAL 0·317 cm.-0·635 cm
H_o=1266 watts/$m^{3/2}$
X EXPERIMENT
— THEORY
T°K
X=x/L
660
640
620
600
580
560
540
0
·1
·2
·3
·4
·5
·6
·7
·8
·9
1·0

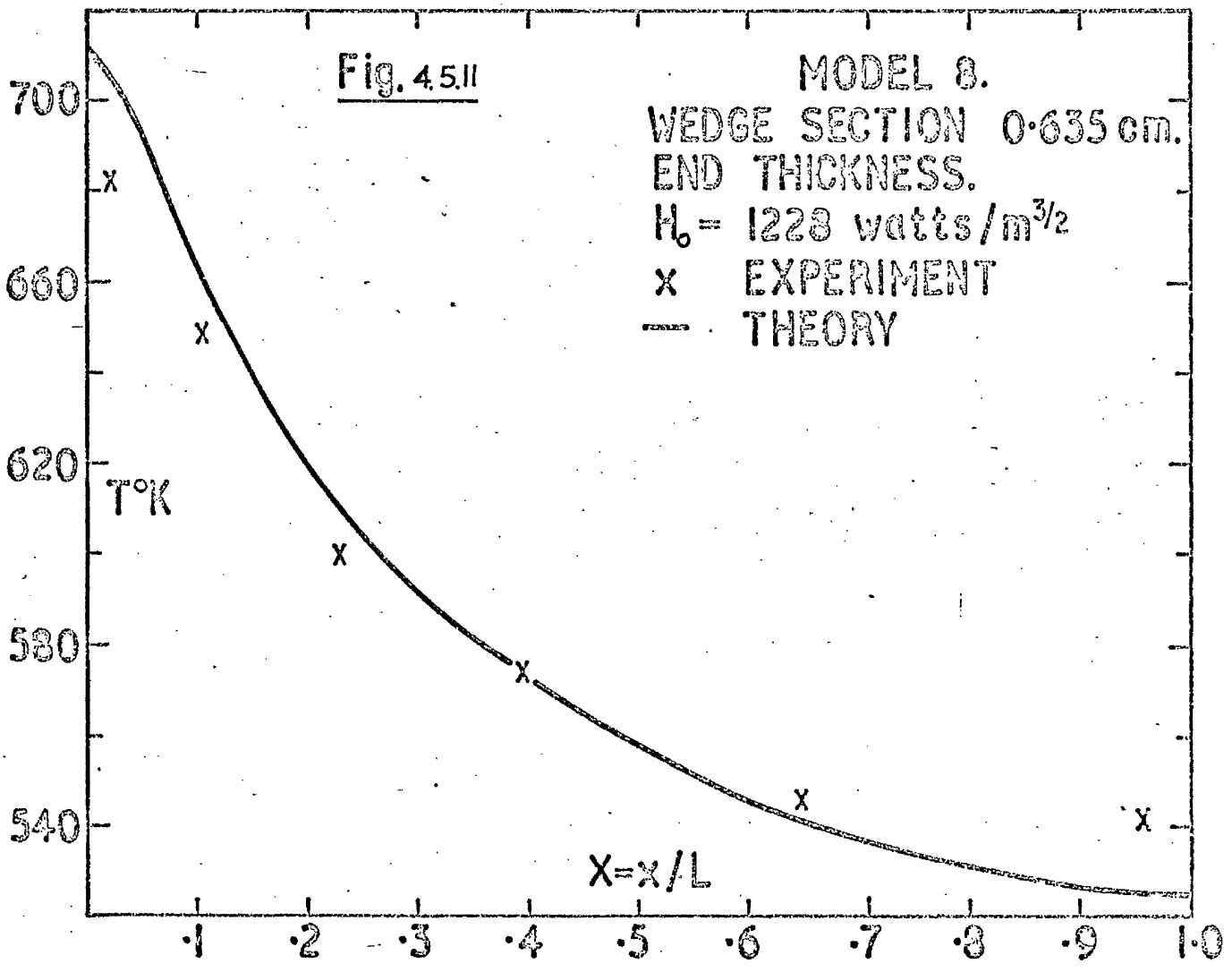
Fig. 4.5.11
MODEL 8.
WEDGE SECTION 0·635 cm.
END THICKNESS.
H_0 = 1228 watts/$m^{3/2}$
x EXPERIMENT
— THEORY
700
660
620
580
540
T°K
X=x/L
·1
·2
·3
·4
·5
·6
·7
·8
·9
1·0

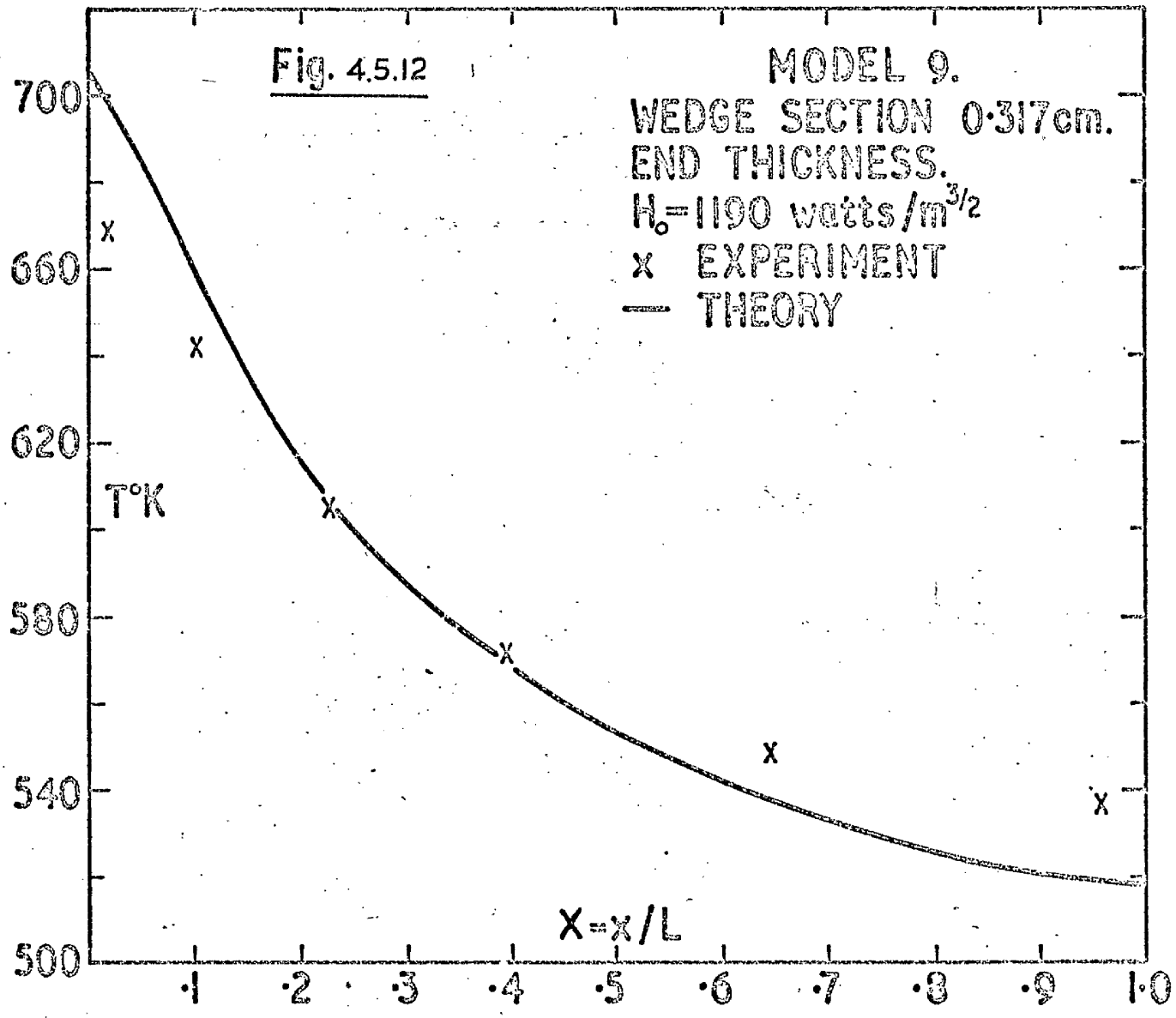
Fig. 4.5.12
MODEL 9.
WEDGE SECTION 0·317cm.
END THICKNESS.
H_o=1190 watts/$m^{3/2}$
x EXPERIMENT
— THEORY
700
660
620
580
540
500
T°K
X=x/L
·1
·2
·3
·4
·5
·6
·7
·8
·9
1·0

calculate the magnitude of the constant H_o (table 4.4.1). This method has been found to yield more reliable values than the radiometer readings, the method adopted by Sinha[10]. In addition to the sources of error already mentioned in section (4.4.1), there is the uncertainty regarding the absolute values of the coefficient of thermal conductivity (k) when seeking the numerical solutions. The values of k and ϵ used are those quoted for the appropriate cases in references 34 and 37 respectively. Even then for these six models the maximum deviation from the calculated results (from equation 3.15 with $X_o = 0.0275$) is only about 2%. For the three wedge models 6, 8 and 9 the agreement between theory and experiment is not quite so good. The calculated temperature gradients are higher than the experimental results and the maximum discrepency in the absolute values of temperature is about 5% for these three models. One of the reasons for this greater discrepency is that by normal workshop standard, it is difficult to machine and then polish an exact wedge shape. Because of the much smaller magnitudes of the nose dimensions involved, any small deviation from the ideal thickness is likely to have an exaggerated effect on the temperature distribution. In the case of trapezoidal and wedge sections the slight but inevitable rounding off of the leading edge could introduce error in the measurement of the nose thickness. Numerical solutions have revealed that to get the same agreement between the test results of the three wedge shaped models and theory as the other six models, we need to increase the product kt by a factor of around 2.0 at the nose of these three models.

In all the models, two rows of thermocouples were embedded at two

different depths to detect any temperature gradients across the thickness of the material. Consistent with the basic assumption, no significant temperature variations across the thickness were measured.

4.6. Fabricated leading edge.

From the results and the discussions already presented in this chapter it is evident that when the reflector is used to simulate the aerodynamic heating in a model the measured temperature distributions correspond to the numerical solutions of equation (3.15) with $X_o = 0.0275$. We now intend to use the reflector to provide analogue temperature distributions where the numerical solutions cannot be conveniently obtained.

A practical wing section is likely to be a complex structure internally. We now make an experimental study of a "practical" leading edge which has internal cavities and a channel section spar parallel to the leading edge. Two "identical" models have been made and tested. The cross-section of the model is shown in figure (4.6.1) and is made out of stainless steel designated Staybrite F D P or AISI 321. Both the skin as well as the spar piece is made out of 18 SWG (0.122cm.) sheet. The spar flange is spot-welded to the skin at a pitch of 1.9cm. The overall size of the model is 0.305m by 0.152m as before (section 4.3). At the leading edge, the top and bottom surface subtend a total angle of 19°. The leading edge of the wing is considered to be symmetrical and therefore we need only consider one half of the section. In order to simulate the effects of an internal cavity, we place a highly polished reflector along the plane of symmetry. The model is isolated from the surroundings by resting

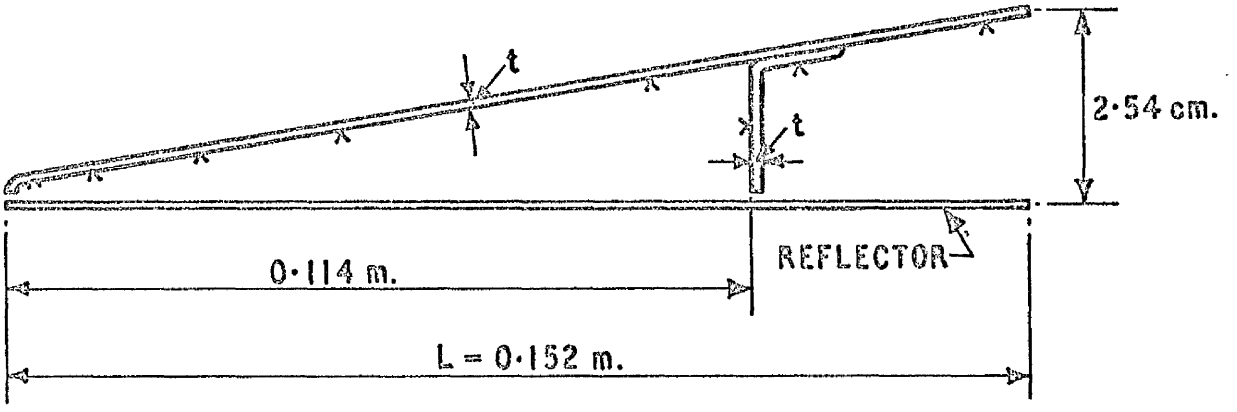

Figure 4.6.1 The fabricated leading edge model.

it on four pointed ceramic pins. The top surface of the model is in the irradiated plane that has a one-dimensional variation of heat flux as shown in figure (4.2.1).

After shot-blasting the top surface with size 80 grit the model was oxidized in air at 900°C for 60 minutes. Subsequently apart from the top surface, the oxide layer was removed from all the other faces (including the web surfaces) by rubbing them with emery paper. The reason for oxidizing the top surface is to increase its absorptivity so that the model absorbs as much as possible of the limited amount of available heating.

The model is given a rounded nose (figure 4.6.1) to represent the nose of a practical leading edge normally constructed by the bending of a sheet. By including this locally rounded shape of the leading edge, we have retained the full thickness of the conducting material at the nose of the model.

Temperature measurements were taken by thermocouples spot-welded in two rows at the centre-section of the model. The experimental set-up and the testing procedure is exactly as explained earlier in section (3.6.3). For the fabricated leading edge the results from the models are presented in table (4.6.1).

In order to discover how the measured temperature distribution compares with the solutions of the two-dimensional heat conduction equation (3.15), we use the following values of the parameters relevant to the model; L = 15.2cms, t = 0.122cms and X_o = 0.0275. The coefficient of thermal conductivity as supplied by the manufacturers (reference 34) is taken as $k = 15.9\ (1 + 0.00039 \times T^{\circ}C)\ W/m^{\circ}K$. For

Table 4.6.1. Experimental results of the fabricated leading edge

	Model 10	Model 11
Total power from heater (W)	1837	1823
Power received by model (W)	202.0	204.0
H_o $(W/_m 3/_2)$	1050	1060
X = x/L	Temperature ^{o} K	Temperature ^{o}K
0.0208	664.1	658.6
	658.7	657.7
0.104	641.6	637.9
	645.4	644.0
0.271	597.0	-
	596.4	-
0.397	560.7	564.4
	559.0	564.2
0.647	520.2	524.9
	523.2	526.9
0.96	507.1	512.7
	501.8	512.7
spar	498.0	503.5
vertical web face	498.0	496.7
spar	501.6	508.5
horizontal flange face	505.6	505.6

t = 0.122 cms.

Material - Stainless Steel AISI 321

the variation of the coefficient of emissivity with temperature, adequate information is not available for this particular type of stainless steel. We have therefore had to develop equipment (reference 35) to investigate the variations of the total hemispherical emissivity of Stainless Steel AISI 321 for several types of surface finish and treatment. From the results presented in reference (36) we represent the variation of the coefficient of emissivity with temperature as $\epsilon = 0.695\ (1 + 0.000288 \times T^{\circ}C)$ for a shot-blasted surface which has been oxidised in air at $900^{\circ}C$ for 60 minutes.

4.7 Discussion of experimental results and comparison with theory.

For the nine models that we discussed earlier on in this chapter, the problem of internal heat exchange by radiation did not occur. In the case of the fabricated leading edge that we have tested, the internal cavities on both sides of the spar web complicate numerical analyses. In addition to heat conduction within the conducting material, we have thermal radiation within the cavities. The effect of heat transfer by radiation would be to moderate the temperature gradients and can thus be seen to "conduct" heat away from the hotter regions of the model to points further downstream. However, because of the vertical web and some heat loss from the rear portion of the model (lower surface), the complications introduced by the cavities cannot be accounted for by a straightforward increase in the effective thermal conductivity of the material. Thermal radiation exchange within the cavity and thermal radiation loss from the vertical web and the lower surface of the rear portion of the skin with the environment can be formulated. The solution for the temperature

distribution taking acoount of these conditions would require the solution of a set of integro-differential equations which would present some mathematical difficulties.

The experimental results for the two models (10 and 11) are plotted in figure (4.7.1). For calculating the temperature distribution we require the value of the appropriate heat input parameter H_o. Integrating the heat loss by radiation from the top surface only gives $H_o = 1000\ W/m^{3/2}$. Using this value leads to an estimate of the nose temperature lower than the measured value by about 3%. However, we know that heat is lost by thermal radiation from the vertical web face and the lower surface of the rear portion of the skin to the water cooled walls of the vacuum chamber. It would be possible to make a rough estimate of this heat loss using the temperature distribution of the skin and the emissivity of the stainless steel in the as received condition (to represent the lower surface of the model) but this is further complicated by the presence of the reflector inclined at 10^o to the model.

However, we have one method of providing a rough approximation to the heat incident on the model. Included in table (4.4.1) are values of the total power dissipated in the filament of the multi-curve reflector for the nine models tested in the verification of the theory together with the quantity of heat actually impinging the models. There exists some indication of the value of H_o as a percentage of the total power dissipated in the filament. The experimental results presented in figure (4.7.1) are for power dissipations of 1838 and 1823 watts. Using a mean correlating factor, we obtain at a value of

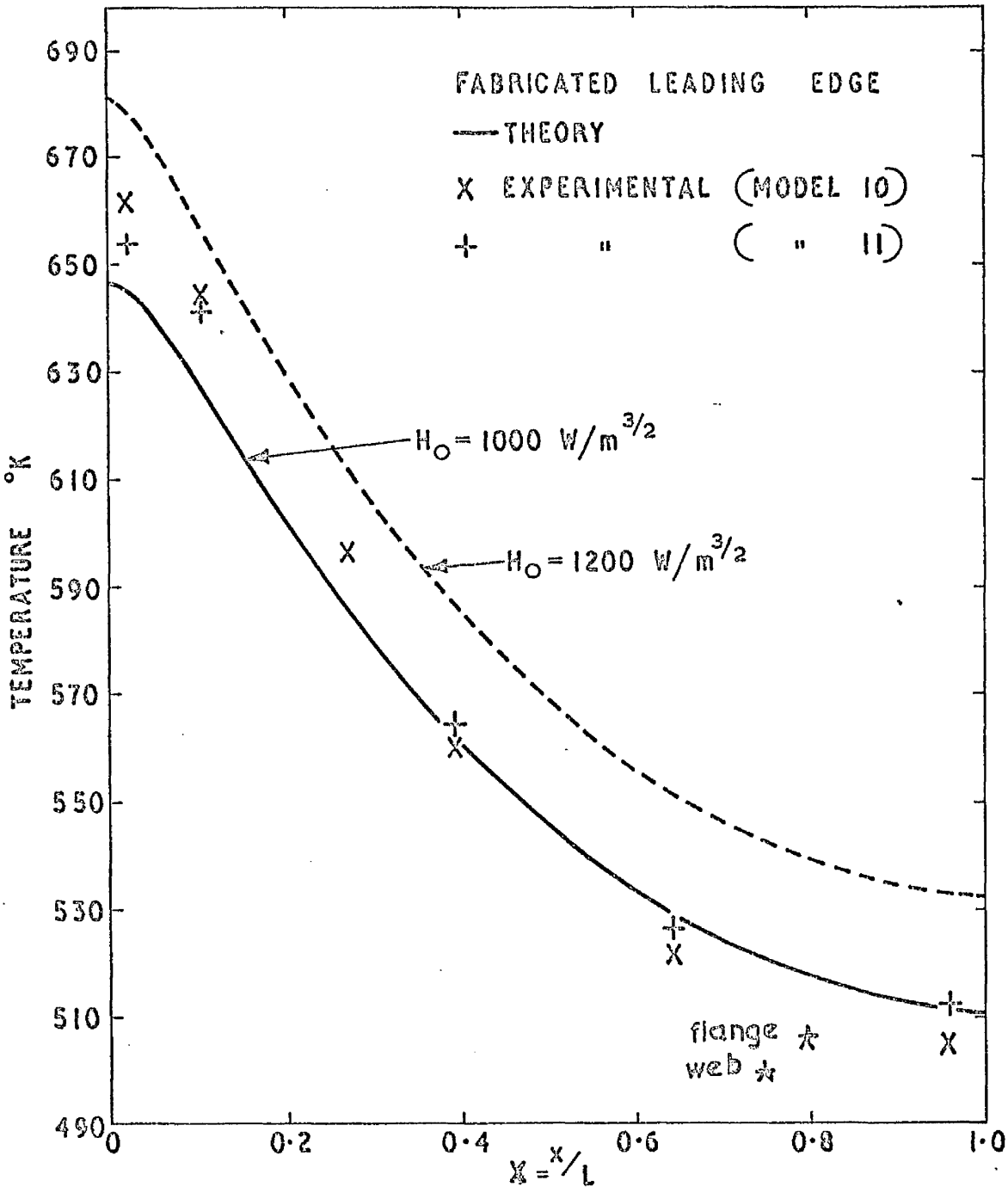

Figure 4.7.1 Experimental results for the fabricated leading edge.

H_o = 1200 W/m$^{3/2}$. Calculated results for H_o = 1200 W/m$^{3/2}$ are also plotted in figure (4.7.1).

The effect of the cavity is expected to moderate the temperature distribution as compared with the slab of the same thickness. However, the measured temperature distribution exhibits the opposite trend. We already know that the temperature distribution is fairly sensitive to the nose thickness of the conducting material. In the calculations we have used a slab of thickness 0.122cm. to predict the temperature distribution. However if the nose does not have a sufficiently small nose radius to make the skin normal to the plane of symmetry at the nose, then the effective nose thickness is going to be less than the slab value. This seems to be the case and consequently the temperature distribution is not quite so severe as it should be. Under practically the same heat input (table 4.6.1) model 12 exhibits a slightly less severe temperature distribution as compared with model 11, which suggests that the effective nose thickness of model 12 is greater than that of model 11. It is extremely difficult to measure the variation of the material thickness close to the rounded leading edge and therefore the calculated temperature distributions are presented only for the equivalent constant thickness model.

Since the calculated temperature distributions have not taken into account the effect of radiation exchange from one part to another or that heat is lost from the rear portion of the model, a comparison of theory and experimental results shows us how under the same heat input, the two temperature distributions are likely to vary. A set of controlled experiments could provide an insight into the heat transfer

phenomena taking place inside cavities where radiation equilibrium exists.

For given leading edge configurations the experimental set-up we have developed is capable of providing us with the analogue distributions of temperature. This is particularly useful when numerical solutions cannot be easily obtained which is generally the case in realistic wing sections.

Finally, in figure (4.7.1) we have also plotted the temperatures recorded on the spar. The addition of the vertical web does not seem to have produced any discontinuity or a marked change of slope in the measured temperature distribution.

CHAPTER V

Three-dimensional heat conduction in leading edge heating

5.1 Introduction

One of the aims of the present study is to extend the two-dimensional investigations to more realistic wing planforms suitable for hypersonic flight, by including the effect of sweep and apex geometry. As before we envisage the use of thin wing sections with the leading edge thicknesses of the order of 1cm. or less as compared with a chord of several meters, and opposed to the blunt body configuration where the leading edges may well exceed 1m. in thickness.

Relatively little information is available on the hypersonic flow over three-dimensional slender wings with sharp leading edges. It is therefore in general extremely difficult to formulate the coefficient of aerodynamic heat transfer to a hypersonic leading edge. In this chapter wherever necessary, we utilise the flow pattern of a "caret" wing which was first suggested by Nonweiler.[4,5] At its design cruise speed, this wing supports an attached plane shock between the leading edges along the lower surface and the flow is relatively simple being parallel to the centre-section of the wing everywhere. This gives us an opportunity to extend the two-dimentional investigations to include the effects of finite span and sweep-back.

In this chapter we present the theory and solutions of the three-dimensional heat conduction equation. Details are given of a computer programme we have developed which is capable of producing temperature distributions over the leading edge section of a swept wing subjected

to any general form of aerodynamic heating.

5.2. Heat transfer to the three-dimensional leading edge.

Nonweiler[4,5] first suggested the use of "caret" wings in hypersonic flight. These wings have a delta planform and support a plane shock wave along the leading edge and are one example of the family of "wave-rider" wings. The prominent feature of the caret wing is that at the design mach number the streamlines stay parallel to the plane of symmetry over the entire wing surface and the flow is uniform. We therefore assume that the heat input is a function of the streamwise distance from the leading edge.

The restriction put on the variation of heat transfer does not reduce the generality of the results as it may appear to do. At hypersonic mach numbers the influence of a disturbance in the flow is limited in the spanwise direction to regions within a narrow mach cone. We are concerned with the heating to a narrow strip of the order of the conduction length (l) parallel to the leading edge, and particularly that part of the strip close to the apex of the wing. Provided elsewhere unit order changes do not occur in the rates of heat transfer over lengths of the order of l in the spanwise direction, our results may be applied on a quasi-two-dimensional basis (as in para. 5.7) allowing reasonable estimates to be made of the leading edge temperatures of any swept wing, even if the streamlines are no longer strictly parallel to the plane of symmetry of the wing.

Although the hypersonic flow over the caret is well defined, the

solution of the heat conduction equation still presents some problems. A caret wing which supports a plane shock wave would be of the shape shown in figure (5.2.1)

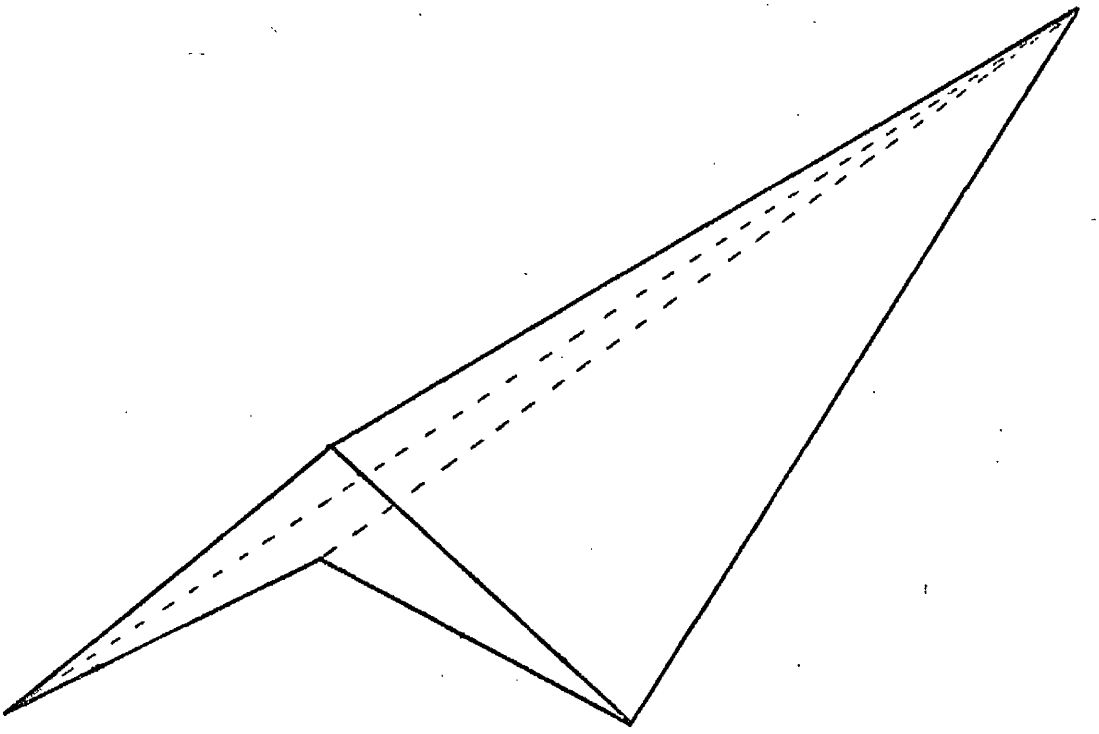

Figure 5.2.1 A Caret wing.

Since the two wing surfaces of a caret are inclined to one another, heat exchange by radiation would occur between these two surfaces. The formulation as well as the solution of the governing heat transfer equations would be extremely difficult. For two inclined surfaces it can be easily shown that the radiation exchange decreases

very rapidly as the included angle between the two surfaces increases. In practical caret wings this angle is likely to be well over 90°. We therefore expect the heat transfer from one surface to the other, by thermal radiation to be small and this effect is ignored in the formulation of heat transfer equation for the three-dimensional wing where we replace a carat wing by an equivalent plane delta wing as shown in figure (5.2.2.).

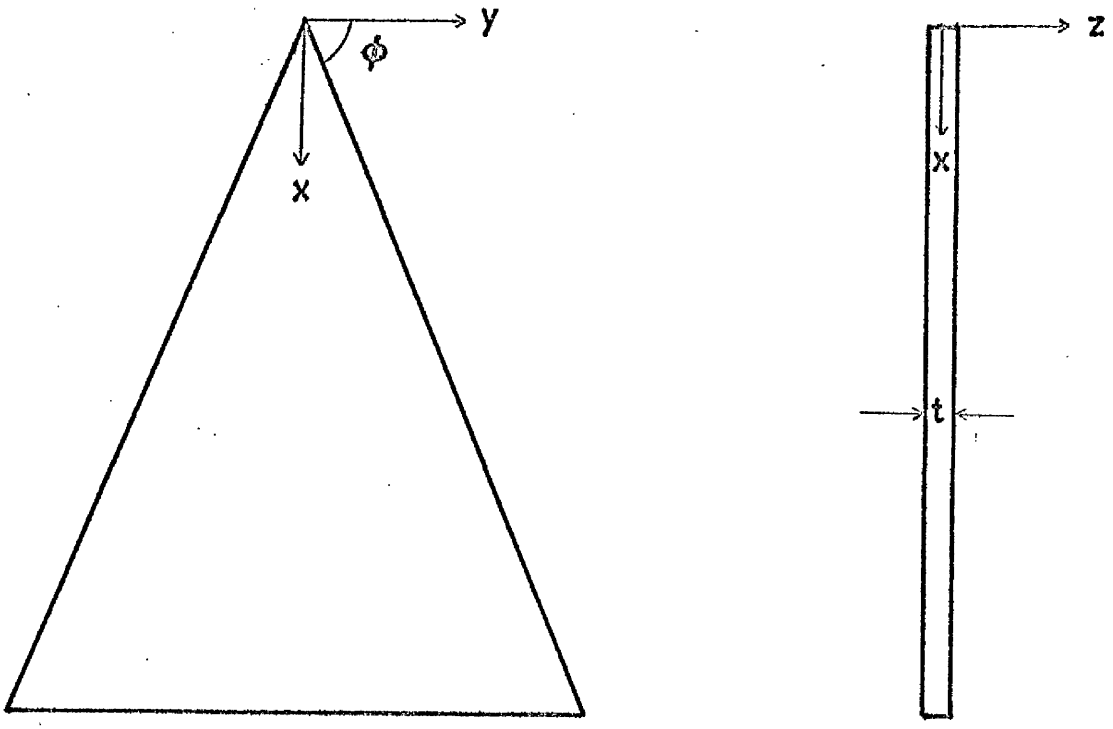

Figure 5.2.2 Idealised hypersonic delta wing.

Consistent with the preceding chapters the coefficient of aerodynamic heat transfer is taken to vary as inversely proportional to the square root of the chordwise distance measured from the leading edge. The assumptions already made in the last chapter in the theory

of conducting plates remain unchanged and will not be repeated here.

We can now write the heat transfer equation for the three-dimensional wings under consideration as,

$$\frac{\partial}{\partial x}\left(kt\frac{\partial T}{\partial x}\right) + \frac{\partial}{\partial y}\left(kt\frac{\partial T}{\partial y}\right) = \epsilon\sigma T^4 - \frac{H_o}{(x+x_o-y\tan\phi)^{\frac{1}{2}}} \qquad (5.1)$$

where x_o is a constant to eliminate the singularity along the leading edge, $x = y \tan\phi$.

Once again we seek the solution of equation (5.1) over a closed interval of x of length L (measured from the leading edge) and we define non-dimensional notation as before:

$$X = \frac{x}{L}, \quad Y = \frac{y}{L}, \quad \Theta = \frac{T}{T_L}, \quad e = \frac{\epsilon}{\epsilon_L}; \quad K = \frac{kt}{k_L t_L} \qquad (5.2)$$

Here the subscript L refers to the values of parameters at a distance L from the apex of the delta. Also we have

$$T_L = \left[\frac{Q_L}{\epsilon_L \sigma}\right]^{\frac{1}{4}} \qquad (5.3)$$

and

$$\tau = \frac{kt}{(\epsilon_L \sigma Q_L^3)^{\frac{1}{4}} . L^2} \qquad \text{or} \quad \tau_o = \left(\frac{\ell}{L}\right)^2 K \qquad (5.4)$$

where the conduction length ℓ is defined as

$$\ell = \left(\frac{kt\, T_L}{Q_L}\right)^{\frac{1}{2}} \qquad (5.5)$$

On substituting equation (5.2) - (5.4) into equation (5.1) we get the non-dimensional form of the heat transfer equation as

$$\frac{\partial}{\partial X}\left(\tau\frac{\partial\theta}{\partial X}\right) + \frac{\partial}{\partial Y}\left(\tau\frac{\partial\theta}{\partial Y}\right) = e\theta^4 - \frac{1}{(X+X_o-Y\tan\phi)^{\frac{1}{2}}} \qquad (5.6)$$

For the aerodynamic heat transfer varying as $(x + x_o)^{-\frac{1}{2}}$ where x is measured from the leading edge, we have defined, as before a conduction length, ℓ (equation 5.5) and precisely the same reasoning as before suggests that over this length thermal conduction plays an important role in the determination of the temperature distribution. We need only solve equation (5.6) for lengths L of the order of ℓ in order to discern the effects of thermal conduction on the temperature distribution. If L is much larger than ℓ, the temperature would in general be very close to the radiation equilibrium value and much lower than the apex or the leading edge temperature. On the other hand when L is much smaller than 1, the temperature would in general be more or less uniform and close to the "infinite" conductivity value. A delta wing has a plane of symmetry ($y = 0$) and therefore we need only solve the equation over one half ($y \geqslant 0$, say) and the area of interest to us is shown shaded in figure (5.2.3)

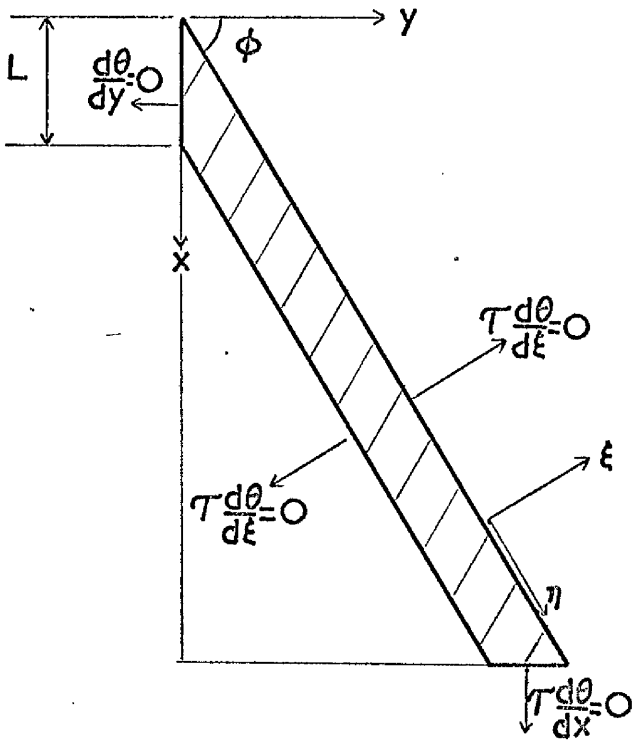

Figure 5.2.3 Leading edge portion of the delta wing with Boundary conditions.

5.3 Boundary conditions

We assume that there is no heat transfer normal to the edges of the strip parallel to the leading edge. Across the plane of symmetry it is evident that $\frac{d\theta}{dx} = 0$. Aong the two free edges the conducting material vanishes and the boundary conditions used are

$$\tau \frac{d\theta}{d\xi} = 0 \qquad (5.7)$$

where ξ is measured normal to the leading edge (see figure 5.2.3) which is simply an extension of the argument presented earlier for the two-dimensional plate. Similarly we consider the edge $X=L-Y\tan\phi$ to be the chordwise limit of the conducting region. Further downstream the conduction effects are negligible and the temperature distribution follows very closely the radiation equilibrium condition. The heat transfer normal to the edge can thus be ignored without affecting the solution.

5.4 Solution of the three-dimensional heat transfer equation.

We solve equation (5.6) with two objectives in mind. First we try to find where and how the two-dimensional solutions and similarity laws can be applied to the more general case of swept leading edges. Secondly we investigate the effects of the extra parameters that occur in equation (5.6), namely finite-span and sweep-back, on the temperature distribution.

The numerical solution of equation (5.6) has been obtained by employing the method of over-relaxation which is the easiest of the three methods described in section (3.5) to be generalised to include

the extra dimension (Y). Equation (5.6) is first linearised and then expressed in the finite-difference form using the central difference notation.

The leading edge area is divided into a rectangular grid of length h_c (chordwise direction) and width h_s (spanwise dimension). In order that all the edges are always coincident with a grid point, we choose h_c and h_s such that

$$h_c = h_s \tan\phi$$

Full details of the derivation of equation (5.6) in the finite differences form is given in Appendix C and the set of (N+1)x(M+1) equations can be represented by

$$\theta^i_{n,m} = (1-\omega)\theta^{i-1}_{n,m} + \omega\Bigg\{ \frac{1}{(n+X_o-m\tan\phi)^{\frac{1}{2}}} + 3e_n(\theta^{i-1}_{n,m})^4 + \theta^{i-1}_{n+1,m}\left[\frac{1}{h_c^2}.\tau_{n+\frac{1}{2},m}\right]$$

$$+ \theta^{i}_{n-1,m}\left[\frac{1}{h_c^2}.\tau_{n-\frac{1}{2},m}\right] + \theta^{i-1}_{n,m+1}\left[\frac{1}{h_s^2}.\tau_{n,m+\frac{1}{2}}\right] + \theta^{i}_{n,m-1}\left[\frac{1}{h_s^2}.\tau_{n,m-\frac{1}{2}}\right]\Bigg\} \Bigg/$$

$$\left(\frac{1}{h_c^2}\left[\tau_{n+\frac{1}{2},m} + \tau_{n-\frac{1}{2},m}\right] + \frac{1}{h_s^2}\left[\tau_{n,m+\frac{1}{2}} + \tau_{n,m-\frac{1}{2}}\right]\right.$$

$$\left. + 4e_n(\theta^{i-1}_{n,m})^3 \right\} \qquad (5.8)$$

with n = O(1)N and m = O(1)M.

The boundary conditions along the four edges (see figure 5.2.3) become

as follows:

Along the edge parallel to the x - axis,

$$\theta_{(n,m+1)} = \theta_{(n,m-1)} \qquad (5.9)$$

Along the edge parallel to the y-axis,

$$\theta_{(n+1,m)} = \theta_{(n-1,m)} \qquad (5.10)$$

and along the edges inclined at the sweep angle ϕ to the y-axis,

$$h_c^2 \left[\theta_{(n,m+1)} - \theta_{(n,m-1)} \right] = h_s^2 \left[\theta_{(n+1,m)} - \theta_{(n-1,m)} \right] \qquad (5.11)$$

For $\phi < 45^\circ$, $h_c < h_s$ and we use equation (5.11) in the form

$$\theta_{(n+1,m)} - \theta_{(n-1,m)} = \frac{h_c^2}{h_s^2} \left[\theta_{(n,m+1)} - \theta_{(n,m-1)} \right] \qquad (5.12)$$

On the other hand this equation leads to instability in the solution of the equations (5.8) for $\phi > 45^\circ$ when $h_c > h_s$, and we utilise the alternative form of equation (5.11) which is

$$\theta_{(n,m+1)} - \theta_{(n,m-1)} = \frac{h_s^2}{h_c^2} \left[\theta_{(n+1,m)} - \theta_{(n-1,m)} \right] \qquad (5.13)$$

The main impact of attempting the numerical solution of equations given by (5.8) is the very large storage required to store all the unknowns. Instead of handling (N+1)x3 terms, we now have (N+1)x(M+1). Even for a moderate sized grid (N=64, say) the core-store necessary to store all the array terms is beyond the maximum available on our English Electric KDF 9 digital computer. In order to cope with this storage problem we use two additional magnetic tapes to supplement the basic core-store of the computer.

Essentially the iterative procedure of the computer programme is

the same as described for the solution of the two-dimensional equation (section 3.5.2). It consists of an inner iterative loop that obtains a solution of the linearised equation and an outer loop which approximates the solution of the linearised equations to the solution of the non-linear heat conduction equation (equation 5.8). The program starts with a quessed value of temperature and a coarse grid mesh (N=4, say). At any given time the computer handles only three columns of the vector $\underline{\theta}$, namely θ_{n-1}, θ_n, θ_{n+1}. During each iteration, the columns are read, in order, from one magnetic tape and after the process of over-relaxation has been carried out on every term of the column θ_n, the columns are written on to the other magnetic tape. At the end of each iteration, the magnetic tapes change places and the reiterative procedure is repeated. Convergence and discretisation error criteria are as described in section (3.5.2), with the summation being carried out over the entire grid. The ALGOL text of a computer program together with a summary of the major steps are provided in Appendix D.

As compared with the solution of the two-dimensional equation this computer program has to carry out something of the order of (N+1) x M more calculations for each iteration and each calculation involving at least twice as many mathematical operations. In addition the operation is further slowed considerably by the transfer of data to and from the magnetic tapes. Whereas an acceptable solution of the two-dimensional heat conduction equation can be obtained in about 20 secs. of computational time, we now require at least 40 minutes of actual computational time and another 15-20 minutes to cover the manipulation of the magnetic tapes. These times just quoted are for $X_o = 10^{-2}$. For a lower value

of X_o the computer times required are well in excess of 1 hour. With the facilities available at present it is not feasible to obtain solutions of the required accuracy for $X_o < 10^{-3}$, say. Instead an alternative approach, if required, can be used to estimate the temperature distribution for $X_o \longrightarrow 0$. In this case solutions are obtained for three different values of X_o (all greater than 10^{-3}, say) and the values of the corresponding points extrapolated graphically or using a simple power law to give the solutions applicable for $X_o \longrightarrow 0$. In this way a solution for $X_o \longrightarrow 0$ can be obtained which is of a higher degree of accuracy than that obtained by using $X_o < 10^{-3}$ but a larger tolerance on the convergence and discretisation error criterions.

To reduce the total computational time to a minimum it is necessary to use the appropriate value of the over-relaxation parameter ω. The dependence on ω is demonstrated by considering a specific example where we take $\tau_o=0.98$, $X_o=10^{-2}$, $\phi=45^o$ and the limit on convergence and discretisation error to be 10^{-4}. In table (5.4.1) are given the number of iterations carried out at each grid size for different values of the over-relaxation parameter ω. Also in figure (5.4.1) we plot the variation of computational time and the total elapsed time against ω.

In table (5.4.2) and figure (5.4.2) we present the solution of the equation with the same parameters but where we have reduced the limit on convergence and discretisation error to 10^{-5}. In obtaining the solutions it is recommended to use an error term $\leqslant 10^{-5}$ in order to ensure sufficient accuracy of the solutions. While the computational times have gone up by a factor of about 15, the additional time required to operate the magnetic tapes has increased from about 4 minutes to

Table 5.4.1 Convergence of a typical three-dimensional solution with tolerance on convergence and discretisation error as 10^{-4}

Over Relaxation Parameter ω	Number of iterations at grid size given by N = M =				Computational time	Total elapsed time
	4	8	16	32		
1.3	13	31	43	1	3 min. 26 sec.	7 min. 25 sec.
1.4	15	27	41	1	3 min. 15 sec.	7 min. 3 sec.
1.5	21	22	38	1	3 min. 02 sec.	6 min. 33 sec.
1.55	25	20	36	1	2 min. 54 sec.	6 min. 56 sec.
1.6	32	20	34	1	2 min. 49 sec.	7 min. 27 sec.
1.7	68	30	28	1	2 min. 52 sec.	7 min. 42 sec.

$\tau_o = 0.98, \quad X_o = 10^{-2}, \quad \phi = 45^o$

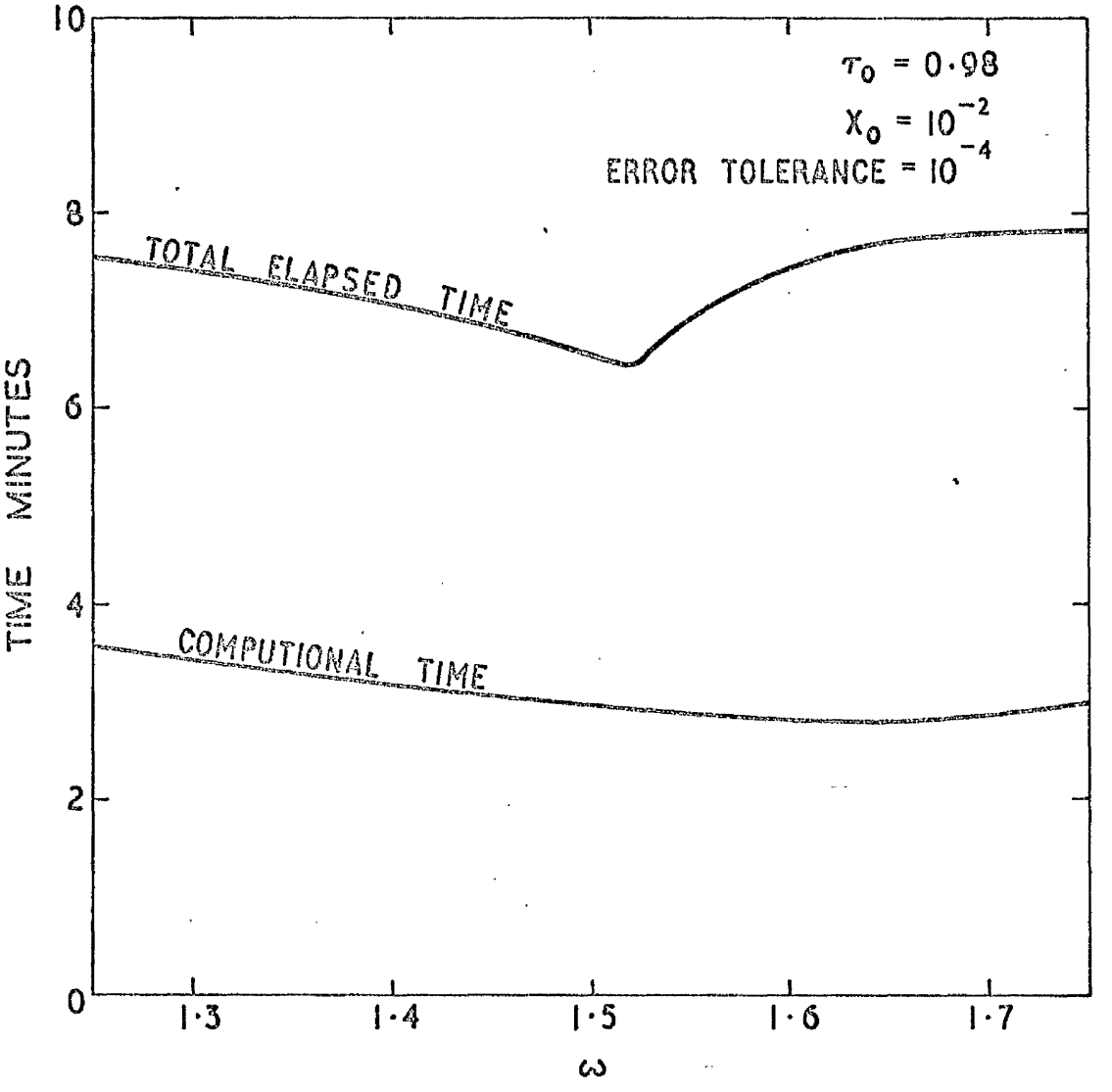

Figure 5.4.1. The effect of ω on computation time.

Table 5.4.2 Convergence of a typical three-dimensional solution with tolerance on convergence and discretisation error as 10^{-5}

Over Relaxation Parameter ω	Number of iterations at grid size given by N = M =						Computational time	Total elapsed time
	4	8	16	32	64	128		
1.4	20	45	113	166	1	-	43 min.37 secs.	60 min.42 secs.
1.5	29	36	95	153	2	1	44 min.06 secs.	55 min.17 secs.
1.6	43	30	77	136	3	1	40 min.14 secs.	56 min.14 secs.
1.7	90	47	60	114	9	1	40 min.01 secs.	61 min.54 secs.

$$\tau_o = 0.98, \quad X_o = 10^{-2}, \qquad \phi = 45^o$$

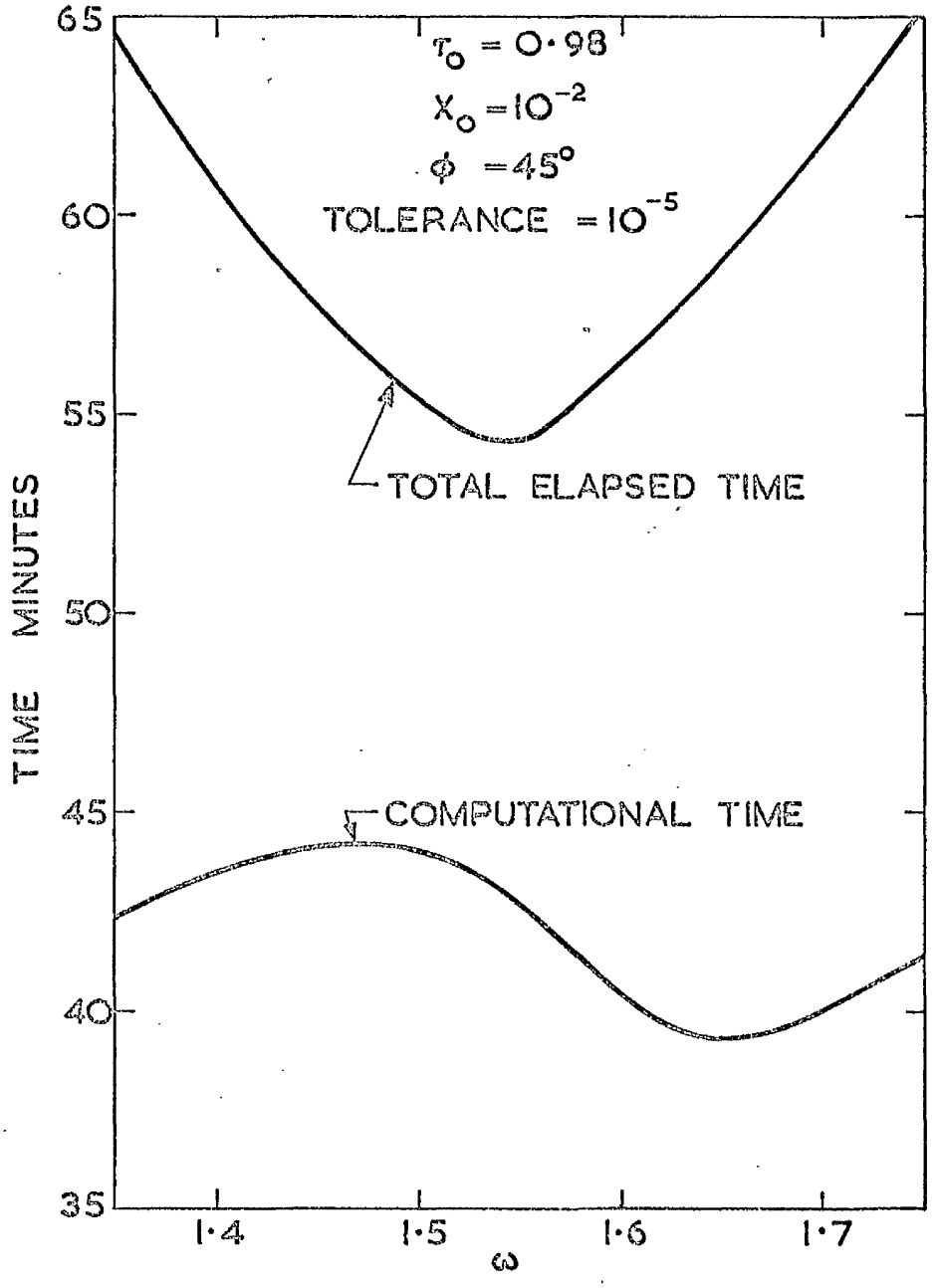

Figure 5.4.2 The effect of over-relaxation parameter on the computational time. Error tolerance 10^{-5}.

about 12 minutes. Based on the results of figure (5.4.2) it is recommended to use $\omega > 1.5$, because a smaller value sometimes terminates the convergence prematurely.

One of the reasons why the solution of the three-dimensional equation takes longer to converge than the two-dimensional equation is the discontinuity in the planform that exists at the apex of the delta. In an effort to speed up the process of convergence, close to the apex, instead of using the relaxation equations (5.8) to provide estimates of temperature, we used a Laplace"s solution (obtained by a change of variables and using a polar system of co-ordinates) of the linearised form of equation (5.6). Such a scheme yields the same temperature distribution but unfortunately took slightly longer to converge.

5.5 The effect of finite span

The solution over the leading edge region of a delta wing (shown in figure 5.2.3) can be divided into three distinct parts. In the vicinity of the apex of the delta, the temperature rises significantly above the two-dimensional nose temperature. This increase of temperature is attributed to the discontinuity in the planform at the apex of the delta wing. The influence of this local discontinuity extends over a relatively short distance in the spanwise direction. In figure (5.5.1) we plot the leading edge temperature against the spanwise distance. As expected, the effect of the apex is limited to lengths of the order of ℓ (conduction length). In fact as the angle of sweepback (Φ) increases the temperature along the leading edge becomes two-dimensional at a smaller value of y. A similar increase in temperature of the leading edge occurs near the wing tip.

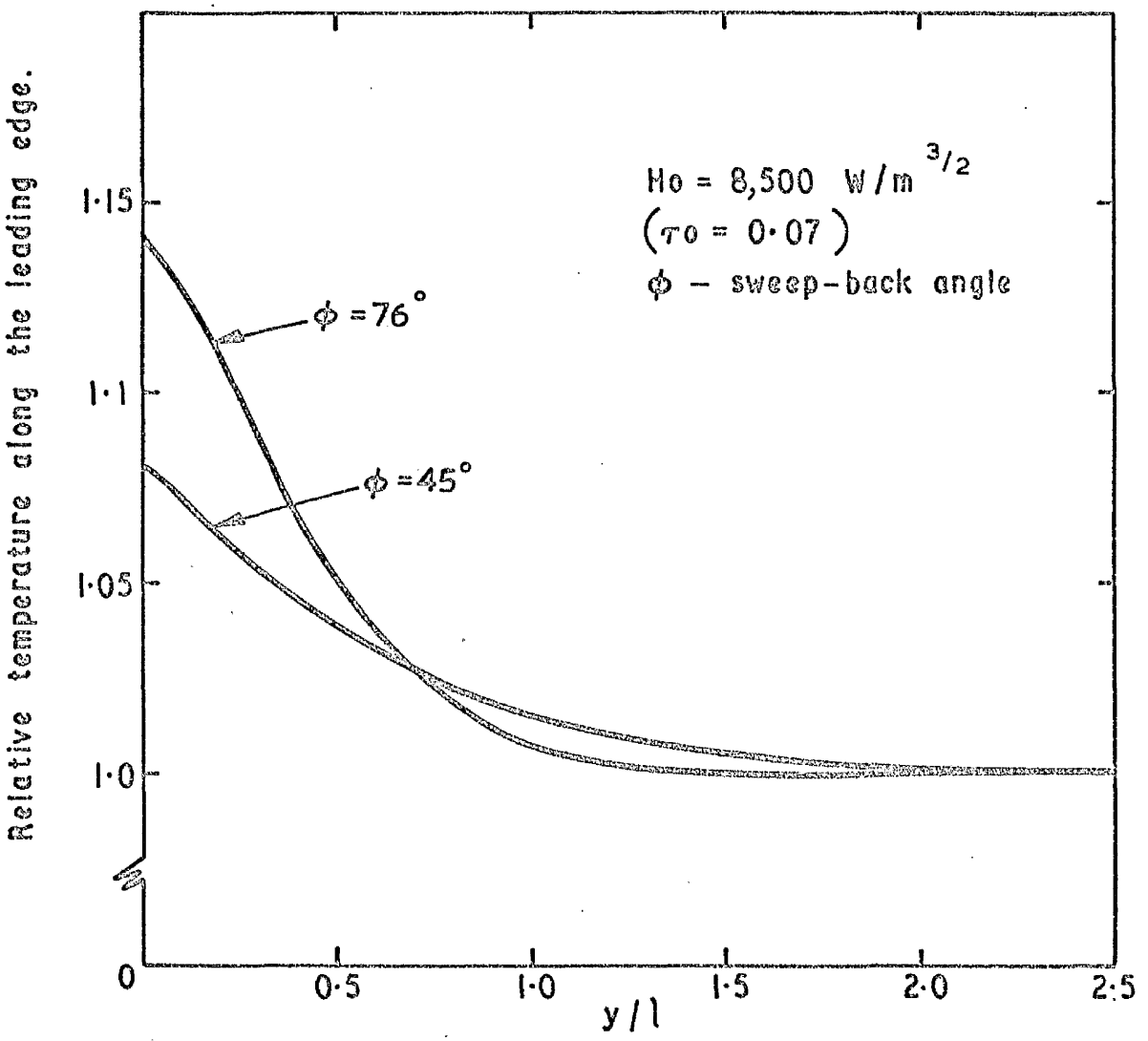

Fig.5.5.1 The effect of conduction length upon the spanwise temperature distribution.

For the region $1 < y < s-1$, (where s is the semi-span) which forms the majority of the wing, the temperature distribution is the same and of course independent of y. Two-dimensional conditions prevail and we shall show later how the results of the last chapter can be modified to include the influence of sweep-back to give the temperature distributions in this region.

At the spanwise tip of a swept wing, with the boundary condition shown in figures (5.2.3) and (5.5.2a) the leading edge temperature reaches a maximum. Instead if we consider a chordwise tip (as for example on a cropped delta) and suppose zero heat transfer normal to the edge (as in figure 5.5.2b) this produces a local minimum in the temperature distribution at the tip. The singularity at the tip can be eliminated by terminating the spanwise dimension normal to the leading edge and assuming no heat transfer parallel to the line of the leading edge (figure 5.5.2c). Since the grid we use is always parallel to the x, y axes, it is much simpler numerically to employ instead the cropped delta configuration as shown in figure (5.5.2d) and the same boundary condition as in figure (5.5.2c) to give two-dimensional temperature values along the leading edge over the range $y > 1$.

In this chapter we investigate the temperature distributions close to the apex region only of the delta wing. In practice the maximum temperature is going to occur at the apex of the delta. Even if there does exist another maximum at the tip such as shown in figure (5.5.2a) we can estimate the temperatures there from results obtained for the apex because the two singularities are basically the same. By limiting the area of investigation adjacent to the nose of the wing ($s=O(1)$, say) a

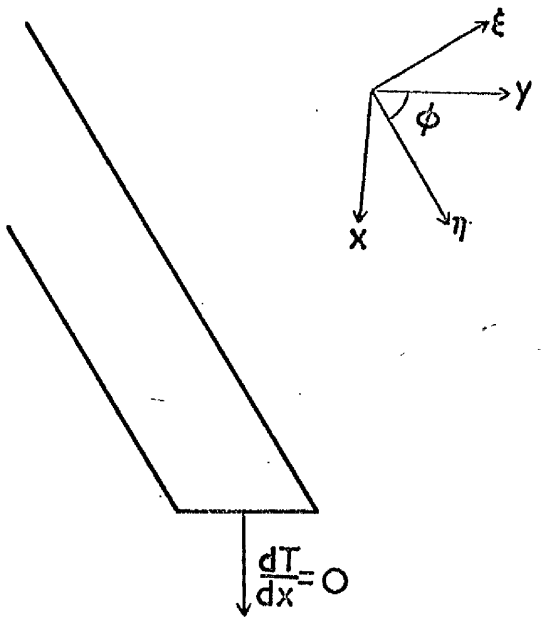

(a) $\theta_{tip} \longrightarrow \theta_{max}$

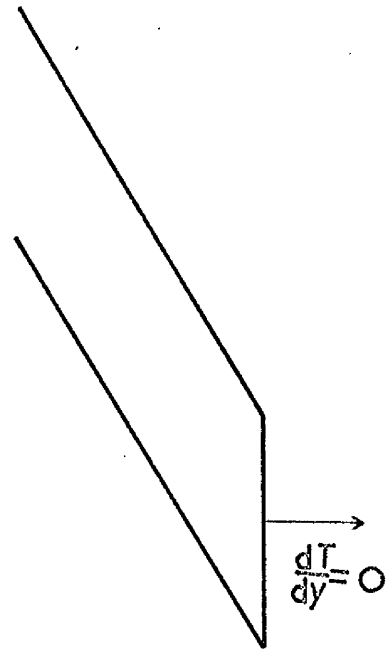

(b) $\theta_{tip} \longrightarrow \theta_{min}$

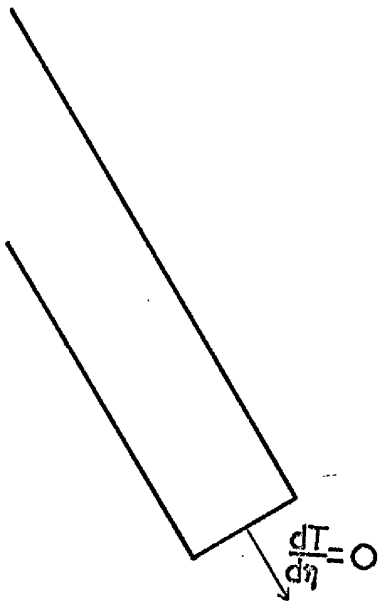

(c) $\theta_{tip} \longrightarrow \theta_{two\text{-}dimensional}$

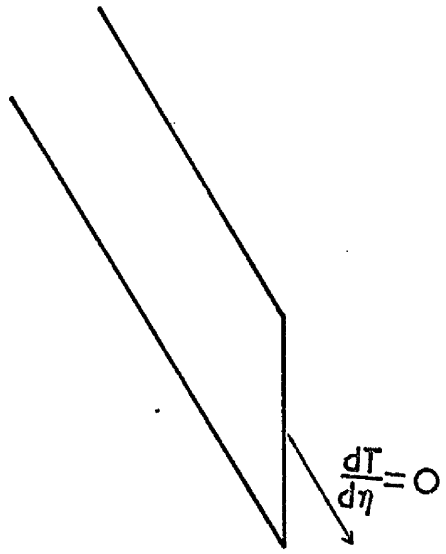

(d) $\theta_{tip} \longrightarrow \theta_{two\text{-}dimensional}$

Figure 5.5.2 The effect of various spanwise tips and boundary conditions on the value of the tip temperature.

considerable saving in computational time is obtained. In fact on present day computers it might not be possible to obtain the temperature distributions close to the leading edge of an entire delta wing within a reasonable computer time. For these reasons we concentrate our efforts to the apex region only which we expect to be the most crucial point from the heat transfer aspect of hypersonic flight.

5.6 The effects of the angle of sweep (ϕ).

In extending the theory to include the extra spanwise dimension we have also introduced one more important parameter, namely the angle of sweep of the leading edge ϕ . To determine the effect of sweep on the leading edge temperature, we vary ϕ from 0° (equivalent to a two-dimensional leading edge) to very nearly 90°. The results for various values of X_o are plotted in figure (5.6.1) where the apex temperature is relative to the corresponding value for an unswept wing. (i.e. same H_o and L as shown in figure (5.6.2)). As mentioned before, actual numerical solutions cannot be obtained for $X_o \longrightarrow 0$. Instead we use a simple power law to extrapolate the apex temperature for $X_o = 0$ based on the results of $X_o = 0.03$, 0.01 and 0.003.

For a given value of ϕ , the changes produced in the apex temperature by varying τ_o are very slight indeed. The results relative to the unswept leading edge temperature being presented in table (5.6.1), in the range of τ_o from 0.28 to 4.1 for $X_o = 10^{-2}$. It must be pointed out that these results are accurate to about $\pm$ 0.1%, which was the tolerance criterion used in obtaining the numerical solutions.

Increasing the angle of sweep can be seen to reduce the amount of conducting material available at the apex and so produce an increase in

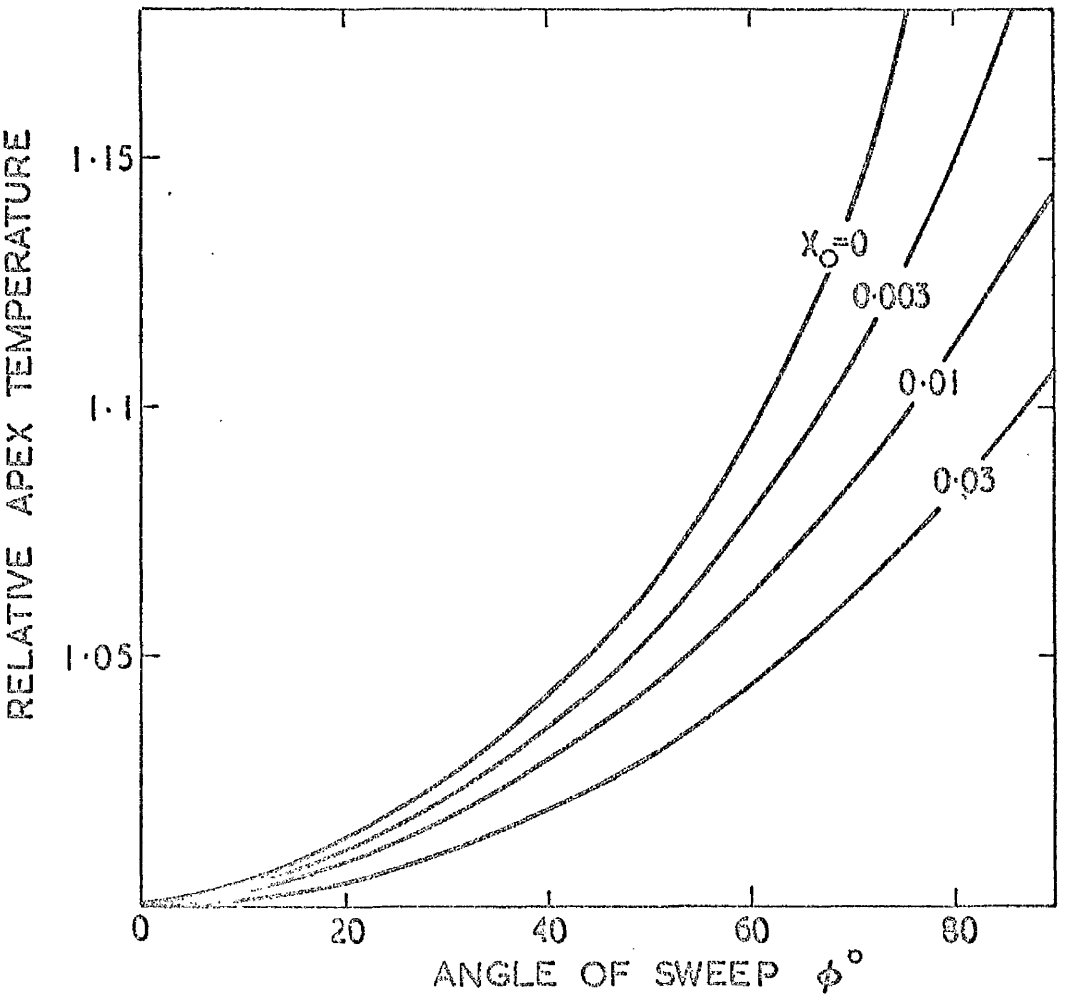

Figure 5.6.1 The effect of sweepback on the sharp apex temperature relative to the two-dimensional value.

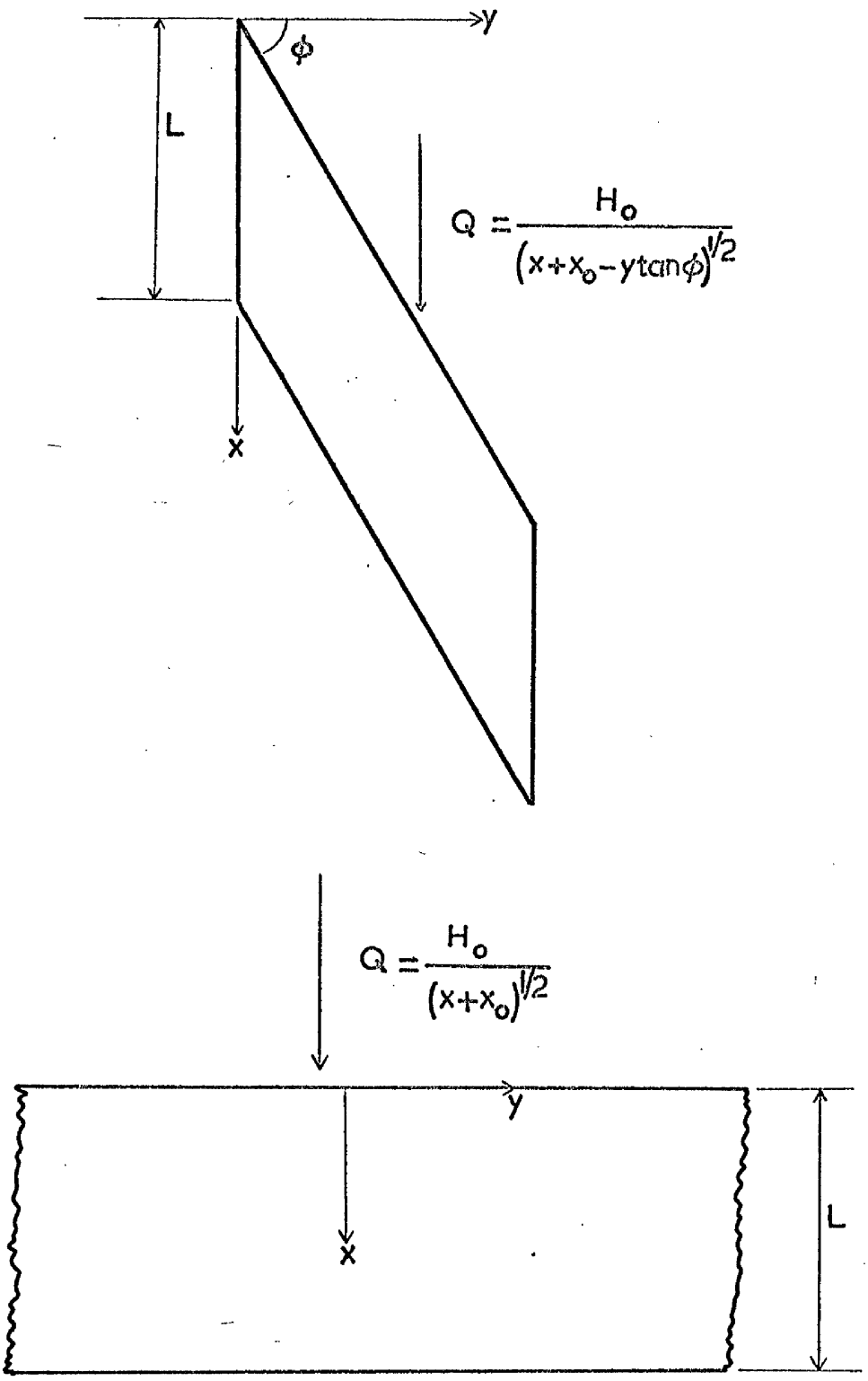

Figure 5.6.2 Basis for comparing results for a leading edge swept at an angle ϕ with the corresponding unswept configuration.

Table 5.6.1 The effect of τ_o on the apex temperature of the delta wing relative to the unswept wing temperature at various values of sweep angle ϕ.

$$X_o = 10^{-2}.$$

ϕ^o \ τ_o	0.285	0.977	4.07
0.	1.0	1.0	1.0
14.0	1.003	1.002	1.002
26.6	1.016	1.014	1.018
45.0	1.04	1.035	1.038
63.4	1.076	1.07	1.08
76.0	1.109	1.102	1.107
84.3	1.14	1.136	1.143

nose temperature as compared to an unswept wing. However, the effect is slight, even for extreme angles of sweep-back, and within the possibilities of control by a locally enhanced provision of conducting material.

We now see how we can modify the previous analysis of the two-dimensional leading edge to give us results for the swept wing. If we suppose that ξ is measured normal to the leading edge, then ξ must replace x in the similarity laws derived for an unswept wing. Thus the heat flux becomes equal to $H_o/(\xi \sec\phi)^{1/2}$ which means that we must replace H_o by $H_o\cos^{1/2}\phi$, and L is interpreted as length of the conducting region perpendicular to the leading edge. Solutions of the three-dimensional equation (5.6) for a swept wing using the values H_o and L, give the same value of the leading edge temperature away from the apex as does the solution of the equation for the two-dimensional leading edge (equation 3.15) provided in the latter case we use the values of the heat input parameter as $H_o\cos^{1/2}\phi$ and $L\cos\phi$. If the sweep-back is envisaged as being achieved by yawing a given wing, then L remains invarient with ϕ, and the reduction in the value of H_o would account for a reduction in temperature by a factor between $\cos^{2/13}\phi$ and $\cos^{1/8}\phi$, depending on whether the ration (L/l) is large or small[13]. On the other hand, if the wing sweep-back is envisaged as being achieved by shearing the wing, then the heat flux at the edge of the conducting region (and so the values associated with Q_L, T_L, and l) remain invariant whilst L decreases in proportion to $\cos\phi$, producing a reduction in the leading edge temperature. In either interpretation, away from the apex of the delta wing, sweepback can be seen to reduce

the leading edge temperature as compared with the corresponding value for the unswept wing where the basis for calculating the two temperature distributions is as shown in figure 5.6.2 (i.e. the same value of H_o and L). The temperature along a swept leading edge is plotted in figure (5.6.3) for a specific example, away from the apex sweepback is seen to play a beneficial role by lowering the temperature along the leading edge with respect to an unswept wing value. Along the rear edge the temperature distribution remains more or less constant, for a given angle of sweep.

5.7 Temperature distribution close to the apex of the delta.

We now plot a typical temperature distribution at the apex of a delta wing - figure (5.7.1). For the example shown, the span to chord ratio is 0.67 ($\phi = 71.6^{\circ}$); and $\tau_o = 0.29$.

The effects of varying the parameters of equation 5.6 are the same as we found in the two-dimensional study of the problem. For example, any increase in the conducting properties (i.e. product kt) produces a moderating effect on the temperature distribution; the temperature gradients are reduced everywhere, and at the same time the leading edge temperatures are reduced at the expense of the temperatures further downstream. The similarity laws derived in reference (12) can be applied directly to provide the variation of temperature with a given parameter (k, t, ϵ, H_o etc.).

Sweepback is seen to produce a local maximum in the leading edge temperature at the apex of the delta wing. Fortunately this increase is small and within control by either locally enhancing the effects of thermal conductio (e.g. increasing kt) or eliminating the sharp apex.

We shall now prove that by placing certian restrictions on the curvature of the leading edge, two-dimensional temperature distributions prevail along the leading edge of the wing and the "undesirable" effects of sweepback can be eliminated.

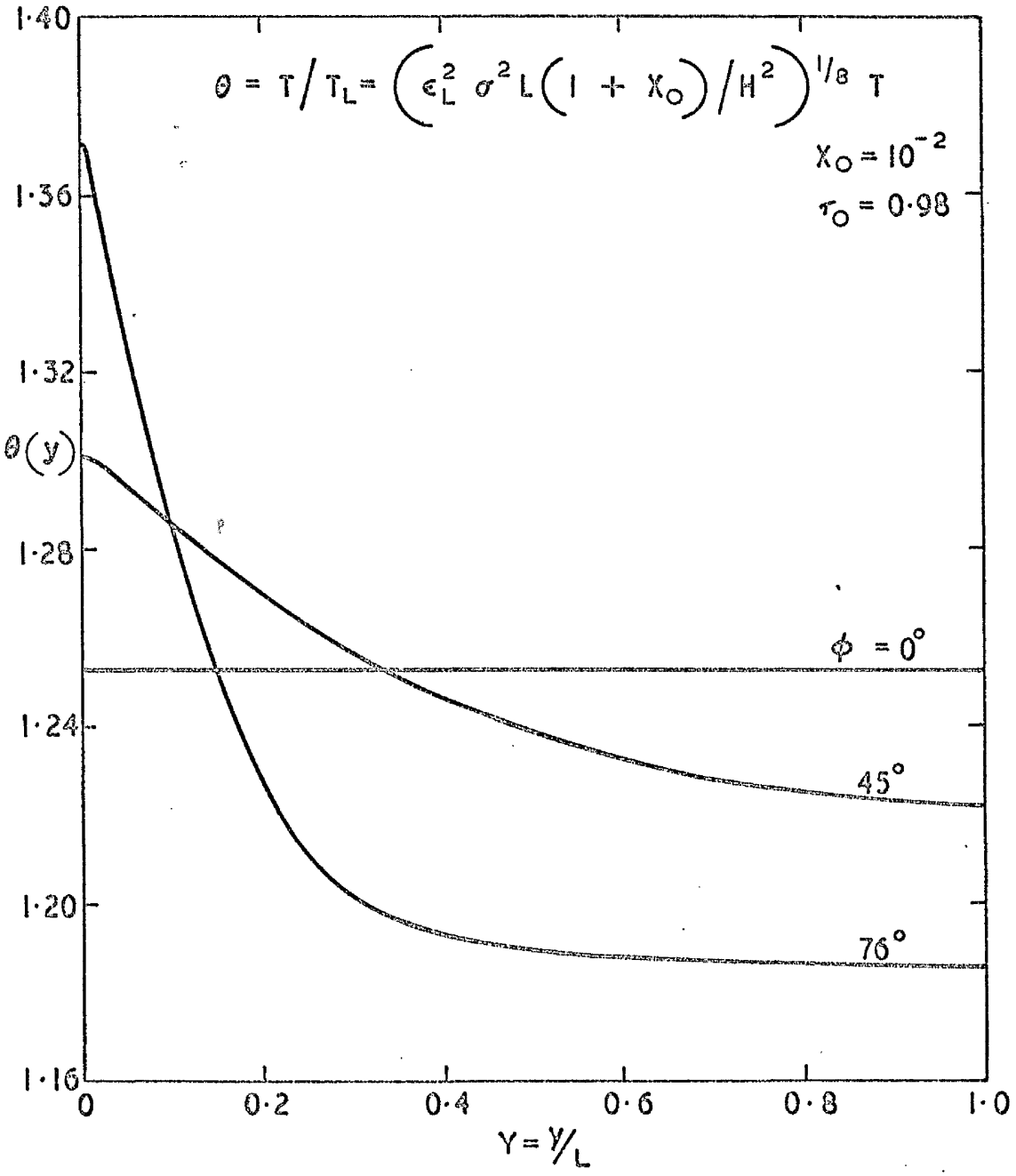

Figure 5.6.3. The effect of sweep angle ϕ on the leading edge temperature.

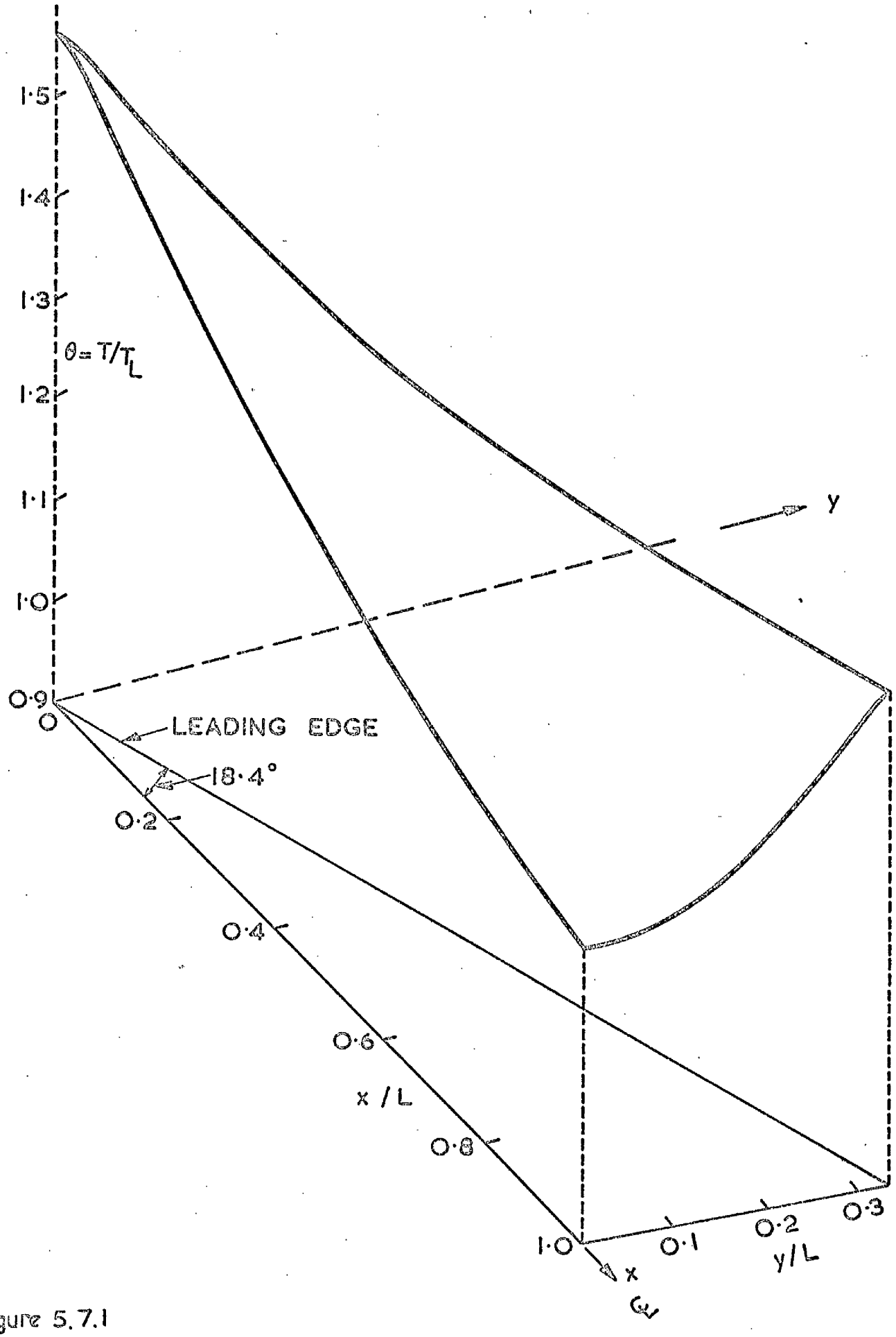

Figure 5.7.1

Temperature distribution in the apex region of a delta wing.

In order to analyse the effects of the leading edge curvature on the temperature distribution it is necessary to derive the heat transfer equation in a set of general orthogonal curvilinear coordinates.

Re-writing the general heat transfer equation in the ordinary rectangular coordinates, we have

$$\frac{\partial}{\partial x}\left(kt\,\frac{\partial T}{\partial x}\right) + \frac{\partial}{\partial y}\left(kt\,\frac{\partial T}{\partial y}\right) = \epsilon\sigma T^4 - Q \qquad (5.14)$$

Now in any general orthogonal system the displacements along the coordinate curves (u = constant and v = constant, say) are equal to $ds_u = h_u\,du$ and $ds_v = h_v\,dv$ and are always mutually orthogonal - see figure (5.7.2)

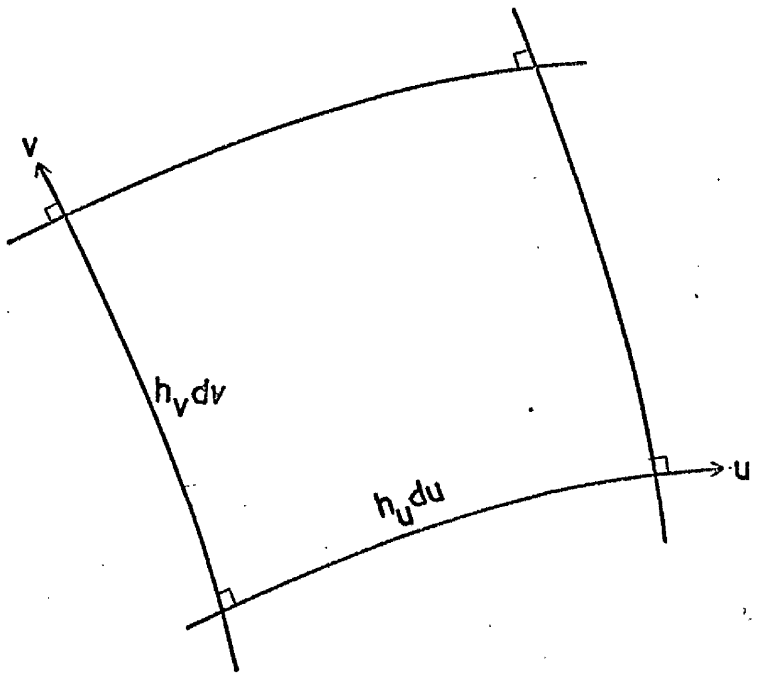

Figure (5.7.2) A system of orthogonal curvilinear coordinates.

In this notation we can express equation (5.14) with the help of references (39 and 40), as follows:

$$\frac{\partial}{\partial u}\left(kt\,\frac{h_v}{h_u}\,\frac{\partial T}{\partial u}\right) + \frac{\partial}{\partial v}\left(\frac{h_u}{h_v}\,\frac{\partial T}{\partial v}\right) = h_u h_v\left(\epsilon\sigma T^4 - Q\right) \qquad (5.15)$$

Expanding equation (5.15) gives

$$kt\,\frac{\partial T}{\partial u}\left(\frac{1}{h_u}\,\frac{\partial h_v}{\partial u} - \frac{h_v}{h_u^2}\,\frac{\partial h_u}{\partial u}\right) + \frac{h_v}{h_u}\,\frac{\partial}{\partial u}\left(kt\,\frac{\partial T}{\partial u}\right) + kt\,\frac{\partial T}{\partial v}\left(\frac{1}{h_v}\,\frac{\partial h_u}{\partial v} - \frac{h_u}{h_v^2}\,\frac{\partial h_v}{\partial v}\right)$$

$$+ \frac{h_u}{h_v}\,\frac{\partial}{\partial v}\left(kt\,\frac{\partial T}{\partial v}\right) = h_u\,h_v\left(\epsilon\sigma T^4 - Q\right) \qquad (5.16)$$

We now consider the application of the curvilinear system to represent the leading edge of a hypersonic wing.

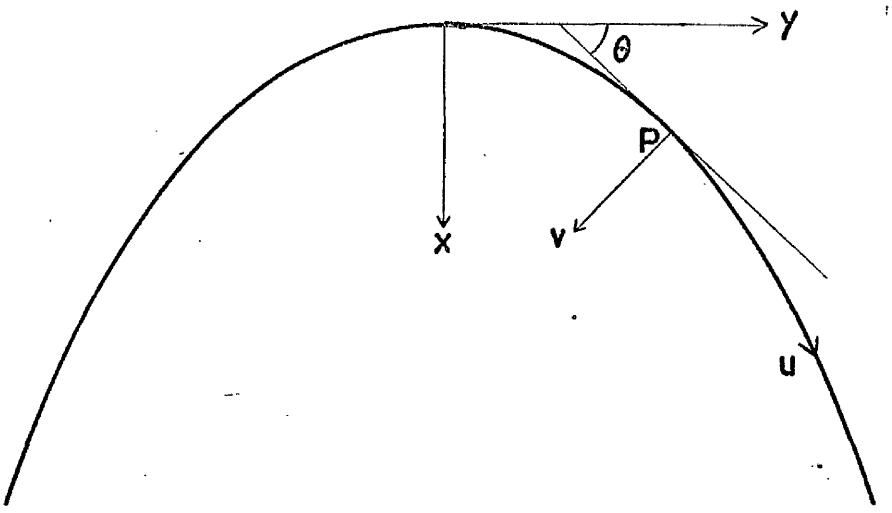

Figure (5.7.3) Transformation to orthogonal curvilinear system of coordinates.

In particular we make one of u - curves to be coincident with the leading edge. The v - curves become straight lines normal to the u - curve. The tangent to the curve at some point (P) makes an angle θ with the y - axis. For the two systems of coordinates, we have

$$x = \int_0^s \cos\theta \, du - v \sin\theta \tag{5.17}$$

and $$y = \int_0^s \sin\theta \, du + v \cos\theta \tag{5.18}$$

Also if s is the arc length (measured from the origin)

$$\frac{d\theta}{ds} = \frac{1}{R}$$

i.e. $$\theta = \int_0^s \frac{1}{R} \, ds$$

where R is the radius of curvature of the leading edge at the point P.

In such a notation the arc length can be expressed as

$$ds^2 = dx^2 + dy^2 = \left(1 - \frac{v}{R}\right)^2 du^2 + dv^2 \tag{5.19}$$

From our definition of the orthogonal system

$$ds^2 = h_u^2 \, du^2 + h_v^2 \, dv^2 \tag{5.20}$$

Comparing equations (5.19) and (5.20) gives

$$h_u = 1 - \frac{v}{R} \tag{5.21}$$

and $$h_v = 1 \tag{5.22}$$

Substituting equations (5.21) and (5.22) into equation (5.16) gives

$$-kt \frac{\partial T}{\partial u} \frac{1}{\left(1 - \frac{v}{R}\right)^2} \cdot \frac{\partial}{\partial u}\left(1 - \frac{v}{R}\right) + \frac{1}{1 - \frac{v}{R}} \frac{\partial}{\partial u}\left(kt \frac{\partial T}{\partial u}\right) + kt \frac{\partial T}{\partial v} \frac{\partial}{\partial v}\left(1 - \frac{v}{R}\right)$$

$$+\left(1 - \frac{v}{R}\right) \frac{\partial}{\partial v}\left(kt \frac{\partial T}{\partial v}\right) = \left(1 - \frac{v}{R}\right)\left(\epsilon \sigma T^4 - Q\right) \tag{5.23}$$

Where we have made use of the relation that

$$\frac{\partial h_v}{\partial u} = \frac{\partial h_v}{\partial v} = 0.$$

Expanding equation (4.16) gives,

$$kt\frac{\partial T}{\partial u}\frac{1}{(1-\frac{v}{R})^2}\left(\frac{v}{R^2}\right)\frac{\partial R}{\partial u} + \frac{1}{(1-\frac{v}{R})}\frac{\partial}{\partial u}\left(kt\frac{\partial T}{\partial u}\right) - \frac{1}{R}kt\frac{\partial T}{\partial v}$$

$$+ (1-\frac{v}{R})\frac{\partial}{\partial v}\left(kt\frac{\partial T}{\partial v}\right) = (1-\frac{v}{R})(\epsilon\sigma T^4 - Q) \qquad (5.24)$$

Note that R is function of u only in the particular system we have defined $\therefore \frac{\partial R}{\partial v} = 0.$

In order to make all the derivatives of generally unit order, we normalise the parameters as follows:

$$R = R_N.\bar{R}, \qquad u = U.\bar{u}, \qquad v = 1.\bar{v} \qquad (5.25)$$

Particularly 1 can be associated with the conduction length normal to the leading edge.

On substituting these relations into equation (5.24) it becomes,

$$\frac{1}{1^2}\left[kt\frac{\partial T}{\partial \bar{u}}\left[\frac{1}{(1-\frac{1}{R_N}\frac{\bar{v}}{\bar{R}})^2}\frac{1^2}{U^2}\frac{1}{R_N}\frac{\bar{v}}{\bar{R}}\frac{\partial \bar{R}}{\partial \bar{u}}\right] + \frac{1}{(1-\frac{1}{R_N}\frac{\bar{v}}{\bar{R}})}\frac{1^2}{u^2}\frac{\partial}{\partial u}\left(kt\frac{\partial T}{\partial \bar{u}}\right)\right.$$

$$\left. - \frac{1}{R_N\bar{R}}kt\frac{\partial T}{\partial \bar{v}} + \frac{\partial}{\partial \bar{v}}\left(kt\frac{\partial T}{\partial \bar{v}}\right)\right] = (1-\frac{1}{R_N}\frac{\bar{v}}{\bar{R}})(\epsilon\sigma T^4 - Q) \qquad (5.26)$$

Now provided $R_N >> 1$ and $U >> 1$, we get the two-dimensional relation,

$$\frac{\partial}{\partial v}\left(kt\frac{\partial T}{\partial v}\right) = \epsilon\sigma T^4 - Q \qquad (5.27)$$

For a wing of finite span we therefore note that, provided the line of the leading edge has a radius of curvature which is large compared

with the conduction length l and provided that there are no spanwise discontinuities in the heat flux, then two-dimensional conditions apply in the determination of the temperature distribution in planes locally perpendicular to the leading edge.

We already know from the results presented in figure (5.6.1) by how much would the nose temperature be lowered if we can so round the leading edge. For example, for $X_o = 0$ (i.e. $Q_o \rightarrow \infty$), at 80^o sweep the sharp delta wing apex exhibits a local temperature which is about 20% higher than the corresponding unswept leading edge. At 45^o sweep, the figure is only about 5%. For finite rates of heat transfer at the nose of the wing, the apex temperature of a delta wing is not quite so severe as compared with a rounded nose, e.g. $X_o = 10^{-2}$ gives about 12% rise at 80% sweep. For practical values of the angle of sweep, the pointed swept wing can be expected to exhibit around 10% - 15% rise in the apex temperature as compared with a two-dimensional leading edge.

CHAPTER VI

Experimental study of three-dimensional wings.

The verification of the two-dimensional theory of a conducting plate by experiments not only has proved the important role played by heat conduction within the material near the leading edge of a hypersonic wing but also has strengthened the belief in the reliability of the general equations so set up for the prediction of the temperature distribution in this region. The three-dimensional theory is in effect the extension of the two-dimensional theory; it is influenced by the same governing factors. What has been found true in the two-dimensional case must apply also to the three-dimensional one. No experimental verification is therefore deemed necessary. Since, however, the numerical solution of a three-dimensional problem is much more complicated it would be of interest to examine the results by some experimental means. Though the models used for the three-dimensional study do not necessarily bear close resemblance to those representing exactly the type of leading edge one would contrive for hypersonic flight, the information thus derived should be useful for two reasons - it will give some indication of the accuracy of the numerical solutions and about the effects of finite span and sweepback on the temperature distribution. The experimental technique to be developed is also in its own right a useful technique for the study of leading edge heating.

6.1 Design and development of the three-dimensional heater.

In order to test experimental models, we require a heater capable

of producing a "realistic" distribution of heat intensities over the model. The heater should fulfil the following requirements:

a) the apex of the delta model should be subjected to the highest rates of heat flux.

b) the distribution of heat intensity impinging on the model must vary at least as $x^{-\frac{1}{2}}$ in the chordwise direction (where x is measured from the leading edge), with the highest gradients in the rates of heat flux occurring at or very close to the leading edge.

c) the distribution of heat flux must be symmetrical with respect to the plane y = 0 (centre-section of the delta).

d) the leading edges of the model should be heated uniformly.

One of the simplest methods of producing varying heat intensity over a surface is by means of a wire (heated electrically) held close to it (see figure below).

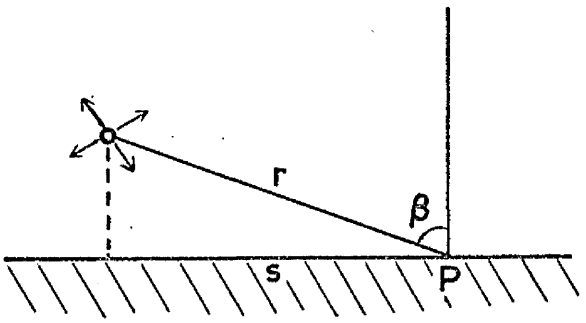

At any point P at a distance r from the wire the heat intensity is proportional to $\frac{\cos\beta}{r^2}$. Therefore, if the wire is held very close to the surface ($s \simeq r$) we can then expect the heat intensities to vary very roughly s^{-2} (s being measured along the surface as shown in the figure above). If we now place the wire directly above

the leading edge of the delta shaped model, we can expect the heat intensities to vary very roughly as x^{-2} over the model surface (where x is measured from the leading edge), which is a much severer variation of heat input than that predicted by the $x^{-\frac{1}{2}}$ distribution.

Before discussing how the rest of the design objectives were realised, we shall present the final configuration (figure 6.1.1) so that the merits of this layout can be judged in comparison with some of the alternative configurations that we tried. Heating is provided electrically by two tantalum wires (1.52mm. diameter) that run alongside the leading edge of the model and join together at the apex of the delta where they are tied together by a fine tantalum wire. The heating wires were always placed in a plane parallel to the surface of the model. We tried using more than two wires which were either spread evenly over the entire delta planform or placed close together near the leading edge. Even with two wires, the convergence at the apex leads to radiation exchange between the two wires producing locally a considerable rise in temperature, this effect becoming more marked as the number of wires is increased. Whereas the theoretical heat input distribution (equation 5.6.) is assumed to be of a constant magnitude along the leading edge, this is very difficult to achieve when we use two or more wires. As the number of wires is increased, not only does the heat intensity increase very rapidly along the leading edge as we approach the apex but also produces a region of maximum heat transfer at some distance away from the apex (along the centre section). Since this is clearly undesirable, it was decided to use just two

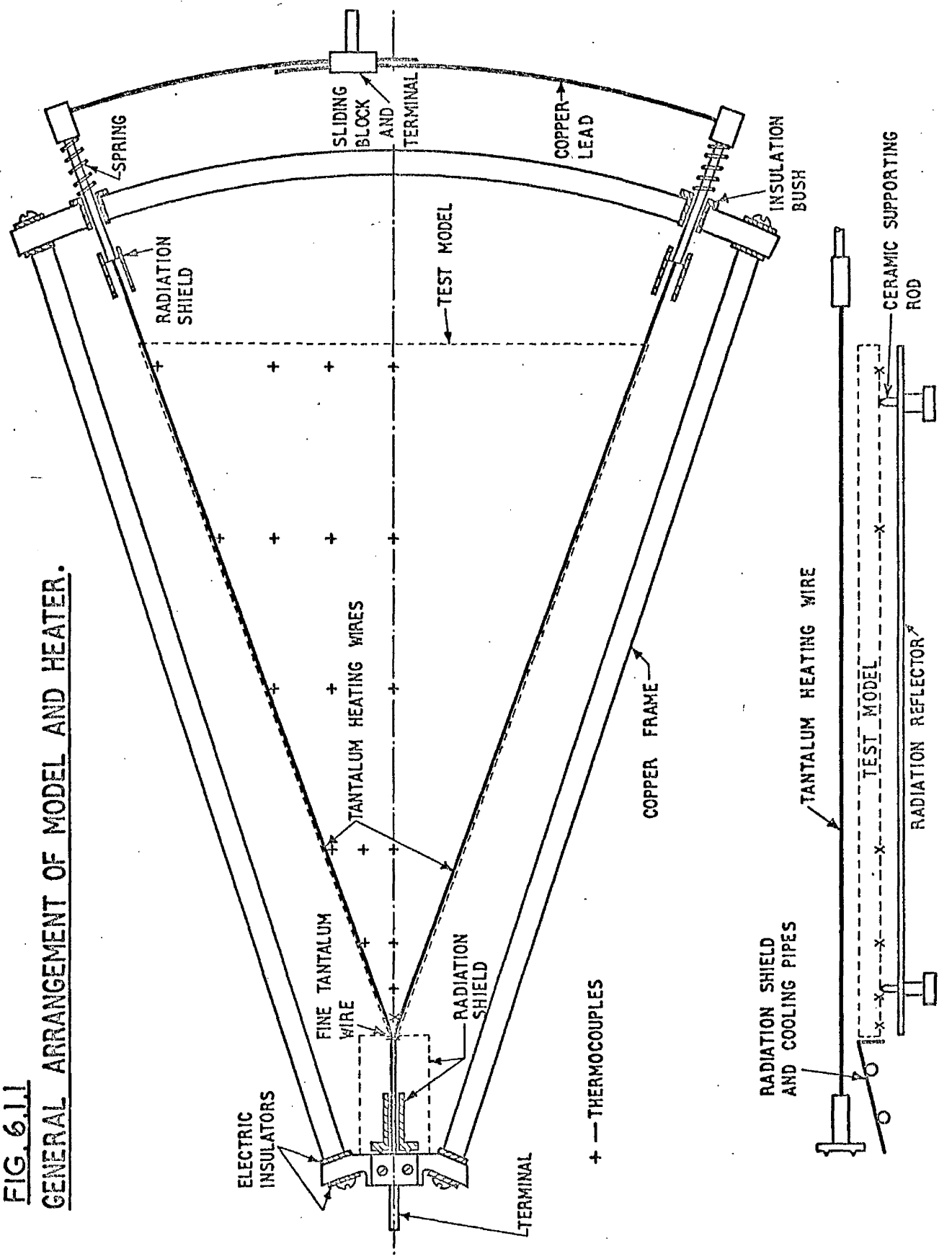

FIG. 6.1.1

GENERAL ARRANGEMENT OF MODEL AND HEATER.

heating wires, one along each leading edge, from the apex to a position further downstream. For this reason it was decided to use just two wires.

The two wires are connected to a fixed terminal at the apex end while the terminals at the other end are spring loaded individually to take up the sagging of the wires at elevated temperatures. To ensure that the two wires are at the same temperature there is a provision to make slight adjustments to the current through each wire by means of the sliding terminal. The two copper terminals are insulated from the copper framework by ceramic bushes and washers, as shown in figure 6.1.1.

For the two wires to dissipate the greatest amount of heat, their diameter must be increased as much as possible. However, as the wires become thicker the added weight causes them to sag even more at the high temperatures and it would require fairly heavy springs to keep them straight. Also the heavier wires would demand greater currents to dissipate a given amount of energy. A 0.152cm. diameter tantalum wire requires about 110A at around 9V giving a total dissipation of about 1kw. Increasing the diameter of the wire would lead to additional contact problems at the terminals across which large currents have to be conducted. Once the terminals are made very large to accommodate the thicker wires quite a high proportion of the heat would be lost at the ends of the wires through thermal conduction.

The heat loss through the terminals by thermal conduction is inevitable. One of the design requirements of the heater is that

the maximum heat flux should occur at the apex. Any cooling of the ends of the wires produces an undesirable effect on the apex heat transfer. To compensate for any heat loss by conduction cooling, the heater is provided with copper radiation shields which are attached to the three terminals. The shields are simply polished copper tubes to reduce the radiation heat dissipation. The length of the wires is kept considerably longer than the model to minimise the end effects and so ensure uniform heating of the leading edge. These precautions proved to be very successful as can be judged from the performance of the heater discussed later on.

6.1.1 Radiometer for measuring the local heat intensity.

The performance of the heater was measured with the aid of a radiometer which is shown on an enlarged scale in figure (6.1.2). It consists of a pair of thermocouples, one sensing the heat intensity impinging upon it and the other embedded in the copper block which is maintained at a constant temperature by circulating cold water through it. The top thermocouple is about 0.025cm. in diameter and painted black (giving the surface an absorptivity of over 0.9). So that the instrument measures the local heat intensity falling on a given plane, only a fraction of the circular thermocouple bead protudes above the copper block. The top surface of the water-cooled copper block defines the irradiated plane and is painted black to prevent any reflections on to the thermocouple. The output of the radiometer is the emf set up by the difference in temperature of the two thermocouples. Since we are measuring the temperature difference between the temperature of the water cooled jacket and the top

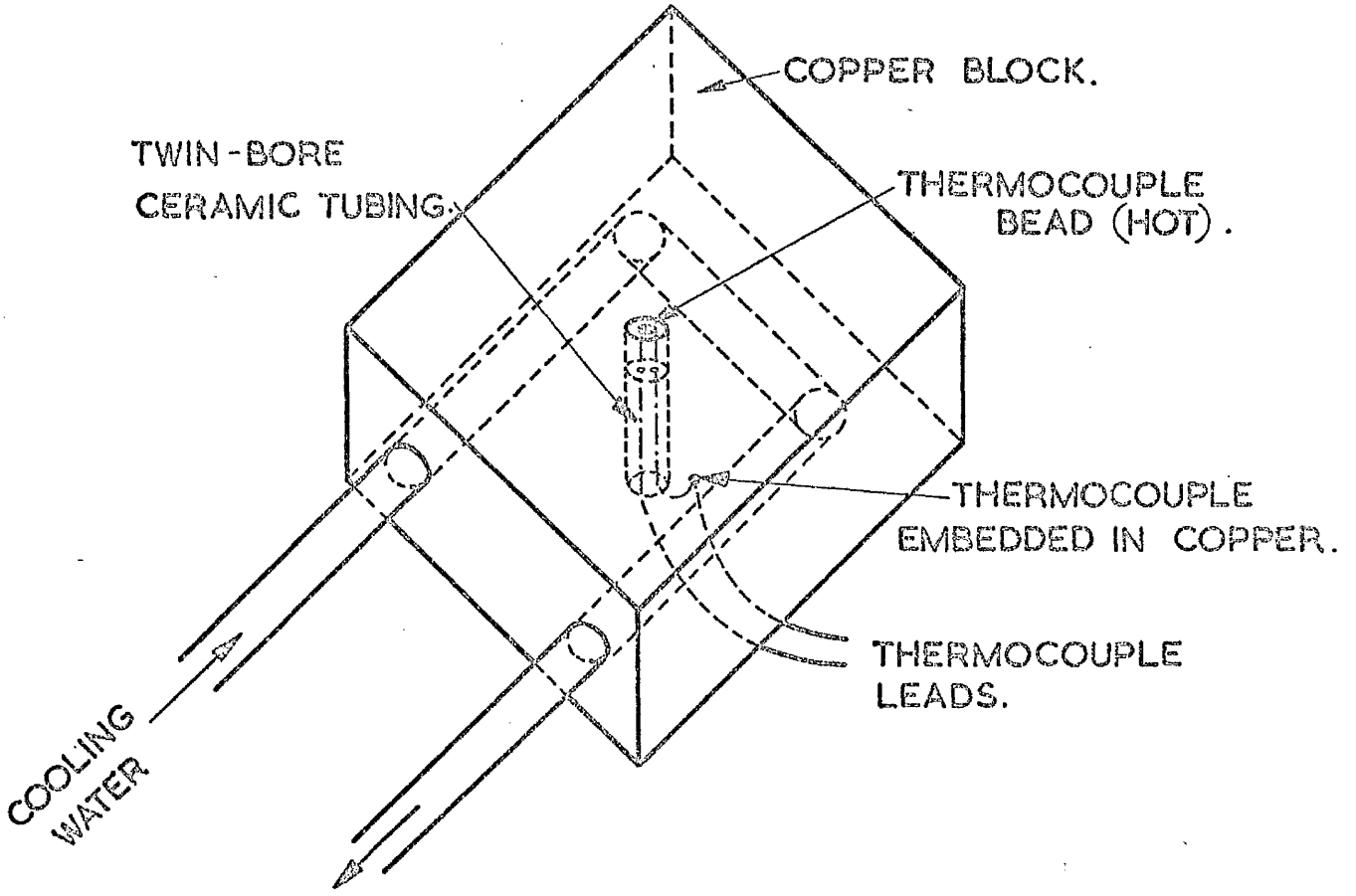

FIG. 6.1.2

Radiometer for measuring the local heat intensity.

(Not drawn to scale.)

thermocouple, the radiometer output is independent of the water temperature, except at the very low magnitudes of heat intensities. Calibration of the radiometer has been carried out with the help of a black-body cavity as a source of infra-red radiation. The radiometer has a linear response to the heat intensity impinging on it.

In order to measure the variation of heat intensity impinging on the model a special mechanism (on which the radiometer is mounted) had to be designed and constructed such that it is capable of traversing the whole of the given plane reliably and accurately.

6.2. Performance of the heater.

The performance of the delta shaped heater is shown in Figure (6.2.1). It shows the variation of heat flux obtained over one half of a delta of chord 20.3cms. and span 15.2cms. The sweep-back of the leading edge can be varied by altering the angle between the two wires at the apex. However, we have carried out the experimental observation of the theory at an angle of sweep-back, $\phi = 69.5^{\circ}$.

The two heating wires are put in a plane parallel to the plane of the model and at some distance (d, say) from it. The variation of heat intensity in the irradiated plane is very sensitive to this distance d. The performance shown in figure (6.2.1) is for d = 0.7cm. Increasing the value of d, reduces considerably the severity of the heat flux at the apex as compared with the downstream value. At the same time the total heat incident on the plane is reduced. Considering that the majority of the heat is lost to the walls of the vacuum chamber, it is important that we utilise as much as possible of

FIG. 6.2.1

MEASURED PERFORMANCE OF HEATER

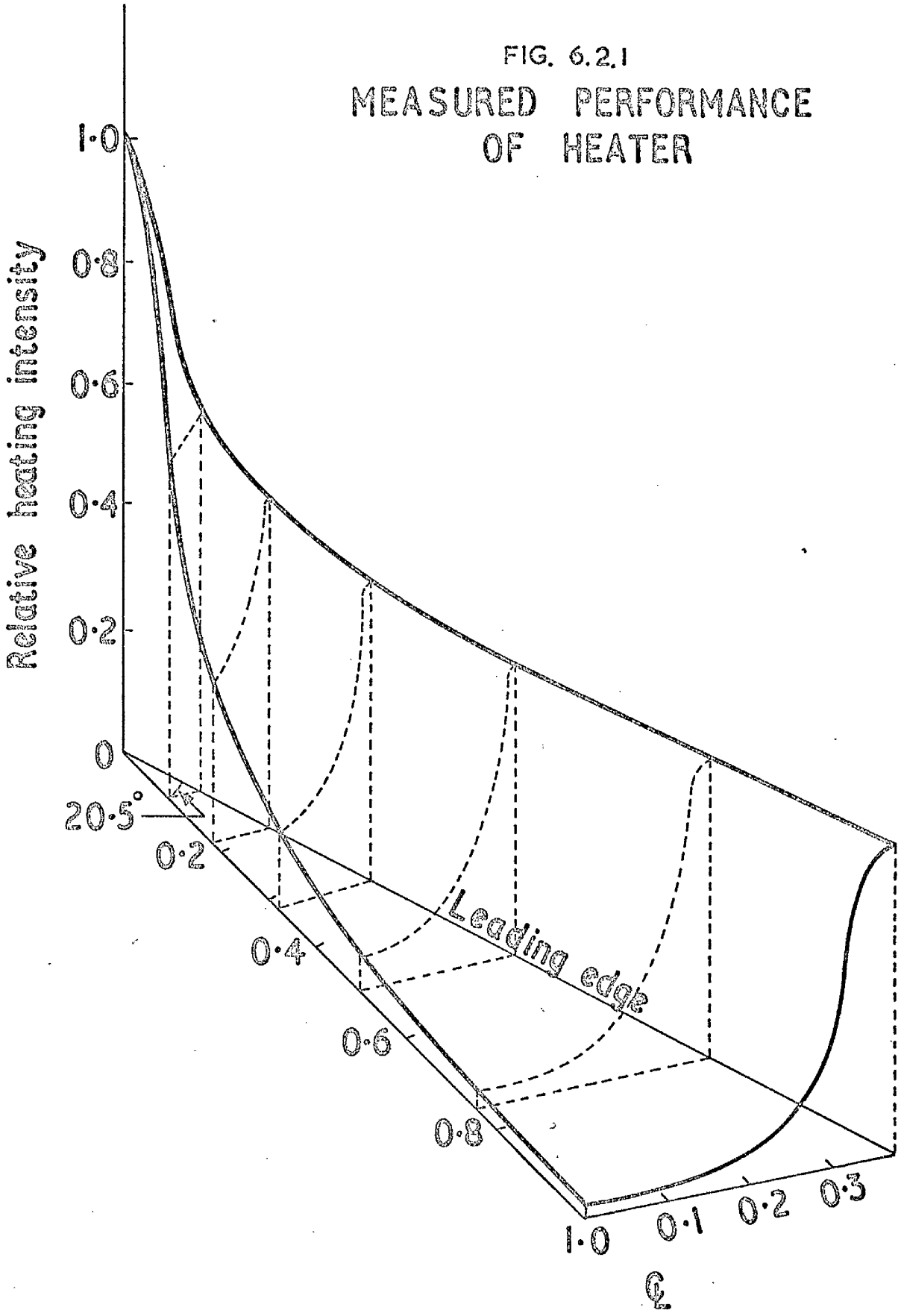

the limited amount of the heating available. However, if we reduce d any further than 0.7cm. any slight variation in d affects the distribution of radiation over the selected plane quite significantly.

We now look more closely at the distribution of heat intensity produced by the heater. Along the centre line the magnitude of heat flux decreases by a factor of over 50 from the apex to the base of the delta. This is indeed a much steeper variation of heat transfer than that given by the $x^{-\frac{1}{2}}$ distribution (except for the region very close to the leading edge). In the theoretical study it was assumed that the heat flux along the leading edge is constant. Since we use two wires (one along each leading edge), the magnitude of heat transfer along the leading edge decreases rapidly from the apex and settles at about half the apex value. For these reasons it is no longer realistic to compare the experimental results with the calculated temperature distribution using the $x^{-\frac{1}{2}}$ variation of heat transfer.

Instead we calculate the distribution of radiant energy incident on the model from an idealized heater where the two wires are replaced by line sources of heat. The calculated performance of such a heater is shown in figure (6.2.2.). A direct comparison of figures (6.2.1) and (6.2.2) reveals very good agreement between the two. The measured performance shows a higher gradient along the leading edge near the apex, and this was due to inter-radiation exchange between the two wires causing an increase in the local temperature of the wire. As a result of the temperature variation along the wire, away from the apex, the leading edge heat transfer is slightly lower than the

FIG. 6.2.2

CALCULATED PERFORMANCE OF HEATER

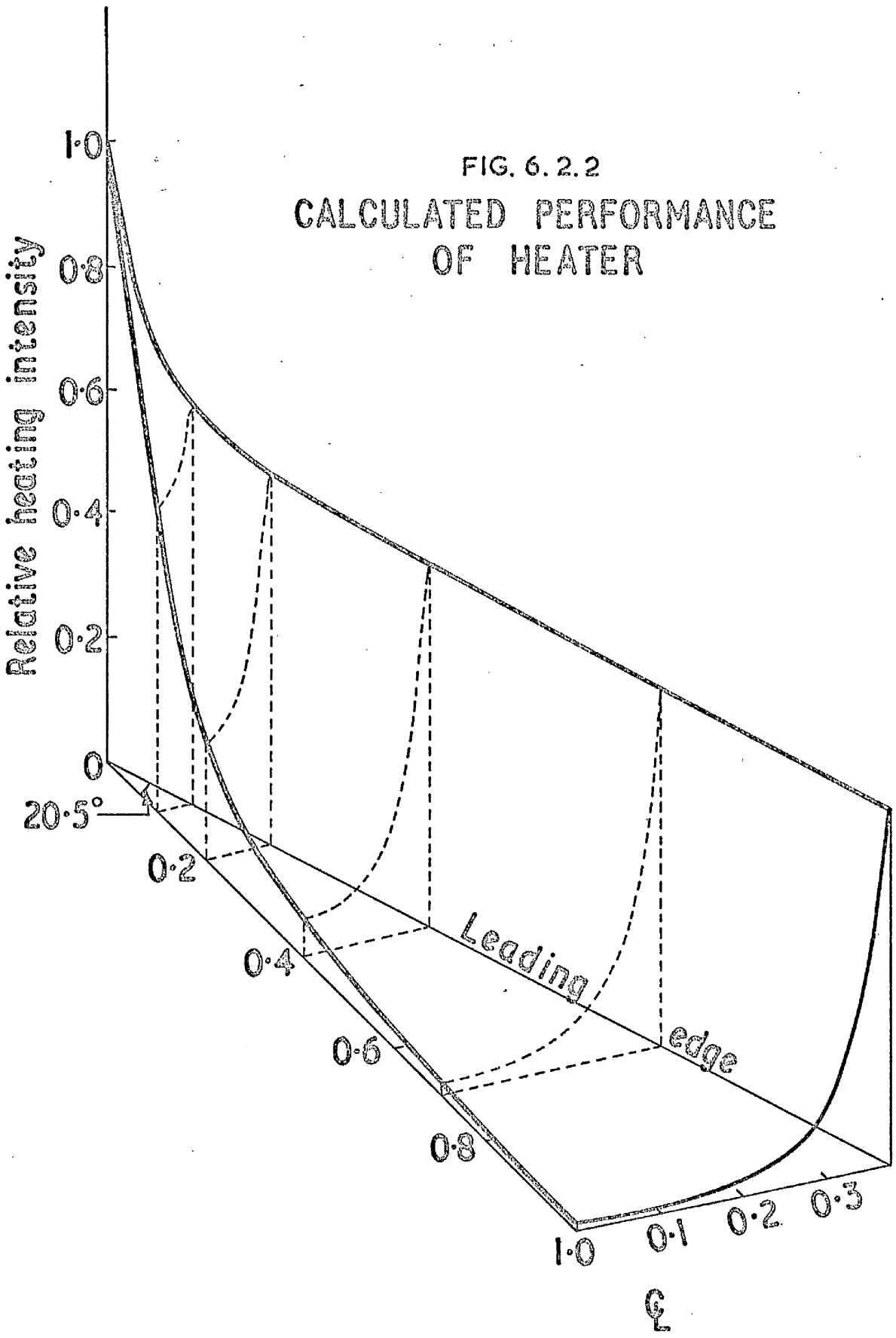

calculated results. If we look at the spanwise variation of heat transfer, we notice that the measured performance has a rounded profile at the leading edge. This is to be expected since we use a 0.152cm. diameter wire instead of a line source of heat. Because the two results are so very similar, we decided to use the theoretical performance of the idealized heater to provide the numerical solutions for comparison with the measured temperature distributions of the model.

6.3. Test Model.

For reasons already outlined in section (4.3) the models are made of stainless steel - Staybrite F.D.P. also designated AISI-321. The model is delta shaped of overall dimensions, chord 20.3cms and span 15.2cms.

Since the mode of heat transfer to the model is by radiation it is imperative that the top surface of the model should have a coefficient of absorptivity close to unity. To satisfy this condition, the top surface is first shot-blasted followed by oxidation in air at 900°C for 60 minutes. The rest of the faces are then highly polished using diamond paste.

For stainless steel (AISI 321) the value of the coefficient of thermal conductivity as given by the manufacturer is $k = 15.9 (1 + 0.00039 \times T^{\circ}C)$ W/m°K. However, very little data is available on the coefficient of total hemispherical emittance. A comprehensive study was, therefore, undertaken to investigate how the emissivity of this particular type of stainless steel varies with temperature and various surface roughness and oxidation conditions. The design of

the equipment is given in reference[35], and the results on stainless steel (AISI 321) in reference 36. The coefficient of emissivity after the model has been shot-blasted and oxidized at 900°C for 60 minutes has been found to be $\epsilon = 0.695\ (1 + 0{,}000288 \times T^{\circ}C)$.

Measurements of temperature are taken with the help of thermocouples embedded in the bottom surface of the model. In all 24 thermocouples are used. Since the delta planform has a plane of symmetry, 21 of the thermocouples are used on one half of the model. The other 3 thermocouples are put on the opposite side to ensure that during testing symmetrical temperature distributions exist at all times. The thermocouples are made out of chromel-alumel wires of 0.012cm. diameter. A batch of these thermocouples has been calibrated against some constantan-eureka thermocouples that were calibrated by The National Physical Laboratory to an accuracy of $\pm 0.2^{\circ}C$.

Two models have been constructed and tested. The first one had a thickness of 1.27cm. and the second one 0.64cm.

A typical test model along with the thermocouple locations is shown in figure (6.3.1).

6.4. Apparatus and experimental procedure.

The experiment is conducted in a high vacuum environment. By using a high vacuum ($\simeq 10^{-5}$ torr) convective heat transfer from the model is eliminated. It has been demonstrated in Appendix B that in addition the heat transfer by free molecular conduction is also negligibly small.

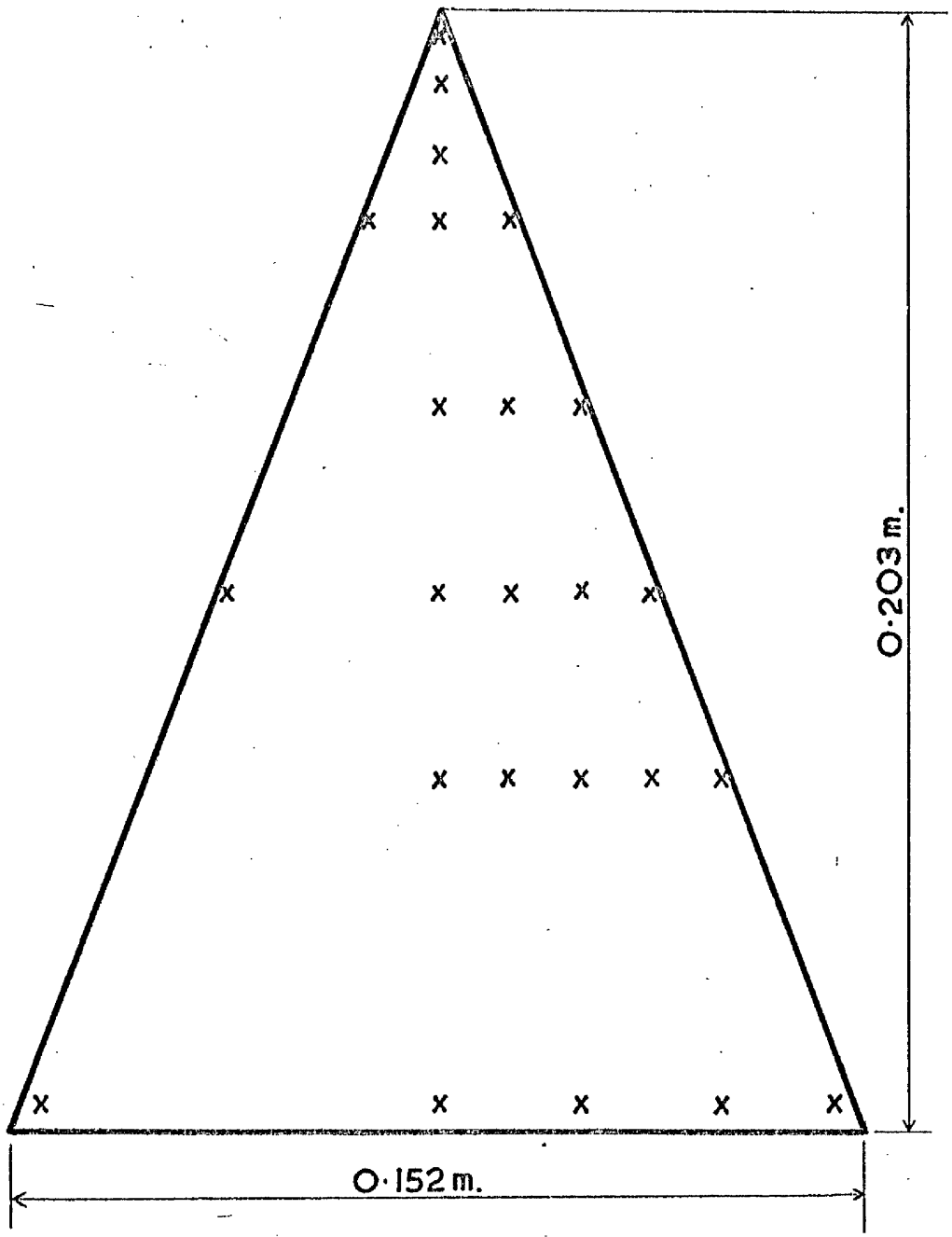

Figure 6.3.1 Test model showing thermocouple locations.

Inside the vacuum chamber the model is supported in position (below the heater) on three pointed ceramic pins. By so isolating the model from the surroundings, the only heat conducted away is either through the ceramic pins or the fine thermocouple wires. However the total amount of heat loss by conduction is so small that it can be ignored.

That leaves radiation as the only means of heat transfer to and from the model. Except the top surface, all the other faces are polished and additional shielding against radiation is provided by placing polished aluminium reflectors parallel to these faces. Thus heat exchange can occur at the top surface only. It receives radiation from the heater wires and the total heat input is considered to be balanced by heat radiated from the top surface to the walls of the chamber. The inside walls of the vacuum chamber are all painted black to prevent any heat from being reflected on to the model. Cooling water is circulated through pipes attached to the outside of the vacuum chamber to keep back-ground radiation to a minimum.

The layout of the heater along with the model and reflector is also shown in figure (6.4.1). The measuring set-up is the same as in figure (4.4.1).

The experimental procedure is the same as has been described in section (4.4). After the working pressures of about $2mN/m^2$ have been achieved, electric power is switched on to the heater. The voltage is increased in definite increments and when steady state temperature distributions have been attained, the readings are noted.

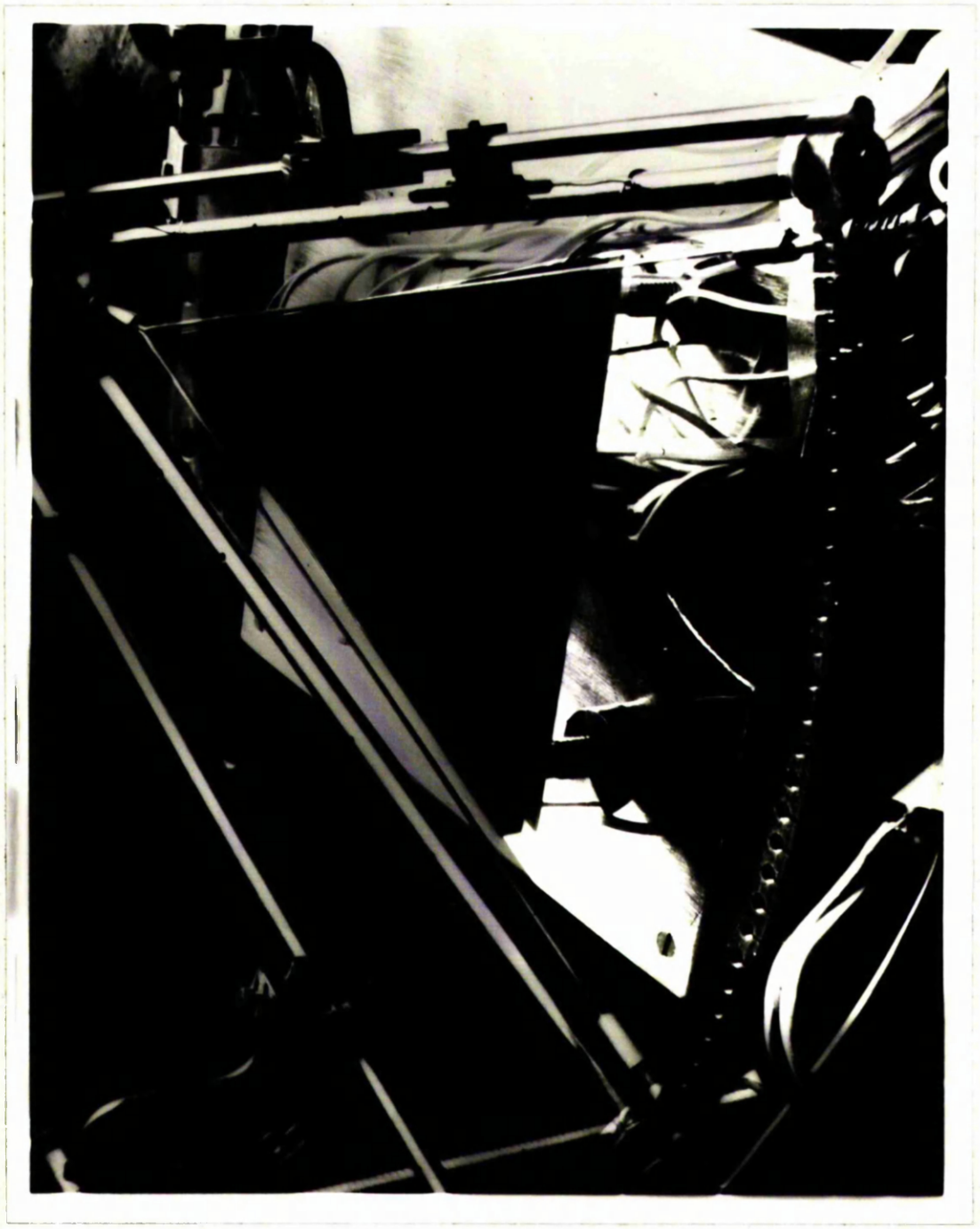

Figure 6.4.1 General arrangement of model and heater.

6.5 Presentation and discussion of results.

For model 1 (1.27cm. thick) the measured temperature values are given in table (6.5.1). At the same power setting the results for model 2 (0.635cm. thick) are provided in table (6.5.2) while table (6.5.3) lists the temperatures measured in this model at a higher power setting. In order to calculate the theoretical temperature distribution we have to subject the mathematical model to the same heat input conditions. We therefore perform numerically,

$$P = 2\iint \epsilon\sigma T^4 . dxdy. \qquad (6.1)$$

where the integration is carried out over the half-delta model, and P represents the total heat dissipated by the top surface of the model. Similarly an integration of the calculated distribution of heat intensities impinging on the model (f(x,y) say, which describes the results presented in figure 6.2.2) gives,

$$P = 2R\iint f(x,y) . dxdy \qquad (6.2)$$

where once again the integration is carried out over the half-delta and R simply represents the appropriate scaling factor. Knowing the measured temperature distribution T(x,y) we can therefore calculate the value of R to compute the theoretical temperature distribution within the model when subjected to the same heat input. Using such a technique for comparing the measured values and the calculated temperature distributions obtained from the three-dimensional heat conduction equation, the results are as presented in figures (6.5.1 - 6.5.3), where we have also given the values of P.

As we pointed out in the discussion on the performance of the

Table 6.5.1 Experimental Results of model 1.

t = 1.27cm. Power dissipated in the heater = 902 watts

Temperature readings in ^{o}K.

Y = y/L → / ↓ X = x/L	0	0.0625	0.125	0.1875	0.25	0.35
0.0125	681.0					
0.0625	676.1					
0.125	673.0					
0.1875	663.7	662.4 662.3 *				
0.35	636.8	636.1	636.5			
0.525	613.4	613.5	614.4	616.0 619.5 *		
0.6875	596.4	595.1	597.1	601.3	605.4	
0.975	579.1	—	579.1	—	590.5	594.9 599.1 *

* values of temperature at the corresponding location given by Y = - Y.

Table 6.5.2 Experimental results of model 2.

t = 0.635cm. Power dissipated in the heater = 908 watts.

Temperature readings in ^{o}K.

$Y = y/L \rightarrow$ / $\downarrow X = x/L$	0	0.0625	0.125	0.1875	0.25	0.35
0.0125	712.2					
0.0625	711.1					
0.125	699.0					
0.1875	682.8	681.8 682.2 *				
0.35	643.2	643.8	645.8			
0.525	609.7	610.3	616.6	621.7 627.2 *		
0.6875	586.2	588.0	592.4	604.5	612.7	
0.975	563.6	—	570.4	—	593.9	613.2 615.8 *

* values of temperature at the corresponding location given by Y = -Y.

Table 6.5.3 Experimental results of model 2.

t = 0.635cm. Power dissipated in the heater = 1095 watts.

Temperature readings in ^{o}K.

Y = y/L → / X = x/L ↓	0	0.0625	0.125	0.1875	0.25	0.35
0.0125	749.2					
0.0625	748.5					
0.125	734.3					
0.1875	716.0	715.0 71[illegible].1 *				
0.35	671.3	671.6	673.9			
0.525	633.6	633.6	641.1	647.7 656.3 *		
0.6875	607.3	608.8	612.4	627.9	637.8	
0.975	582.4	—	589.3	—	626.1	640.3 645.1 *

* values of temperature at the corresponding location given by Y = -Y.

FIG. 6.5.1 MODEL I.

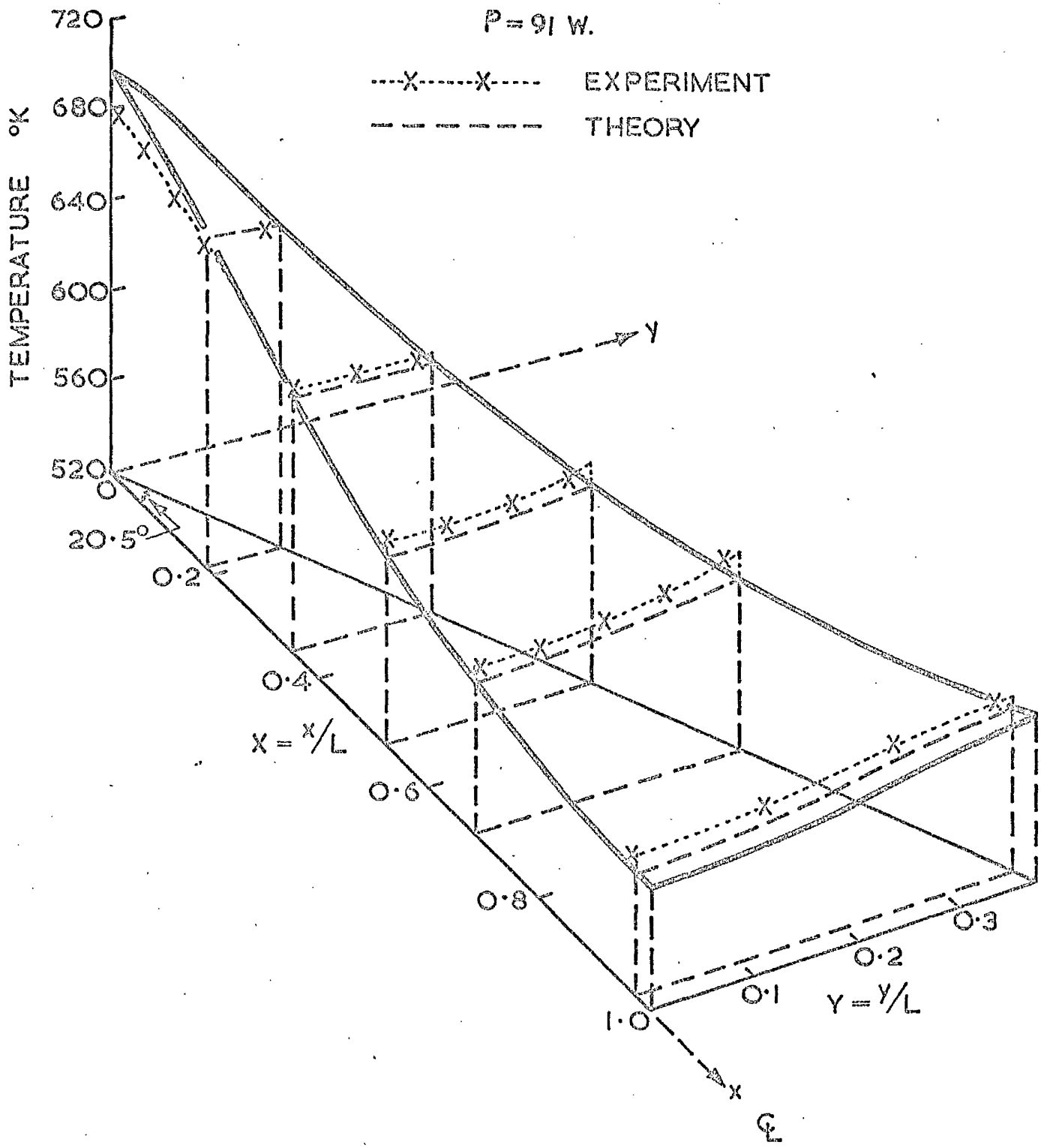

FIG. 6.5.2 MODEL 2.

P = 92 W.

····X·····X····· EXPERIMENT

— — — — — — THEORY

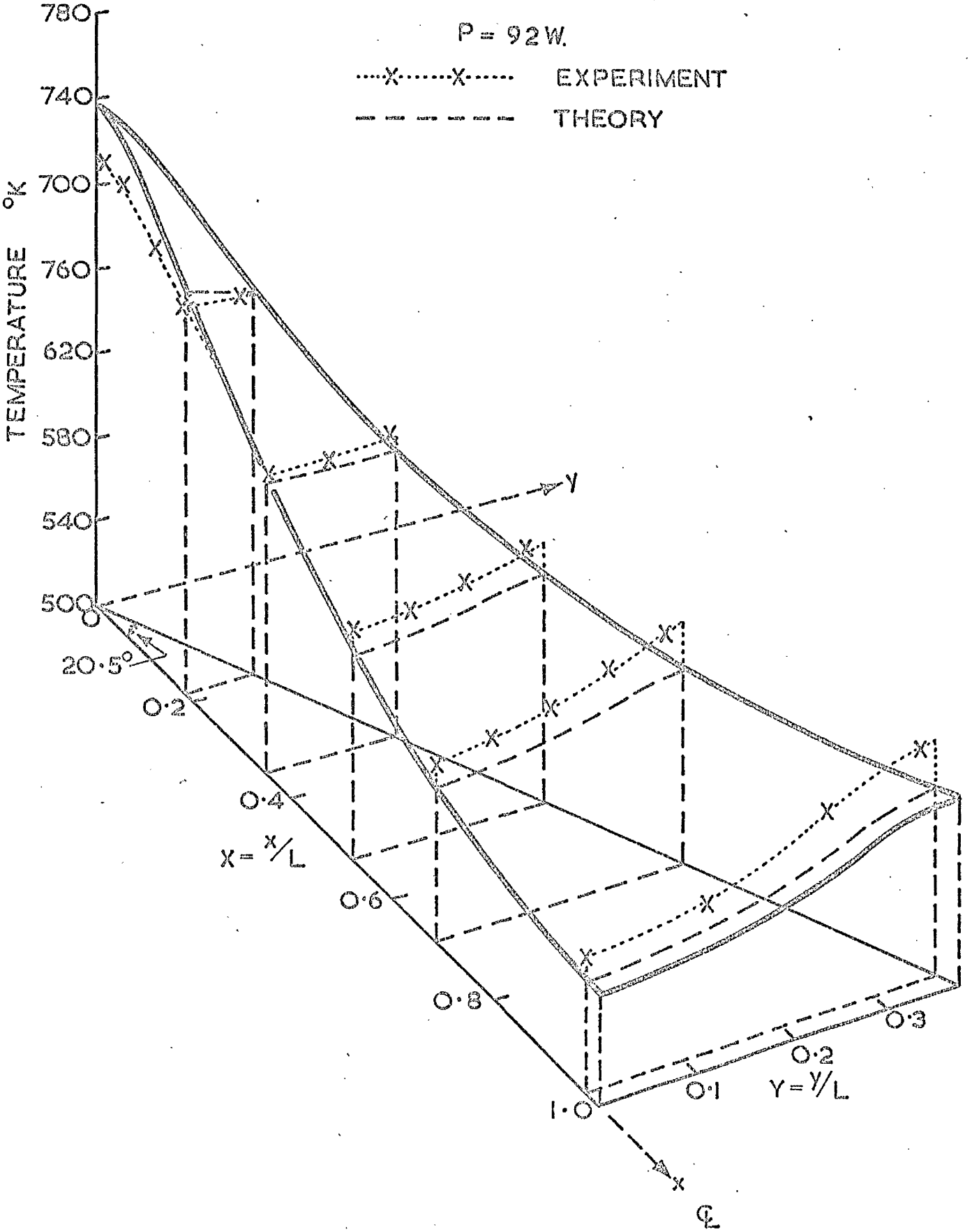

FIG. 6.5.3 MODEL 2.

P = 108 W.

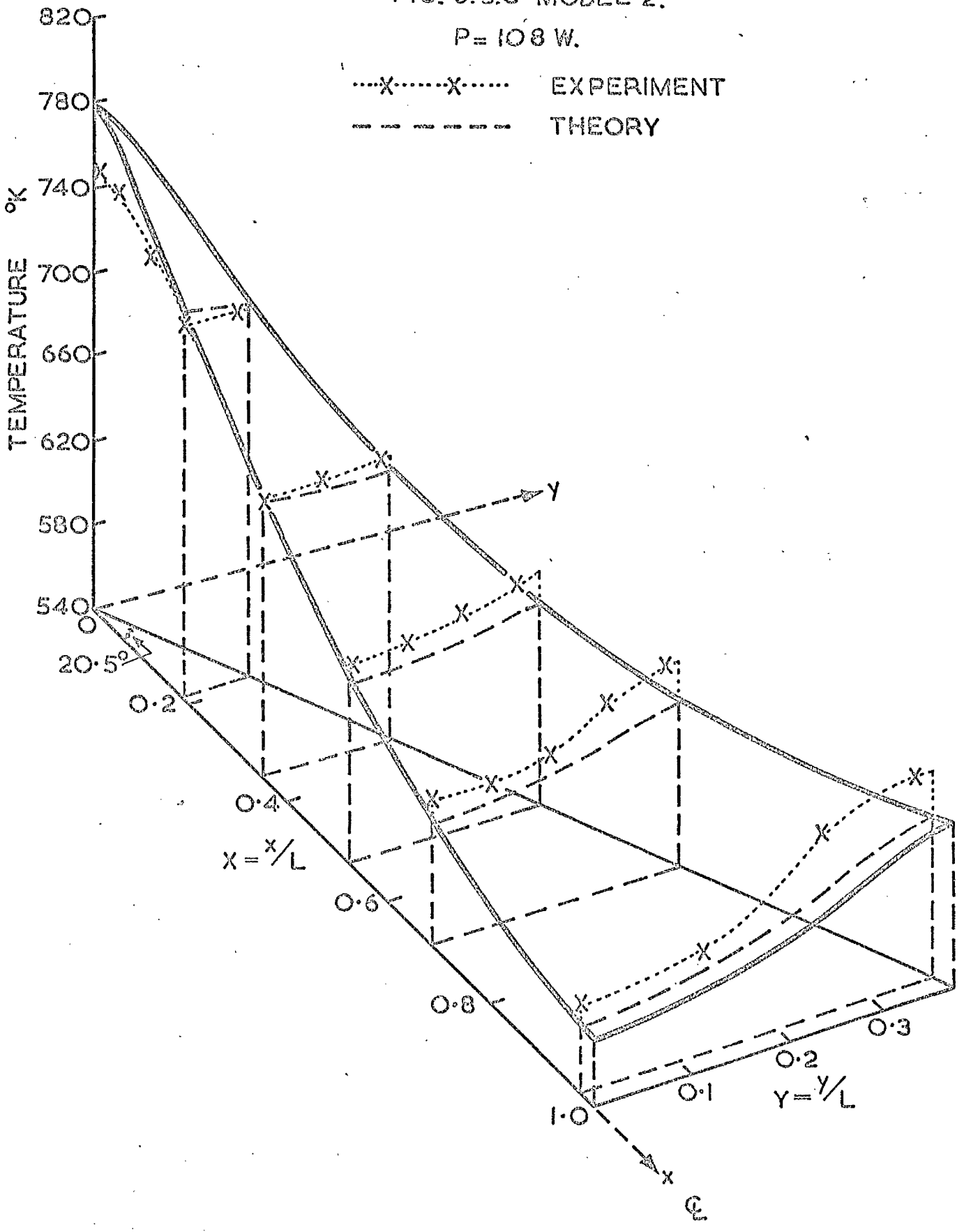

heater, there are discrepencies between the actual heat distribution and the calculated one using the line sources of heat. The two main reasons are non-uniform temperature along the length of the wires and a finite diameter of the actual wires. As a result the measured variation of heat intensity is not quite so steep as the calculated one (both in the x and y direction). This would account for the trends that can be observed from the results plotted in figures (6.5.1 - 6.5.3) where the gradients in the measured temperature distributions are less than those exhibited by the numerical solutions. However, considering all the inherent sources of experimental errors (section 4.4.1), the agreement between experiments and theory is very encouraging with the maximum discrepency being just over 3% (figure 6.5.3).

For the same heat input, model 2 (0.635cm.) displays higher temperature gradients in both the chordwise as well as the spanwise directions as compared with model 1 (1.27cm. thick). Since the model thickness, in this case represents the quantity of conducting material, an increase in thickness as expected produces not only a lower temperature value at the apex but also reduces the temperature gradients everywhere.

In fact, the measured temperature distributions are fairly similar to those predicted by the $x^{-1/2}$ variation of heat input (c.f. figures 5.7.1 and 6.5.1 - 6.5.3). This underlines the findings of the similarity laws which imply that any one parameter does not greatly affect the temperature distribution.

CHAPTER VII

Thermal stresses and stability of the leading edge.

7.1 Introduction

In the design of a high speed wing two main considerations are aerodynamic and structural. The structural requirements are quite often contradictory to the aerodynamic demands on the wing. Hypersonic wings in addition to carrying the normal aerodynamic loads have to withstand extreme rates of heat transfer. Temperature variations in a structure can lead to thermal instability. Various studies have been conducted elsewhere to find out the instability criterion for simple plate geometries under hypothetical temperature variations. In this chapter we investigate the stability of leading edges under purely thermal loads. Particularly we are interested in finding out how the variation of thickness of the leading edge affects the thermal stability.

The thermal stability can be of paramount importance in the design of a hypersonic wing structure. As soon as buckling occurs (even if it is of very small magnitude) the distortion of the surface in general alters the performance of the wing which in itself may be unacceptable but in addition increases the local heat transfer coefficient significantly by a factor of two or more[41]. From every aspect buckling appears to be undesirable and should be designed against.

The author is aware of only two reports (references 42 and 43) that investigate buckling of plates tapered in thickness. Reference (42) is perhaps the only report that calculates the thermal stresses in plates tapered in the chordwise direction and subjected to aerodynamic heat transfer. In calculating the transient temperature

distribution, the report assumes the wing to be instantaneously accelerated to a mach number 3 while the thermal conduction and radiation effects at the leading edge are ignored. However the thermal stresses induced by this temperature distribution were not used to investigate the onset of buckling. On the other hand, reference (43) considers a plate tapered in the spanwise direction and calculates the buckling criterion for a uniform compressive end load.

In this chapter we use the temperature distributions of chapter III to calculate the thermal stresses in infinite plates (two-dimension) for a family of trapezoidal sections (longitudinally) under the influence of a given heat flux parameter H_o. We suggest an appropriate buckle shape and conduct a preliminary investigation into the onset of thermal buckling. In particular we wish to investigate the effect of heat conduction within the material close to the nose of the wing on the thermal stress levels at the leading edge and on the onset of thermal buckling.

7.2 Thermal stress.

When a uniform structure is heated with the heating rate variable over the surface, the temperature distribution within the body varies from point to point. As a rule the resulting natural thermal expansion of the various parts of the structure is geometrically incompatible. For the integrity of the structure, the compatibility of deformations must be re-established automatically by some physical phenomenon. This phenomenon is the development of internal stresses which cause additional deformations of a sufficient magnitude to preserve the

continuity of the structure. These stresses are known as thermal stresses. Thermal stresses can be caused by other factors but we need not go into the details as these are beyond the scope of this investigation.

Close to the leading edge, we have calculated (chapter III) temperature distributions which may be such as to give rise to very high thermal stresses. Since these thermal stresses are induced by temperature gradients which in turn depend upon the heat conduction within the material, we can expect the thermal stresses to be influenced by the thermal conductivity of the material.

We limit our analysis to two-dimensional plates (infinite span) of variable thickness. The assumptions made in the formulation of the equations are as follows:

1. The plate is perfectly elastic.
2. The plate is freely supported along all the edges.
3. The coefficients of thermal expansion (α) and Young's modulus of elasticity (E) are constant.
4. The temperature variation in the plate is one-dimensional, i.e. a function of the chordwise distance only.
5. The thickness of the plate is small and the thickness distribution is symmetrical about the x - axis.

The coordinate axes system and some of the notation used in the following analysis is indicated in figure5.2.1. In this chapter we have replaced the symbols t_o and t_L by h_o and H respectively, to define the nose and rear edge thicknesses.

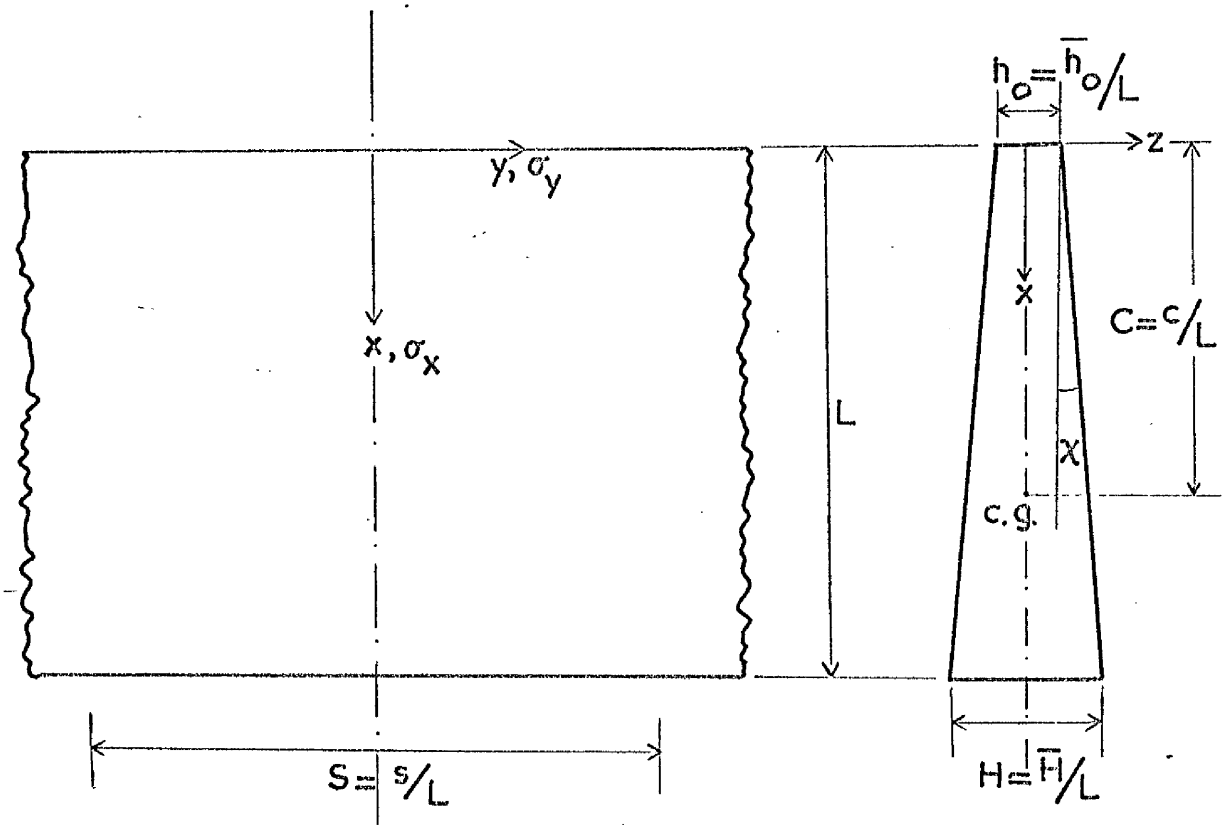

Figure 7.2.1 Notation and co-ordinate system

We consider an infinite plate of unit width, by taking the basic unit of length as L and non-dimensionalising all the other measures of length by dividing by L. As we have shown in Chapter III, for two-dimensional plates it is reasonable to assume that

$$T = f(x) \qquad (7.1)$$

Therefore for an infinite plate freely supported on all edges the following relations must always hold,

$$\left.\begin{aligned} \sigma_x = \tau_{xy} = 0 \\ \text{and in general } \sigma_y = f(x) \neq 0 \end{aligned}\right\} \qquad (7.2)$$

where σ_x, σ_y are the normal stresses in the x and y direction

respectively and are positive for tensile stresses, τ_{xy} represents the shear stress.

Trapezoidal variations of thickness (h) in the notation of figure (7.2.1) can be written as

$$h = 2X \tan\chi + h_o \qquad (7.3)$$

$$\text{with } H = 2\tan\chi + h_o$$

$$\text{or } \tan\chi = \frac{H - h_o}{2} \qquad (7.4)$$

The centroid of the trapezoidal section occurs at a distance x = c where

$$C = {}^{c}/_{L} = \frac{h_o + 2H}{3(h_o + H)} \qquad (7.5)$$

Using reference (44), we can now write equation for thermal stress σ_y as

$$\sigma_y/\alpha E = -T + \frac{\int_o^l Th.dX}{\int_o^l h.dX} + (X-C)\frac{\int_o^l Th(X-C).dX}{\int_o^l h(X-C)^2.dX} \qquad (7.6)$$

Equation (7.6) is valid for temperature distributions which are functions of x only and where the thickness is symmetrical about the plane z = 0.

Substituting equation (7.3) into (7.6) gives on simplification

$$\sigma_y/\alpha E = -T + \frac{\int_o^l T(2X\tan\chi+h_o).dX}{\tan\chi+h_o} + \frac{(X-C)\int_o^l T(2X\tan\chi+h_o)(X-C).dX}{\tan\chi(\frac{1}{2} - \frac{4}{3}C + C^2) + h_o(\frac{1}{3} - C+C^2)} \qquad (7.7)$$

It is a straightforward exercise to show that for a constant temperature (T = constant), equation (7.7) gives $\sigma_y = 0$. After a lot of algebra, even when the temperature distribution is a linear function of x, we get $\sigma_y = 0$ for a trapezoidal section.

The temperature distribution in leading edge models obtained in Chapter III can be expressed by a polynominal series. A sixth-order polynomial has been found to be sufficient to represent analytically the temperature distributions for all thicknesses varying from a wedge to a slab section. In general we can therefore write

$$T = a_o + a_1X + a_2X^2 + a_3X^3 + a_4X^4 + a_5X^5 + a_6X^6 \qquad (7.8)$$

with $0 \leqslant X \leqslant 1$.

Substituting equation (7.8) into (7.7) and integrating, the resulting equation can be reduced to the following expression.

$$\sigma_y/\alpha E = \frac{-1}{(h_o^2+4h_oH+H^2)} \left[\frac{a_2}{10}(h_o^2+6h_oH+3H^2) + \frac{a_3}{10}(h_o^2+7h_oH+4H^2) + \right.$$

$$\left. \frac{3a_4}{35}(h_o^2+8h_oH+5H^2) + \frac{a_5}{14}(h_o^2+9h_oH+6H^2) + \frac{5a_6}{84}(h_o^2+10h_oH+7H^2)\right]$$

$$+ \frac{12X}{(h_o^2+4h_oH+H^2)} \left[\frac{a_2}{30}(2h_o^2+10h_oH+3H^2) + \frac{a_3}{40}(2h_o^2+12h_oH+4H^2) + \right.$$

$$\left. \frac{2a_4}{105}(2h_o^2+14h_oH+5H^2) + \frac{5a_5}{336}(2h_o^2+16h_oH+6H^2) + \frac{a_6}{84}(2h_o^2+18h_oH+7H^2)\right]$$

$$- a_2X^2 - a_3X^3 - a_4X^4 - a_5X^5 - a_6X^6. \qquad (7.9)$$

Since the structure has no external loads, the system of stresses is self-equilibriating and therefore must satisfy the relation

$$\int_o^1 \sigma_y . h . dX = 0 \qquad (7.10)$$

Equation (7.9) can be proved to satisfy the above criterion.

We now consider a specific example to demonstrate how the heat conduction plays an important role in lowering the magnitude of stress in plates tapered in thickness. For a given heat input parameter (H_o = 2700 $W/m^{3/2}$) we calculate, first of all, the appropriate temperature distributions in several plate geometries (a family of trapezoidal sections) using a typical stainless steel model of chord 15.2cms. For stainless steel - Staybrite FCB as explained in Chapter IV, the appropriate values of k and ϵ are k = 15.9 x (1 + 0.00039 x T^oC) W/m^oK and ϵ = 0.735 (1 + 0.000294 x T^oC). This corresponds roughly to a value of the non-dimensional parameter τ_o = 12.3 x t_o/L. (refer to equation 3.25 where t_o is the nose thickness). Table (7.2.1) lists the coefficients of equation (7.8) that are used to determine the stress σ_y from equation (7.9). In figure (7.2.2) we plot the variation of σ_y with X(x/L) for several trapezoidal sections (all having H = 0.0833) having as the two extremes a slab and a wedge section. In all the cases the magnitude of the stress can only be differentiated from one another close to the leading edge.

Figure (7.2.3) shows how the influence of nose thickness of the trapezoidal sections on the temperature distribution and also on the stress at X = 0 ($\sigma_{y_{x=0}}$). In reducing h_o from 0.0833 to 0.000167, the absolute nose temperature is increased by about 35% whereas the stress has increased by a factor of over 30. Figure (7.2.3) shows the values of $\sigma_{y_{x=0}}$ for two plates of constant thickness in nondimensional values, 0.0207 and 0.00833. Although a constant value of τ_o gives an identical temperature distribution for a flat plate

Table 7.2.1 The values of coefficients of the polynomials defining temperature and stress distributions.

Coefficients	Slab h_o=H=0.0833	Trapezoid h_o=0.0417 H=0.0833	Trapezoid h_o=0.00833 H=0.0833	Trapezoid h_o=0.00167 H=0.0833	Wedge h_o=0.000167 H=0.0833	Slab h_o=H=0.0417	Slab h_o=H=0.00833
a_o	784.4	848.9	894.8	973.1	1068.0	848.9	894.8
a_1	-80.0	-318.8	-736.2	-2130.1	-4180.9	-318.8	-736.2
$b_o/\alpha E$	-9.7	-54.0	-107.7	-206.3	-309.2	-40.4	-76.5
$b_1/\alpha E$	-41.9	140.1	556.4	1968.4	4028.0	117.5	507.2
$a_2=-b_2/\alpha E$	-706.1	-1126.5	-18.2	7854.0	21578.3	-1126.5	-18.2
$a_3=-b_3/\alpha E$	2116.4	4942.0	3797.8	-17661.5	-59546.9	4942.0	3797.8
$a_4=-b_4/\alpha E$	-2930.2	-8014.2	-7985.0	22653.6	87170.6	-8014.2	-7985.0
$a_5=-b_5/\alpha E$	2067.1	6096.5	6805.2	-15191.1	-64005.0	6096.5	6805.2
$a_6=-b_6/\alpha E$	-580.1	-1784.3	-2124.2	4131.5	18544.9	-1784.3	-2124.2

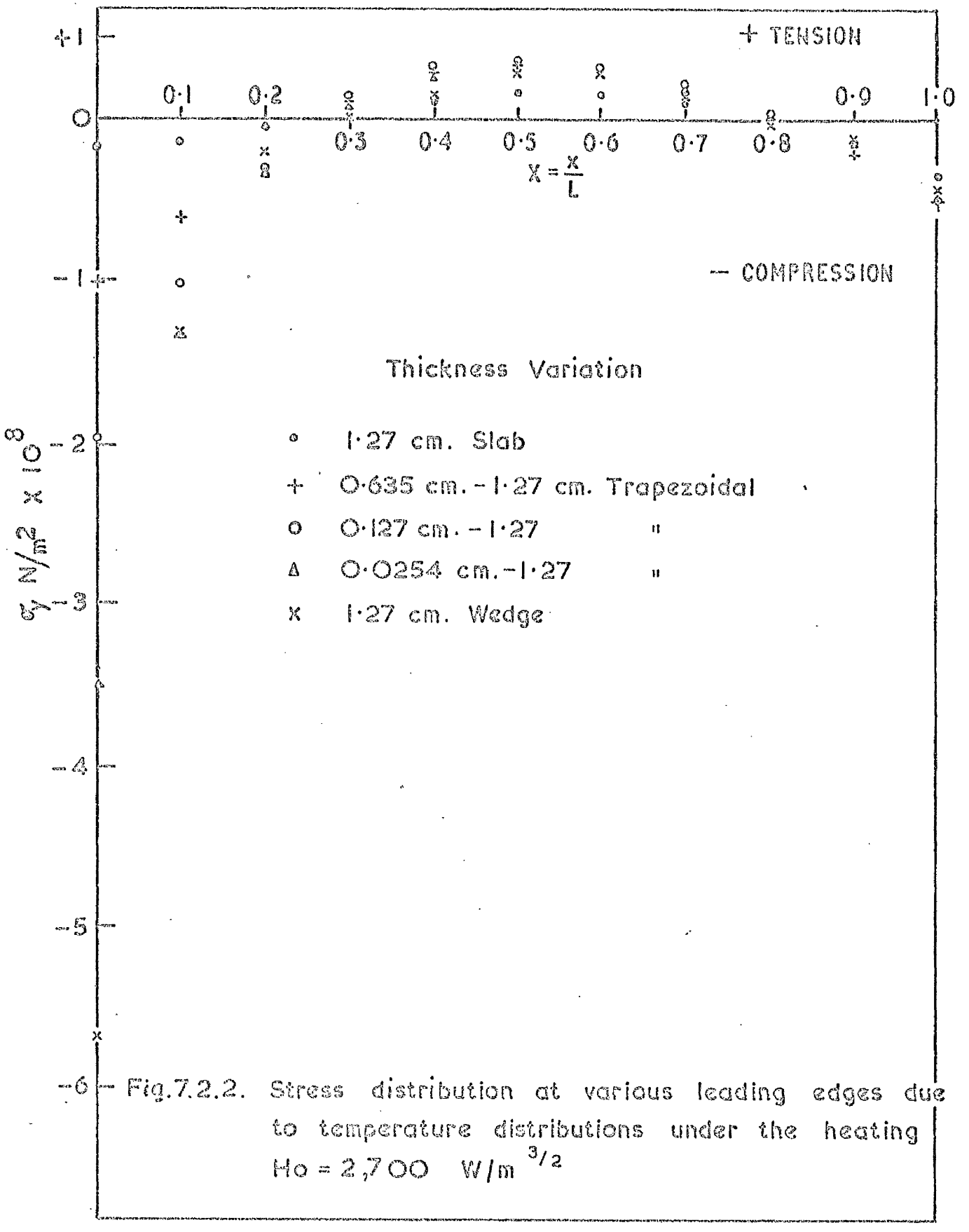

Fig.7.2.2. Stress distribution at various leading edges due to temperature distributions under the heating Ho = 2,700 $W/m^{3/2}$

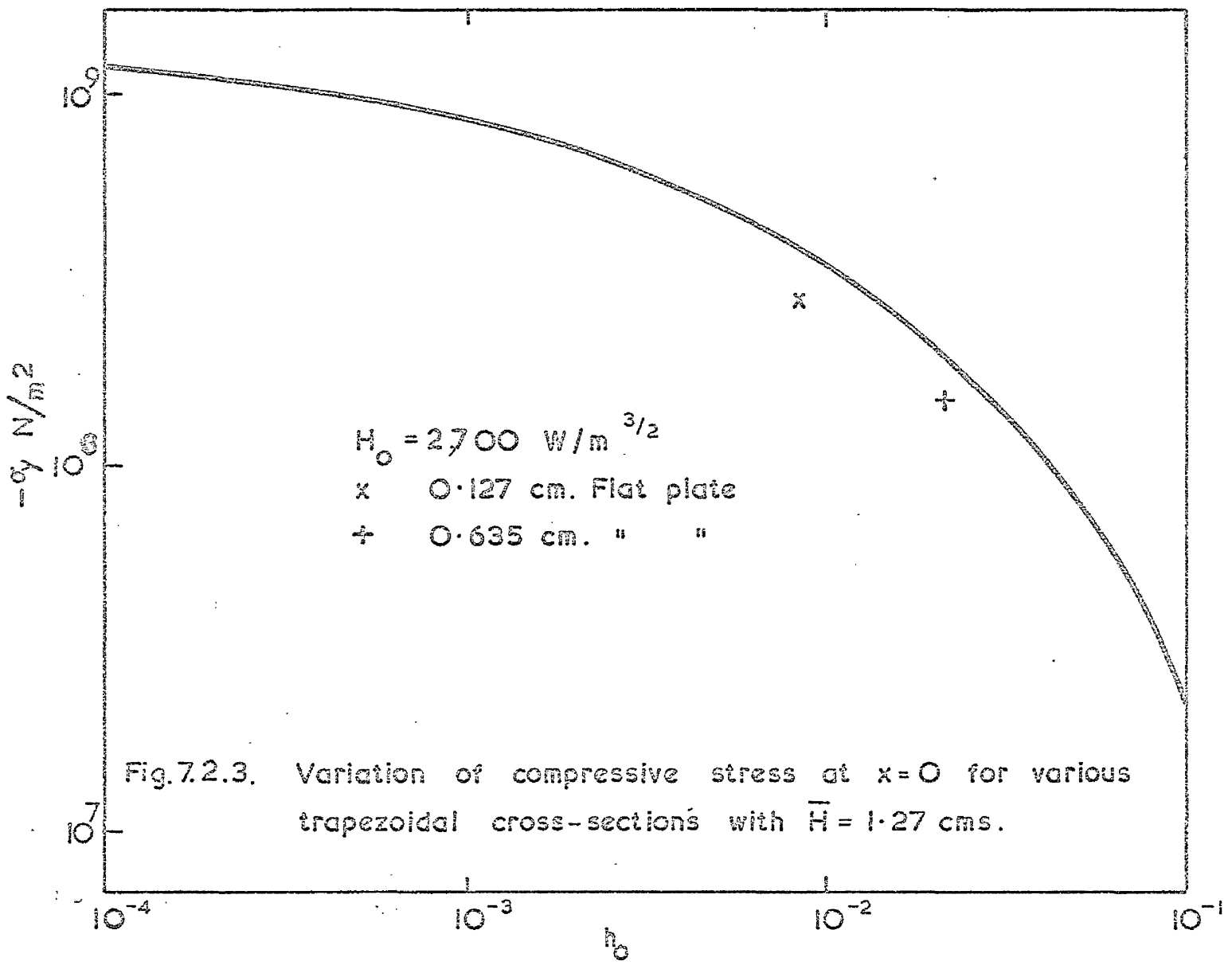

Fig. 7.2.3. Variation of compressive stress at x = 0 for various trapezoidal cross-sections with $\bar{H}$ = 1·27 cms.

and a trapezoidal section provided they have the same nose thickness, the value of $\sigma_{y_{x=0}}$ shows a decrease of about 30% as compared with the trapezoidal section.

Of course when the extra material from the trapezoidal section is taken away to give a plate of the same nose thickness, the whole of the stress pattern is essentially redistributed. For a nose thickness of 0.00833, figure (7.2.4) shows the variations in the two stress distributions. The improvement in the value of the stress at the nose is seen to occur at the expense of the stress level at X = 1.

One interesting observation that can be made from equation (7.9) is that the coefficients a_o and a_1(of equation 7.8) do not appear in it. Hence, we can conclude that a constant or even a linear temperature distribution can never give rise to thermal stress in trapezoidally varying plate sections.

7.3. Thermal buckling.

If the thermal stresses (calculated in the last section) are allowed to increase indefinitely, when their magnitude increases above a given critical value, the conducting plate will suddenly buckle. Buckling is characterised by disproportionately large deformations being produced at slight increases in the thermal stress levels. These deformations (w) take place normal to the plane of the plate in which the temperature gradients have induced compressive stresses.

The "exact" method of investigating such stability problems is to solve the equation for the buckled plate, which is a fourth order partial differential equation. For thermal stresses (σ_y) only, the form of the equation from Timoshenko[45] is

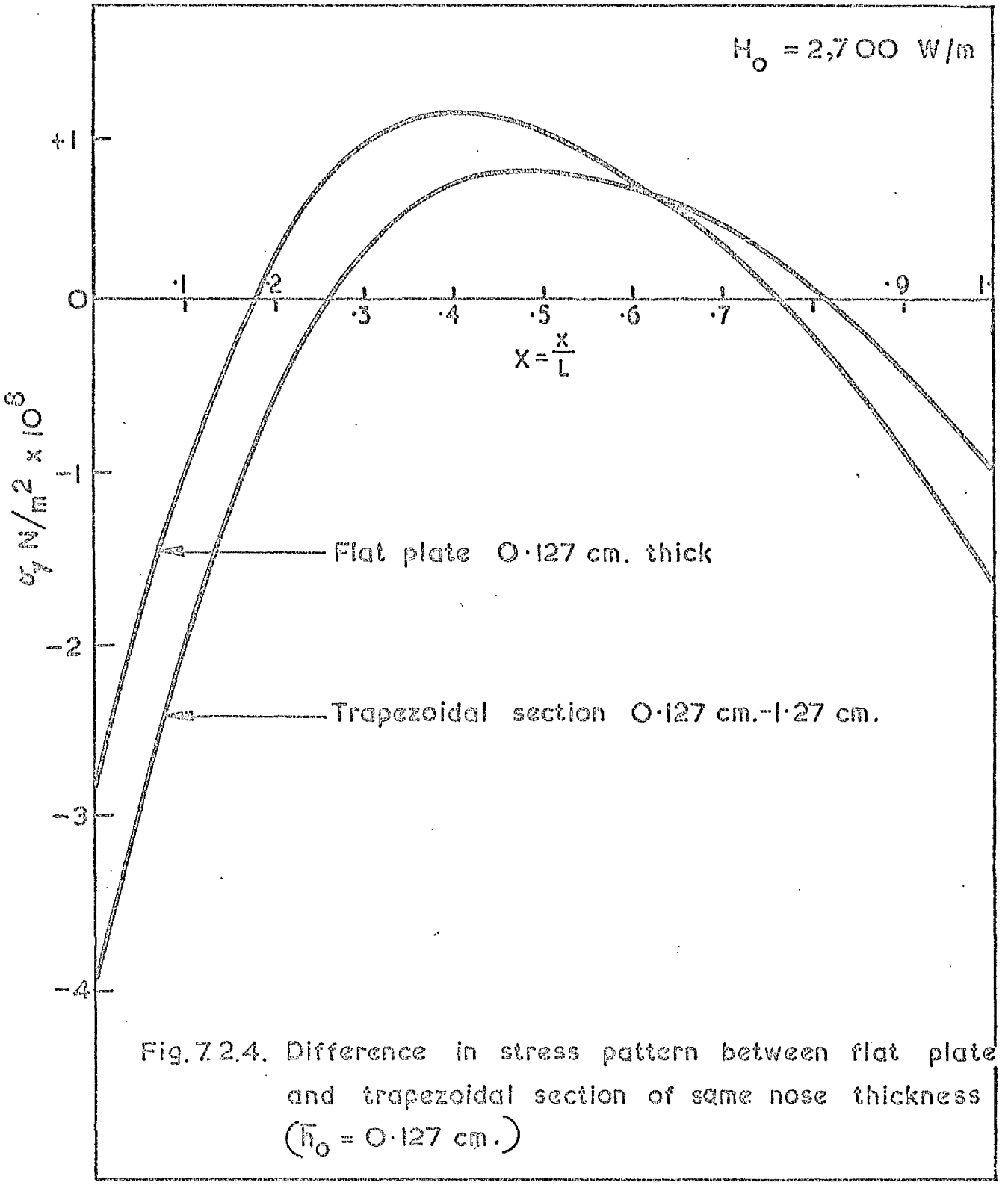

Fig. 7.2.4. Difference in stress pattern between flat plate and trapezoidal section of same nose thickness ($\bar{h}_o$ = 0·127 cm.)

$$\frac{\partial^4 w}{\partial x^4} + 2\frac{\partial^4 w}{\partial x^2 \partial y^2} + \frac{\partial^4 w}{\partial y^4} = \frac{12(1-\nu^2)}{E.\ h^3}\left(\sigma_y . h. \frac{\partial^2 w}{\partial y^2}\right) \qquad (7.11)$$

where w defines the buckled shape. Except for very simple cases this equation is difficult to solve because it requires the knowledge of the term w.

The energy method also can be used in investigating buckling of plates. This method is especially useful in those cases where a solution of equation (7.11) is difficult to obtain. We assume that the plate undergoes some small lateral bending consistent with given boundary conditions. For pure thermal stresses we need consider only the strain energy of bending (V) and the corresponding work done by the thermal "loads" (U). The onset of buckling can be predicted from the relation, $U = V$ (7.12)

With the help of reference (45), we now derive the expressions for U and V. In general, we can write that for an element of volume d x dy dz the change in strain energy per unit volume is

$$\delta V = \frac{1}{2}\left(\sigma_x . \epsilon_x + \sigma_y . \epsilon_y + \tau_{xy} . \gamma_{xy}\right) \qquad (7.13)$$

Therefore the total strain energy of the plate is obtained by integrating over the whole of the plate

$$V = \frac{1}{2}\iiint\left(\sigma_x . \epsilon_x + \sigma_y . \epsilon_y + \tau_{xy} . \gamma_{xy}\right) dx dy dz \qquad (7.14)$$

where ϵ_x, ϵ_y and γ_{xy} are the strain components, calculated on the basis of the assumptions of plane stress and that sections which are plane and perpendicular to the middle surface ($z = 0$) remain so after bending. Due to the stretching of the fibres parallel to the neutral surface, we get

$$\epsilon_x = -z.\frac{\partial^2 w}{\partial x^2} \qquad (7.15)$$

$$\epsilon_y = - z.\frac{\partial^2 w}{\partial y^2} \qquad (7.16)$$

$$\gamma_{xy} = - 2z.\frac{\partial^2 w}{\partial x \partial y} \qquad (7.17)$$

where the terms $\frac{\partial^2 w}{\partial x^2}$ and $\frac{\partial^2 w}{\partial y^2}$ are in fact the curvatures of the plate.

The corresponding stresses in the plate are

$$\sigma_x = \frac{E}{1 - \nu^2} (\epsilon_x + \nu \epsilon_y) \qquad (7.18)$$

$$\sigma_y = \frac{E}{1 - \nu^2} (\epsilon_y + \nu \epsilon_x) \qquad (7.19)$$

$$\tau_{xy} = \frac{E}{2(1 + \nu)} \gamma_{xy} = \frac{E}{2(1 - \nu^2)} (1 - \nu) \gamma_{xy} \qquad (7.20)$$

Substituting equations (7.15 - 7.20) into the expression for the total strain energy of the plate (equation 7.14) gives

$$V = \frac{1}{2}\iiint \left[\frac{E}{1-\nu^2} \left(-z.\frac{\partial^2 w}{\partial x^2} - \nu z.\frac{\partial^2 w}{\partial y^2}\right)\left(-z.\frac{\partial^2 w}{\partial x^2}\right) + \right.$$

$$\frac{E}{1-\nu^2} \left(-z.\frac{\partial^2 w}{\partial y^2} - \nu z.\frac{\partial^2 w}{\partial x^2}\right)\left(-z.\frac{\partial^2 w}{\partial y^2}\right) +$$

$$\left. \frac{E}{1-\nu^2} \left(-2z\frac{(1-\nu)}{2}.\frac{\partial^2 w}{\partial x \partial y}\right)\left(-2z.\frac{\partial^2 w}{\partial x \partial y}\right)\right] dxdydz. \qquad (7.21)$$

On re-arranging the terms,

$$V = \frac{E}{2(1-\nu^2)} \iiint z^2 \left(\left(\frac{\partial^2 w}{\partial x^2} + \frac{\partial^2 w}{\partial y^2} \right)^2 - 2(1-\nu)\left[\frac{\partial^2 w}{\partial x^2}.\frac{\partial^2 w}{\partial y^2} - \left(\frac{\partial^2 w}{\partial x \partial y}\right)^2 \right] \right) dxdydz \qquad (7.22)$$

Similarly for the work done by thermal loads (self-equilibriating) we can write from equation (7.3) that

$$U = \iiint (\sigma_y . \epsilon_y) dxdydz \qquad (7.23)$$

since for an infinite plate $\sigma_x = \tau_{xy} = 0$.

The component of strain is obtained from the stretching of the neutral surface and it is,

$$\epsilon_y = \frac{1}{2}\left(\frac{\partial w}{\partial y}\right)^2 \qquad (7.24)$$

Substituting into equation (7.23) gives

$$U = \frac{1}{2}\iiint \sigma_y \cdot \left(\frac{\partial w}{\partial y}\right)^2 dxdydz \qquad (7.25)$$

where σ_y is positive for a tensile stress.

The total potential energy of the plate is therefore simply U + V.

The next step is to assume an appropriate buckled shape of the plate. In our analysis we have a trapezoidal variation of the thickness of the plate coupled with the stress distributions of figure (7.2.2) which exhibit a higher level of stress at the nose as compared with the rest of the plate. It seems reasonably therefore to assume that the plate would buckle into sine waves in the y-direction where the magnitude of the deformation would decay in some form in the x - direction. We, therefore, suggest the following buckle shape as appropriate under the conditions that we seek a solution,

$$w = \sum_{n=1}^{\infty} w_n \cdot \cos\frac{n\pi}{S} Y \cdot e^{-BX} \qquad (n = 1,2,3.....\infty) \qquad (7.26)$$

We shall from here onwards adopt the non-dimensional notation already introduced in the last section. The constant B determines the rate of decay of the sine wave over the region X = 0,1. The value

of B can vary from 0 (giving the Euler mode of buckling) to ∞. The coefficient w_n is a constant providing the magnitude of the buckled shape for the given number of waves. The function for has to satisfy the boundary conditions. For infinite plates, the integration need only be carried out over half the wave-length ($-\frac{S}{2}$ to $\frac{S}{2}$) of the fundamental sine wave (n = 1). Hence for a freely supported plate along the edges $Y = -\frac{S}{2}$ and $Y = \frac{S}{2}$, equation (7.26) complies with the condition that w must be zero. Along the edges X = 0,1 the plate can have some finite deflections.

In order to calculate the work done by thermal stresses (U_i) an analytical expression for σ_y is needed. Thermal stresses were calculated using a sixth order polynomial for the temperature distribution. It is evident that in turn equation (7.9) is also a sixth order polynomial in X describing the variation of σ_y. We therefore write for a given H_o that

$$\sigma_y = b_o + b_1X + b_2X^2 + b_3X^3 + b_4X^4 + b_5X^5 + b_6X^6 \qquad (7.27)$$

Unfortunately, for a given model, an increase in the value of H_o does not produce a proportional increase in σ_y. We make one further assumption that

$$\sigma_y = \lambda(b_o + b_1X + b_2X^2 + b_3X^3 + b_4X^4 + b_5X^5 + b_6X^6) \qquad (7.28)$$

which is, in general, not strictly true but may be used as an approximation to indicate by what factor (λ) can the level of the stress function σ_y be increased before the onset of thermal buckling. An iterative process can then lead to the determination of the critical value of H_o that would initiate buckling for a given plate geometry.

We are now in a position to use equations (7.22) and (7.25) to calculate the potential energy of a plate which has a trapezoidal variation of thickness and is subjected to aerodynamic heating. Substituting equations (7.3), (7.26) and (7.28) into equations (7.22) and (7.25) gives on simplification,

$$V = \sum_{n=1}^{\infty} \frac{EL w_n^2}{24(1-\nu^2)} \iint (2X\tan\chi + h_o)^3 \, e^{-2BX} \left[\cos^2 \frac{n\pi Y}{S} \; B^2 - \frac{n^2\pi^2}{S^2} + 2(1-\nu).\frac{B^2 n^2 \pi^2}{S^2} \right] dX dY \qquad (7.29)$$

and

$$U = \sum_{n=1}^{\infty} \lambda L w_n^2 \frac{n^2\pi^2}{2S^2} \iint \left[(b_o + b_1 X + b_2 X^2 + b_3 X^3 + b_4 X^4 + b_5 X^5 + b_6 X^6) \right.$$

$$\left. (2X\tan\chi + h_o) \sin^2 \frac{n\pi Y}{S} \, e^{-2BX} \right] dX dY \qquad (7.30)$$

where $U = \lambda U_i$.

These two equations are integrated over the interval $X = 0,1$ and $Y = -\frac{S}{2}, \frac{S}{2}$. Unfortunately, the equations become extremely lengthy and after a lot of algebra and re-arranging of terms can be expressed as follows:

$$V = \sum_{n=1}^{\infty} \frac{ELw_n^2 S}{48B(1-\nu^2)} \left(h_o^3\left(1 - e^{-j}\right) + 6h_o^2 \tan\chi \left[\frac{1}{j} - e^{-j}\left(1 + \frac{1}{j}\right)\right] \right.$$

$$+ 12h_o \tan^2\chi \left[\frac{2}{j^2} - e^{-j}\left(1 + \frac{2}{j} + \frac{2}{j^2}\right)\right]$$

$$\left. + 8\tan^3\chi \left[\frac{6}{j^3} - e^{-j}\left(1 + \frac{3}{j} + \frac{6}{j^2} + \frac{6}{j^3}\right)\right]\right)$$

$$\left[\frac{1}{2}\left(B^2 - \frac{n^2\pi^2}{S^2}\right) + 2(1-\nu)\frac{B^2 n^2 \pi^2}{S^2}\right] \qquad (7.31)$$

where $j = 2B$, and

$$U = \sum_{n=1}^{\infty} \lambda Lw_n^2 S n^2 \pi^2 / 8BS^2 \left(h_o b_o (1 - e^{-j}) + (h_o b_1 + 2b_o \tan\ )\left[\frac{1}{j} - e^{-j}\left(1+\frac{1}{j}\right)\right] \right.$$

$$+(h_o b_2 + 2b_1 \tan\chi)\left[\frac{2}{j^2} - e^{-j}\left(1 + \frac{2}{j} + \frac{2}{j^2}\right)\right]$$

$$\left. +(h_o b_3 + 2b_2 \tan\chi)\left[\frac{6}{j^3} - e^{-j}\left(1 + \frac{3}{j} + \frac{6}{j^2} + \frac{6}{j^3}\right)\right]\right\} \qquad (7.32)$$

$$+(h_o b_4 + 2b_3 \tan\chi)\left[\frac{24}{j^4} - e^{-j}\left(1 + \frac{4}{j} + \frac{12}{j^2} + \frac{24}{j^3} + \frac{24}{j^4}\right)\right]$$

$$+(h_o b_5 + 2b_4 \tan\chi)\left[\frac{120}{j^5} - e^{-j}\left(1 + \frac{5}{j} + \frac{20}{j^2} + \frac{60}{j^3} + \frac{120}{j^4} + \frac{120}{j^5}\right)\right]$$

$$+(h_o b_6 + 2b_5 \tan\chi)\left[\frac{720}{j^6} - e^{-j}\left(1 + \frac{6}{j} + \frac{30}{j^2} + \frac{120}{j^3} + \frac{360}{j^4} + \frac{720}{j^5} + \frac{720}{j^6}\right)\right]$$

$$\left. + 2b_6 \tan\chi \left[\frac{5040}{j^7} - e^{-j}\left(1 + \frac{7}{j} + \frac{42}{j^2} + \frac{210}{j^3} + \frac{840}{j^4} + \frac{2520}{j^5} + \frac{5040}{j^6} + \frac{5040}{j^7}\right)\right]\right)$$

The critical value of λ is obtained from the expression

$$\lambda = \frac{V}{U_l} \qquad (7.33)$$

For the calculation of λ it is necessary to find, in each particular case, the unknown constants in the expression for w which make expression (7.33) a minimum, i.e. the derivative of the fraction (7.33) with respect to that particular constant must be zero[45].

With infinite plates under compression it has been found[45] that by taking the first term only (n = 1) from the infinite series (as in equation 7.26) one can obtain reasonable estimates of the critical values of the stress sufficient to initiate buckling. For infinite plates the first mode of buckling is also such that the plate buckles into sinusoidal waves of wave-length 2L. In this preliminary investigation we shall further assume that

$$S = L \qquad (7.34)$$

and present the values of λ obtained with the first term only of the series (equation 7.26) included.

Using the stress distributions that we calculated in the last section using equation (7.9), we investigate the critical values of λ. Table (7.2.1) also lists the coefficients of equation (7.27) that are obtained for the various cross-sections subjected to aerodynamic heating given by $H_o = 2700\ W/m^{3/2}$. ($\tau_o \simeq 12.3 \times t_o/L$).

The determination of the minimum value of λ consists of feeding the various constants necessary into equation (7.33) and to calculate numerically the minimum value of λ by varying the value of B. Note that w_n does not appear in the ratio (equation 7.33) and since we are not concerned with the exact buckled shape, for this study it is

sufficient to say that w_n is non-zero.

In figure (7.3.1) we plot the variation of λ with the nose thickness h_o. It is evident that under a constant heat transfer rate as the nose thickness of the trapezoidal sections is reduced, the critical value of the stress level at which buckling would occur is considerably reduced. For a given plate geometry, the stress function is directly influenced by the temperature distribution which in turn depends upon the similarity laws derived in Chapter III. Hence for low values of nose thickness the leading edge would buckle under very much lower values of heating. Here again the importance of conducting material at the nose of a wing is emphasized in delaying the onset of thermal buckling.

Also shown in figure (7.3.1) are the critical values of λ for plates of constant thickness (0.0208 and 0.00833) subjected to the same heating. Both the values fall well below the corresponding results from the trapezoidal sections. Although the stress at X = 0 is lower for the plate, the reason it buckles earlier is that as compared with the trapezoidal section it has a much lower flexural rigidity. As the rear edge thickness is increased, both the parameters V and U_l register an increase, but the strain energy of bending (V) displays a proportionally higher increase leading to a greater value of the critical λ. Whereas the extra mass at the rear plays no part in the temperature distribution at the leading edge and in fact has an adverse effect on the stress value at X = 0, when it comes to thermal buckling, it does seem to have a favourable effect by increasing the stiffness of the plate and so delaying buckling.

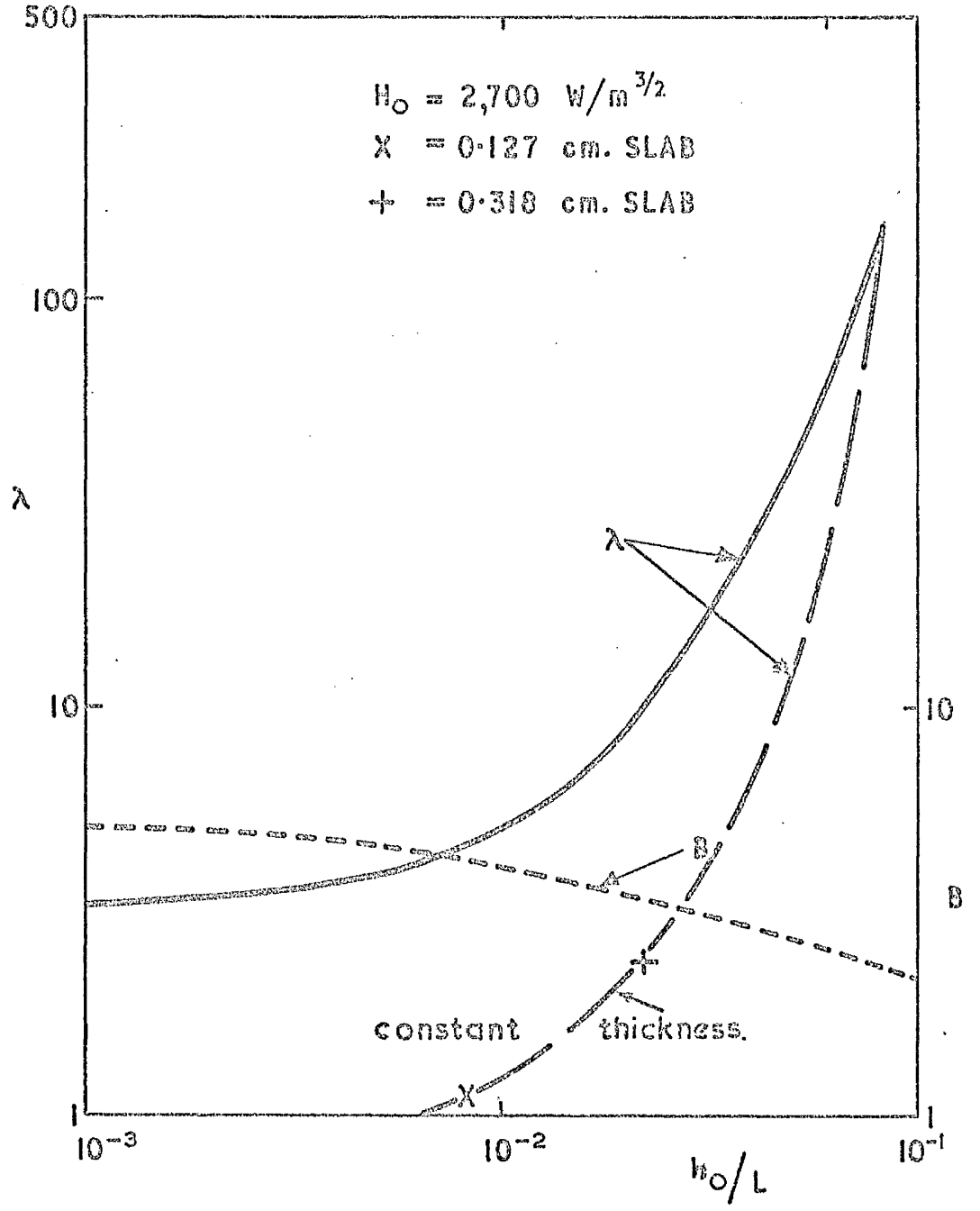

Fig. 7.3.1. VARIATIONS OF CRITICAL BUCKLING FACTOR FOR VARIOUS TRAPEZOIDAL CROSS-SECTIONS WITH $\bar{H} = 1 \cdot 27$ cms.

We also show in figure (7.3.1) the values of B that give the minimum value of equation (7.33) for trapezoidal variations of thickness. As expected (and consistent with our assumption) the value of B increases as the nose thickness is reduced. This indicates that the deformation of the plate (normal to the x - y plane) is confined more and more to regions close to the leading edge as the nose thickness is reduced, under the temperature distributions specified in this study.

What can be said of the effects of thermal conductivity on the thermal stability of the leading edges? Increasing the heat conduction at the nose of the wing reduces the variation of temperature which in turn would lead to lower stress levels. Similarly a decrease in the heat conduction would produce the opposite effects. Of all the shapes considered in Chapter III for the calculation of the temperature, the "ideal" shape from the buckling aspect is the one that produces a linear variation of temperature. Since the particular case of the optimal variation of thickness (to give a specified nose temperature) also displays a lower variation of temperature (compared with the slab section, say) suggesting that it would remain structurally stable for much higher rates of heat input than the other sections (with the exception of the linear temperature one, of course), it would indeed be a useful exercise to analyse its buckling behaviour by fitting some analytical expression to describe the optimal variation of thickness.

CHAPTER VIII

8.1 The Present Investigation in Retrospect.

In this investigation on the role of heat conduction at the leading edge of a hypersonic wing, the author claims originality for the following contributions.

The heat conduction equation for two-dimensional leading edges has been solved by three independent numerical methods. Theory of conducting plates has been formulated for the three-dimensional hypersonic wings, and the governing equation has been numerically solved by the iterative method of over-relaxation. Solutions have been presented where the streamwise cross-section of the material is trapezoidal and is subjected to an aerodynamic distribution of heat input varying as $(x + x_o)^{-\frac{1}{2}}$, x being measured in the stream direction from the leading edge. However, the computer programs that have been developed are quite general and capable of providing temperature distributions close to the leading edge of a hypersonic wing for any appropriate choice of the parameters (such as k, t, ϵ and Q) provided of course no singularity is encountered over the range of x and y that is of interest. It makes no difference to the operation of the programs if these parameters are represented by an analytical expression or are being obtained from a table of figures, as we have demonstrated where the rates of heat input were being interpolated from the actual measured values.

The theory of conducting plates has been extensively verified by the testing of eleven stainless steel models. It is desirable to conduct the experiments under as high a value of heating (given by the

parameter H_o) as possible. A theoretical study was carried out to discover what material would give the maximum power output from the electric filament. By replacing oxidized nickel wire by a tantalum one, an increase of 50% has been obtained. In order to measure exactly the local heat intensities impinging on the experimental models, it was necessary to develop special instruments. The design and development of a radiometer capable of measuring one-dimensional thermal radiation intensity has been published in reference (30).

Another line of research stemming from the main study, for reasons outlined in Chapter IV, was an investigation into the surface emissivity of stainless steel used in the making of experimental models, Of particular interest was ways and means of obtaining values of surface emissivity close to unity. Since adequate information was not available, equipment has been developed to measure the total hemispherical emissivity - (reference 35). Both electrically conducting and non-conducting solid materials can be tested because an indirect heating of the specimen is employed. The variation of surface emissivity with temperature for various surface roughness and oxidation conditions is presented in reference 36.

A study has been initiated to investigate the temperature distributions that can be expected to exist within wing structures which may be fairly complex internally. Where numerical solutions may not be easily obtainable, we propose to extract useful information from the experimental set up. Initial results from a two-dimensional hollow leading edge region have already been presented in Chapter IV.

The use of a reflector to simulate aerodynamic heating (as in

two-dimensional models) has been superseded by the use of a heated wire held close to the model and alongside the leading edge. With further development (discussed later on) it seems possible that the models could be tested under much higher average rates of heat flux.

For a conducting plate, the equations for a rounded apex region have been formulated. It is shown that provided the nose radius is considerably greater than the conduction length two-dimensional results are applicable for swept leading edges. The results presented in Chapters V and VI have been obtained for the first time. Some of the contents of Chapter III to VI have already been published in references 12 and 13.

A preliminary study into the stability of leading regions has been undertaken where actual temperature distributions that can be expected to exist there have been used to calculate the variation of thermal stresses. To estimate the onset of thermal buckling, a buckle shape appropriate to a plate tapered in the stream direction is assumed. This approach has been applied successfully to provide reasonable results.

8.2 Discussion of results and conclusions.

In this study which is based on the theory of conducting plates, we have investigated the effects of various parameters on the temperature distribution in the vicinity of a leading edge which is subjected to aerodynamic heat transfer likely to be encountered at hypersonic mach numbers. More particularly we have demonstrated the importance of the role of thermal conductivity in moderating the temperature distribution.

Whereas the classical boundary layer theory predicts the variation of heat transfer as $x^{-\frac{1}{2}}$ (x being measured in the stream direction from the leading edge), the infinite rates of heat input at $x = 0$ can never exist in practice. We have therefore modified this relation to give a $(x + x_o)^{-\frac{1}{2}}$ distribution of heat transfer, where x_o is a small fixed length. This enables us to subject the leading edge to appropriate finite rates of heat transfer while away from the nose the distribution essentially varies as $x^{-\frac{1}{2}}$. We have presented solutions in a parametric form of the governing heat transfer equations for a range of values of x_o that may be of interest.

From the results that we have presented, the following observarions can be made.

a) Ignoring the effects of thermal conduction within the material gives rise to radiation equilibrium temperature values everywhere. The thermal conductivity of the material plays a dominant role, over distances from the leading edge of the order of a "conduction" length (which we have defined as 1, and which is usually no more than a few centimeters in size), by reducing the temperature gradients everywhere. Heat is transported, within the material away from the leading edge to regions further downstream where the input of heat flux is considerably less than that at the nose.

If it is to have any effect, the conducting material must, therefore, be placed close to the leading edge of the wing. If the streamwise cross-section of this material is trapezoidal (i.e. it has a linear distribution of thickness), the nose thickness alone virtually determines the temperature distribution. For example, if

we keep the nose thickness fixed, an increase by a factor of 10 in the total amount of conducting material produces a change of less than 1% in the temperature distribution. If the same quantity of material is used to increase the nose thickness, however, we get nose temperatures which are lower by over 10%.

b) The effects of the thermal conductivity are important over lengths of the order of l (the conduction length) both in the chordwise and the spanwise directions. This enables us to divide the leading edge regions of a swept wing (with pointed apex) into three distinct strips - close to the apex, close to the tip, and the region between. The apex temperature is generally a maximum, but that at the tip may be another maximum, or a minimum, depending on its configuration. In the intermediate region, which represents the majority of the leading edge, the temperature distribution can be very easily estimated from the two-dimensional theory.

Even for the most highly swept leading edges it is shown that fortunately the temperature at a sharp apex does not rise by very much more than 10% over the corresponding unswept wing (two-dimensional) if we base the results on a common H_o and L. It is possible to keep this rise of apex temperature to a minimum by either locally enhancing the conducting properties (i.e. increasing the thickness or the thermal conductivity of the material) or eliminating the sharp apex of the planform by rounding the leading edge, - subject to the restriction that $R/l \gg 1$, where R is the nose radius. Since l is usually of the order of a few cm., this suggests that the radius of curvature of the leading edge might be about 1m. or so. Away from

the apex region (whether it is rounded or sharp), sweepback is seen to reduce the leading temperature below the corresponding two-dimensional value (see figure 5.6.3) where the basis for comparison is common values of H_o and L.

To estimate the apex temperature of a swept wing with pointed apex we first calculate the appropriate leading edge temperature of the unswept wing (from figures presented in Chapter III depicting plots of θ_o vs. τ_o). The effect of sweepback angle ϕ is then added on from figure (5.6.1).

c) The two-dimensional theory of conducting plates has been experimentally tested in the range of $\tau_o = (\frac{1}{L})^2$ where L is the downstream length, between 0.3 and 15. A family of trapezoidal sections (i.e. with a linear variation of thickness), comprising nine stainless steel models have been tested. The experimental results from six of these models have shown good agreement with the results predicted by the theory, with the maximum discrepency being less than 2%. However, for the three wedge sections the maximum discrepancy rises to about 5%. As well as other forms of unavoidable experimental error, we must now add the complication of machining and polishing a "sharp" wedge whose nose thickness is difficult to define. The effect of any small deviation in measurement from zero is expected to have a disproportionate effect upon the calculated temperature distribution, and particularly the nose value. Using the measured temperature as a basis for estimating the nose thickness (t_o) suggests that in our interpretation of the nose thickness of the wedge sections we have underestimated the value of this parameter.

d) The experimental set up is capable of providing useful analogue results for leading edge sections which may be difficult to analyse theoretically. As a first stage, we have tested two models to represent a practical two-dimensional leading edge with a hollow cross-section. The heat exchange by radiation within the cavity is not only difficult to formulate but would also present some difficulties when attempting numerical solutions. A comparison of test results with calculated temperature distributions that can be expected within a slab of the same thickness as the skin has revealed agreement to within - 3 to 4%. This further strengthens the usefulness of our simplified theory is estimating the nose temperatures. However, it is perhaps too early to draw any definite conclusions from the results of these two models regarding the effects upon the temperature distribution due to thermal radiation exchange within a cavity.

e) The measured performance of the reflector shows marked deviations from the theoretically assumed heat transfer distribution. However, these local disturbances have an insignificant effect upon the temperature distribution when we compare the calculated results based on the actual rates of heat transfer with those obtained for an ideal distribution of heat input using an appropriate value of the constant x_o.

f) In the testing of models to represent two-dimensional leading edges the simulated experimental rates of heat flux to the model were made to vary closely as a theoretically assumed form of heat transfer distribution. However, in the three-dimensional theory of conducting plates we have developed a heater capable of producing a hypothetical variation of heat intensities over a delta shaped model. Using an

analytical approach to represent approximately the output from this heater the heat conduction equation has been solved to give temperature distributions within about 3 - 4% of the actual measured values from two models that have been tested. This further strengthens our belief in the capability of the simplified theory of conducting plates to provide reasonable estimates of the temperature distribution along the surface subjected to appropriate aerodynamic rates of heat input.

g) For models with $\frac{L}{t} >> 1$, the temperature measurements across the thickness of the material indicate negligible temperature differences. This result is consistent with the basic assumption of the conducting plate theory which enables us to reduce the dimensionality of the heat transfer equations by one.

h) The preliminary investigation of the thermal stability of the two-dimensional leading edge reveals the existence of considerable thermal stresses due to the temperature variation in the chordwise dimension. Once again we have presented results for a family of trapezoidal sections with various values of the nose thickness subjected to the same heating conditions. Based on the numerical solutions giving the temperature distributions (Chapter III) that can be expected to exist, variation of thermal stress are calculated. As the nose thickness is decreased, the thermal stresses at the nose increase very rapidly, for example, reducing the nose thickness of a slab of fineness ratio $\frac{L}{t} = 12$ to a wedge with the same rear thickness, while increasing the nose temperature by about a third, also increases the stress by a factor of over 30. For all the sections, the stress levels

differ from one another only over a fraction of the length which is adjacent to the leading edge. The increase in the local value of the compressive stress at $x = 0$ produces a corresponding reduction in the value of the critical buckling factor. As expected the slab is capable of withstanding much higher values of heating than a wedge before thermal instability sets in.

Whereas a slab and a trapezoidal section of the same nose thickness have practically an identical temperature distribution, the stress pattern in the two sections are different, with the trapezoidal section displaying a higher compressive stress at the nose. The extra material at the rear of the trapezoidal section, however, adds to the flexural rigidity of this section as compared with the slab of the same nose thickness and as a result the slab section would buckle earlier.

8.3. Suggestions for further work.

The present investigation has made the author aware of several related topics of interest that need further attention.

In this study, the numerical solutions of the governing heat transfer equations for a conducting plate have been obtained assuming a heat input distribution given by a solution of the classical boundary layer theory. Such an approach had to be followed because of the lack of actual values of the rates of heat transfer likely to be encountered in hypersonic flight. The numerical methods that have been developed to provide the temperature distributions close to the leading edge can, however, be applied quite readily to predict the nose temperature under any appropriate form of aerodynamic heat

transfer to the wing. It would be very interesting to solve the heat conduction equations with the actual values of the local heat intensities and compare the results so obtained with the estimates of temperature distribution presented in this dissertation.

The actual wing structure is likely to be a complex affair with internal cavities, ribs and spar booms. The formulation of the heat transfer equations to these sections could be extremely complicated and the solution may even be impossible on the present day computers. However, as we have demonstrated with the help of the experimental apparatus that has been developed, analogue solutions can be readily obtained. Therefore, not only would it be possible to provide the temperature distributions that can be expected in realistic structures but the solutions may provide an insight into the complex phenomena governing the heat transfer. In this respect a study has been initiated to investigate the effects of internal cavities.

The wing surface may also be a composite structure with some special material possessing extremely high values of thermal conductivity placed at the leading edge to accentuate the moderating effect upon the nose temperature. However, where this material joins the rest of the load carrying structure deserves some attention. Once again work is well advanced to study the effects across a junction between two different materials and in particular the effect of this junction on the overall temperature distribution.

The thermal stability of leading edge sections subjected to aerodynamic heating has not yet received sufficient attention. A

preliminary investigation has been presented to provide some information as to the onset of buckling. A rigorous study of the problem is essential before making definite conclusions. As soon as finite span is introduced, end effects start to dominate the temperature distribution. In addition the three-dimensional wing is likely to have spanwise variations of temperature which, if included, is going to complicate the analysis considerably.

From the heat transfer considerations the surface of the wing should have as high a value of emissivity as possible to radiate away the maximum amount of heat. For most metals, the simplest way to increase the coefficient of emissivity is to roughen the surface and then oxidize it at a high temperature. However, this surface roughness is not consistent with the assumptions made in the analysis of the boundary layer and especially the effects of surface roughness on the heat transfer coefficient. This aspect has received hardly any consideration and some data on this problem would be very desirable.

The heater that has been constructed to test three-dimensional leading edges has shown considerable promise. With the development of small circular reflectors it seems possible that the proportion of power dissipated within the heating wire that actually reaches the model can be considerably increased over the present figure of about 10%. By superimposing the effects of more than one wire along the leading edge it would be possible to simulate aerodynamic heating with much higher rates of heat input (H_o) and so avoid the necessity of carrying out experiments on a scaled down temperature range. If necessary, several heating wires suitably arranged over the leading edge region of a wing may be used to simulate a given variation of heat intensity.

Appendix A

Derivation of the two-dimensional heat conduction equation in a finite differences form

The methods of Bandsolve and relaxation necessitate the derivation of the heat conduction equation in the finite differences form. We have adopted the central difference notation. The interval $X = 0, 1$ is divided into N equal divisions with end points $X_o, X_1, \ldots X_N$, (where $X_o = 0$ and $X_N = 1$). If we denote the value of θ at X_n by θ_n the equation (A.1) can be re-written (using reference 47) in the form,

$$\frac{1}{h}\left[\tau_{n+\frac{1}{2}}(\theta_{n+1} - \theta_n)\right] - \frac{1}{h}\left[\tau_{n-\frac{1}{2}}(\theta_{n-1} - \theta_n)\right] = h\left(e_n\theta_n^4 - \frac{1}{(n+X_o)^{\frac{1}{2}}}\right) \qquad (A.1)$$

with $h = 1/N$.

On re-arranging we get

$$\tau_{n+\frac{1}{2}}\theta_{n+1} - (\tau_{n+\frac{1}{2}} + \tau_{n-\frac{1}{2}})\theta_n + \tau_{n-\frac{1}{2}}\theta_{n-1} = h^2\left(e_n\theta_n^4 - \frac{1}{(n+X_o)^{\frac{1}{2}}}\right) \qquad (A.2)$$

i.e. $$\tau_{n+\frac{1}{2}}\theta_{n+1} - (\tau_{n+\frac{1}{2}} + \tau_{n-\frac{1}{2}} + h^2 e_n\theta_n^3)\theta_n + \tau_{n-\frac{1}{2}}\theta_{n-1}$$

$$= -\frac{1}{(n+X_o)^{\frac{1}{2}}} \quad \text{where} \quad n = 0(1)N \qquad (A.3)$$

Equation (A.3) represents (N + 1) simultaneous equations with N + 3 unknowns, namely $\theta_{-1}, \theta_o, \ldots \theta_n, \ldots \theta_{N+1}$. The values of θ_{-1} and θ_{N+1} occuring in the equation at n = 0 and n = N, respectively do not exist: However, the boundary conditions at X = 0, 1 supply us with the two additional relations necessary. We know

$$\frac{d\theta}{dX} = 0 \quad \text{at} \quad X = 0, 1. \qquad (A.4)$$

and in the present notation these can be expressed as

$$\theta_{-1} = \theta_1 \; ; \qquad \text{and} \qquad \theta_{N+1} = \theta_{N-1} \tag{A.5}$$

Unfortunately, of course, equations (A.3) are not a set of linear equations. However, there may exist a convergent iterative method of solution. If $\theta_n^{(i)}$ denotes the value of θ_n after the completion of the ith iteration ($\theta_n^{(o)}$ being a starting value), then

$$\left[\theta_n^{(i+1)}\right]^4 = \left[\theta_n^{(i)} + \left(\theta_n^{(i+1)} - \theta_n^{(i)}\right)\right]^4$$

and expanding

$$\text{i.e.} \quad \left[\theta_n^{(i+1)}\right]^4 = \theta_n^{(i)4} + 4\theta_n^{(i)3}\left[\theta_n^{(i+1)} - \theta_n^{(i)}\right] + R \tag{A.6}$$

where R is small (of second order) if the difference between the interpolates is small. Substituting equation (A.6) into (A.3) gives

$$\tau_{n+\frac{1}{2}}\theta_{n+1}^{(i-1)} + \tau_{n-\frac{1}{2}}\theta_{n-1}^{(i)} - \left[\tau_{n+\frac{1}{2}} + \tau_{n-\frac{1}{2}} + 4h^2 e_n \theta_n^{(i-1)3}\right]\theta_n^{(i)}$$

$$= -h^2\left[\frac{1}{(n+X_o)^{\frac{r}{2}}} + 3e_n\theta_n^{(i-1)4}\right] \tag{A.7}$$

where $\theta_{n+1}^{(i)}$ has also been replaced by $\theta_{n+1}^{(i-1)}$.

Equation (A.7) can be more concisely represented by the matrix equation

$$\underline{C} \cdot \underline{\theta} = \underline{B} \tag{A.8}$$

where $\underline{\theta}$ is the vector $(\theta_o, \theta_1, \ldots \theta_n, \ldots\ldots\ldots \theta_N)$; $\underline{B}$ is the column vector whose general element is $-h^2\left(\frac{1}{(n+X_o)^{\frac{r}{2}}} + 3e_n\theta_n^{(i)4}\right)$ and $\underline{C}$ is the band matrix.

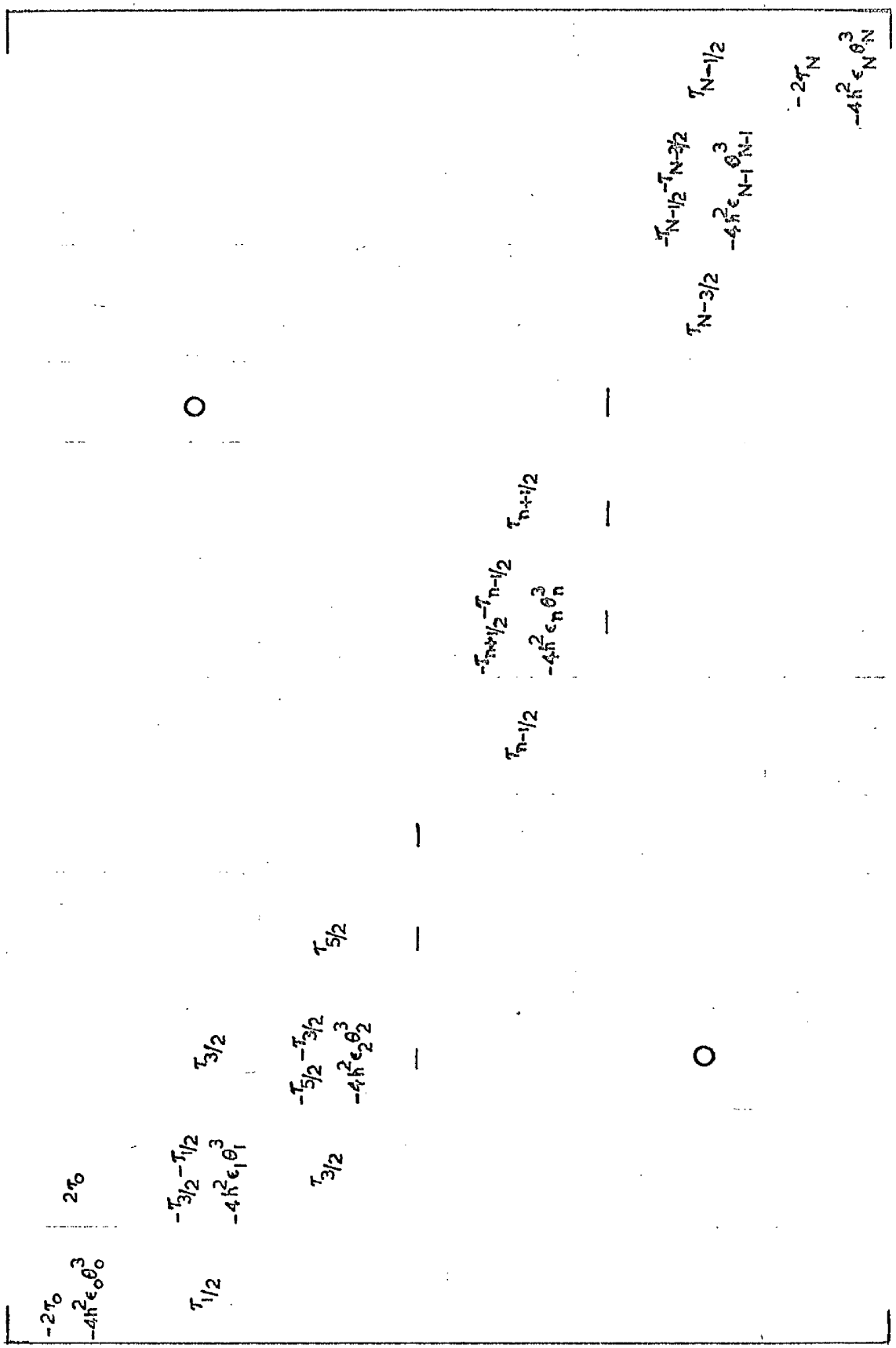
$-2\tau_0$
$-4h^2\epsilon_0\theta_0^3$
$2\tau_0$
$\tau_{1/2}$
$-\tau_{3/2}-\tau_{1/2}$
$-4h^2\epsilon_1\theta_1^3$
$\tau_{3/2}$
$\tau_{3/2}$
$-\tau_{5/2}-\tau_{3/2}$
$-4h^2\epsilon_2\theta_2^3$
$\tau_{5/2}$
$\tau_{n-1/2}$
$-\tau_{n+1/2}-\tau_{n-1/2}$
$-4h^2\epsilon_n\theta_n^3$
$\tau_{n+1/2}$
$\tau_{N-3/2}$
$-\tau_{N-1/2}-\tau_{N-3/2}$
$-4h^2\epsilon_{N-1}\theta_{N-1}^3$
$\tau_{N-1/2}$
$-2\tau_N$
$-4h^2\epsilon_N\theta_N^3$

Fig.

Under the specified boundary conditions (equation A.4 or A.5) for n = 0 and n = N, the following relations have been used in the matrix for the vector $\underline{C}$,

$$\left.\begin{aligned} \tau_{\frac{1}{2}} &= \tau_{-\frac{1}{2}} \\ \text{and } \tau_{N+\frac{1}{2}} &= \tau_{N-\frac{1}{2}} \end{aligned}\right\} \qquad (A.9)$$

Also for sufficiently small value of h,

$$\left.\begin{aligned} \tau_{\frac{1}{2}} + \tau_{-\frac{1}{2}} &\simeq 2\tau_{o} \\ \text{and } \tau_{N+\frac{1}{2}} + \tau_{N-\frac{1}{2}} &\simeq 2\tau_{N} \end{aligned}\right\} \qquad (A.10)$$

are valid approximations.

We can now write

$$\underline{C}^{(i-1)} \cdot \underline{\theta}^{(i)} = \underline{B}^{(i-1)} \qquad (A.11)$$

to represent that $\theta_n = \theta_n^{(i-1)}$ is used in the elements of $\underline{C}$ and $\underline{B}$ whilst solving for $\theta_n^{(i)}$.

Appendix B

The influence of high vacuum on heat transfer.

The concept of mean free path is extremely important in vacuum engineering in that it defines the boundaries of two different types of gaseous flow. At atmospheric pressure or low vacuum conditions, the mean free path is exceedingly small. Hence, the molecules are in a constant state of intercollision, transferring energy, or momentum through the gas. The momentum transfer from molecule to molecule leads to the concept of gas viscosity, and the flow itself is called viscous flow.

As the pressure decreases to the high vacuum regions, the mean free path becomes much longer than the dimensions of the confining chamber, with the result that the molecules will collide more frequently with the walls of the chamber than with each other. Gas flow in such a molecular flow regime is no longer dependent on momentum transfer between molecules, but now depends only on the statistical motion of the independently moving molecules.

All the experimental investigations have been carried out in a high vacuum environment with pressures of around 2 $m^1/_m{}^2$. To find out the effects of vacuum on the modes of heat transfer recourse has to be made to the kinetic theory of gases. For a Maxwell-Boltzmann distribution of molecular velocities, reference (46) quotes for the mean free path λ,

$$\lambda = 8.589 \times \frac{\eta}{P} \left(\frac{T}{M}\right)^{\frac{1}{2}} \text{ cm.} \qquad (B.1)$$

where η = coefficient of dynamic viscosity measured in Poise.

T = absolute temperature.

P = pressure measured in torr.

M = molecular mass of the gas.

At low densities the Knusden number (Kn) is used to separate the free molecular from the viscous flow where convective heat transfer can occur. For the range $10 < Kn < 100$ free molecular conditions prevail. The Knusden number is defined as

$$Kn = \frac{\lambda}{L} \qquad (B.2)$$

where L is the body characteristic length.

Inside the vacuum chamber different parts attain various temperatures (from as high as $3000^{\circ}K$ on the heater filament wire to about $300^{\circ}K$ on the vacuum chamber wall.) To complicate matters further the coefficient of dynamic viscosity decreases at extremely low pressures and increases with temperature. The molecular weight of air also undergoes a small reduction at low pressures. Assuming a representative temperature of about $800^{\circ}K$, equations (B.1) and (B.2) give $Kn \simeq 50$ where L = 30cms.

Thus in addition to heat exchange by radiation some free molecular conduction transfer can occur. To assess the magnitude of heat loss due to free - molecular conduction (E_o) reference (46) suggests

$$E_o = \frac{1.47 \times 10^{-7}}{M^{\frac{1}{2}}} \left(\frac{\gamma + 1}{\gamma - 1}\right) \quad W/cm^2 /^{\circ}K$$

where γ is the ratio of the specific heats.

A calculation based on some representative values of parameters indicates that as compared with the amount of heat dissipated by radiation from the top surface of the model, the effect of free-molecular heat conduction loss would be less than 0.05%.

Appendix C

Derivation of the three-dimensional heat transfer equation in the finite differences form

The equation to be solved is

$$\frac{\partial}{\partial X}\left(\mathcal{T}\frac{\partial\theta}{\partial X}\right) + \frac{\partial}{\partial Y}\left(\mathcal{T}\frac{\partial\theta}{\partial Y}\right) = e\theta^4 - q \qquad (C.1)$$

where $q = (X + X_o - y\tan\phi)^{-\frac{1}{2}}$

In order to express the equation in a form suitable for a numerical solution to be attempted we linearise the equation and also derive it in a finite - differences form (not necessarily in that order). The latter process is essential for seeking a solution by the method of over-relaxation.

As explained in Chapter V, we solve this equation over a strip of length L (measured in the x-direction) parallel to the leading edge swept at an angle ϕ. The area of interest lies close to the apex of the delta wing and is shown in figure (C.1) which also shows the boundary conditions imposed on the four edges of this strip. The units of length have been non-dimensionalised by dividing them by L.

We divide the interval X = 0,1 into N equal divisions with $h_c = \frac{L}{N}$. In order that the four edges always coincide with grid points, the grid has, in general to be rectangular such that $h_s = h_c \cdot \frac{S}{C}$, where we have divided the interval (0,S) of Y into M equal divisions of length h_s each. Therefore,

$$M = \frac{S}{h_s} = \frac{C}{L}\ N$$

We shall denote the value of θ at X_n and Y_m by $\theta_{n,m}$ where

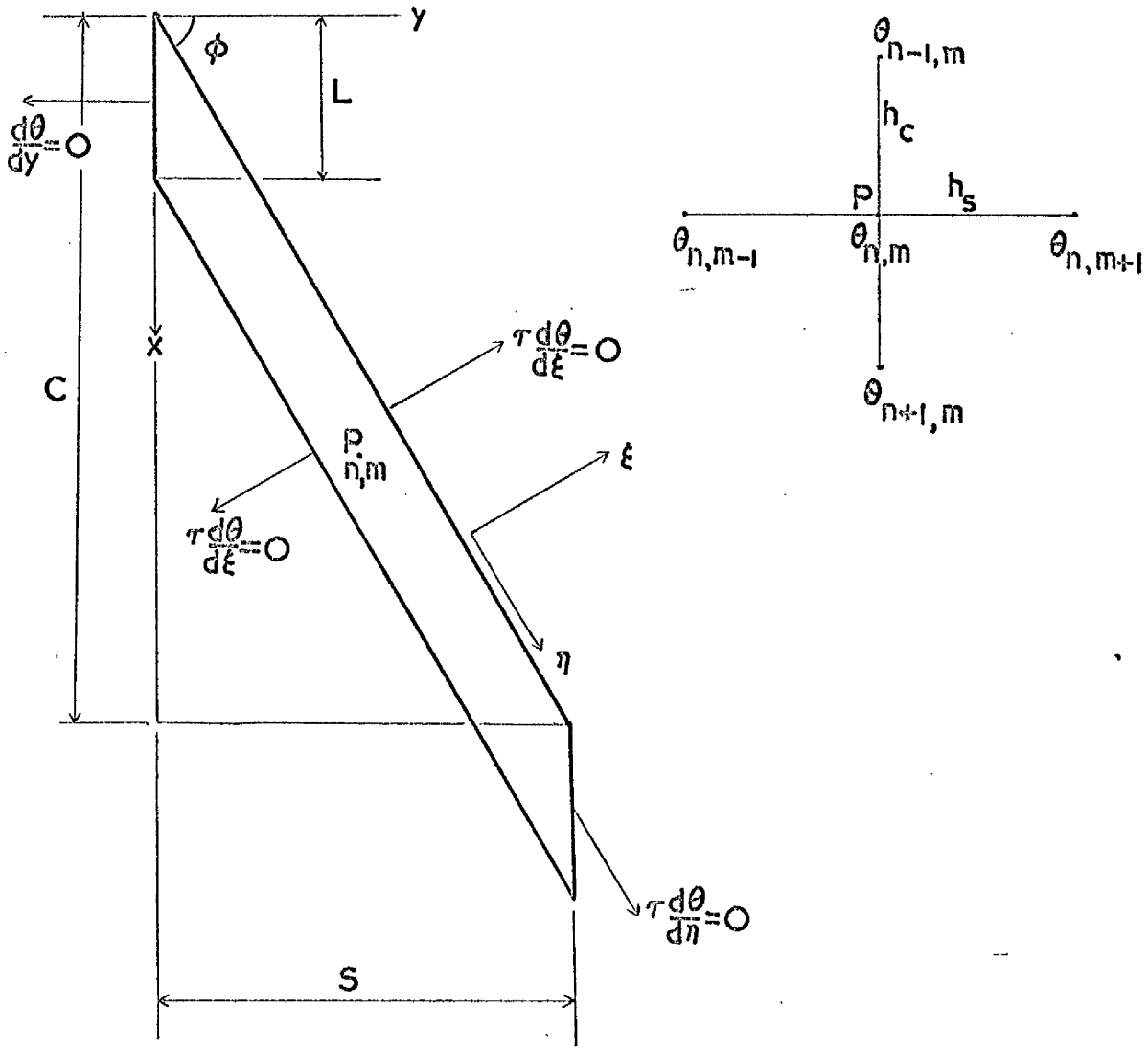

Figure C.1 Mathematical model of the cropped-delta wing.

$n = 0,1,\ldots N$ and $m = 0,1 \ldots M$. Using the central difference notation we can express the value of $\theta_{n,m}$ at any general point P in terms of the values of the four surrounding points (shown in the insert in figure C.1). Using reference (47) we can express equation (C.1) into the finite differences form which is

$$\frac{1}{h_c^2}\left\{ \tau_{n+\frac{1}{2},m}(\theta_{n+1,m} - \theta_{n,m}) - \tau_{n-\frac{1}{2},m}(\theta_{n,m} - \theta_{n-1,m})\right\}$$

$$+ \frac{1}{h_s^2}\left\{ \tau_{n,m+\frac{1}{2}}(\theta_{n,m+1} - \theta_{n,m}) - \tau_{n,m-\frac{1}{2}}(\theta_{n,m} - \theta_{n,m-1})\right\}$$

$$= e_{n,m}\theta_{n,m}^4 - q \qquad (C.2)$$

where $q = (n + X_o - m \tan \phi)^{-\frac{1}{2}}$

Re-arranging equation (C.2) gives

$$-\theta_{n,m}\left\{\frac{1}{h_c^2}(\tau_{n+\frac{1}{2},m} + \tau_{n-\frac{1}{2},m}) + \frac{1}{h_s^2}(\tau_{n,m+\frac{1}{2}} + \tau_{n,m-\frac{1}{2}}) + e_{n,m}\theta_{n,m}^3\right\}$$

$$+ \frac{\theta_{n+1,m}}{h_c^2} \times \tau_{n+\frac{1}{2},m} + \frac{\theta_{n-1,m}}{h_c^2} \times \tau_{n-\frac{1}{2},m} + \frac{\theta_{n,m+1}}{h_s^2} \times \tau_{n,m+\frac{1}{2}}$$

$$+ \frac{\theta_{n,m-1}}{h_s^2} \times \tau_{n,m-\frac{1}{2}} = -q \qquad (C.3)$$

We now linearise the set of equations given by (C.3.) If we denote the value of $\theta_{n,m}$ after ith iteration by $\theta^i_{n,m}$ ($\theta^o_{n,m}$ being the starting value), then

$$(\theta^i_{n,m})^4 = \left[\theta^{i-1}_{n,m} + (\theta^i_{n,m} - \theta^{i-1}_{n,m})\right]^4$$

$$= (\theta^{i-1}_{n,m})^4 + 4(\theta^{i-1}_{n,m})^3(\theta^i_{n,m} - \theta^{i-1}_{n,m}) + R \qquad (C.4)$$

where R is small (of the second order) if the difference between the interpolates is small.

On re-arranging equation (C.4), we get

$$(\theta^{i}_{n,m})^{4} = -3(\theta^{i-1}_{n,m})^{4} + 4(\theta^{i-1}_{n,m})^{3}.\theta^{i}_{n,m} \qquad (C.5)$$

Substituting equation (C.5) into equation (C.3) and a little re-arranging gives the iterative form of equation (C.3) as

$$-\theta^{i}_{n,m}\left\{\frac{1}{h_c^2}(\mathcal{T}_{n+\frac{1}{2},m} + \mathcal{T}_{n-\frac{1}{2},m}) + \frac{1}{h_s^2}(\mathcal{T}_{n,m+\frac{1}{2}} + \mathcal{T}_{n,m-\frac{1}{2}}) + 4e_{n,m}(\theta^{i-1}_{n,m})^{3}\right\}$$
$$+\frac{\theta^{i}_{n+1,m}}{h_c^2}\times\mathcal{T}_{n+\frac{1}{2},m} + \frac{\theta^{i}_{n-1,m}}{h_c^2}\times\mathcal{T}_{n-\frac{1}{2},m} + \frac{\theta^{i}_{n,m+1}}{h_s^2}\times\mathcal{T}_{n,m+\frac{1}{2}}$$
$$+\frac{\theta^{i}_{n,m-1}}{h_s^2}\times\mathcal{T}_{n,m-\frac{1}{2}} = -q - 3e_{n,m}(\theta^{i-1}_{n,m})^{4} \qquad (C.6)$$

Equation C.6 can be modified to give

$$\theta^{i}_{n,m} = \left[q + 3e_{n,m}(\theta^{i-1}_{n,m})^{4} + \frac{\theta^{i-1}_{n+1,m}}{h_c^2}\times\mathcal{T}_{n+\frac{1}{2},m} + \frac{\theta^{i}_{n-1,m}}{h_c^2}\times\mathcal{T}_{n-\frac{1}{2},m}\right.$$
$$\left.+\frac{\theta^{i-1}_{n,m+1}}{h_s^2}\times\mathcal{T}_{n,m+\frac{1}{2}} + \frac{\theta^{i}_{n,m-1}}{h_s^2}\times\mathcal{T}_{n,m-\frac{1}{2}}\right] \Bigg/ \left[\frac{1}{h_c^2}(\mathcal{T}_{n+\frac{1}{2},m} + \mathcal{T}_{n-\frac{1}{2},m})\right.$$
$$\left.+\frac{1}{h_s^2}(\mathcal{T}_{n,m+\frac{1}{2}} + \mathcal{T}_{n,m-\frac{1}{2}}) + 4e_{n,m}(\theta^{i-1}_{n,m})^{3}\right] \qquad (C.7)$$

where $\theta^{i-1}_{n+1,m}$ and $\theta^{i-1}_{n,m+1}$ just determined from the previous iteration is used in place of $\theta^{i}_{n+1,m}$ and $\theta^{i}_{n,m+1}$ respectively. To use the method of over-relaxation we introduce the over-relaxation parameter ω into equation C.7 to give,

$$\theta^{i}_{n,m} = (1-\omega)\theta^{i-1}_{n,m} + \omega\left[q + 3e_n(\theta^{i-1}_{n,m})^4 + \frac{1}{h_c^2}\left\{\theta^{i-1}_{n+1,m}.T_{n+\frac{1}{2},m} + \theta^{i}_{n-1,m}.T_{n-\frac{1}{2},m}\right\}\right.$$

$$\left. + \frac{1}{h_s^2}\left\{\theta^{i-1}_{n,m+1}.T_{n,m+\frac{1}{2}} + \theta^{i}_{n,m-1}.T_{n,m-\frac{1}{2}}\right\}\right] \Bigg/ \left[\frac{1}{h_c^2}\left\{T_{n+\frac{1}{2},m} + T_{n-\frac{1}{2},m}\right\}\right.$$

$$\left. + \frac{1}{h_s^2}\left\{T_{n,m+\frac{1}{2}} + T_{n,m-\frac{1}{2}}\right\} + 4e_{n,m}(\theta^{i-1}_{n,m})^3\right] \qquad (C.8)$$

with n= 0,1,2,.....N and m= 0,1,2,.....M.

Equation C.8 therefore represents a set of (N+1)x(M+1) simultaneous equations.

Appendix D

ALGOL - 60 Computer Programme

D.1. Description of computer programme. The input of data is done with the aid of the procedure "RW". All the quantities are non-dimensionalised with respect to the leading edge length (LE), thermal conductivity (k) at $0^{\circ}C$ and the Stefan-Boltzman constant (sigma) which give for a reference temperature $TR = \left(\frac{k_o}{\sigma x\ LE}\right)^{1/3}$. Execution of the main programme starts with a call on the procedure "TempDist".

The leading edge section of the delta wing (see figure C.1.) is divided into a coarse grid, the length LE being divided into 4 intervals only. In the spanwise direction the intervals are decided upon by the geometry of the wing. Generally, the grid is rectangular such that all the edges of the cropped delta fall on grid points. A starting value of temperature which in this case happens to be a fraction of the radiation equilibrium temperature is allocated to every point of the coarse grid.

To supplement the core store of the computer all the grid points are stored in columns on a magnetic tape. At any given time the computer handles a maximum of three columns. The middle column is relaxed term by term (the terms being updated at the same time) inside the procedure "overelax". The first column is then transferred to the second magnetic tape and one more column is read from the first magnetic tape. In this fashion, all the columns are progressively over-relaxed. Special arrangements are necessary for the first and the last columns of the grid because of the boundary conditions. At

the end of each iteration, if the covergence criterion (equation 3.21) is not satisfied, the whole grid is relaxed again. The two magnetic tapes are interchanged so that columns are now being read from the tape on which they were being written during the previous iteration.

Once a converged solution has been obtained, the number of intervals are doubled. The new points thus introduced in any column are interpolated using a third order relationship within the procedure "SUBTAB". On the other hand the terms of the new columns are calculated on a linear basis between the existing columns.

The whole of the grid is repeatedly relaxed again until a new converged solution is obtained. Next, a check is made on the "discretisation" error and if this criterion (equation 3.22) is not satisfied the internal points are doubled once again and the re-iterative process repeated. When both the criterions have been simultaneously satisfied, the solution is accepted and output. Equations 3.21 and 3.22, having to be summed over n = 0(1)N and m = 0(1)M.

The procedure "overelax" calls upon the procedures "Q", "kt" and "emissivity" to supply the values of these parameters corresponding to the relevant positions and the latest estimate of the temperature.

Outlet is provided from the procedure "TempDist", if the solution does not converge within a specified number of iterations, via the label UNCON. On the other hand, if the solution demands too fine a grid size (i.e. if it is necessary for the length LE to be divided into more than 1024 intervals) control is switched to the label "DISCRETE".

On successful completion of the programme the output consists of the data followed by the temperature distribution which is arranged in columns. To economise on computer time as well as paper, every

fourth term only is output.

D.2. The computational plan of the ALGOL text is summarised below in terms of the block structure and line numbers (25 lines to a page).

LINE 1 begin heading and introductory comment.

LINE 17 real procedure RW, reads in data from paper tape and prints out a copy of the description of the parameter followed by the value of the actual parameter.

LINE 23 real procedure kt, calculates the product of thermal conductivity and the thickness of the model.

LINE 31 real procedure Q, supplies the value of the rate of heat input at the specified location.

LINE 36 real procedure emissivity, provides the value of the coefficient of emissivity.

LINE 41 procedure TempDist, heading and full descriptive comment.

LINE 62 begin body of TempDist.

LINE 63 procedure overelax followed by descriptive comment.

LINE 70 begin body of overelax wherein the columns are assigned values using the latest estimates of temperature.

LINE 115 end overelax.

LINE 122 begin manipulation of magnetic tapes and transferring columns from tape to programme and back to the other tape.

LINE 188 begin check on convergence error.

LINE 206 goto UNCON.

LINE 212 begin check on discretisation error.

LINE 225 begin block to double the number of intervals, full descriptive comment.

LINE 237 procedure SUBTAB, with descriptive comment.

LINE 254 end SUBTAB.

LINE 282 end doubling the column size.

LINE 284 goto DISCRETE.

LINE 287 start the output of columns.

LINE 335 end TempDist.

LINE 346 Data input and non-dimensionalising of parameters.

LINE 381 call TempDist.

LINE 408 label DISCRETE.

LINE 410 label UNCON.

LINE 415 end programme.

D.3. The following is the text of a working ALGOL computer programme reproduced directly from paper tape. It starts on line 1 on the next page and thereafter the first line on the following pages are numbered 25, 50, 75, ... etc., to facilitate quick reference.

```
begin
  comment  SOLVES THE HEAT TRANSFER EQUATION FOR THREE-
  DIMENSIONAL DELTA WINGS.  THE METHOD OF OVER-RELAXATION
  IS USED ON THE EQUATION IN THE FINITE DIFFERENCES FORM.
```

The shape of the body is the leading edge portion of a delta wing (defined by the chord and semi-span). The tip cut-off is parallel to the centre line of the wing (i.e, a cropped-delta). The thermal conductivity, surface emissivity and the thickness of the material can all be functions of temperature and position. In the particular non-dimensional system used in this program, the three basic parameters used are k at 0 degC, sigma and the leading edge characteristic length L, together with the reference temperature TR= (k0/(sigma×L))↑(1/3);

```
  comment the program must have two magnetic tapes available
  at run time;
  real procedure RW(S);  string S;
    begin real t;
      RW:= t:= read (20);
      write text (70,S);  space (70,3);  output(70,t);
      newline (70,1);
    end LINE 22,   RW;
  real procedure kt (T,x,y);  value x,T,y;  real T,x,y;
    comment provides the product of thermal conductivity and
```

```
    the thickness of the model.  k and t can both be functions
    of temperature, x and y;
    comment uses non-local variable alpha and array data;
    begin comment assume constant t;
      kt:= (1.0 + alpha × (T - 273.15/TR))×data[1];
    end LINE 30,    kt;
real procedure Q(x);  value x;  real x;
    comment provides the heat input to the model.
    begin comment uses non-local variables Q0 and x0;
     Q:= Q0/sqrt(x+x0);
    end LINE 35,    Q;
real procedure emissivity(T);  value T;  real T;
    comment provides the variation of emissivity with temperature;
    begin comment uses non-local variables em and beta;
      emissivity:= em × (1.0 + beta × (T - 273.15/TR));
    end LINE 40,    emissivity;
procedure TempDist(f1,f2,f3,LE,ndchord,ndsemispan,TR,Tstart,
    TOL,omega,DISCRETE,UNCON,T00,TN0,T0M,TNM);
    integer f1,f2,f3,ndchord;
    real LE,TR,Tstart,TOL,omega,ndsemispan,T00,TN0,T0M,TNM;
    label DISCRETE,UNCON;
    comment over-relaxation is started by assigning the value
    Tstart to a coarse grid (the characteristic chord length LE
    being divided into 4 intervals).  The whole grid is
    repeatedly relaxed until the convergence error TOL has been
```

satisfied. After a converged solution has been obtained for the whole grid, the number of intervals are doubled and the points relaxed again. This process of doubling is repeated until the discretisation error is of the same order as the convergence error (i.e. TOL). Control is switched to the label UNCON if the the number of iterations allowed prove to be insuffiecient for convergence. Similarly, if the discretisation error demands too fine a grid (N > 1024) outlet is provided via label DISCRETE. The use of the optimum value of the over-relaxation parameter, omega is essential for an efficient use of the program;
comment uses non-local procedures Q, kt and emissivity;

```
begin
  procedure overelax(h,l,TA,TO,TB,N,d,M,omega);
    value h,l,d,N,M,omega;      integer d,N,M;
    real h,l,omega;      array TA,TO,TB;
    comment performs a single cycle of over-relaxation with
    given relaxation parameter omega and expects to find
    values of T[k] already assigned from previous iteration;
    comment uses non-local procedures Q,kt, and emissivity;
    begin real e,t1,t2;     integer k;
      e:=1.0-omega;
      t1:=1.0/(h×h);     t2:= 1.0/(l×l);
      for k:=0 step 1 until N do
      begin real rhs; array rn,rs,rw,re[1:2];
```

```
rhs:=Q(k×h)+3.0×emissivity(TO[k])×TO[k]↑4.0;
if d=0 then
begin
  rw[1]:=t2×kt(0.5×(TO[k]+TB[k-1]),h×k,1×(d+0.5));
  rw[2]:=rw[1]×TB[k-1]
end
else
begin
  rw[1]:=t2×kt(0.5×(TO[k]+TA[k+1]),h×k,1×(d-0.5));
  rw[2]:=rw[1]×TA[k+1];
end LINE 85;
if d=M then
begin
  re[1]:=t2×kt(0.5×(TO[k]+TA[k-1]),h×k,1×(d-0.5));
  re[2]:=re[1]×TA[k-1]
end
else
begin
  re[1]:=t2×kt(0.5×(TO[k]+TB[k-1]),h×k,1×(d+0.5));
  re[2]:=re[1]×TB[k-1];
end LINE 95;
rn[1]:=t1×kt(0.5×(TO[k]+TO[k-1]),h×(k-0.5),d×1);
rn[2]:=rn[1]×TO[k-1];
rs[1]:=t1×kt(0.5×(TO[k]+TO[k+1]),h×(k+0.5),d×1);
rs[2]:=rs[1]×TO[k+1];
```

```
        TO[k]:= eXTO[k]+omegaX(rhs+rs[2]+rn[2]+re[2]+rw[2])/
            (rs[1]+rn[1]+rw[1]+re[1]+4.0Xemissivity(TO[k])X
            TO[k]↑3.0);
      end LINE 103;
      if d=0 then
      begin TO[-1]:=TO[1];    TB[-1]:=TO[0];
      end
      else if d>0 and d<M then
      begin
        TB[-1]:=TA[1]+t1/t2X(TO[1]-TO[-1]);
        TA[N+1]:= TB[N-1] - t1/t2X(TO[N+1] - TO[N-1]);
      end
      else if d=M then
      begin TA[N+1]:= TO[N];    TO[N+1]:= TO[N-1];
      end LINE 114;
    end LINE 115,    over relax;
integer w,r,j,N,M;          real l,h,term,spt,sum;
w:= 100;    r:= 101;
find(w,[********]);     find(r,[DG150003]);
N:= 4;       M:= ndchord X N;
for j:= 1 step 1 until 9 do
begin
  begin integer c, d, k, NPLUS1;        real eps;
    array TA,TO,TB,TCOPY[-1:N+1];       boolean swing;
    NPLUS1:= N+1;
```

```
h:= 1.0/N;  l:= ndsemispan/M;
eps:= -TOL × (M+1) × (N+1);     term:= -TOL × (N÷2+1);
swing:= j≠1;
if swing then
begin
  readbinary (r,TO,[LABEL]);  writebinary(w,TO,[LABEL]);
  readbinary (r,TO,[LABEL]);  readbinary(r,TB,[LABEL])
end
else
for c:= -1 step 1 until NPLUS1 do TO[c]:= TB[c]:= Tstart;
for c:= 0 step 1 until N do  TCOPY[c]:= TO[c];
for k:= 1 step 1 until 200 do
begin
  sum:= eps;
  for d:= 0 step 1 until M do
  begin
    overelax(h,l,TA,TO,TB,N,d,M,omega);
    if d= 0 then
    begin
      for c:=0 step 1 until N do
      sum:= sum+abs(TCOPY[c]-TO[c]);
      for c:= -1 step 1 until NPLUS1 do
      begin TA[c]:= TO[c];  TO[c]:=TCOPY[c]:= TB[c];
      end LINE 148;
      if j= 1 then writebinary(w,TA,[LABEL]);
```

```
    if j= 1 and k= 1 then
    begin
      for c:= -1 step 1 until NPLUS1 do TB[c]:=Tstart
    end
    else readbinary(r,TB,[LABEL]);
  end
  else if d=1 then
  begin
    for c:= 0 step 1 until N do
    sum:= sum+abs(TCOPY[c]-TO[c]);
    writebinary(w,TA,[LABEL]);
    for c:= -1 step 1 until NPLUS1 do
    begin  TA[c]:= TO[c];  TO[c]:= TCOPY[c]:= TB[c];
    end LINE 163;
    if j= 1 and k= 1 then
    begin
      for c:= -1 step 1 until NPLUS1 do TB[c]:= Tstart
    end
    else readbinary(r,TB,[LABEL]);
  end
  else if d<M then
  begin
    for c:=0 step 1 until N do
    sum:= sum+abs(TCOPY[c]-TO[c]);
    writebinary(w,TA,[LABEL]);
```

```
        for c:= -1 step 1 until NPLUS1 do
        begin TA[c]:= TO[c];  TO[c]:= TCOPY[c]:= TB[c];
        end LINE 177;
        if d= M-1 then goto PASS;
        if j= 1 and k= 1 then
        begin
          for c:= -1 step 1 until NPLUS1 do
          TB[c]:= Tstart;
        end
        else readbinary(r,TB,[LABEL]);
PASS:
      end
      else
      begin
        for c:= 0 step 1 until N do
        sum:= sum + abs(TCOPY[c]-TO[c]);
        writebinary(w,TA,[LABEL]);
        writebinary(w,TO,[LABEL]);
      end LINE 193;
    end LINE 194,   transferring terms to magnetic tape
    w at the end of one iteration;
    interchange(w);   rewind(w);   rewind(r);
    if sum<0 then goto RETURN;
    c:= w;   w:= r;   r:= c;
    interchange(w);
```

```
        readbinary(r,TA,[LABEL]);
        if j>1 then  writebinary(w,TA,[LABEL]);
        readbinary(r,TO,[LABEL]);
        readbinary(r,TB,[LABEL]);
        for c:= 0 step 1 until N do TCOPY[c]:= TO[c];
      end LINE 205;
      goto UNCON;
RETURN:
      write text (70, [[c]**N*=**]);   write(70,f1,N);
      write text (70, [*****ITERATIONS*=**]);
      write (70,f1,k);
      if swing then
      begin readbinary(w,TA,[LABEL]);
        readbinary(w,TB,[LABEL]);
        for c:= 0 step 2 until N do
        term:= term + abs(TA[c]-TB[c]);
        if term<0 and k=1 then
        begin TO0:= TB[0]×TR;    TN0:= TB[N]×TR;
          goto OUT;
        end LINE 219;
        rewind(w);   rewind(r);
      end LINE 221;
    end LINE 222,    a converged solution for the whole
    grid has been obtained;
    begin
```

```
comment This block expects to read from magnetic
tape (x) columns of array T (each column of size
[-1:N+1]). For each column the number of internal
points are doubled, the new points thus introduced
are interpolate using the procedure SUBTAB from the
existing points. The doubling process also involves
interpolating new columns of the array T. Columns
of array T and size [-1:2N+1] are transferred step
by step onto magnetic tape (y). Upon exit the values
of N and M are twice that on entry;
integer c,d,NPLUS1,oldn,x,y,mold;
array a[-1:N+1],TA,TO,TB[-1:N+N+1];
procedure SUBTAB(a,l,b); value l; integer l;
  array a,b;
  comment values of a[k] are supposed known for
  k= -1(1)l+1. This procedure assigns values to the
  array b[-1:2l+1]. The even numbered subscripts
  have the same value as in array <a> while the odd
  ones are interpolated using a third order
  relationship;
  begin integer k;
    for k:= l step -1 until 0 do  b[k+k]:= a[k];
    for k:= l+l-3 step -2 until 3 do
    b[k]:= (9.0×(b[k+1]+b[k-1])-b[k+3]-b[k-3])/16.0;
    b[-1]:= (5.0×(a[-1]+3.0×a[0]-a[1])+a[2])/16.0;
```

```
      b[1]:= (9.0×(a[1]+a[0])-a[2]-a[-1])/16.0;
      b[1+1-1]:= (9.0×(a[1]+a[1-1])-a[1+1]-a[1-2])/16.0;
      b[1+1+1]:= (5.0×(a[1+1]+3.0×a[1]-a[1-1])+
                  a[1-2])/16.0;
    end LINE 254,    SUBTAB;
x:= w;    y:= r;      interchange(y);
readbinary(x,a,[LABEL]);  readbinary(x,a,[LABEL]);
mold:= M;     oldn:= N;
SUBTAB(a,N,TA);
N:= N + N;     M:= M + M;
NPLUS1:= N + 1;
writebinary(y,TA,[LABEL]);
for d:= 1 step 1 until mold do
begin
  readbinary(x,a,[LABEL]);
  SUBTAB(a,oldn,TB);
  for c:= -1 step 1 until NPLUS1 do
  TO[c]:= (TA[c] + TB[c])×0.5;
  if d=1 then TO[0]:= TA[0]-0.25×(TA[0]-TB[0]);
  comment The new columns are interpolated using a
  linear relationship between the points of the
  existing columns.  At the apex the heat transfer
  across the centre-line is zero and therefore, a
  second order relationship is used;
  writebinary(y,TA,[LABEL]);
```

```
            writebinary(y,TO,[LABEL]);
            for c:= -1 step 1 until NPLUS1 do TA[c]:= TB[c];
          end LINE 277;
          writebinary(y,TB,[LABEL]);
          interchange(r);   rewind(w);   rewind(r);
          w:= x;   r:= y;
          interchange(w);
        end LINE 282,   doubling the grid size;
      end LINE 283;
      goto DISCRETE;
OUT:
      rewind(w);
      write text(70,[[p2c]***GRID**SIZE[c]***N*=**]);
      write(70,f1,N);
      write text(70,[[10s]M*=**]);   write(70,f1,M);
      l:= l × LE;   h:= h × LE;
      for j:= 0 step 16 until M do
      begin integer c,k,COUNT;    array A,B,C,D[-1:N+1];
        write text(70,[[3c][4s]N[6s]X*METRE]);
        for c:=j,c+4 while c≤ (if j=M then j else j+12) do
        begin
          write text(70,[*****M*]);   write(70,f1,c);
        end LINE 297;
        newline(70,1);
        space(70,20);
```

```
for c:= 0, c+4 while c≤ (if j=M then 0 else 12) do
begin
  write(70,f2,(j+c)×1);    space(70,4);
end LINE 303;
newline(70,2);
if j=M then
begin
  readbinary (w,A,[LABEL]);
  for k:= 0 step 4 until N do
  begin
    write(70,f1,k);  space(70,3);
    write(70,f2,h×k);    space(70,3);
    write(70,f3,A[k]×TR);     newline (70,1);
  end LINE 313;
  TOM:= A[0]×TR;     TNM:= A[N]×TR;
  goto ENOUGH;
end LINE 316;
if j= 0 then readbinary (w,A,[LABEL]);
readbinary (w,A,[LABEL]);  skip(w,+3);
readbinary(w,B,[LABEL]);  skip(w,+3);
readbinary (w,C,[LABEL]);  skip(w,+3);
readbinary(w,D,[LABEL]);  skip(w,+3);
for k:= 0 step 4 until N do
begin
  write(70,f1,k);  space(70,3);
```

```
            write(70,f2,h×k);  space(70,3);
            write(70,f3,A[k]×TR);  space(70,5);
            write(70,f3,B[k]×TR);  space(70,5);
            write(70,f3,C[k]×TR);  space(70,5);
            write(70,f3,D[k]×TR);  newline(70,1);
          end LINE 330;
          write text(70,[[p]]);
        end LINE 332;
ENOUGH:
        close(w);      close(r);
      end LINE 335,    TempDist;
    integer ndchord,f1,f2,f3;
    real chord, semispan,LE,k0,TR,Q0,x0,Tstart,TOL,alpha,em,
     beta,omega,SIGMA,ndsemispan,T00, TN0,TOM,TNM,H,TAU;
    array  data[1:10];
    open (20); open (70);
    SIGMA:= 5.67₁₀₋8;  comment Sigma has units in W/SQ.M/DEGK↑4;
    f1:= format ([-ndddd]);
    f2:= format ([-ndd.dddd]);
    f3:= format ([-ndddd.d]);
LOOP:
    chord:= RW([[p2c]WING*CHORD*LENGTH*-*UNITS***METRE]);
    semispan:= RW([WING*SEMI-SPAN*-*UNITS***METRE]);
    LE:= RW([LEADING*EDGE*CHARACTERISTIC*LENGTH*PARAMETER*-*
              UNITS***METRE]);
```

```
ndchord:= chord/LE;
ndsemispan:= semispan/LE;
comment the chord and semi-span lengths have been non
dimensionalised as multiples of the leading edge
parameter, LE;
data[1]:= RW([THICKNESS*OF*MODEL*-*UNITS***METRE]);
k0:= RW([THERMAL*CONDUCTIVITY*AT*0*DEGC*-*UNITS***W/M/DEGK]);
TR:= (k0/SIGMA/LE)↑(1/3.0);
x0:= RW([CUT*OFF*FACTOR*-*UNITS***METRE])/LE;
em:=  RW([EMISSIVITY*AT*0*DEGC]);
TAU:= RW([TAU0*-*1/L↑2.0]);
H:= ((k0×data[1]/TAU)↑8.0/(em×SIGMA)↑2.0/LE↑13.0)↑(1.0/6.0);
write text(70,[HEAT*FLUX*-*UNITS***W/M↑1.5***]);
write (70,f3,H);     newline(70,2);
Q0:= H×LE/k0/TR;
data[1]:= data[1]/LE;
beta:= RW([THERMAL*VARIATION*OF*EMISSIVITY*-*
            UNITS***PER*DEGC])×TR;
Tstart:= (H/SIGMA/em/sqrt(LE/2.0))↑0.25/TR;
TOL:= RW([TOLERANCE*ON*SUCCESSIVE*ITERATIONS*AND*
          DISCRETISATION*ERROR]);
alpha:= RW([CO-EFFICIENT*OF*THERMAL*CONDUCTIVITY*-*
            UNITS***PER*DEGC])×TR;
omega:= RW([OVER-RELAXATION*PARAMETER]);
newline(70,3);
```

```
write text (70,[REFERANCE*TEMPERATURE*DEGK**=***]);
write (70,f3,TR);    newline(70,2);
write text(70,[FINE-NESS*RATIO**=***]);
write(70,f2,data[1]);    newline(70,2);
write text(70,[ANGLE*OF*SWEEP-BACK**=***]);
write(70,format([-ndd.ddcc]),arctan(ndchord/ndsemispan)×57.3);
TempDist(f1,f2,f3,LE,ndchord,ndsemispan,TR,Tstart,TOL,omega,
    DISCRETE,UNCON,TOO,TNO,TOM,TNM);
write text(70,[[p2c]TEMPERATURE*AT*TIP*-*T**O,M*=***]);
write (70,f3,TOM);
write text(70,[[3c]RADIATION*EQUILIBRIUM*TEMPERATURE*-*
    T**N,O*=***]);
TR:= (H/SIGMA/em/sqrt(LE))↑0.25;
write (70,f3,TR);
write text(70,[[5c]NON-DIMENSIONAL*TEMPERATURES*WITH*
   RESPECT*TO*TIP*VALUE]);
write text(70,[[2c]T*O,O*=***]);
write (70,f2,TOO/TOM);
write text(70,[[2c]T*N,O*=***]);
write (70,f2,TNO/TOM);
write text(70,[[3c]T*N,M*=***]);
write (70,f2,TNM/TOM);
write text(70,[[5c]NON-DIMENSIONAL*TEMPERATURES*WITH*
   RESPECT*TO*TR*AT*T**N,O]);
write text(70,[[2c]T*O,O*=***]);
```

```
    write (70,f2,TOO/TR);
    write text(70,[[2c]T*N,O*=***]);
    write (70,f2,TNO/TR);
    write text(70,[[3c]T*O,M*=***]);
    write (70,f2,TOM/TR);
    write text(70,[[2c]T*N,M*=***]);
    write (70,f2,TNM/TR);
    goto if read boolean (20) then LOOP else FINISH;
DISCRETE: write text(70,[DISCRETISATION*ERROR*TOO*SMALL***
      SUGGEST**ALLOW*SMALLER*GRID*OR*INCREASE*TOL]);
UNCON: write text(70,[SOLUTION*NOT*CONVERGED***SUGGEST**
      INCREASE*NUMBER*OF*ITERATIONS**OR*INCREASE*TOL]);
    if read boolean (20) then goto LOOP;
FINISH: close(20);     close(70);
    comment Data contains (12, boolean);
end LINE 415;→
```

D. 4 The input to the computer program consists of a set of 12 parameters followed by a boolean statement. If the boolean is declared true then the program expects to read another set of 12 parameters. The run is terminated by making the boolean false. The 12 parameters required by the program must appear in the following order:-

1. Chord, C, see figure C.1 - units m.
2. Semispan, S, see figure C.1 - units m.
3. Leading edge length, L, see figure C.1 - units m.
4. Thickness of model - units m.
5. Thermal conductivity at $0^{o}C$ - units W/m ^{o}K.
6. X_o (non-dimensional).
7. Emissivity at $0^{o}C$.
8. Tau(non-dimensional).
9. Beta, coefficient of thermal emissivity - units $/^{o}C$.
10. Tolerance on convergence and discretisation error.
11. Alpha, coefficient of thermal conductivity - units $/^{o}C$.
12. omega, over-relaxation parameter.

A typical data tape might therefore consist of,
1.0; 0.5; 0.5; 0.02; 24.0; 10^{-2}; 0.7; 1.0; 3.0×10^{-4}; 10^{-5}; 2.5×10^{-4}; 1.6; false;

The output consists of a descriptive list of inputparameters together with certain other constants. An account of iterations taken at each grid size is also printed. The main output is arranged in columns (each column representing a constant value of Y) with the absolute values of local temperature in ^{o}K. Finally, a few of the temperature values (described adequately) are printed non-dimensionally with respect to various values of reference temperature.

Appendix E.

Theoretical modelling of experimental heat input to delta models.

The delta shaped heater used to simulate aerodynamic heat transfer to the apex region of a delta wing performs very differently from the distribution predicted by the $x^{-\frac{1}{2}}$ law. In order to correlate the experimental results with theory it is therefore necessary to subject the computer model to a heat distribution similar to the performance of the heater. This was achieved by replacing the wires of the heater by line sources of heat. Using a line source instead of a wire of finite thickness affords considerable simplification to the formulation of the equation. We make one further assumption, that the line sources of heat have a constant radiation intensity along the entire lengths.

The notation used in this section does not have the same significance elsewhere in this dissertation. Some of the nomenclature is indicated in figure E.1.

The two wires are inclined to the x-axis at a semi-apex angle γ If l is the length of each wire measured from the origin then

$$l = a + b = a_1 + b_1 \qquad \text{(E.1.)}$$

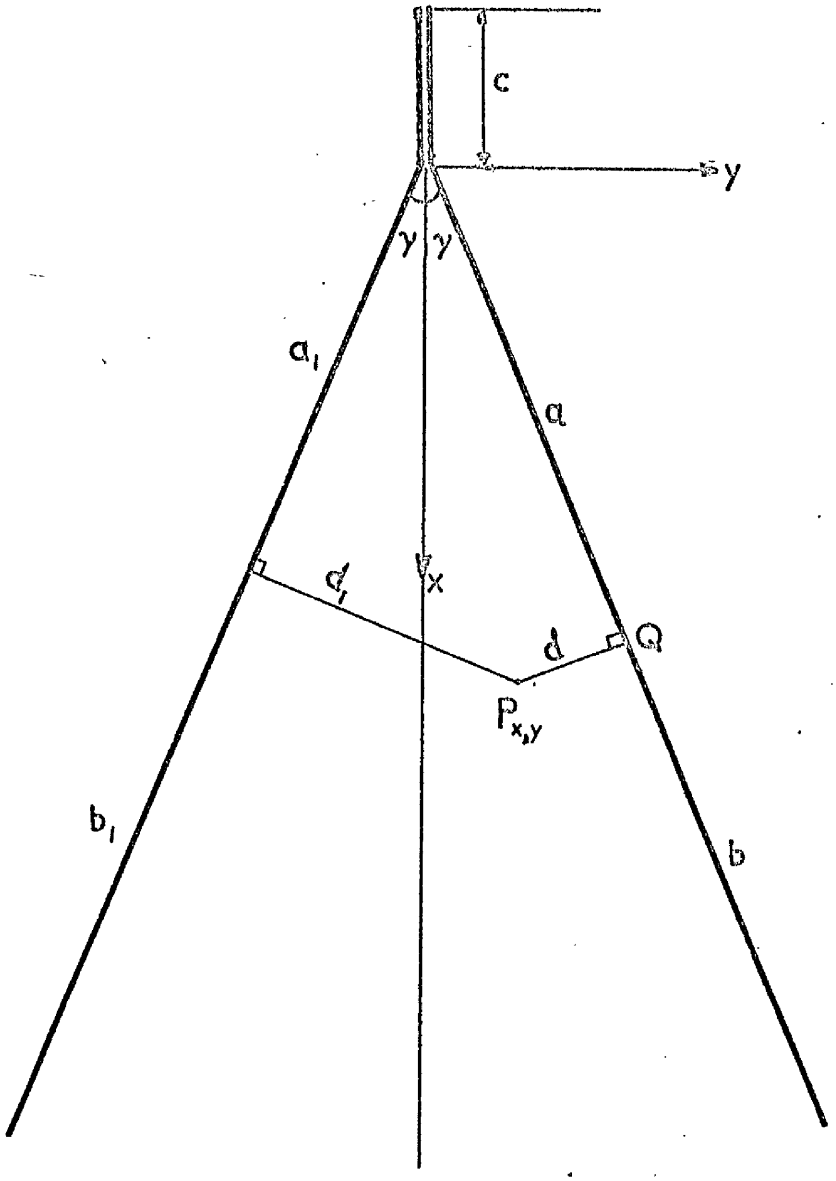

Figure E.1. Nomenclature and axes system for the line sources of radiation intensity along the leading edge.

Consider a general point P (x,y) in the plane of the model. We can associate the following distances with this point P.

$$a = x \cos\gamma + y \sin\gamma \qquad \text{(E.2.)}$$

$$b = 1 - (x \cos\gamma + y \sin\gamma) \qquad \text{(E.3.)}$$

$$a_1 = x \cos\gamma - y \sin\gamma \qquad \text{(E.4.)}$$

$$b_1 = 1 - (x \cos\gamma - y \sin\gamma) \qquad \text{(E.5.)}$$

$$d = x \sin\gamma - y \cos\gamma \qquad \text{(E.6.)}$$

$$d_1 = x \sin\gamma + y \cos\gamma \qquad \text{(E.7.)}$$

where the distance d is in the plane of the model.

We further define additional parameters as shown in figure E.2.

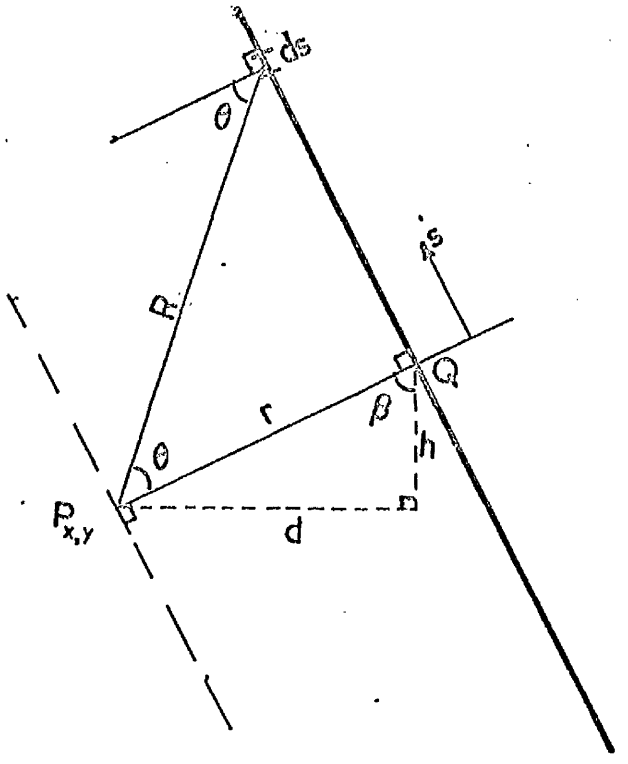

Figure E.2.

The two wires are held in a plane parallel to the top surface of the model at a height h above it. Consider an element ds at a distance s from the point Q on one of the wires as indicated in figure E.2. Let I be the radiation intensity of the line source. Through

the point P, in a plane parallel to the line source of heat, if E_p is the heat flux per unit area impinging on this plane, then we can write

$$E_p = \int_{-b}^{a} \frac{I}{R^2} \cos^2\theta \, ds. \qquad (E.8.)$$

where $R^2 = s^2 + r^2$ (E.9.)

and $r^2 = h^2 + d^2$ (E.10.)

Also $\cos^2\theta = \left(\frac{r}{R}\right)^2 = \frac{h^2 + d^2}{s^2 + h^2 + d^2}$ (E.11.)

Substituting equations (E.9) - (E.11) into equation (E.8.) gives

$$E_p = \int_{-b}^{a} \frac{I\,(h^2 + d^2)\, ds}{(s^2 + h^2 + d^2)^2}$$

$$= I.(h^2 + d^2) \left[\frac{s}{2(h^2+d^2)(h^2+d^2+s^2)} + \frac{1}{2(h^2+d^2)(h^2+d^2)^{\frac{1}{2}}} \tan^{-1} \frac{s}{(h^2+d^2)^{\frac{1}{2}}} \right]_{-b}^{a}$$

$$= \frac{I}{2r} \left[\tan^{-1}\frac{a}{r} + \tan^{-1}\frac{b}{r} + \frac{a.r}{(r^2+a^2)^{\frac{1}{2}}} + \frac{b.r}{(r^2+b^2)^{\frac{1}{2}}} \right] \qquad (E.12.)$$

Resolving E_p in the plane of the model, if E_1 is the heat flux per unit area impinging on the model, which comes from one wire, we can write

$$E_1 = E_p \cos\beta = \frac{I.h}{2r^2} \left[\tan^{-1}\frac{a}{r} + \tan^{-1}\frac{b}{r} + \frac{a.r}{(r^2+a^2)^{\frac{1}{2}}} + \frac{b.r}{(r^2+b^2)^{\frac{1}{2}}} \right] \qquad (E.13.)$$

Similarly we can derive the contribution from the other wire. In the notation we have used E_2 can be simply written down by replacing the parameters a,b,d and r by a_1, b_1, d_1, r_1, respectively, so that

$$r_1^2 = h^2 + d_1^2 \qquad (E.14.)$$

and $$E_2 = \frac{I.h}{2r_1^2} \left[\tan^{-1}\frac{a_1}{r_1} + \tan^{-1}\frac{b_1}{r_1} + \frac{a_1 r_1}{(r_1^2 + a_1^2)^{\frac{1}{2}}} + \frac{b_1 r_1}{(r_1^2 + b_1^2)^{\frac{1}{2}}} \right] \qquad (E.15.)$$

Near the apex of the delta, the distribution of heat transfer to the model is strongly influenced by the short length of the wire, c. (see figure E.1.)

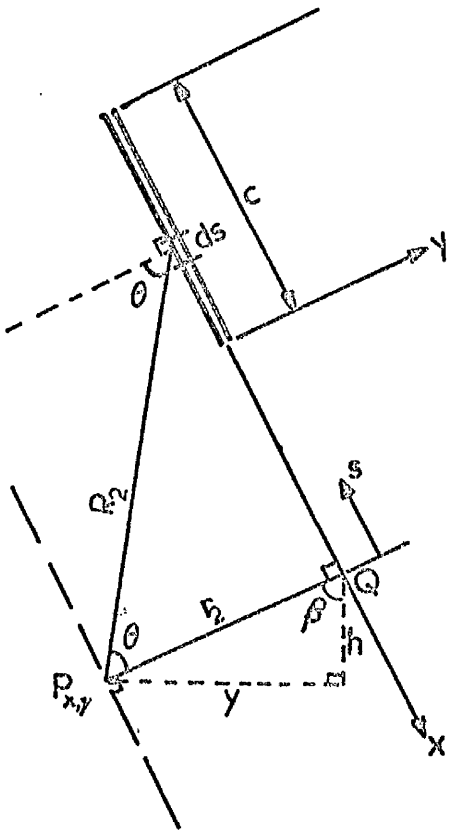

Figure E.3.

An approach similar to that of figure E.2. indicates that we now have d = y. Therefore,

$$r_2^2 = h^2 + y^2 \qquad \text{(E.16.)}$$

The contribution to the heat flux being radiated to the model by the two wires (E_3) can be written down as

$$E_3 = 2I \int_x^{(x+c)} \frac{(h^2 + y^2)\, ds \cos\beta}{(h^2 + y^2 + s^2)^2}$$

which on integration becomes

$$E_3 = \frac{I.h}{r_2^2}\left[\tan^{-1}\frac{c+x}{r_2} - \tan^{-1}\frac{x}{r_2} + \frac{(c+x)r_2}{(r_2^2+(c+x)^2)^{\frac{1}{2}}} - \frac{x.r_2}{(r_2^2+x^2)^{\frac{1}{2}}}\right] \qquad (E.17.)$$

The total heat flux (E) impinging on a unit area of the model is

$$E = E_1 + E_2 + E_3 \qquad (E.18.)$$

An ALGOL procedure has been developed to calculate the variation of heat transfer to the model based on equation (E.18.). This procedure was incorporated in the computer programme (replacing the real procedure Q), whose text is included in Appendix D, to calculate the temperature distribution in models subjected to approximately the experimental simulation of the aerodynamic heat transfer.

REFERENCES

No.	Author	Titles etc.
1.	Dorrance W.H.	Viscous hypersonic flow. McGraw-Hill Book Co. Inc. 1962.
2.	Cox R.N. Crabtree L.F.	Elements of hypersonic aerodynamics. The English Universities Press Ltd. 1965.
3.	Furey R.J.	Minimum energy hypersonic nose and leading edge shapes. AIAA paper No 70 - 825, July 1970.
4.	Nonweiler T.R.F.	Aerodynamic problems of space vehicles. J.R. Ae. Soc. 63 (585) 1959.
5.	Nonweiler T.R.F.	Delta wings of shapes amenable to exact shock wave theory. ARC 22644 HYP 165, March 1961. Also J.R. Ae. Soc. 67(625)1963.
6.	Nonweiler T.R.F.	Surface conduction of the heat transferred from a boundary layer. COA Report No.59, 1952.
7.	Nonweiler T.R.F.	Skin temperatures and heat transfer over wedge wings at extreme speeds. COA Report No. 105, 1956.
8.	Capey E.C.	Alleviation of leading-edge heating by conduction and radiation. R.A.E. Tech. Note No. 66311, October, 1966.
9.	Hanawalt A.J. Blessing A.H. Schmidt C.F.	Thermal analysis of stagnation regions with emphasis on heat-sustaining nose shapes at hypersonic speeds. J. Aero/Space Sciences - Vol. 26 No. 5 May 1959.
10.	Sinha B.P.	Conduction of heat within a body subjected to aerodynamic heating at hypersonic speeds. Ph.D. Thesis, University of Glasgow, September, 1966.

11.	Naysmith A. Woodley J.G.	Equilibrium temperatures on lifting surfaces at mach numbers between 5 and 12 at altitudes from 80,000ft. up to 150,000ft. RAE TR 67114, May 1967.
12.	Nonweiler T.R.F. Wong H.Y. Aggarwal S.R.	The role of heat conduction in leading edge heating - Theory and experiment, Glasgow University Report No. 6901, June, 1969. Also Aeronautical Research Council ARC Report No.31445,HYP 775 Also ARC CP.No.1126.
13.	Nonweiler T.R.F. Wong H.Y. Aggarwal S.R.	The role of heat conduction in leading edge heating. Presented at EUROMECH - 20 held at Cambridge, July 70. Also Ingenieur - Archiv
14.	Nonweiler T.R.F.	The two-dimensional laminar boundary layer at hypersonic speeds. COA Report No. 67, 1953.
15.	Heyes W.D. Probstein R.F.	Hypersonic flow theory. Academic Press, 1959.
16.	Truitt R.W.	Hypersonic Aerodynamics. The Roland Press Company 1959.
17.	Holloway P.F. Sterrett J.R.	Effect of controlled surface roughness on boundary-layer transition and heat transfer at Mach numbers of 4.8 and 6.0 NASA TN D-2054, April, 1964.
18.	Shorenstein M.L. Probstein R.F.	The hypersonic leading-edge problem. AIAA Journal, Vol. 6, No.10 October,1968.
19.	McCroskey W.J. Bogdonoff S.M. McDougall J.G.	An experimental model for the sharp flat plate in rarefied hypersonic flow. AIAA Journal, Vol.4, No. 9 September, 1966.
20.	Rudman S. Rubin S.G.	Hypersonic viscous flow over slender bodies with sharp leading edges. AIAA Journal Vol. 6, No.10, October, 1968.

21. Klineberg J.M. Lees L. — Theory of laminar viscous-inviscid interactions in supersonic flow. AIAA Journal, Vol.7, No.12, December 1969.

22. Kemp J.H. Jr. — Hypersonic viscous interation on sharp and blunt inclined plates. AIAA Journal, Vol.7, No.7, July 1969.

23. Stone H.W. — The leading-edge effects on the laminar flat-plate boundary layer and the aerodynamic heating at Mach 10.4. NASA TN D-5160. May, 1969.

24. Neal L.Jr. — A study of the pressure, heat transfer, and skin friction on sharp and blunt flat plates at Mach 6.8. NASA TN D-3312. April, 1966.

25. Arrington J.P. — Heat-transfer and pressure distributions due to sinusoidal distortions on a flat plate at Mach 20 in Helium. NASA TN D-4907, November, 1968.

26. Rubin S.G. Lin T.C. Pierucci M. Rudman S. — Hypersonic interactions near sharp leading edges AIAA Journal Vol. 7, No.9, September, 1969.

27. Bertram M.H. Everhart P.E. — An experimental study of the pressure and heat transfer distributions on a 70° sweep slab delta wing in hypersonic flow NASA TR R-153, December, 1963.

28. Wong H.Y. Sinha B.P. — Design of an infra-red radiation reflector for simulating aerodynamic heating. Aeronautical Research Council Report No. 29218, 1967.

29. Aggarwal S.R. — Design and development of a radiometer for measuring high radiation intensity with high radiation gradients. Glasgow University, Department of Aeronautics and Fluid Mechanics, Final Year Research Project, Report, 1966.

30. Wong H.Y. Aggarwal S.R. — Radiometer for measuring thermal radiation of one-dimensional intensity. Laboratory Practice, Oct. 1968.

31. Murex Ltd. — Technical Data Sheets. P. 25.

32. Hargrave D.P. — Molybdenum and Tungsten. Paper 5, conference on New Engineering Materials, 1965.

33. Touloukian Y.S. — Thermophysical properties of high temperature solid materials. The MacMillan Company, Vol. 1, 1965.

34. Firth-Vickers — Stainless Steel Ltd., Technical Data Sheet No. 103/17.

35. Wong H.Y. Aggarwal S.R. — Measurement of total hemispherical emittance. Laboratory Practice Jan. 1969.

36. Wong H.Y. Aggarwal S.R. — Total hemispherical emittance of stainless steel AISI 321. To be published.

37. Sully A.H.S Brandes E.A. Waterhouse R.B. — Some measurements of total emissivity and the variation of emissivity with temperature Brit. App. Phys., 3, 1952.

38. Jacob M. — Heat transfer. Vol. I, Chapman & Hall Ltd., 1959.

39. Howarth L. — Modern developments in fluid dynamics - High speed flow. Vol. I, Clarendon Press, Oxford, 1953.

40. Brase R. — Vector Analysis. Sir Isaac Pitman & Sons Ltd., London, 1968.

41. Arrington J.P. — Heat transfer and pressure distributions due to sinusoidal distortions on a flat plate at Mach 20 in helium. NASA TN D-4907, November, 1968.

42. Singer, Anliker M., Lederman S. — Thermal stresses and thermal buckling. WADC Tech. Rep. 57-69, ASTIA Document No. AD 118287, April, 1957.

43. Pope G.G. — The buckling of plates tapered in thickness. R.A.E. Report No. Strustures 272, October, 1961.

44. Timoshenko S., Goodier J.W. — Theory of elasticity. McGraw-Hill Book Co., 1951.

45. Timoshenko S. — Theory of elastic stability. McGraw-Hill Book Co., 1936.

46. Dushman S., Lafferty J.M. — Scientific foundations of vacuum technique. John Wiley & Sons, 1962.

47. Collatz L. — The numerical treatment of differential equations. Springer-Verlag, 1960.